Massachusetts Institute of Technology
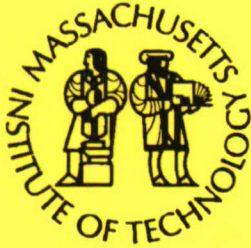# Woods Hole Oceanographic Institution

Joint Program in Oceanography/ Applied Ocean Science and Engineering

---

DOCTORAL DISSERTATION

Oceanic Lithosphere Magnetization: Marine Magnetic Investigations of Crustal Accretion and Tectonic Processes in Mid-Ocean Ridge Environments

by

Clare M. Williams

September 2007

MIT/WHOI

2007-21

Oceanic Lithosphere Magnetization: Marine Magnetic Investigations of Crustal Accretion and Tectonic Processes in Mid-Ocean Ridge Environments

by

Clare M. Williams

Massachusetts Institute of Technology
Cambridge, Massachusetts 02139

and

Woods Hole Oceanographic Institution
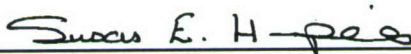Woods Hole, Massachusetts 02543

September 2007

DOCTORAL DISSERTATION

Approved for Distribution:

Susan E. Humphris

Susan E. Humphris, Chair
Department of Geology and Geophysics

Paola Malanotte-Rizzoli

Paola Malanotte-Rizzoli
MIT Director of Joint Program

James A. Yoder

James A. Yoder
WHOI Dean of Graduate Studies

Oceanic lithosphere magnetization: marine magnetic investigations of crustal accretion and tectonic processes in mid-ocean ridge environments

By

Clare Margaret Williams

MSci. Geophysical Sciences
University of Leeds (UK), 2001

Submitted in partial fulfillment of the requirements for the degree of
Doctor of Philosophy
at the
MASSACHUSETTS INSTITUTE OF TECHNOLOGY
and
WOODS HOLE OCEANOGRAPHIC INSTITUTION

September 2007

Author..
Joint Program in Oceanography, Massachusetts Institute of Technology and
Woods Hole Oceanographic Institution
August 22nd, 2007

Certified by...
Maurice A. Tivey
Thesis Co-Supervisor, WHOI

Certified by...
Deborah K. Smith
Thesis Co-Supervisor, WHOI

Accepted by...
J. Gregory Hirth
Chair, Joint Committee for Marine Geology and Geophysics
Massachusetts Institute of Technology and Woods Hole Oceanographic Institution

Oceanic lithosphere magnetization: marine magnetic investigations of crustal accretion and tectonic processes in mid-ocean ridge environments

By

Clare Margaret Williams

Submitted in partial fulfillment of the requirements for the
degree of Doctor of Philosophy
at Massachusetts Institute of Technology
and Woods Hole Oceanographic Institution

September 2007

Abstract

The origin of symmetric alternating magnetic polarity stripes on the seafloor is investigated in two marine environments; along the ridge axis of the fast spreading East Pacific Rise (EPR) (9° 25'-9° 55'N) and at Kane Megamullion (KMM) (23° 40'N), near the intersection of the slow-spreading Mid Atlantic Ridge with Kane Transform Fault. Marine magnetic anomalies and magnetic properties of seafloor samples are combined to characterize the magnetic source layer in both locations. The EPR study suggests that along-axis variations in the observed axial magnetic anomaly result from changing source layer thickness alone, consistent with observed changes in seismic Layer 2a. The extrusive basalts of the upper crust therefore constitute the magnetic source layer along the ridge axis and long term crustal accretion patterns are reflected in the appearance of the axial anomaly. At KMM the C2r.2r/C2An.1n (~ 2.581 Ma) polarity reversal boundary cuts through lower crust (gabbro) and upper mantle (serpentinized peridotites) rocks exposed by a detachment fault on the seafloor, indicating that these lithologies can systematically record a magnetic signal. Both lithologies have stable remanent magnetization, capable of contributing to the magnetic source layer. The geometry of the polarity boundary changes from the northern to the central regions of KMM and is believed to be related to changing lithology. In the northern region, interpreted to be a gabbro pluton, the boundary dips away from the ridge axis and is consistent with a rotated conductively cooled isotherm. In the central region the gabbros have been removed and the polarity boundary, which resides in serpentinized peridotite, dips towards the ridge axis and is thought to represent an alteration front. The linear appearance of the polarity boundary across both regions indicates that the two lithologies acquired their magnetic remanence during approximately the same time interval. Seismic events caused by detachment faulting at Kane and Atlantis Transform Faults are investigated using hydroacoustic waves (T-phases) recorded by a hydrophone array. Observations and ray trace models of event propagation show bathymetric blockage along propagation paths, but suggest current models of T-phase excitation and propagation need to be improved to explain observed characteristics of T-phase data.

Thesis Co-Supervisor: Maurice A. Tivey
Title: Associate Scientist, WHOI

Thesis Co-Supervisor: Deborah K. Smith
Title: Senior Scientist, WHOI

Thesis Committee:
Dr. Henry Dick, WHOI
Dr. Hans Schouten, WHOI
Prof. Ben Weiss, MIT
Dr. Wenlu Zhu, WHOI

Acknowledgements

A thesis may have your name on the title page, but it is truly the joint effort of many people that gets you through to the end of a Ph.D.. I am very grateful to my main thesis advisor Maurice Tivey, who taught me so much about magnetics and always had time to talk about my research when I knocked on his door. Learning to write a scientific paper has been a long learning curve and I really appreciate Maurice's editing skills and stamina for reading drafts of my papers. I have been lucky enough to be in the right place at the right time to work on some excellent datasets, particularly the Kane Megamullion data that makes up the majority of my thesis, and I thank Maurice for directing those opportunities my way. I also worked closely with Debbie Smith during the first couple of years of my degree. I am grateful to Debbie for being supportive throughout this process and introducing me to hydroacoustic data.

I would also like to thank the rest of my committee who have supported me during my degree, even if that required challenging me at times I know you only wanted to get the best from me. Thanks to Hans Schouten for his insightful questions about my research and for sharing his knowledge of all things magnetic. Thanks to Wenlu Zhu for focusing on the big picture outlook of my thesis and Ben Weiss for his rock magnetic and paleomagnetic expertise. Henry Dick, who joined my thesis committee during the last year of my degree, made important contributions to the Kane Megamullion chapters. Finally, thanks to Greg Hirth for chairing my defense. One of the main advantages of the Joint Program is the opportunity to work with other scientists in addition to thesis advisors and I have enjoyed working with Brian Tucholke, Ralph Stephens, Johan Lissenberg, Dan Fornari, Adam Soule and Joe Cann.

I am very grateful to the Geological Society of America for a Graduate Student Research Grant that funded the rock magnetic and paleomagnetic measurements for Chapter 3 of this thesis. Thanks also to Laurie Brown (University of Massachusetts, Amherst) and John Tarduno (University of Rochester) for making their labs available to me, and to Rory Cottrell and Margaret Sulanowska for their technical help in the lab. Interacting with the paleomagnetic groups at these two universities was a highlight during my time at graduate school.

And would the graduate experience be without all the opportunities to travel? I was lucky enough to participate in multiple field trips, conferences and four research cruises during my time in the Joint Program, spending a total of five months at sea. The traveling associated with these cruises has found me in many exotic locations including Costa Rica, Bermuda, Guam and San Diego. The time I have spent on the research ships has been a unique experience that I will cherish. Diving on the submersible Alvin was a huge highlight and I thank Dan Fornari for that opportunity.

There are many people at WHOI whom I would also like to thank for their assistance over the last six years. The Academic Programs Office at WHOI and Joint Programs Office at MIT provide academic, emotional and financial support for so many of us. Marsha, Julia, Shona, John, Judy, Jim and Ronnie- you make our lives so easy! Thanks also to Christine, Pam, Andrew and Marianne for their administrative support.

Friends become family when you are far from your own and I have been blessed with meeting many friends during the last six years. Jessica, Carlos, Anna, Masaya, Rachel, Emily, Petra, Elke, Lara, Alex, Rose, Carolyn, Adam, Brian and Diane, thank you so much for your support and friendship. We have spent so many great times together; eating Rachel's delicious food, spending Friday evenings at the Kidd, swimming in the ponds and watching British comedy series. I wish the very best for you as we scatter and start the next stage in our lives.

Kundalini yoga has also been an important part of my life during graduate school. I went to my first class in Falmouth on the evening of my thesis proposal and this was the start of a life changing experience for me. Thanks to my teachers Celine and Kim, as well as Michele and Karen and, of course, Yogi Bhajan and Gurunam. Kundalini yoga has changed my outlook on life and definitely helped me develop the mental stamina needed to finish graduate school.

My family has been a constant support for me and it is hard to express how much I love and appreciate them. All I can say is that my brother will now have to stop telling me to get a proper job!

And finally, my fiancé Charlie. Our relationship is truly global. We have made it through six years of a long distance relationship between the States, Trinidad, Norway and the UK. Thank you for your love and patience, particularly in the last couple of months, and for being the constantly optimistic person that you are. Now we can truly start our life together!

Dedicated to my grandfathers

Contents

CHAPTER 1

Introduction

1.1 Background and motivation

The network of mid-ocean ridges (MOR) that circles the globe marks the location of active spreading centers. Variability in ridge thermal state due to the underlying mantle and spreading rates produces a range of mid-ocean ridge morphologies that represent different styles of melt generation and crustal accretion. The slow-spreading northern Mid-Atlantic Ridge (MAR) and fast spreading East Pacific Rise (EPR) are centers of focused investigation in MOR environments because they lie at opposite ends of the spreading rate spectrum. The EPR morphology is typically that of an axial rise, assumed to be controlled by two-dimensional, plate-driven mantle flow that results in relatively continuous magmatic crustal accretion. The MAR, in comparison, has a tectonically dominated rift valley morphology commonly associated with three-dimensional patterns of mantle upwelling and intermittent volcanism.

Our understanding of oceanic lithosphere emplacement and evolution relies on multidisciplinary studies of the seafloor and ophiolites. Samples collected by dredging, or in situ during submersible dives and from drill holes yield detailed information about oceanic crustal composition and its vertical structure, but are limited spatially. In contrast, multibeam bathymetry and sidescan sonar provide maps and images of the seafloor that cover large geographical areas, but provide only surface and shallow crustal information. Geophysical methods, including magnetic and hydroacoustic seismic surveys, offer a means of acquiring data over large areas of seafloor that also contain subsurface structure information.

Oceanic lithosphere is characterized by a distinctive magnetic anomaly pattern of symmetric, alternating polarity stripes about the axes of MORs. These patterns were first observed in the early 1960's and provide evidence for seafloor spreading and the theory

13

of plate tectonics [*Morely and Larochelle*, 1964; *Vine and Matthews*, 1963]. Young oceanic lithosphere at the spreading axis acquires a remanent magnetization in the direction of the ambient geomagnetic field, resulting in stripes of alternating normal and reverse polarity crust that reflect Earth's frequent polarity reversals. The oceanic crust is therefore analogous to a magnetic tape recorder that preserves a record of magnetic field reversals. Correlation of this magnetic anomaly pattern with the age-constrained terrestrial record represented a significant advancement in understanding the evolution and tectonics of MOR systems.

Marine magnetic anomalies result from the integrated contribution of magnetic properties across the entire vertical section of the magnetic source layer in oceanic lithosphere. Defining which lithologies constitute the magnetic source layer in oceanic lithosphere is more complex than the simple alternating polarity block models suggested originally by *Vine and Matthews* [1963] (see *Harrison* [1987] and *Smith* [1990] for reviews). Quantifying the relative contributions made by different lithological units, how these properties may change over time and the shape of polarity boundaries are fundamental to understanding the source of marine magnetic anomalies.

Models of magnetic source layer structure have evolved from one layer with constant source layer thickness and uniform, alternating magnetization [e.g. *Talwani et al.*, 1971; *Vine and Matthews*, 1963] to two or more layers with differing source layer thicknesses (0.5 km to 15 km) [e.g. *Cande and Kent*, 1976; *Dyment et al.*, 1997; *Wilson and Hey*, 1981]. The early one layer models assume that the upper crust extrusive lavas make the strongest magnetic contribution, due to the high remanent magnetization of basalts, and have vertical polarity boundaries [*Atwater and Mudie*, 1973; *Irving et al.*, 1970; *Talwani et al.*, 1971]. More recently, arguments have been made that the lower crust (gabbros) and upper mantle (serpentinized peridotites) rocks can have high natural remanent magnetizations (NRM) and represent significant magnetic sources in slow spreading ridge environments [*Gee et al.*, 1997; *Gee and Meurer*, 2002; *Harrison*, 1987;

14

Kikawa and Ozawa, 1992; *Oufi et al.*, 2002; *Pariso and Johnson*, 1993a; *Pariso and Johnson*, 1993b; *Tivey and Tucholke*, 1998]. Two-layer models frequently assume that polarity boundaries in the second layer, analogous to the gabbros in many cases, follow the curve of a conductively cooling isotherm that results in delayed acquisition of magnetization at depth [e.g. *Cande and Kent*, 1976; *Dyment et al.*, 1997].

Important questions related to the magnetic source layer include; timing of NRM acquisition in the gabbros and serpentinized peridotites, variations in the magnetic contribution of different oceanic lithologies over time, whether the lithologies can record a magnetic signal in a systematic way and if the signal from different lithologies interfere constructively or destructively.

1.2 Thesis Overview

This Thesis uses magnetic anomaly data and rock magnetic properties to investigate the magnetic source layer in two very different ridge environments; along the axis of the fast spreading EPR between 9° 25°- 9°55'N and off axis at Kane Megamullion (23° 40'N) at the ridge intersection of the MAR and Kane Transform Fault. These two study areas provide ideal locations to address fundamental questions about the thickness of the magnetic source layer and its magnetic properties because they isolate the magnetic signal from the upper crust (EPR) and lower crust/upper mantle (Kane Megamullion) respectively.

Chapter 2 presents a near-bottom magnetic survey collected in 2001 (AT7-4) along the ridge axis of the EPR (to ~ 5 km off axis). The region is dominated by the Central Anomaly Magnetization High (CAMH), a linear magnetic anomaly that lies along the spreading axis. We test different potential sources of along–axis variations in the CAMH including: paleointensity variations, geochemical modulation and changing thickness of the extrusive basalt layer. Our results show that the source of variations in the amplitude of the CAMH can be explained by changing source layer thickness alone,

consistent with observed changes in seismic Layer 2a. This implies that the extrusive basalts constitute the magnetic source layer along the ridge axis. Along-axis variations or deviations in the CAMH's appearance coincide with bathymetric discontinuities (e.g., 9° 37'N overlapping spreading center) and other changes in seafloor morphology, such as asymmetric lava deposition, indicating that the CAMH is indeed modulated by crustal accretion processes. Additional rock magnetic results presented in Appendix 2 identify a trend of increasing NRM from north to south in the same EPR study area, which may be due to a zoned magma chamber, evolution of the magma processes, or asymmetric location of the magma chamber relative to the ridge axis.

Magnetic contributions from the lower crust and upper mantle are addressed in Chapters 3 and 4. Both chapters focus on Kane Megamullion; an ocean core complex formed by long-term movement on a detachment fault, which has removed the upper crust and exposed lower crust and upper mantle rocks on the seafloor. Kane Megamullion is unique because a ridge-parallel magnetic polarity reversal boundary cuts through the eastern side of the megamullion. The presence of the polarity boundary is important because it indicates that gabbros and peridotites are able to record a magnetic signal in a coherent and systematic manner. The study is divided into two chapters.

Chapter 3 presents rock magnetic and paleomagnetic results from dredge samples and in situ samples collected across Kane Megamullion in 2004 (KN180-2). The origin of remanence for each of the four sampled lithologies (basalts, diabase, gabbros and serpentinized peridotites) are defined and quantified. Both normal and reverse polarity samples are identified and serpentinized peridotites are found to have higher, but less stable, NRMs than gabbros.

Chapter 4 focuses on the geometry of the polarity reversal boundary and subsurface magnetic structure of Kane Megamullion. We use the analytic signal approach to calculate the dip of the boundary, assuming an initial remanent magnetization direction

parallel to the geocentric axial dipole. The geometry of the polarity boundary is observed to change between the northern and central regions of Kane Megamullion. In the northern region, interpreted to be a gabbro pluton, and polarity boundary dips at $134°±14°$ away from the ridge axis. This contrasts with the polarity boundary in the central serpentinized peridotite region, which dips towards the ridge axis at $41°±17°$. Both these dip estimates assume ~35° of counter clockwise rotation at Kane Megamullion, based on the appearance of the magnetic anomaly across a linear basalt ridge in the northern region. Two dimensional thermal modeling indicates that the northern polarity boundary is consistent with a conductively cooled isotherm, while the polarity boundary in the central region is thought to represent an alteration front associated with fluid flow along the detachment fault. The linear appearance of the polarity boundary across Kane Megamullion implies that both lithologies acquired their remanence close to the ridge axis during approximately the same time interval.

Finally, Chapter 5 digresses from marine magnetic anomalies, but continues to focus on detachment faulting along the MAR. T-phases, or hydroacoustic waves, recorded by an array of six hydrophones in the North Atlantic show thousands of seismic events along the MAR. We focus on two study areas, the Atlantis Massif and the Kane Inside Corner High, which are both interpreted as ocean detachment surfaces and show anomalously high numbers of T-phase events. Our goal is to understand whether these are currently active, as suggested by the T-phase data. Comparisons of variables such as event magnitude versus water depth at the event and source to receiver distances show no simple patterns and highlight the complex nature of T-phases. Ray trace models show that bathymetric blockage by shallow bathymetric features along the source to receiver path are significant and should be investigated further in areas of mountainous seafloor, such as the MAR. An OBS study concurrent with hydrophone monitoring is essential to answer many of the remaining questions on the accuracy of hydroacoustically recorded event locations.

References

Atwater, T., and J.D. Mudie (1973),A detailed near-bottom geophysical study of the Gorda Rise, *J. Geophys. Res.*, *78*, 8865-8886.

Cande, S.C., and D.V. Kent (1976),Constraints imposed by the shape of marine magnetic anomalies on the magnetic source, *J. Geophys.Res.*, *81*, 4157-4162.

Dyment, J., J. Arkani-Hamed, and A. Ghods (1997),Contribution of serpentinized ultramafics to marine magnetic anomalies at slow and intermediate spreading centers: Insights from the shape of the anomaly, *Geophys. J. Int.*, *129* (691-701).

Gee, J., R.M. Lawrence, and S.D. Hurst (1997),Remanence characteritics of gabbros from the MARK area: Implications for crustal magnetization, *Proc. Ocean Drill. Program Sci. Results*, *153*, 429-436.

Gee, J., and W.P. Meurer (2002),Slow cooling of middle and lower oceanic crust inferred from multicomponent magnetizations of gabbroic rocks from the Mid-Atlantic Ridge south of the Kane fracture zone (MARK) area, *J. Geophys. Res.*, *107* (B7), EPM 3, doi:10.1029/2000JB000062,18.

Harrison, C.G.A. (1987), Marine magnetic anomalies- The origin of the stripes, *Annu. Rev. Earth. Planet. Sci*, *15*, 505-543.

Irving, E., W.A. Robertson, and F. Aumento (1970),The Mid-Atlantic Ridge near 45° N VI, Remanent intensity, susceptibility, and iron content of dredge samples, *Can. J. Earth Sci.*, *7*, 226-238.

Kikawa, E., and K. Ozawa (1992),Contribution of oceanic gabbros to sea-floor spreading magnetic anomalies, *Science*, *258*, 796-799.

Morely, L.W., and A. Larochelle (1964),Paleomagnetism as a means of dating geological events, *Roy. Soc. Can. Spec. Publ.*, *8*, 39-50.

Oufi, O., M. Cannat, and H. Horen (2002),Magnetic properties of variably serpentinized abyssal peridotites, *Journal of Geophysical Research*, *107*, 10.1029/2001JB000549.

Pariso, J.E., and H.P. Johnson (1993a),Do layer 3 rocks make a significant contribution to marine magnetic anomalies? In situ magnetization of gabbros from Ocean Drilling Program Hole 735B, *J. Geophys. Res*, *98*, 16033-16032.

Pariso, J.E., and H.P. Johnson (1993b),Do lower crustal rocks record reversals of the Earth's magnetic field? Magnetic petrology of oceanic gabbros from ocean drilling program Hole 735B., *J. Geophys. Res*, *98*, 16013-16032.

Talwani, M., C.C. Windisch, and M.G. Langseth (1971),Reykjanes ridge crest:a detailed geophysical study, *J. Geophys. Res.*, *76*, 473-517.

Tivey, M.A., and B.E. Tucholke (1998),Magnetization of 0-29 Ma ocean crust on the Mid-Atlantic Ridge, 25° 30'N to 27° 10'N, *J. Geophys. Res.*, *103* (B8), 17807-17826.

Vine, F.J., and D.H. Matthews (1963), Magnetic anomalies over oceanic ridges, *Nature*, *199*, 947-949.

Wilson, D.S., and R.N. Hey (1981),The Galapagos axial magnetic anomaly: evidence for the Emperor event within the Brunhes and for a two-layer magnetic source, *Geophys. Res. Letts.*, *8*, 1051-1054.

CHAPTER 2

The Central Anomaly Magnetization High documents variations in crustal accretionary processes along the East Pacific Rise (9° 55'- 9° 25'N)

Clare M.Williams, Maurice A. Tivey, Hans Schouten and Daniel J. Fornari

Abstract

Near-bottom magnetic data collected along the crest of the East Pacific Rise between 9° 55'-9° 25'N identify the Central Anomaly Magnetization High (CAMH), a geomagnetic anomaly modulated by crustal accretionary processes over time scales of ~10^4 yrs. A significant decrease in CAMH amplitude is observed along-axis from north to south, with the steepest gradient between 9° 42'-36'N. The source of this variation is neither a systematic change in geochemistry, nor varying paleointensity at the time of lava eruption. Instead, magnetic moment models show that it can be accounted for by an observed ~50 % decrease in seismic Layer 2A thickness along-axis. Layer 2A is assumed to be the extrusive volcanic layer and we propose that this comprises most of the magnetic source layer along the ridge axis. The 9° 37'N overlapping spreading center (OSC) is located at the southern end of the steep CAMH gradient and the 9° 42'-36'N ridge segment is interpreted to be a transition zone in crustal accretion processes, with robust magmatism north of 9° 42'N and relatively low magmatism south of 9° 36'N. The 9° 37'N OSC is also the only bathymetric discontinuity associated with a shift in the CAMH peak, which deviates ~0.7 km to the west of the axial summit trough, indicating southward migration of the OSC. CAMH boundaries (defined from the maximum gradients) lie within or overlie the neovolcanic zone (NVZ) boundaries throughout our survey area, implying a systematic relationship between recent volcanic activity and CAMH source. Maximum flow distances and minimum lava dip angles are inferred, based on the lateral distance between the NVZ and CAMH boundaries. Lava dip angles average ~14° towards the ridge axis, which agrees well with previous observations, and offers a new method for estimating lava dip angles along fast-spreading ridges where volcanic sequences are not exposed.

2.1. Introduction

Accretion of new oceanic crust at mid-ocean ridges (MOR) is a fundamental geological process that involves complex relationships between magma supply and emplacement, which vary spatially and temporally throughout the MOR system. Much of our understanding of oceanic crustal structure and lithology is derived from ophiolite studies [*Cann,* 1974; *Kidd,* 1977] as well as marine seismic surveys, dredged rock samples, shallow crustal drilling and submersible dives, particularly along fault scarps that form tectonic windows into the crust [e. g., *Auzende et al.,* 1989; *Karson,* 1998; *Lagabrielle et al.,* 1998]. Studies of oceanic crust accretion focus frequently on the narrow zone of youngest crust at the spreading axis, known as the neovolcanic zone (NVZ). Magnetic surveys have identified the Central Anomaly Magnetization High (CAMH), a ubiquitous region of high crustal magnetization located at the spreading axis of many MORs, including the East Pacific Rise (EPR) between 8° - 10° N [*Klitgord,* 1976; *Klitgord and Mammerickx,* 1982; *Carbotte and Macdonald,* 1992; *Lee et al.,* 1996; *Schouten et al.,* 1999; 2003]. The CAMH is believed to reflect the presence of young (< 10 kyrs), highly magnetic lavas [*Klitgord,* 1976], which record the recent peak in geomagnetic field intensity [*Gee et al.,* 1996] and document patterns in distribution of the lavas that comprise the NVZ. The CAMH is therefore the time-integrated magnetic contribution of the entire magnetic source layer and reflects vertical and temporal properties of the crust at and near the ridge axis (< 5km). This additional information on three dimensional, time-dependent processes can enhance the interpretation of seafloor observations, particularly along sections of MOR not covered by seismic surveys.

2.1.1 Regional setting

Our survey area extends between 9° 55'N and 9° 25'N on the EPR, along the northern section of the ridge bounded by the Clipperton and Siqueiros Transform Faults (TF) (Fig. 2-1a). As with other MORs, the spreading axis along this section is divided into multiple segments by various bathymetric discontinuities [*Macdonald and Fox,* 1983, 1988; *Lonsdale,* 1983; *Macdonald et al.,* 1984, 1987, 1988; *Haymon et al.,* 1991,

1993; *Fornari et al.*, 1998, 2004, *White et al.*, 2006]. These discontinuities offset the ridge axis over a range of scales, from the large 9° 03'N overlapping spreading center (OSC) [*Lonsdale*, 1983; *Macdonald and Fox*, 1983], with 8 km offset, to multiple small "devals" (deviations in axial linearity, recognized by *Langmuir et al.*, 1986; *Toomey et al.*, 1990; *Haymon et al.*, 1991; 1993) or "SNOOs" (small nonoverlapping offsets, *Batiza and Margolis*, 1986) with offsets < 0.5 km. The larger discontinuities are thought to represent boundaries between adjacent magmatic systems and are known to migrate along the ridge axis (e.g., the 9° 03'N OSC migrates at a rate of ~50 mm/yr, *Carbotte and Macdonald*, [1992]) [*Macdonald et al.*, 1992; *Kent et al.*, 1993; *White et al.*, 2002].

Our understanding of lithospheric structure between 8°- 10° N is based on seismic surveys that have identified both upper and lower crustal features. An axial magma chamber (AMC) has been detected ~1.2-2 km beneath the axis in the surveyed area and the continuity of the AMC reflector is disrupted at several locations along-axis (e.g., at 9° 17'N and 9° 53'N), suggesting possible individual magma systems [*Detrick et al.*, 1987; *Kent et al.*, 1993; *Vera and Diebold*, 1994; *Toomey et al.*, 1994] or locally enhanced mantle melt supply [*Dunn et al.*, 2000]. Above the AMC, in the upper crust, the reflection from the base of seismic Layer 2A is observed to increase in depth from ~0.2 km at the axis to ~0.5 km at 1-2 km off axis [*Christeson et al.*, 1992; *Harding et al.*, 1993; *Kent et al.*, 1993]. Seismic Layer 2A is assumed to be equivalent to the extrusive volcanic layer, to first approximation or an alteration front located between the base of the extrusive layer and the top of the dike layer [*Christeson et al.*, 2007]. The doubling in Layer 2A thickness is thought to be caused by significant transport and accumulation of lavas off axis due to eruption overflows from the axial summit trough (AST), by efficient transport through networks of lava tubes and channels [*Hooft et al.*, 1996; *Carbotte et al.*, 1997; *Schouten et al.*, 2003], or by off-axis volcanism fed by dikes that are separate from those that feed the EPR axis [*Goldstein et al.*, 1994; *Perfit et al.*, 1994; *Sohn and Sims*, 2005 and references therein]. *Schouten et al.* [1999] show that the thickening of Layer 2A is reflected in the shape of the cross-axis CAMH, indicating that the extrusive lavas of

Layer 2A are a significant magnetic source. The center of present magmatic activity is thought to be located at the northern end of our survey area. Indeed, documented eruptions in both 1991 and 2006 between 9° 51'- 46' N [*Haymon et al.*, 1993; *Rubin et al.*, 1994; *Gregg et al.*, 1996; *Tolstoy et al.*, 2006; *Cowen et al.*, 2007] and extensive hydrothermal activity in the area [*Haymon et al.*, 1993] support this interpretation.

2.1.2. Magnetic surveys between 8° and 10° N

Previous sea surface magnetic studies in the study area identified the CAMH [*Klitgord and Mammerickx*, 1982; *Carbotte and Macdonald*, 1992; *Lee et al.*, 1996] and magnetic discontinuities along the ridge axis that correspond approximately with the location of bathymetric discontinuities at 9° 25'N, 9° 37'N and 9° 46'N [*Lee et al.*, 1996]. However, any correlation between the CAMH and the ridge morphology, and consequently crustal accretion processes, has remained ambiguous because of the inherent low resolution of the sea surface magnetic data used in these studies and the difficulty in mapping the NVZ. As the CAMH represents a time-integrated signal, a magnetic discontinuity would indicate ridge processes that were stable on timescales of a few thousand to tens of thousands of years [*Macdonald et al.*, 1991; *Carbotte and Macdonald*, 1992; *Lee et al.*, 1996; *White et al.*, 2002]. A correlation between the location of a present day bathymetric discontinuity and a magnetic discontinuity would provide evidence for the relatively stable position of the ridge discontinuity over these timescales.

The near-bottom magnetic survey that we report on here was conducted between 9° 55'-25' N, during acquisition of sidescan sonar data that covered the ridge axis and flanks out to ~5 km (cruise AT7-4, *Fornari et al.*, 2004; *Escartin et al.*,2006; *Soule et al.*, in prep.). The study area encompasses several previous, smaller scale magnetic surveys and the new data provide a regional context for the CAMH. The data were collected ~100 m above the seafloor using a sensor mounted on the deep-towed DSL-120A vehicle, a 120 kHz sidescan sonar system operated by the National Deep Submergence Facility [e.g.

Scheirer et al., 2000 and references therein]. The survey lines were run parallel to the ridge axis, with a line spacing of ~0.5 km, and covered an area of ~440 km^2 (Fig. 2-1b). Our dataset ties together several high resolution, near-bottom magnetic profiles collected by Alvin at ~5 m altitude [*Schouten et al.*, 1999], and high density grids collected by the Autonomous Benthic Explorer (ABE) at ~40 m altitude and 40 m line spacing (Fig. 2-1b) [*Schouten et al.*, 2003; *Fornari et al.*, 2004, *Tivey et al.*, in prep.].

Our dataset provides a unique opportunity to compare and contrast the CAMH directly with various physical attributes of the NVZ, including the AST and sea floor morphology, which have been interpreted from sidescan data collected concurrently with the magnetic data [*Fornari et al.*, 2004; *Soule et al.*, 2005]. The AST varies in width (<50-400 m) and depth (<5-15 m) [*Fornari et al.*, 1998, 2004] along-axis and is discontinuous at several locations in our survey area (Fig. 2-1c). Four main AST discontinuities have been identified, the largest of which is a right-stepping OSC located between 9° 36'- 38'N (labelled 9° 37'N OSC in Fig. 2-1c, ~0.5 km offset) [*Haymon et al.*, 1991; *Macdonald et al.*, 1992; *Smith et al.*, 2001; *White et al.*, 2002;]. Establishing the position and character of the CAMH relative to these four discontinuities is important for understanding the stability of small-scale bathymetric discontinuities along fast-spreading MORs over time.

In this paper magnetic moment models show an observed decrease in CAMH amplitude along-axis can be explained by variations in seismic Layer 2A thickness alone, implying that the extrusive volcanic layer comprises the majority of the magnetic source layer along-axis. A steep gradient in CAMH amplitude between 9° 42-36'N is interpreted to be a transition zone in ridge crustal accretion processes. The 9° 37'N OSC is located at the southern end of the steep gradient and is associated with a magnetic "deviation" of the CAMH peak to the west of the AST. Together, these observations suggest that 9° 37'N OSC is a significant ridge discontinuity along this section of the EPR. Finally, the CAMH boundaries lie within or align along the NVZ boundaries throughout the survey

area, indicating a relationship between recent volcanic deposits and the CAMH source. The lateral distance between the CAMH and NVZ boundaries is used to interpret flow distances and lava dip angles.

2.2. Methods

Geomagnetic field data were collected during research cruise AT7-4 aboard the R/V Atlantis in 2001 using a 3-axis magnetometer mounted on the side scan sonar vehicle. Vehicle attitude data (pitch, roll, and heading) were recorded at a sampling frequency of 2 Hz and three component magnetic data at a sampling rate of 10 Hz. A calibration turn was executed before the first line of the survey to correct the data for the permanent and induced magnetic fields of the sonar vehicle using the approach of *Isezaki* [1986] and *Korenaga* [1995]. The calibration calculation entails a least squares inversion to minimize the difference between the observed and a predicted field based on the IGRF [*IAGA Division V Working Group, International Geomagnetic Reference Field 2000,* 2000]. After the calibration correction was applied to the data, the ~3000 nT effect of the vehicle was reduced by an order of magnitude. A second, additional correction was made to adjust the data for azimuth of the survey line by fitting a cosine curve to the total magnetic field data.

The observed magnetic data were interpolated along the survey lines and resampled to a 1 minute sampling frequency, equivalent to a ~40 m along-track data spacing. The non-crustal contribution of the magnetic field was removed from the anomaly by subtracting the IGRF for 2001 [*IAGA Division V Working Group, International Geomagnetic Reference Field 2000,* 2000]. The resulting residual magnetic anomaly along each track line is shown in Fig. 2-2a. We did not correct the data for diurnal variation because our magnetic anomaly amplitudes are more than an order of magnitude greater than typical diurnal variations at this latitude (N.B. typical diurnal variations are less than 30 nT, *Lee et al.,* [1996] and the average CAMH amplitude is ~1000 nT cross axis). We also checked for the occurrence of magnetic storms at the

nearest geomagnetic observatory (Huaycan, Peru). The only period during the survey when storms were active (November 24th-25th) was at the end of the last line of the survey and had little appreciable affect on our data. The along-track residual magnetic anomaly data (Fig. 2-2a) were interpolated into a residual anomaly grid with an anisotropic grid spacing of 0.11 km along-axis and ~0.25 km across axis in order to weight the grid in favour of the higher resolution data along-axis. The residual magnetic anomaly grid was on an uneven plane due to the varying depth of the DSL-120A along each track line. In order to continue the grid to a level datum, and reduce edge effects of the Fast Fourier Transform (FFT) analysis during processing, we increased the area of the residual anomaly grid from ~ 56 km x 8 km to ~95 km x 73 km by adding data to the edges of the grid from the *Carbotte and Macdonald* [1992] magnetic anomaly grid (original grid spacing 1 km by 1 km). The *Carbotte and Macdonald* [1992] grid is an extensive compilation of sea surface magnetic data from the National Geophysical Data Center data collected between 1967-1992 and encompasses the entire segment of the EPR from the Clipperton TF to the Siqueiros TF. The *Carbotte and Macdonald* [1992] grid was continued downwards to 2.5 km water depth using a cosine tapered band pass filter with short wavelength cut off of 3 km and long wavelength cut off of 64 km and resampled to the same grid spacing as the DSL-120A anomaly grid. The residual magnetic anomaly grid was then embedded in the center of the resampled *Carbotte and Macdonald* (1992) grid and the two grids combined by minimum curvature interpolation. This new regional residual anomaly grid was then continued upwards to both 2.5 km water depth (Fig. 2-2b) and the sea surface using the iterative FFT method of *Guspi* [1987].

The topographic contribution to the magnetic anomaly and both the phase shift and amplitude distortion due to latitude were removed by inverting the data for crustal magnetization, assuming the topography forms the top boundary of a source layer with constant thickness. The *Parker and Huestis* [1974] FFT inversion method was used as adapted by *Macdonald et al.*, [1980] for three-dimensional problems. Two multibeam

bathymetry grids were combined, in the same way as the *Carbotte and Macdonald* [1992] and near-bottom anomaly grids, to provide bathymetric data over the same spatial area as the residual magnetic anomaly grid. The two multibeam bathymetry grids used were the *Cochran et al.* [1999] grid, covering the area along and near the ridge axis (grid spacing ~0.08 km), and the more spatially extensive grid of *Macdonald et al.,* (1992) (grid spacing ~0.3 km). The inversion assumes that the magnetization is uniform with depth and oriented parallel to an axial geocentric dipole (i.e. a declination of 0° and inclination of 32°). A cosine-tapered band-pass filter (short wavelength cut-off of 0.5 km and long wavelength cut-off of 45 km) was applied and a constant source layer thickness of 0.25 km assumed. The oceanic crust in our survey area was accreted during the Brunhes, an interval of normal polarity, therefore all the crustal magnetization results from the inversion should be positively magnetized. We adjusted the magnetization solution to all positive values by adding the annihilator multiplied by a factor. The annihilator is a magnetization distribution that produces no external field when convolved with the topography of the survey area [*Parker and Huestis*, 1974]. For our survey, eighteen times the annihilator was required to shift the crustal magnetization results to all positive values (Fig. 2-2c). No significant change in the pattern of magnetization is observed when adding this amount of annihilator, other than shifting the DC-level of the magnetization solution.

A comparison of our inversion results with several previous studies show similar ranges in magnetization intensities for this segment of the EPR. The magnetization range for our data (herein referred to as the near-bottom data) is ~ 22 A/m. *Lee et al.* [1996] intensities range from 8-16 A/m assuming a source layer thickness of 0.5 km. To a first order, the magnetization magnitude scales linearly with source layer thickness, so that 8-16 A/m would be equivalent to 16 to 32 A/m (16 A/m range) for a 0.25 km thickness. *Carbotte and Macdonald* [1992] studied the entire segment from 8° N-10° 30' N and calculated intensities of ~4-10 A/m between 9° 25' N and 10° N for a source layer

thickness of 1 km, equivalent to a range of 24 A/m for a source layer thickness of 0.25 km.

2.3. Results

Our inversion results show the CAMH morphology is an elongate, linear magnetic high, centered about the ridge axis (Fig. 2-3c). The boundaries of the CAMH are defined by the maximum gradient on each limb (blue solid lines in Fig. 2-3c). Variations exist in both the location of the CAMH boundaries and amplitude and location of the CAMH maximum, or peak. The most significant variation in our study area is a decrease in the CAMH peak amplitude from north to south. The CAMH peak amplitude is relatively high between 9° 55-43'N (average 47 A/m) and decreases dramatically between 9° 42'-36'N, to a low of 30 A/m (Fig. 2-3c). The CAMH amplitude then remains relatively low south of 9° 36'N. Superimposed on this long wavelength magnetic feature are small scale variations (0.25-1 km) in the CAMH width and location of the CAMH peak. The interpreted backscatter data [*Fornari et al.*, 2004; *Escartin et al.*,2006; *Soule et al.*, in prep.] collected concurrently with the near-bottom magnetic data allows us to compare directly the appearance of the CAMH with the NVZ and present day AST location.

Overlaying the CAMH and NVZ boundaries shows that the CAMH boundaries lie entirely within or along the NVZ boundaries (Fig. 2-3b). This result strongly suggests a systematic relationship between the source of the CAMH and the young lavas within the NVZ. MOR lavas are observed to dip towards the ridge axis in cross section exposures within transform faults and other windows into ocean crust [*Kidd*, 1997; *Macdonald et al.*, 1983; *Tivey*, 1996; *Karson et al.*, 2002]. The relative locations of the CAMH and NVZ boundaries can therefore be used to determine lava flow distances and infer lava dip angles (discussed in more detail in section 4.2). The NVZ boundaries are continuous throughout our study area, indicating recent flows on both flanks [*Fornari et al.*, 2004; *Soule et al.*, 2005; *Soule et al.*, in prep.] (Fig. 2-3a), but they are very irregular compared

with the CAMH boundaries. This difference in appearance is expected because the CAMH boundaries are not only band-pass filtered (0.5 km short wavelength cut-off), but they also represent the averaged magnetic signal from the entire magnetic source layer. Both the NVZ and CAMH show along-axis variations in width, the most significant of which is a decrease in width on the eastern flank between 9° 48-46'N and south of 9° 33'N (Fig. 2-3b). These two regions are also associated with deviations in the location of the CAMH maximum or peak away from the AST (herein referred to as magnetic deviations).

The CAMH peak does not overlie the AST trace throughout the study area, but deviates up to 0.7 km onto the ridge flanks (e.g., between 9° 50'-46'N, 9° 45'-42'N, 9° 42'-36'N and south of 9° 33'N, outlined by the grey boxes in Fig. 2-3b). It is interesting to note that three of these four magnetic deviations are to the west of the AST; a result which agrees with the ABE magnetic grids at 9° 50'N and 9° 29'N [*Tivey et al., in prep.*]. The resolution threshold of the near-bottom data is ~0.75 km, based on comparison with the ABE high-resolution grids and multibeam bathymetry (Appendix A2). The two northernmost deviations, between 9° 50-46'N and 9° 45-42'N, are well below the 0.75 km resolution threshold and cannot be quantitatively corroborated (Fig. 2-3b). Between 9° 42'-36'N variations in both the CAMH peak amplitude and location are more striking with the CAMH peak amplitude decreasing dramatically by ~ 15 A/m over the ~11 km distance (Fig. 2-3c). In addition, the CAMH peak diverges up to ~0.7 km west of the AST as it approaches the 9° 37'N OSC from the north (Fig. 2-3b). The CAMH peak overlies the AST again at 9° 38'N, where the AST forms the western limb of the 9° 37'N OSC, which suggests that the magnetic deviation is associated with the bathymetric discontinuity. South of 9° 33'N the CAMH width narrows on the eastern flank and the CAMH peak shifts onto the western flank, ~0.65 km from the AST, resulting in a significant asymmetric location of the CAMH relative to the AST (Fig. 2-3b). The NVZ boundaries are also asymmetric about the ridge axis, with a narrow, irregular eastern boundary and a western boundary extending beyond the survey area (Fig. 2-3b). Both

28

these magnetic deviations (9° 42'-36'N and south of 9° 33'N) are very close to the near-bottom resolution threshold of 0.75 km.

2.4. Interpretation and discussion

In the absence of magnetic polarity changes and anomalous topography, magnetic anomalies are generated by two basic mechanisms; either there is more magnetic material, such as a change in volume of the source layer, or the crust is simply more magnetic. The source of the CAMH has been discussed at length in the published literature [*Klitgord*, 1976; *Tivey and Johnson*, 1987; *Gee et al.*, 1996; *Schouten et al.*, 1999; *Gee et al.*, 2000; *Bowles et al.*, 2006]. At this time, the most widely accepted explanation for the formation and distribution of the CAMH is the recent maximum in geomagnetic intensity and its modulation by crustal accretionary processes in young oceanic crust [*Schouten et al.*, 1999; *Gee et al.*, 2000]. We investigate the relationship between the CAMH and crustal accretion in our study area by integrating our interpretation of the near-bottom data with several other datasets including seismic data, backscatter data and multibeam bathymetry. The resulting combined interpretation allows us to better understand the source of the CAMH and identify variations in its appearance that result from crustal accretionary processes.

2.4.1. Source of variations in the along-axis CAMH amplitude

The magnitude of the peak CAMH decreases by ~40% from north to south in the survey area (Fig. 2-3c). We discuss potential sources of this along-axis magnetic gradient, which can be divided into variations in magnetic properties (magnetization) and volume of the magnetic source layer. At least three processes can affect the magnetic properties of crustal rocks; low temperature oxidation/alteration of the magnetic minerals, geochemical variability and variations in geomagnetic field intensity. In axial and near axis locations extrusive basalts are assumed to comprise the majority of the magnetic source layer [*Atwater and Mudie*, 1973; *Smith and Banerjee*, 1986; *Pariso and Johnson*, 1991]. The primary carrier of magnetic moment in basalts is titanomagnetite, which is

29

altered to lower magnetic moment titanomaghemite [*Irving et al.*,1970; *Marshall and Cox*, 1973; *Pariso and Johnson*, 1991]. This type of low-temperature alteration is a gradual, continuous process which takes place over several millions of years [*Zhou et al.*, 1997]. Therefore, we expect low-temperature alteration to reduce the overall amplitude of magnetic anomalies with age from the ridge axis, but the process is likely to be too slow to account for the CAMH [*Zhou et al.*, 1997] and we rule it out as source of the along-axis gradient in the CAMH.

The second potential source of differences in magnetic properties are geochemical variations and we draw on a large body of published geochemical data from our survey area (e.g. *Batiza and Niu*, 1992; *Perfit et al.*, 1994; *Perfit and Chadwick,* 1998; *Reynolds and Langmuir,* 2000; *Smith et al.*, 2001; *Sims et al.*, 2002; *Soule et al.*, 2005) to evaluate this possibility. Simply stated, the more iron that is present in MORB, the greater the magnetization of the rock. *Gee and Kent* [1997] propose an empirical relationship between FeO content of basalts and their natural remanent magnetization (NRM = 4.44 (FeO) - 25.8). The FeO composition of surface axial basalts in our study area exhibit a trend of increasing FeO weight percent from north to south [*M. Perfit*, in prep.] (Fig. 2-4b). The average FeO concentrations at $9°$ 50'N and $9°$ 37'N are approximately 9.0% and 10.5% respectively, which implies an increase in NRM of ~6 A/m from north to south (assuming the *Gee and Kent* [1997] relationship, Fig. 2-4b). This trend in FeO concentration opposes the observed gradient in the along-axis CAMH. We conclude that, although variations in FeO concentrations can affect rock magnetization and we are only sampling surficial rocks, it is unlikely that a systematic variation in geochemical composition is the dominant source of variations in axial magnetization along this section of the EPR.

A third possible source of magnetization variation are paleointensity fluctuations in Earth's magnetic field. Global changes in the geomagnetic field have been dramatic over the last 10 kyrs [*Guyodo and Valet,* 1999; *Gee et al.*, 2000; *Yang and Shaw*, 2000;

Korte and Constable, 2005]. Based on these records, lavas extruded 5 kyrs ago would have magnetization intensities approximately one third less than a lava flow extruded 2 kyrs ago, and lavas extruded today would have magnetization intensities approximately one third less than a lava flow extruded 2 kyrs ago. Comprehensive analyses of paleointensities from basalt glasses in our study area are presented in *Bowles et al.* [2006]. Their results from both axial and off-axis surface samples show that young lavas (< 2 kyrs) are present at the AST throughout the study area. There are no systematic differences in paleointensity recorded by the glasses that would result in the observed along-axis CAMH gradient. In fact, paleointensities in the 9° 30-35'N region are ~7 μT higher, on average, than those between 9° 46-50'N; the opposite trend to the along-axis CAMH peak. Based on this result, the lavas between 9° 30-35'N are assumed to be older, which agrees with the interpretation of surface morphology and density of fractures by *Wright et al.* [1995]. It must be kept in mind, however, that these paleointensity data represent the surface lavas only. We are extrapolating these surface data to the entire magnetic source layer. If we discount changes in magnetic properties of the crust as a source of the along-axis variation observed in the peak CAMH, an alternative explanation is a change in magnetic source layer thickness.

The thickness of the magnetic source layer has been found to correlate positively with the seismically defined Layer 2A on the Endeavour segment of the Juan de Fuca Ridge [*Tivey and Johnson*, 1993] and along cross-axis profiles at 9° 50'N and 9° 31'N on the EPR [*Schouten et al.*, 1999]. *Christeson et al.* [2007] made a direct comparison of geologic and seismologic structure of oceanic crust along the fast spreading EPR crust near Hess Deep and the intermediate spreading Juan de Fuca crust near the Blanco transform fault. They found that while seismic Layer 2A is located at the top of the sheeted dike complex at Hess Deep, it lies within the lava layer at Blanco. *Christeson et al.* suggest that the Layer 2A reflector may instead be an alteration boundary. However, it is clear that in fast spreading crust seismic Layer 2A appears to be a good first order estimate of extrusive lava thickness.

Four cross axis seismic profiles (Fig. 2-2c, 2-3b- three Common Depth Profiles (CDP) [*Harding et al.*, 1993] and one wide angle profile (WAP) profile [*Vera and Diebold*, 1994]) and several other shorter profiles (conventional airgun data [*Christeson et al.*, 1996] and refraction study profiles [*Christeson et al.*, 1994]) show that seismic Layer 2A thickness at the axis decreases from north to south (Fig. 2-4c). Seismic Layer 2A has a maximum thickness of ~250 m at 9° 50'N and a minimum thickness of ~130 m at 9° 31'N. The greatest change in Layer 2A thickness (90m) is between seismic profiles WAP 507 (9° 35'N) and CDP 29 (9° 39'N).

The source layer thickness required to produce the along-axis variation in the peak CAMH can be calculated using magnetic moment, which is the product of magnetization intensity and source layer thickness. Our inversion assumes a constant source layer thickness of 0.25 km, which we multiply with the computed magnetization profile (Fig. 2-4a) to obtain magnetic moment. A series of source layer models are then generated from this magnetic moment, assuming fixed magnetization values of 20-70 A/m in 10 A/m increments (Fig. 2-4d). The model results show a decrease in source layer thickness from north to south, with the steepest gradient between 9° 39'-35'N. Increasing the magnetization of the source layer reduces the thickness required to produce the CAMH. Our model results for a crustal magnetization of 45 A/m produces the best fit to the seismic Layer 2A thickness (RMS misfit shown in Fig. 2-4d). This value of crustal magnetization compares well with published NRM values of ~55 A/m for axial lavas at 12° N on the EPR [*Gee and Kent*, 1994].

Our comparison of the magnetic source layer thickness with seismic Layer 2A thickness is limited by the sparseness of the seismic dataset. Seven datapoints are available to constrain Layer 2A thickness, with only two between 9° 55-35'N (Fig. 2-4c). Our model of the magnetic source layer produces a more detailed picture of the variations in the along-axis source layer thickness and constrains the largest variation to between 9° 42-36'N. This region coincides with the 9° 37'N OSC at its southern end and reflects an

along-axis transition zone which begins at 9° 42'N and terminates at 9° 36'N. In comparison, there is no significant change in magnetic source layer thickness near the magnetic deviation south of 9° 33'N or at the two northern bathymetric discontinuities. Our results agree with previous studies which have highlighted the importance of the 9° 37'N OSC and suggested that this bathymetric discontinuity represents a boundary between magmatic systems [*Lee et al.*, 1996; *Smith et al.*, 2001]. *Haymon and White* [2004] proposed that ridge segments between discontinuities that offset the ridge 0.5-3 km arise from processes controlling melt supply in the mid-to lower crust, whereas shorter ridge segments between small (< 0.5 km) discontinuities are due to upper crustal processes. In light of this, the 9° 42-36'N magnetic deviation and transition zone likely results from variations in lower crustal melt supply, which may be evident from the changing Layer 2A thickness.

We conclude from our model that the along-axis gradient in the CAMH peak is well accounted for by variations in magnetic source layer thickness that are also reflected in seismic Layer 2A thickness. Consequently, the thickness of seismic Layer 2A and the covariance of the magnetic source layer can be explained by changes in the thickness of the extrusive layer. The caveat being that seismic Layer 2A is only a good approximation of the extrusive layer at fast spreading ridges [*Christenson et al.*, 2007], which may also be the case for the magnetic source layer too.

2.4.2 Comparison of CAMH and NVZ boundary locations

The CAMH boundaries lie within or are aligned along the NVZ boundaries throughout our study area (Fig. 2-3b). In general, the CAMH and NVZ boundaries show both the most variability and greatest difference in respective locations on the eastern flank, particularly between 9° 42-40'N, where networks of channels deposit lavas far from the axis and increase the width of the NVZ beyond our survey area (> 3km, Fig. 2-3a) [*Soule et al.*, 2005; *Garry et al.*, 2006]. In these regions the elongate off axis flows are not accompanied by an increase in the width of the CAMH, which implies that the

contribution these flows make to the computed magnetization is not significant compared with the total magnetic source layer. These flows most likely form a thin carapace over older flows and reflect either a sequence of thin flows not recorded by the CAMH, but preserved in the NVZ boundary, or a single lava flow event. We calculate the minimum thickness of a lava flow required to influence the shape of the CAMH based on the resolution of our data. The largest uncertainty in our data is ~300 nT, due to the calibration correction for the magnetic effects of the DSL-120A sonar vehicle. Assuming 300 nT is the minimum amplitude anomaly detected, we construct a plane layer model, analogous to a young flow on top of an older flow. Our results show that a flow > 17 m thick with a magnetization contrast of 10 A/m between the young and older flows produces an edge anomaly > 300 nT. The greater the magnetization contrast between the older and younger flows, the thinner the required flow (Table 2-1).

Table 2-1. Lava flow thickness

Magnetization Contrast (A/m)	Thickness (meters)
5	38
10	17
25	7
50	3

Typical magnetization intensities of mid-ocean ridge basalts range from several A/m up to 60 A/m [*Gee and Kent,* 1994; *Sempere et al.,* 1998] and magnetization contrasts of 25 A/m may exist, requiring only a 7 m thick flow to modify the CAMH. However, it is difficult to estimate the flow thickness using this approach without further information on the NRM contrasts between lavas inside and outside the NVZ in our survey area.

The fact that the CAMH boundary is shifted towards the AST and away from the NVZ boundary implies that lava flows dip towards the spreading axis and is consistent with observations of upper crustal architecture [*Kidd,* 1977; *Macdonald et al.,* 1983; *Tivey,* 1996; *Karson et al.,* 2002]. Lava flows deposited at or near the ridge axis are rafted away during seafloor spreading and the proximal parts of the earlier flows are covered by

subsequent flows, resulting in isochrons which dip towards the ridge axis in the upper crust section. A cartoon of this approach is shown in Fig. 2-5a. The lateral distance between the NVZ and CAMH boundaries can be used to calculate lava flow distances and, given an estimate of extrusive layer thickness, infer lava dip angles if we assume a constant magnetization with depth. We define the maximum lava flow distance as twice the lateral distance between the NVZ and CAMH boundaries (distance $2d$, Fig. 2-5b). This distance, $2d$, is the maximum flow distance because the NVZ boundary represents the longest rather than the average flow distance.

In our study area the maximum flow distance ($2d$) is smallest north of 9° 50'N and between 9° 35-33'N (Fig. 2-5b). *Kurras et al.* [2000] mapped in detail the surface morphology of the NVZ on the eastern flank between 9° 52-49'N. They observed that most flows were deposited < 0.5 km from AST, while occasional flows reach 0.5-1.5 km from the axis. These relatively short lava flows are reflected in the NVZ, which is narrowest, on average, north of 9° 49.5'N (Fig. 2-3a). Possible explanations for the narrow NVZ and small $2d$ values are either shorter lava flows due to reduced magma supply, or disrupted lava deposition where local topography controls the distribution of lava, such as a fault [*Escartin et al.*,2006]. The 9° 50'N region has the shallowest bathymetry, a dome-shaped cross-section and two documented lava flow eruptions in the past 15 years [*Haymon et al.*, 1993; *Tolstoy et al.*, 2006; *Cowen et al.*, 2007] indicating enhanced, rather than reduced, magma supply. Therefore, lava deposition is most likely controlled by local topographic features such as faulting at the surface. Ridge-parallel normal faults can act as barriers, limiting the off-axis extent of lava flows and locally diverting their course along-axis [*Escartin et al.*, 2006]. If this situation persists over long periods of time it could change the appearance of the CAMH. *Schouten et al.* [2003] cite a mostly buried normal fault as the source of the linear magnetic anomaly observed along the eastern flank in the 9° 50'N ABE grid (Fig. 2-A2). They propose that the fault restricts off-axis transport of lava flows that originate at the AST and causes ponding of significant volumes of lava. Short flows between 9° 35-33'N (small $2d$ values, Fig. 2-5b)

may also be due to surface faulting. *Escartin et al.* [2006] mapped a large number of surface exposed faults close to the ridge axis in this region. In contrast, areas with large 2*d* values coincide with the regions we interpret to be covered by a single, or multiple thin, elongate flows (e.g. on the eastern flank between 9° 42-40'N), or long-term asymmetric lava deposition and have fewer observed surface faults. (e.g., on the western flank south of 9° 33'N).

We can estimate the minimum dip of the lava flows, due to burial by subsequent lava flows, using the 2*d* value and seismic Layer 2A as a proxy for the thickness of the extrusive layer along the four seismic profiles CDP 27, CDP 29, WAP 507 and CDP 31 (Fig. 2-3b, Table 2-1) [*Schouten and Denham,* 1979; *Karson et al.,* 1992, 2002; *Hooft et al.*, 1996]. The lava dip angle is a minimum because the 2d value is the maximum flow distance.

Table 2-2. Minimum lava dip angles

Seismic Line	Dip angle (°)	
	West Flank	East Flank
CDP 27	41 (±40)	-21[a] (±20)
CDP 29	6 (±2)	9[b] (±1)
WAP 507	12 (±18)	8 (±3)
CDP 31	4[b] (±2)	10 (±2)

[a]: negative dip angle, i.e. away from the ridge axis
[b]: not the minimum dip angle as NVZ boundary extends beyond the limit of survey
Error estimates shown in parenthesis

The lava dip angles vary significantly along-axis from 4-41°, with the steepest dips at CDP 27 (~ 9° 50'N) and the shallowest at CDP 31 (~9° 30'N). Error estimates, defined by maximum and minimum dip angles (shown in parentheses in Table 2-2) are calculated based on ± 50 m accuracy of Layer 2A thickness [*Harding et al.,* 1993] and the width of one grid cell in the near-bottom data (228 m), which defines the accuracy of the flow distance 2*d*. Shallow dip angles (e.g. < 10°) have low error estimates compared with the steep dip angles, calculated in areas where the CAMH and NVZ boundaries are located close to each other. The dip angles for profiles CDP 29, WAP 507 and CDP 31 agree very well with the isochrons modeled by *Hooft et al.* [1996]. In their model, the

upper extrusives, composed of long flows, have shallow dip angles ranging from 0-15°
(compared with 4-12° in this study). *Karson et al.* [2002] also observed lava dip angles
that varied from 20-30° in the upper extrusives along fault scarps the Blanco Transform
Fault. The steep and negative dip angles at CDP 27 may reflect a change in lava
deposition patterns, with shorter flows defined by the NVZ, compared with longer flows
in the past (as recorded by the CAMH). Our method for calculating the minimum lava dip
angle has widespread application along other fast spreading MORs, where the extrusive
lava sequence is not exposed.

2.4.3. Comparison of magnetic deviations and bathymetric discontinuities

The near-bottom magnetic data provides a regional context for the CAMH and the
unique opportunity to compare the CAMH directly with both the present day AST and
NVZ (Fig. 2-3a) that represents recent crustal accretion (< 10 kyrs, *Goldstein et al.,*
1994), and multibeam bathymetry (Fig. 2-1c), which represents long-term accretion on
the ridge equal to the age of the crust (the maximum age of the crust in our survey area is
65 kyrs, based on a constant spreading rate of 108 mm/yr [*Carbotte and Macdonald,*
1992]). We observe a general westward trend of the CAMH peak away from the AST
and identify three regions that show significant variations in the CAMH boundaries and
peak location relative to the NVZ boundaries and AST (9° 48-46'N, 9° 42-36'N and south
of 9° 33'N, Fig. 2-3b). One of the main focuses of our study is to compare the location of
present day bathymetric discontinuities and changes in the appearance of the CAMH
(magnetic deviations) to discern if ridge processes have been stable over magnetic
timescales. Of the four main bathymetric discontinuities identified in the AST (Fig. 2-1c),
only the 9° 37'N OSC appears to be associated directly with a magnetic deviation. The
lack of a magnetic deviation at the other three bathymetric discontinuities may be
because they are too young to form a magnetic deviation and/or they migrate over
timescales less than 10^3-10^4 yrs. Alternatively, these discontinuities may produce
magnetic deviations that are below the spatial resolution of our dataset (~0.75 km). The

three regions which show significant variations in CAMH boundary and CAMH peak location are described from north to south below.

In the 9° 48-46'N region, the width of the CAMH boundary on the eastern flank decreases by ~0.7 km and coincides with a short wavelength indentation or narrowing of the NVZ at 9° 47.5'N (Fig. 2-6c) and a similar narrowing of the 2.6 km contour in the multibeam bathymetry between 9° 48-46'N (Fig. 2-6a). There is also a small decrease of 4 A/m in the CAMH peak amplitude at 9° 47'N (Fig. 2-4a), which agrees well with a decrease in CAMH amplitude observed at 9° 46'N in the inversion results of *Lee et al.* [1996] (2.5 A/m for a 0.5 km source layer thickness, which is ~5 A/m for a 0.25 km source layer thickness). We interpret these magnetic and bathymetric features to be the result of disrupted lava deposition by ridge-parallel normal faults, as discussed in section 4.2. However, we cannot identify a specific surface fault that could have caused this disruption in either the backscatter data or still images from near-bottom camera tows in the region (*S. Soule*, personal communication). It is possible that part of the fault was covered by the elongate off-axis flow mapped between 9° 47-46'N on the eastern flank (Fig. 2-3a). A small break in the AST occurs at 9° 47'N, but there are no other physical features that explain the disruption. A higher resolution survey would better define any magnetic deviation of the CAMH peak and possibly identify a bathymetric source for the narrowing of the NVZ and CAMH.

South of 9° 40'N, we observe a divergence of the CAMH peak up to 0.7 km to the west of the AST as it approaches the 9° 37'N OSC from the north (Fig. 2-7b). The 9° 37'N OSC offsets the AST ~0.7 km to the west (the same distance as the magnetic deviation) and the CAMH peak overlies the AST again at 9° 38'N, where the AST forms the western limb of the 9° 37'N OSC (Fig. 2-7b). The NVZ boundaries and multibeam bathymetry both show along-axis changes between 9° 42 and 9° 36'N. The width of the NVZ and lateral distance of the 2.55-2.6 km contours from the AST are much greater on the eastern flank than the western flank between 9° 42-39'N (Fig. 2-7a and c). This

asymmetry in the NVZ and bathymetry is reduced gradually with distance south of 9° 39'N to 9° 36'N, as the NVZ and the bathymetric contours narrow, but differences in the CAMH gradients persist on both flanks, with steeper gradients to the east compared to the west (Fig. 2-9).

Lee et al. [1996] also observe a magnetic deviation or discontinuity around 9° 37'N, defined by a decrease in CAMH amplitude of ~2 A/m (equivalent to ~4 A/m for a 0.25 km source layer thickness) and previous studies have identified the 9° 37'N OSC as a significant ridge axis discontinuity along this section of the EPR [Haymon et al., 1991, Batiza and Niu, 1992; Wright et al., 1995; Smith et al., 2001; White et al., 2002]. Smith et al. [2001] proposed that the 9° 37'N OSC is propagating to the south based on geochemical, biological and hydrothermal fluid chemistry data, and seafloor morphology at the overlapping limb tips. Their work suggests that the eastern overlapping limb of the OSC is actively propagating to the south, due to a more robust magma supply north of the discontinuity, compared with the western limb, which lacks signs of recent magmatic and hydrothermal activity from the seafloor morphology. The southward propagation of the eastern limb of the OSC follows the same migration direction as the much larger 9°03'N OSC to the south [Carbotte and Macdonald, 1992; Bazin et al., 2001]. We interpret the westward divergence of the CAMH peak north of the 9° 37'N OSC to be the magnetic expression of this OSC's southward migration. The magnetic deviation from the AST marks the encroaching dominance of the eastern limb over the western limb as it propagates to the south. The backscatter data supports this interpretation with the scalloped edges of sheet lava flows extending throughout the NVZ, implying normal lava deposition, with the exception of an anomalous group of pillow mounds around the terminus of the eastern limb of the 9° 37'N OSC (Fig. 2-7c). White et al. [2002] frequently observed pillow mounds at the ends of small scale segments (~20 km in length) along the EPR and suggest their presence may indicate an area of disrupted or reduced lava deposition. We would expect these pillow mounds to be covered by sheet flow lavas in the future, as the eastern limb of the OSC propagates to the south.

The CAMH peak and boundaries south of 9° 33'N are asymmetrically located to the west relative to the ridge axis (Fig. 2-8b, 2-9) and coincide with both asymmetric NVZ boundaries (Fig. 2-8c) and greater ridge volumes to the west, based on the bathymetric contours (Fig. 2-8a). The narrowing of the eastern CAMH boundary and more irregular appearance of the eastern NVZ boundary also corresponds with a dramatic increase in the number of surface faults on the eastern flank at 9° 33'N [*Escartin et al.*, 2006]. This high density of surface faults continues to the south and is interspersed with pillow mounds (Fig. 2-8c). By comparison, the western flank is dominated by the scalloped edges of sheet lava flows extending from the AST to the edge of the survey. These flows are cut by multiple surface exposed lava channels suggesting significant volcanic deposition in this area (Fig. 2-3a). *Schouten et al.* [1999] interpret the results of an Alvin magnetic profile at 9° 31'N as showing the predominantly westward transportation of lava from the AST in contrast to the eastern flank, where numerous faults and hanging basins disrupt lava deposition. The shape and location of the CAMH thus accurately reflects the dominant lava deposition to the west in this region.

2.4.4. Along-axis patterns of lava deposition

We propose that the variability of the CAMH reflects patterns of lava deposition along the ridge axis and should, therefore, document changes in these patterns. Recent lava distribution patterns (< 10 kyrs) are defined by the NVZ, as opposed to long-term patterns shown by changing ridge morphology in bathymetric surveys. By comparing the appearance of the CAMH with the distribution patterns in both the NVZ and multibeam bathymetry we can determine whether the CAMH has been dominated by short-term patterns, long-term patterns, or both.

On a broad scale there is less variability in the NVZ, CAMH widths and flow distances on the western flank compared with the eastern flank (Fig. 2-10a and b). This suggests more consistent recent lava deposition on the western flank throughout our survey area. In contrast, the eastern NVZ boundary shows significant variations, for

example, between 9° 45-38'N the NVZ is at its widest extent and the distance between the NVZ and CAMH boundaries reaches its greatest value (Fig. 2-10a and b). The greater variability observed on the eastern flank may be due to the increased number of surface exposed faults on this flank [*Escartin et al.,*2006]. The western flank appears to be cut by individual east-facing faults that extend long distances along-axis (~10 km) and control the western boundary of the NVZ. The eastern flank is very different in appearance, with clusters of shorter (> 1 km) west-facing faults that are interspersed with lava covered regions, including elongate flows (Fig. 2-3a). The large number of exposed surface faults on the eastern flank indicates decreased lava deposition or increased tectonic activity, but it is difficult to tell which process occurred first and resulted in the present day morphology. The consistent appearance of both the NVZ and CAMH shows that the CAMH documents short-term (< 10 kyrs) patterns of lava distribution. The step-like gradient in the CAMH peak amplitude is also a recent feature (< 10 kyrs), as it is located along or close to the ridge axis (Fig. 2-10d).

The EPR bathymetry reflects the long-term complex relationship between magma supply, lava deposition and thermal structure. To quantify long-term lava deposition patters we calculate a proxy for the ridge volume from the cross sectional area of the top 120 m of the ridge axis (Fig. 2-10e) using the multibeam bathymetry data (the calculations are made for each grid cell, ~110 m along-axis). Both flanks show varying ridge volumes from north to south (< 0.2 km^2 to ~0.4 km^2), but the eastern flank has greater volumes and more gentle slopes on average (Fig. 2-10e and f, the slope is calculated along the same cross-axis profiles as the cross sectional area). The top 120 m of the ridge axis represents < ~50 kyr old crust, greater than five times the age of the surface flows in the NVZ. In general, the ridge volume shows significant along-axis variations on both flanks, which differs from the CAMH and NVZ boundaries that show more variation on the eastern flank. However, there is a correlation between reduced ridge volumes on the eastern flank and the two regions where the eastern CAMH narrows between 9° 49-46'N and 9° 32-28'N (Fig. 2-10a and e, indicated by the light blue boxes).

The ridge volumes also become asymmetric to the west in the region south of 9° 33'N, similar to the CAMH and NVZ boundaries. These areas of disrupted lava deposition are therefore interpreted as being long lived features (up to ~ 50 kyrs) that have modified the shape of the CAMH. Other correlations between the CAMH boundary location and changing ridge volumes are very subtle and we are limited by the resolution of our dataset. In summary, the CAMH reflects several regions of long-lived disruptions in lava deposition identified in the bathymetric data (between 9° 49-47'N and 9° 32-29'N, Fig. 2-10e). It has also been modified by more recent patterns of lava deposition, as defined by the NVZ (Fig. 2-10a), which shows more consistent lava deposition on to the western flank and the importance of ridge-parallel normal faults in controlling the location of lava deposition.

2.5. Conclusions

We have conducted a detailed study of the CAMH between 9° 55'N and 9° 25'N on the EPR. The study focuses on identifying the sources of variations in the CAMH and linking these variations to crustal accretion patterns. The process of crustal accretion modifies the shape of the CAMH by controlling the thickness of the magnetic source layer and the deposition of young, highly magnetic lavas. We make the following conclusions:

1. The most significant magnetic feature in our survey area is an along-axis gradient in the CAMH peak amplitude between 9° 42-36'N, where the calculated crustal magnetization decreases by ~40 % and remains low to the south. Discounting changing geochemistry and paleointensity as the source of the gradient, we propose that variations in magnetic source layer thickness alone can account for this gradient. Our magnetic moment model shows that the source layer has approximately the same thickness as seismic Layer 2A for crustal magnetizations of 45 A/m. Assuming that seismic Layer 2A is a proxy for the extrusive lava layer, the peak CAMH gradient can be accounted for by an

observed decrease of ~50 % in the extrusive lava layer thickness along-axis (from 250 m to 125 m). The 9° 37' N OSC coincides with the southern end of the CAMH gradient and we interpret the 9° 42-36'N ridge section to be a transition zone in crustal accretion processes, with a robust magmatic segment north of 9° 42'N and a relatively less robust segment south of 9° 36'N.

2. The CAMH boundaries lie entirely within or along the boundary of the NVZ, as defined by the backscatter data, suggesting a systematic relationship between the CAMH source and sequences of young lava flows that make up the NVZ. The fact that the CAMH boundaries lie within the NVZ boundaries is further evidence that the lava flows dip towards the axis. The minimum lava flow dip angles, calculated from the difference in boundary locations and Layer 2A thickness, agree well with both crustal accretion models [*Hooft et al.,* 1996] and observations [*Karson et al.*, 2002], and provides an alternative method to estimate lava dip angles along fast spreading ridges where the extrusive volcanic sequence is not exposed. Occasional elongate flows (e.g., on the eastern flank between 9° 42-40'N) that deposit lavas up to 3 km from the AST form thin carapaces over older seafloor and do not have enough volume to contribute to the CAMH and thus do not affect its width or shape.

3. Only the 9° 37'N OSC has a magnetic deviation associated with it. Approaching the OSC from the north, the CAMH peak shifts from the AST to the western limb of the OSC, reflecting the southward migration of the bathymetric discontinuity. These results, combined with the along-axis gradient in the CAMH amplitude that terminates near the 9° 37'N OSC, indicate that this is a significant ridge discontinuity along this section of the EPR.

4. Finally, the CAMH reflects both long-term patterns in lava deposition (~ 50 kyrs), defined by the multibeam bathymetry, and short term patterns, defined by

the NVZ (< 10 kyrs). Long-term patterns include disrupted lava deposition on the eastern flank due to ridge-parallel surface faults, while recent patterns show increased lava deposition onto the western flank. The correlation between morphological features and variations in the CAMH appearance show that the CAMH, when mapped using near-bottom data, documents crustal accretion processes over timescales of ~10^4 yrs and may be used to interpret along-axis changes at other fast spreading ridges.

2.6. Appendix A: Data Resolution Comparison

A comparison of the near-bottom magnetic data with other magnetic datasets of varying resolution and spatial extent in our survey area provides a unique opportunity to test the quality and resolution of the near-bottom data. This comparison also allows us to address the issue of resolution versus area of surveyed seafloor when designing these types of experiments. The magnetic datasets used for the comparison are sea-surface data [*Carbotte and Macdonald*, 1992], and two high resolution ABE grids collected at 9° 50' and 9° 29'N [*Tivey et al.*, in prep].

2.A.1. Sea Surface Data

The sea surface CAMH of *Carbotte and Macdonald* [1992] and the near-bottom CAMH, continued to the sea surface, are very similar in their general appearance (Fig. 2-A1). The Carbotte and Macdonald magnetic data were processed using the same approach as the near-bottom data (see *Carbotte and Macdonald* [1992] for the location of survey lines). The inversion results show a broad lineated CAMH, with the maximum or peak in amplitude located slightly west of the AST (~300 m). In general, the amplitude of the CAMH decreases from north to south with three discrete highs located at 9° 48'N, 9° 41.5'N and 9° 32.5'N (Fig. 2-A1a). When comparing the Carbotte and Macdonald seasurface CAMH with the near-bottom CAMH (Fig. 2-A1b), the latter has higher resolution than the Carbotte and Macdonald CAMH, but the overall appearance of the two CAMHs anomaly patterns compare well. The near-bottom CAMH is more symmetric about the AST but there are peaks in amplitude at the same locations as the

Carbotte and Macdonald CAMH. As expected, the near-bottom CAMH better defines the CAMH, with steeper gradients and higher amplitudes, and provides more information about along and across axis variations over short spatial scales (< 2 km) .

2.A.2. Near- Bottom ABE Data

The resolution of two ABE magnetic grids in our survey area is much greater than the near-bottom magnetic data; but similar wavelength (> 0.75 km) magnetic features are observed in both datasets (Fig. 2-A2). The two spatially dense ABE magnetic data grids were acquired at 9° 50'N and 9° 29'N in 2001 (cruise AT7-4, Fig. 2-1b) using a 3-axis magnetometer, mounted on the autonomous vehicle ABE [*Yoerger et al.*, 1996; *Schouten et al.*, 2003; *Tivey et al.*, in prep]. The ABE residual magnetic anomaly grids were continued upwards to ~2.5 km water depth for direct comparison with the near-bottom residual magnetic anomaly at 2.5 km water depth. At this time we compare only patterns in the overall anomaly and not anomaly amplitudes.

The ABE 9° 50'N anomaly grid shows that the central anomaly (CA) has a double peak across the axis, with the intermediate low centered on the AST (Fig. 2-A2b). The peak on the western flank has greater amplitude and is located ~0.5 km west of the AST. The most striking magnetic feature in the ABE grid is the steep gradient and linear appearance of the magnetic low that defines the eastern edge of the CA, ~1.5 km from the axis (Fig. 2-A2b). The eastern edge of the CA in the near-bottom data shows the same steep gradient and linear character as the ABE data (Fig. 2-A2c). This is a feature that is not well resolved by the sea-surface data. The near-bottom CA is very broad with the maximum or peak offset to the west by ~1 km. More near-bottom survey lines close to the AST would be required to resolve a double peak and intermediate low at the AST, as observed in the ABE grid (Fig. 2-A2b). There appears to be a correlation between the ABE CA and seafloor morphology, implying that the shape of the CA reflects recent patterns of crustal accretion and may be able to resolve features ~0.25 km in size, based on the dimensions of lava flow fronts identified in the backscatter data (see *Schouten et*

al., 2003). In contrast to the ABE resolution limit, the near-bottom data is able to resolve features ~0.75 km in size (such as the linear eastern edge of the anomaly).

In the ABE magnetic anomaly grid at 9° 29'N, the CA is double-peaked with both peaks located asymmetrically on the western flank, at 0.5 and 1 km west of the AST (Fig. 2-A2e). The eastern edge of the CA has an irregular appearance (unlike the linear feature in the 9° 50'N grid). The near-bottom CA at 9° 29'N also has the same asymmetric nature but resolves only one magnetic high ~ 0.75 km west of the AST (Fig. 2-A2f). Other major features of the near-bottom magnetic anomaly compare well with the ABE data. As in the 9° 50'N area, we believe that near-bottom data are able to resolve features on a scale of ~0.75 km.

In summary, our comparison of the near-bottom magnetic data with the sea-surface CAMH and the ABE magnetic data at 9° 50'N and 9° 29'N show that the near-bottom magnetic survey is a valuable dataset which allows for extrapolation of magnetic data between the two ABE grids along this section of the EPR. The near-bottom magnetic data provide a high quality, albeit somewhat low-pass filtered version of the CA and crustal magnetization over the spreading center.

Acknowledgements

References

Atwater, T., and J.D. Mudie (1973), A detailed near-bottom geophysical study of the Gorda Rise, *J. Geophys. Res.*, *78*, 8865-8886.

Auzende, J.-M., E. Bonatti, M. Cannat, et al. (1989), Direct observation of a section through slow spreading oceanic crust, *Nature*, *337*, 726-729.

Batiza, R., and Y. Niu (1992),Petrology and Magma Chamber Processes at the East Pacific Rise ~9° 30'N, *J. Geophys. Res.*, *97*, 6779-6797.

Batiza, R., and S.H. Margolis (1986), A model for the origin of small nonoverlapping offsets (SNOOs) of the East Pacific Rise, *Nature*, *320*, 439-441.

Bazin, S., A.J. Harding, G.M. Kent, et al. (2001),Three-dimensional shallow crustal emplacement at the 9° 03'N overlapping spreading center on the East Pacific Rise: Correlations between magnetization and tomographic images, *J. Geophys. Res.*, *106*, 16010-16117.

Bowles, J., J.S. Gee, D.V. Kent, et al. (2006), Paleointensity applications to timing and extent of eruptive activity, 9°-10° East Pacific Rise, *Geochem. Geophys. Geosyst.*, *7*, doi:10.1029/2005GC001141.

Cann, J.R. (1974), A model for oceanic crustal structure developed, *Geophys. J R. Astron. Soc.*, *39*, 169-187.

Carbotte, S., and K.C. Macdonald (1992), East Pacific Rise 8°-10° 30'N: Evolution of Ridge Segments and Discontinuities From SeaMARC II and Three-Dimensional Magnetic Studies, *J. Geophys. Res.*, *97*, 6959-6982.

Carbotte, S., and J.C. Mutter (1997),Inferences from the geometry of seismic Layer 2A on volcanic and tectonic processes within the plate boundary zone, EPR 17° S, *Eos, Transactions, American Geophysical Union*, *78*, No. 46, Suppl., pp.705

Christeson, G.L., G.M. Purdy, and G.J. Fryer (1992), Structure of young upper crust at the East Pacific Rise near 9° 30'N, *Geophys. Res. Letts.*, *19*, 1045-1048.

Christeson, G.L., G.M. Purdy, and G.J. Fryer (1994), Seismic constraints on shallow crustal emplacement processes at the fast spreading East Pacific Rise, *J. Geophys.Res*, *99*, 17957-17973

Christeson, G.L., G.M. Kent, G.M. Purdy, and R.S. Detrick (1996), Extrusive thickness variability at the East Pacific Rise, 9°-10°N: Constraints from seismic techniques, *J. Geophys. Res*, *101*, 2859-2873.

Christeson, G.L., K.D. McIntosh, and J.A. Karson (2007),Inconsistent correlation of seismic layer 2a and lava layer thickness in oceanic crust, *Nature*, *445*, doi:10.1038/nature05517.

Cochran, J.R., D.J. Fornari, R. Coakley, et al. (1999),Continuous near-bottom gravity measurements made with a BGM-3 gravitmeter in DSV Alvin on the East Pacific Rise crest near 9° 31'N and 9° 50'N, *J. Geophys. Res.*, *104*, 10,841-10,861.

Cowen, J.P., D.J. Fornari, T. Shank, B. Love, B. Glazer, A. Treusch, R.C. Holmes, S.A. Soule, E.T. Baker, M. Tolstoy, and K.R. Pomranig (2007),Volcanic eruptions at East Pacific Rise near 9° 50'N, *EOS Trans. AGU*, *88* (81), doi:10.1029/2007EO070001.

Detrick, R.S., P. Buhl, E. Vera, et al. (1987),Multi-channel seismic imaging of a crustal magma chamber along the East Pacific Rise, *Nature, 326*, 35-41.

Dunn, R.A., D.R. Toomey, and S.C. Solomon (2000),Three-dimensional seismic structure and physical properties of the crust and shallow mantle beneath the East Pacific Rise at 9° 30'N, *J. Geophys. Res., 105* (B10), 23537-23555.

Escartin, J., S.A. Soule, D.J. Fornari, M.A. Tivey, H. Schouten, and M.R. Perfit (2006),Interplay between faults and lava flows in construction of the upper oceanic crust: The East Pacific Rise crest 9°25'-9°58'N, *Geochem. Geophys. Geosyst., 8*, Q06005, doi:10.1029/2006GC001399.

Fornari, D.J., R.M. Haymon, M.R. Perfit, et al. (1998), Axial summit trough of the East Pacific Rise 9°-10°N:Geological characteristics and evolution of the axial zone on fast spreading mid-ocean ridges, *J. Geophys. Res., 103*, 9827-9855.

Fornari, D.J., M.A. Tivey, H. Schouten, et al. (2004), Submarine lava flow emplacement at the East Pacific Rise 9° 50'N: Implications for uppermost crust statigrahpy and hydropthermal fluid circulation, in *The Thermal Structure of the Ocean Crust and the Dynamics of Hydrothermal Circulation*, pp. 187-217, AGU, Washington D.C.

Garry, W.B., T.K.P. Gregg, S.A. Soule, and D.J. Fornari (2006),Formation of submarine lava channel texture: Insights from laboratory simulations, *J. Geophys. Res., 111*, doi:10.1029/2005JB003796.

Gee, J., and D.V. Kent (1994),Variations in Layer 2a thickness and the origin of the central anomaly magnetic high, *Geophys.Res.Lett., 21*, 297-300.

Gee, J., D.A. Schneider, and D.V. Kent (1996), Marine magnetic anomalies as recorders of geomagnetic intensity variations, *Earth. Plan. Sci. Lett., 144*, 327-335.

Gee, J., and D.V. Kent (1997), Magnetization of axial lavas from the southern East Pacific Rise (14°-23° S): Geochemical controls on magnetic properties, *J. Geophys .Res., 102*, 24873-24886.

Gee, J., S.C. Cande, J.A. Hildebrand, et al. (2000), Geomagnetic intensity variations over the past 780 kyr obtained from near-seafloor magnetic anomalies, *Nature, 408*, 827-832.

Goldstein, S.J., M.R. Perfit, R. Batiza, et al.(1994),Off-axis volcanism at the East Pacific Rise detected by uranium-series dating of basalts, *Nature, 367*, 157-159.

Gregg, T.K.P., D.J. Fornari, M.R. Perfit, et al. (1996), Rapid emplacement of a mid-ocean ridge lava flow on the East Pacific Rise at 9° 46'-51N, *Earth Planet. Sci. Letts., 144*, E1-E7.

Guspi, F. (1987), Frequency- domain reduction of potential field measurements to a horizontal plane, *Geoexploration, 24*, 87-98.

Guyodo, Y., and J. Valet (1999), Global changed in intensity of the Earth's magnetic field during the past 800kyr, *Nature, 399*, 247-252.

Harding, A.J., G.M. Kent, and J.A. Orcutt (1993),A multichannel seismic investigation of upper crustal structure at 9°N on the East Pacific Rise: implications for crustal accretion, *J. Geophys. Res., 98*, 13925-13944.

Haymon, R.M., D.J. Fornari, M.H. Edwards, et al. (1991), Hydrothermal vent distribution along the East Pacific Rise crest (9° 09'-54'N) and its relationship to magmatic

and tectonic processes on fast-spreading mid-ocean ridges, *Earth Planet. Sci. Letts.*, *104*, 513-534.

Haymon, R.M., D.J. Fornari, K.L. Von Damm, et al. (1993), Volcanic eruption of the mid-ocean ridge along the East Pacific Rise crest at 9° 45'-53'N: Direct submersible observations of seafloor phenomenon associated with an eruption event in April, 1991, *Earth Planet. Sci. Letts.*, *119*, 85-101.

Haymon, R.M., and S.M. White (2004), Fine-scale segmentation of volcanic/hydrothermal systems along fast-spreading rdiges crests, *Earth Planet. Sci. Letts.*, *226*, 367-382.

Hooft, E.E.E., H. Schouten, and R.S. Detrick (1996), Constraining crustal emplacement processes from the variation in seismic layer 2A thickness at the East Pacific Rise, *Earth Planet. Sci. Letts.*, *142*, 289-309.

IAGA Division V Working Group (2000), International geomagnetic reference field 2000, *Geophys. J. International*, *141*, 256-262.

Irving, E. (1970),The Mid-Atlantic Ridge at 45° N, XIV, Oxidation and magnetic properties of basalts; review and discussion, *Can. J. Earth Sci.*, *7*, 1528-1538.

Isezaki, N. (1986),A new shipboard three-component magnetometer, *Geophysics*, *51*, 1992-1998.

Karson, J.A., S.D. Hurst, and P. Lonsdale (1992), Tectonic rotations of dikes in fast-spreading oceanic crust exposed near Hess Deep, *Geology*, *20*, 685-688.

Karson, J.A. (1998), Internal structure of oceanic lithosphere: a perspective from tectonic windows, in *Faulting and Magmatism at Mid-Ocean Ridges*, edited by W.R. Buck, P.T. Delaney, J.A. Karson, and Y. Lagabrielle, AGU, Washington D.C.

Karson, J.A., M.A. Tivey, and J.R. Delaney (2002),Internal structure of uppermost oceanic crust along the Western Blanco Transform Scarp: Implications for subaxial accretion and deformation at the Juan de Fuca Ridge, *J. Geophys. Res.*, *107*, doi:10.1029/2000JB000051.

Kent, G.M., A.J. Harding, and J.A. Orcutt (1993), Distribution of magma beneath the East Pacific Rise near the 9° 03'N overlapping spreading center from forward modeling of common depth point data, *J. Geophys. Res.*, *98*, 13,971-13,995.

Kidd, R.G.W. (1977), A model for the process of formation of the upper oceanic crust, *Geophys. J R. Astron. Soc.*, *50*, 149-183.

Klitgord, K.D. (1976), Sea-floor spreading: The central anomaly magnetization high, *Earth Planet. Sci. Letts.*, *29*, 201-209.

Klitgord, K.D., and J. Mammerickx (1982), Northern East Pacific Rise: Magnetic anomaly and bathymetric framework, *J. Geophys. Res.*, *87*, 6725-6750.

Korenaga, J. (1995), Comprehensive analysis of marine magnetic vector anomalies, *J. Geophys. Res.*, *100*, 365-378.

Korte, M., and C.G. Constable (2005), The geomagnetic dipole moment over the last 7000 years- new results from a global model, *Earth Planet. Sci. Letts.*, *236*, 348-358.

Kurras, G.J., D.J. Fornari, M.H. Edwards, et al. (2000), Volcanic morphology of the East Pacific Rise crest 9° 49'-52'N: Implications for volcanic emplacement processes at fast-spreading mid-ocean ridges, *Mar. Geophys. Res.*, *21*, 23-41.

Lagabrielle, Y., D. Bideau, M. Cannat, et al. (1998), Ultramafic-mafic plutonic rock suites along the Mid-Atlantic Ridge (10° N- 30° N): symmetrical distribution and implications for seafloor spreading processes, in *Faulting and Magmatism at Mid-Ocean Ridges*, edited by W.R. Buck, P.T. Delaney, J.A. Karson, and Y. Lagabrielle, pp. 153-176, AGU, Washington D.C.

Langmuir, C.H., J.F. Bender, and R. Batiza (1986), Petrological and tectonic segmentation of the East Pacific Rise, 5°30'-14°30'N, *Nature, 322*, 422-429.

Lee, S.M., S.C. Solomon, and M.A. Tivey (1996), Fine-scale crustal magnetization variations and segmentation of the East Pacific Rise, 9° 10'-9° 50'N, *J. Geophys. Res., 101*, 22033-22050.

Lonsdale, P. (1983), Overlapping rift zones at the 5.5° S offset of the East Pacific Rise, *J. Geophys. Res., 88*, 9393-9406.

Macdonald, K.C., and P.J. Fox (1983), Overlapping spreading centers: new accretion geometry on the East Pacific Rise, *Nature, 301*, 55-58.

Macdonald, K.C., and P.J. Fox (1988), The axial summit graben and cross-sectional shape of the East Pacific Rise as indicators of axial magma chambers and recent volcanic eruptions, *Earth Planet. Sci. Letts., 88*, 119-131.

Macdonald, K.C., S.P. Miller, S.P. Huestis, and F.N. Spiess (1980),Three-dimensional modeling of a magnetic reversal boundary from inversion of deep-tow measurements, *J. Geophys. Res., 85*, 3670-3680.

Macdonald, K.C., S.P. Miller, B.P. Luyendyk, et al. (1983),Investigation of a Vine-Matthews magnetic lineation from a submersible: The source and character of marine magnetic anomalies,, *J. Geophys. Res, 88*, 3403-3418.

Macdonald, K.C., J.-C. Sempere, and P.J. Fox (1984), East Pacific Rise from Siqueiros to Orozo Fracture Zones: along-strike continuity of axial neovolcanic zone and structure and evolution of overlapping spreading center, *J. Geophys. Res., 89*, 6049-6069.

Macdonald, K.C., J.-C. Sempere, P.J. Fox, and R. Tyce (1987), Tectonic evolution of ridge-axis discontinuities by the meeting, linking, or self decapitation of neighboring ridge segments, *Geology, 15*, 993-997.

Macdonald, K.C., P.J. Fox, L.J. Perram, et al. (1988),A new view of the mid-ocean ridge from the behaviour of ridge axis discontinuities, *Nature, 335*, 217-225.

Macdonald, K.C., D.S. Scheirer, and S.C. Carbotte (1991), Mid-ocean ridges: discontinuities, segments and giant cracks, *Science, 253*, 986-994.

Macdonald, K.C., P.J. Fox, S.P. Miller, et al. (1992), The East Pacific Rise and its flanks, 8°-18° N: History of segmentation, propagation and spreading direction based on SeaMARC II and Sea Beam studies, *Mar. Geophys. Res., 14*, 299-344.

Marshall, M., and A. Cox (1971), Magnetism of pillow basalts and their petrology, *Geol. Soc. Am. Bull, 82*, 537-552.

Pariso, J.E., and H.P. Johnson (1991), Alteration processes at Deep Sea Drilling Project/Ocean Drilling Program Hole 504B at the Coast Rica Rift, *J. Geophys. Res., 96*, 11,703-11,722.

Parker R. L., and S. P. Huestis (1974), The inversion of magnetic anomalies in the presence of topography, *J. Geophys. Res., 79*, 1587-1594.

Perfit, M.R., D.J. Fornari, and M.C. Smith (1994), Small-scale spatial and temporal variations in mid-ocean ridge crest magmatic processes, *Geology, 22*, 375-379.

Perfit, M.R., and J. W.W. Chadwick (1998), Magmatism at mid-ocean ridges: Constraints from volcanological and geochemical investigations, in *Faulting and Magmatism at Mid-Ocean Ridges*, edited by W.R. Buck, P. Delaney, J.A. Karson, and Y.Lababrille, pp. 57-115, AGU, Washington D.C.

Reynolds, J.R., and C.H. Langmuir (2000), Identification and implications of off-axis lava flows around the East Pacific Rise, *Geochem. Geophys. Geosyst., 1,* doi:10.1029/1999GC000033.

Rubin, K.H., J.D. Macdougall, and M.R. Perfit (1994), ^{210}Po-^{210}Pb dating of recent volcanic eruptions on the sea floor, *Nature, 368*, 841-844.

Scheirer, D.S., D.J. Fornari, S.E. Humphris, and S. Lerner (2000),High-resolution seafloor mapping using the DSL-120 sonar system: Quantitative assessment of sidescan and phase-bathymetry data from the Lucky Strike segement of the Mid-Atlantic Ridge, *Mar. Geophys. Res., 21* (121-142).

Schouten, H., and R. Denham (1979), Modeling the oceanic magnetic source layer, in *Implications of deep drilling results in the Atlantic Ocean*, edited by M. Talwani, and M. Ewing, Series 2, pp. 151-159, AGU, Washington D.C.

Schouten, H., M.A. Tivey, D.J. Fornari, and J.R. Cochran (1999), Central anomaly magnetization high: constraints on the volcanic construction and architecture of seismic layer 2A at a fast-spreading mid-ocean ridge, the EPR at 9° 30'-50'N, *Ear. Planet. Sci. Letts, 169*, 37-50.

Schouten, H., M.A. Tivey, D.J. Fornari, et al. (2003), CA Magnetization High: Constraints on the volcanic construction and architecture of young upper oceanic crust, EPR 9°-10° N, *Ridge 2000 Events* (April), 30-34.

Sempere, J.-C., A. Meshkov, M. Thommeret, and K.C. Macdonald (1988), Magnetic properties of some young basalts from the East Pacific Rise, *Mar. Geophys. Res., 9*, 131-146.

Sims, K. W. W., S.J. Goldstein, J. Blichert-Toft, et al. (2002), Chemical and isotropic constraints on the generation and transport of magma beneath the East Pacific Rise, *Geochimica et Cosmochimica Acta., 66* (19), 3481-3504.

Smith, G.M., and S.K. Banerjee (1986), Magnetic structure of the upper kilometer of the marine crust at Deep Sea Drilling Project hole 504B, eastern Pacific Ocean, *J. Geophys. Res., 91*, 10,337-10,354.

Smith, M.C., M.R. Perfit, D.J. Fornari, et al. (2001), Magmatic processes and segmentation at a fast spreading mid-ocean ridge: Detailed investigation of an axial discontinuity on the East Pacific Rise crest at 9° 37'N, *Geochem. Geophys. Geosyst., 2*, 2000GC000134.

Sohn, R.A., and K.W.W. Sims (2005), Bending as a mechanism for triggering off-axis volcanism on the East Pacific Rise, *Geology, 33* (93-96).

Soule, S.A., D.J. Fornari, M.R. Perfit, et al. (2005), Channelized lava flows at the East Pacific Rise crest 9°-10° N: The importance of off-axis lava transport in developing the architecture of young oceanic crust, *Geochemistry, Geophysics, Geosystems, 6*, doi:10.1029/2005GC000912.

Tivey, M.A., and H.P.Johnson (1987), The central anomaly magnetic high: implications for ocean crust construction and evolution, *J. Geophys.Res.*, *92*, 12685-12694.

Tivey, M.A., and H.P. Johnson (1993), Variations in oceanic crustal structure and implications for the fine scale magnetic anomaly signal, *Geophys. Res. Letts.*, *20*, 1879-1882.

Tivey, M.A. (1996), Vertical magnetic structure of ocean crust determined from near-bottom magnetic field measurements, *J. Geophys. Res.*, *101*, 20275-20296.

Tolstoy, M., J.P. Cowen, E.T. Baker, et al. (2006),A sea-floor spreading event captured by seismometers, *Science, 314*, 1920-1922.

Toomey, D.R., G.M. Purdy, S.C. Solomon, and W.S.D. Wilcock (1990),The three-dimensional seismic velocity structure of the East Pacific Rise near latitude 9° 30'N, *Nature, 347*, 639-645.

Toomey, D.R., S.C. Solomon, and G.M. Purdy (1994),Tomographic imaging of the shallow crustl structure of the East Pacific Rise at 9° 30'N, *J. Geophys. Res.*, *99*, 24,135-24,157.

Vera, E.E., and J.B. Diebold (1994), Seismic imaging of oceanic layer 2A between 9° 30'N and 10° N on the East Pacific Rise from two-ship wide -aperture profiles, *J. Geophys. Res.*, *99*, 3031-3041.

White, S.M., R.M. Haymon, D.J. Fornari, et al. (2002), Correlation between volcanic and tectonic segmentation of fast spreading ridges: Evidence from volcanic structures and lava flow morphology on the East Pacific Rise at 9°-10° N, *J. Geophys. Res.*, *107*, 2001JB000571.

White, R.S., R.M. Haymon, and S. Carbotte (2006),A new view of ridge segmentation and near-axis volcanism at the East Pacific Rise, 8°-12° N, from EM300 multibeam bathymetry, *Geochem. Geophys. Geosyst.*, *7* (12), Q12O05,doi:10.1029/2006GC001407.

Wright, D.J., R.M. Haymon, and D.J. Fornari (1995), Crustal fissuring and its relationship to magmatic and hydrothermal processes on the East Pacific Rise crest (9° 12' to 54'N), *J. Geophys. Res.*, *100*, 6097-6120.

Yang, S., H. Odah, and J. Shaw (2000),Variations in the geomagnetic dipole moment over the last 12000 years, *Geophys. J. Int.*, *140*, 158-162.

Yoerger, D. et al. (1996), Near-bottom magnetic survey of the Coaxial Ridge segment using the Autonomous Benthic Explorer survey vehicle, *RIDGE Events*, 7, 5-9.

Zhou, W., R. Van der Voo, and D.R. Peacor (1997), Single-domain and superparamagnetic titanomagnetite with variable Ti content in young ocean-floor basalts: No evidence for rapid alteration, *Earth Planet. Sci. Letts.*, *150*, 353-362.
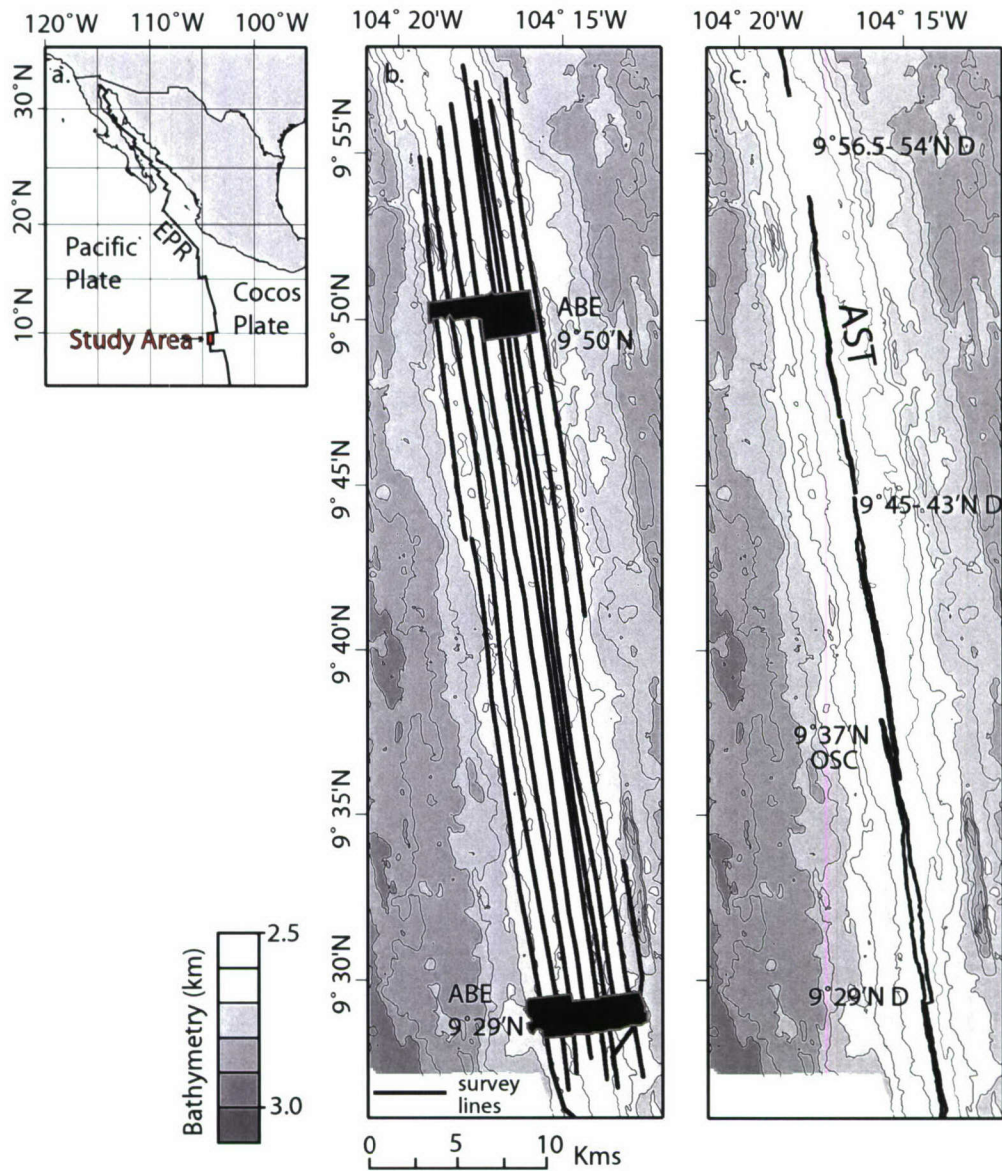
Figure 2-1.a. Regional location map of the eastern Pacific showing the East Pacific Rise (EPR). Our study area, located between 9° 55'N and 9° 25'N on the EPR, is ~58 km by ~ 8 km and centered on the ridge axis. **b**. Location map of DSL-120A survey lines (bold black lines) and two ABE (Autonomous Benthic Explorer) survey grids (filled boxes [*Schouten et al.*, 2003]) overlaid on a multibeam bathymetry grid with 50 m contour intervals [*Cochran et al.*, 1999]. **c**. Axial Summit Trough (AST, solid black line)[Fornari et al., 2004; Escartin et al., in press, Soule et al., in prep], represents the present day spreading axis of the EPR. There are four discontinuities in the AST; the 9°56.5-54'N D (Discontinuity), 9° 45-42'N D, 9° 37'N OSC and 9° 29'N D.
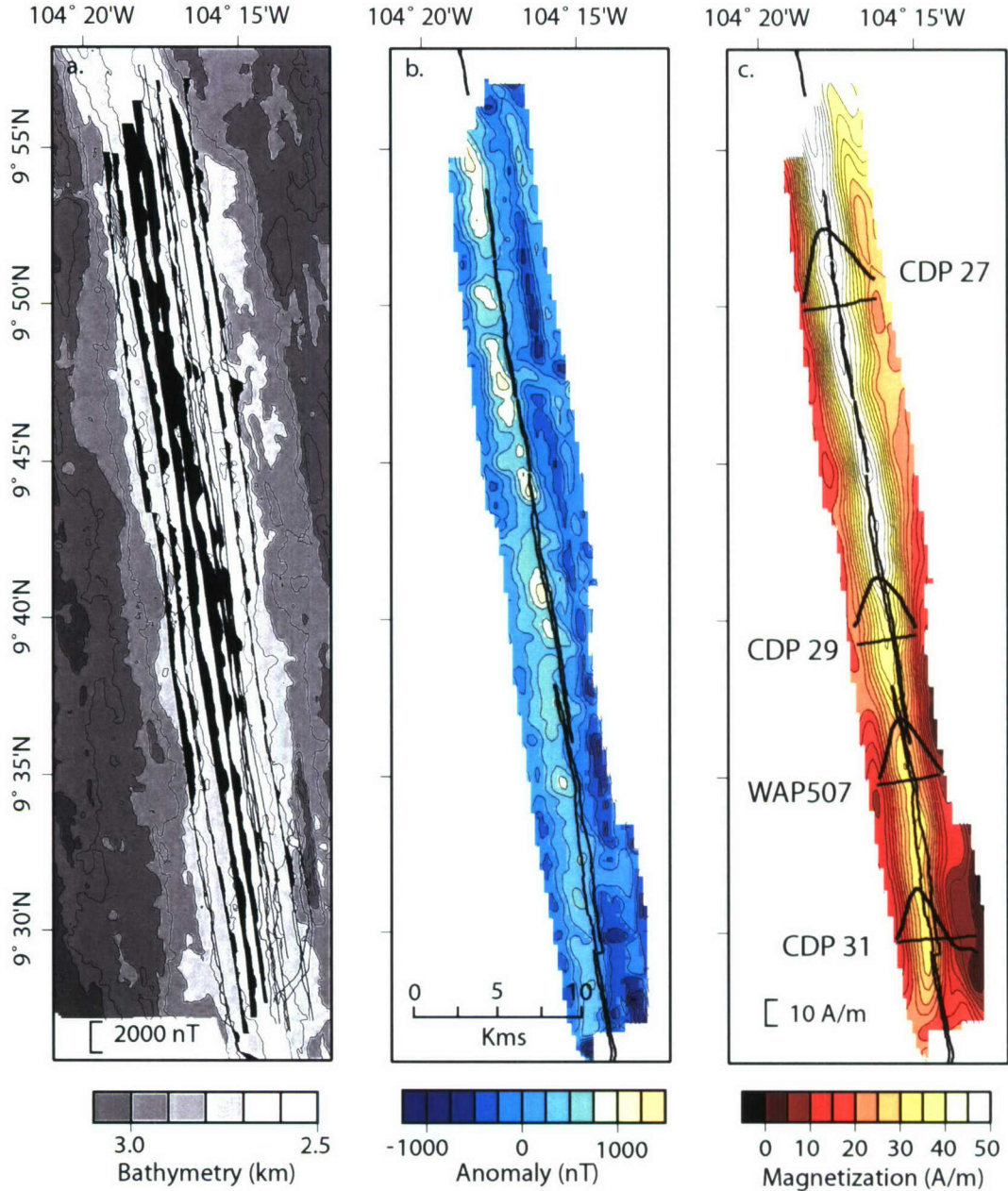
Figure 2-2.a. Near-bottom residual magnetic anomaly data along the survey lines (positive anomalies are filled). **b.** The data are gridded (0.11 km along-axis and 0.25 km across axis grid spacing) and the residual anomaly grid continued upwards to a level plane at 2.5 km water depth. **c.** The continued grid is inverted for crustal magnetization assuming a constant source layer thickness of 0.25 km. Eighteen times the annihilator are added to the grid to shift the magnetization to all positive values. The inversion results show the Central Anomaly Magnetization High (CAMH) located along the ridge axis. The four CAMH cross-axis profiles shown are located along seismic profiles CDP 27, 29 and 31 [*Harding et al.*, 1991; *Kent et al.*, 1993] and WAP 507 [*Vera and Diebold*, 1994]. The contour interval is 2.5 A/m.
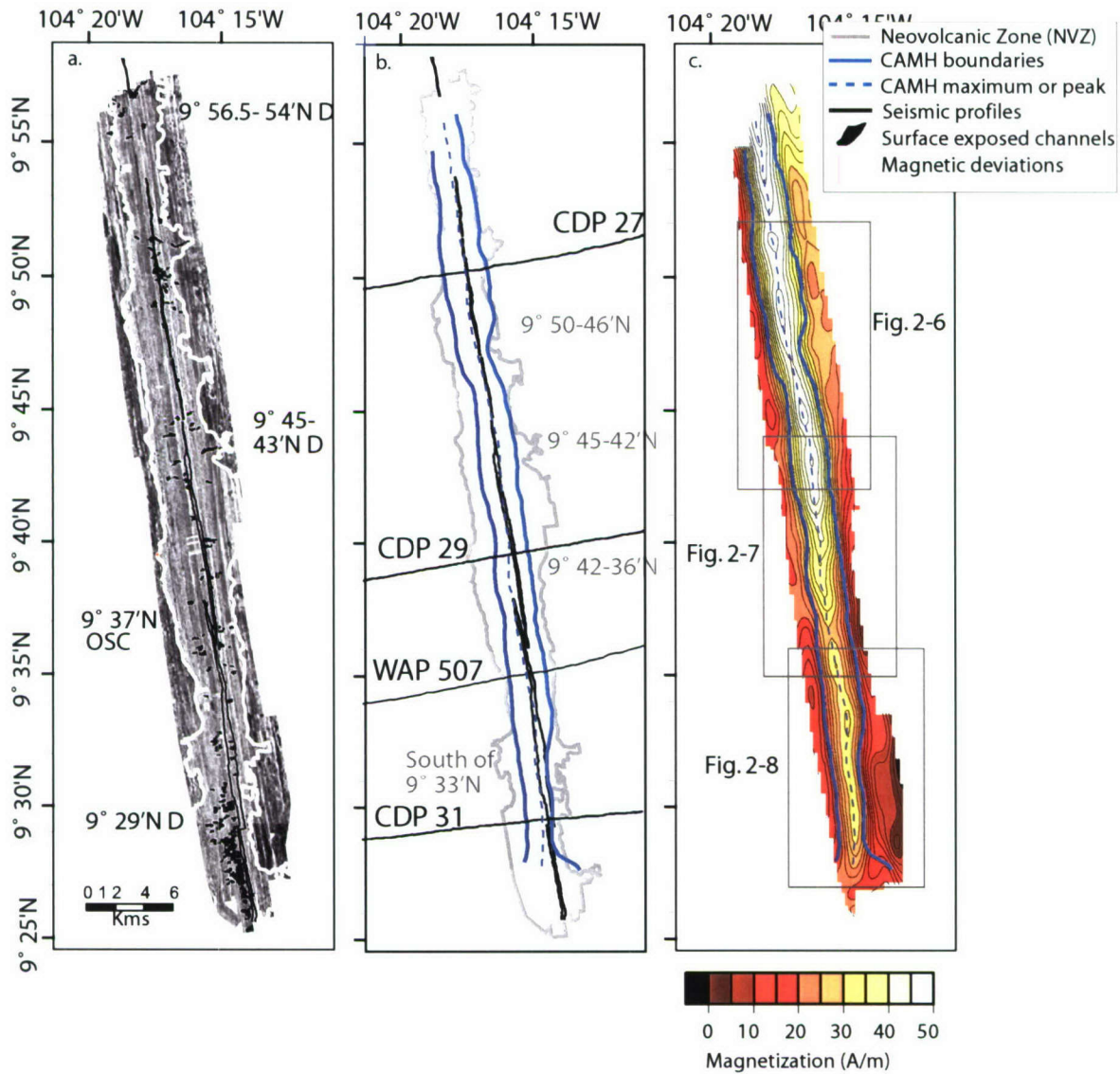
Figure 2-3.a. Side scan sonar backscatter data. Areas of high backscatter intensity (bright areas) indicate smooth surfaces and are interpreted as the glassy, sediment free surface of recent volcanic terrain. Areas of low backscatter intensity (dark areas) indicate rougher surfaces such as pillow lavas and faulted terrain. The off-axis, short black lines represent surface exposed channels [*Soule et al.*, 2005]. The extent of recent volcanism (<10 kyrs) defined as the neovolcanic zone (NVZ) is shown by the white boundary [*Fornari et al.*, 2004; *Escartin et al.*, 2006]. **b.** Comparison of the NVZ boundary (grey line) with the CAMH boundaries and CAMH peak (blue solid and dashed lines, taken from Figure 2-3c.). CDP 27, 29 and 31 and WAP 507 refer to the four seismic profiles. The grey boxes define the four regions where the CAMH peak deviates from the AST **c.** Near-bottom CAMH grid with the CAMH boundaries (solid blue lines) calculated from the maximum cross-axis gradient of the CAMH. The location of the CAMH peak is shown by the blue dashed line. Contour interval is 2.5 nT.

55

Figure 2-4.a. Along-axis CAMH peak (assuming a constant source layer thickness of 0.25km) and the location of the 1991 lava flow (green box) and the 9°29'N, 9° 37'N and 9° 45'- 43' N bathymetric discontinuities (grey boxes). **b**. Along-axis NRM calculated from the FeO content of the basalts (*M. Perfit et al.*, in prep.) assuming the empirical relationship of *Gee and Kent* [1994] where NRM(A/m)= 4.44(FeO) - 25.8. A running average of the NRM values was calculated and the linear trend shown by the solid blue line. The R^2 value of 0.746 is statistically low and this is due to the cluster of high NRM values around 9° 53'N. If these data are excluded from the running average calculation the linear trendline has an R^2 value of 0.940. **c**. Variation in seismic Layer 2A thickness along the ridge axis. Data from four seismic cross-axis experiments are shown. **d**. Model of magnetic source layer thickness required to produce the along-axis variation in the peak CAMH calculated from magnetic moment and a constant magnetization. The model was run for magnetizations of 20-70 A/m in 10 A/m increments and the resulting source layer thicknesses are shown by the black dashed lines. The red lines encompass the solutions which fall close to the Layer 2A thickness. The best fit solution is a crustal magnetization of 45 A/m, shown by the RMS misfit inset.
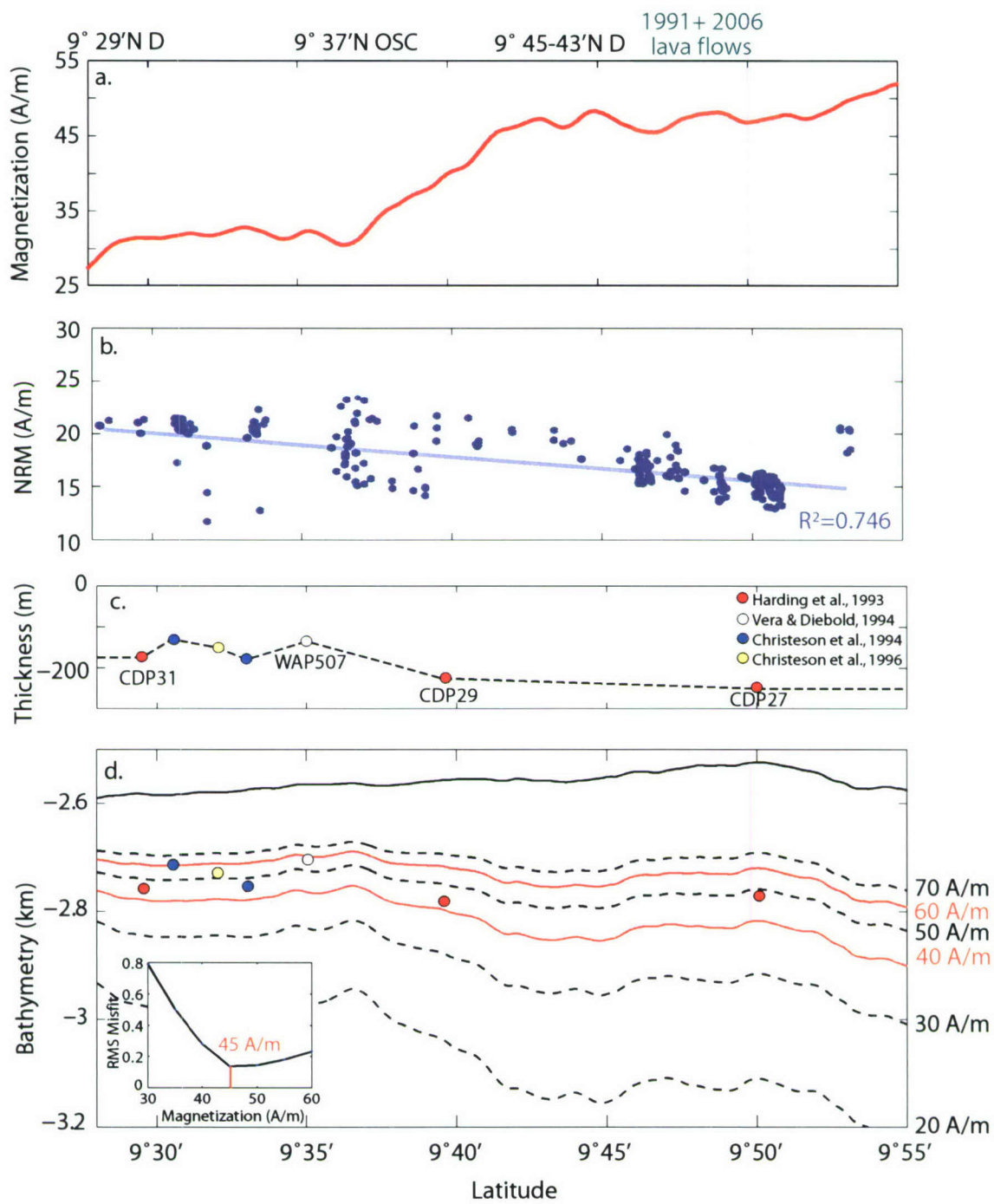
Figure 2-4
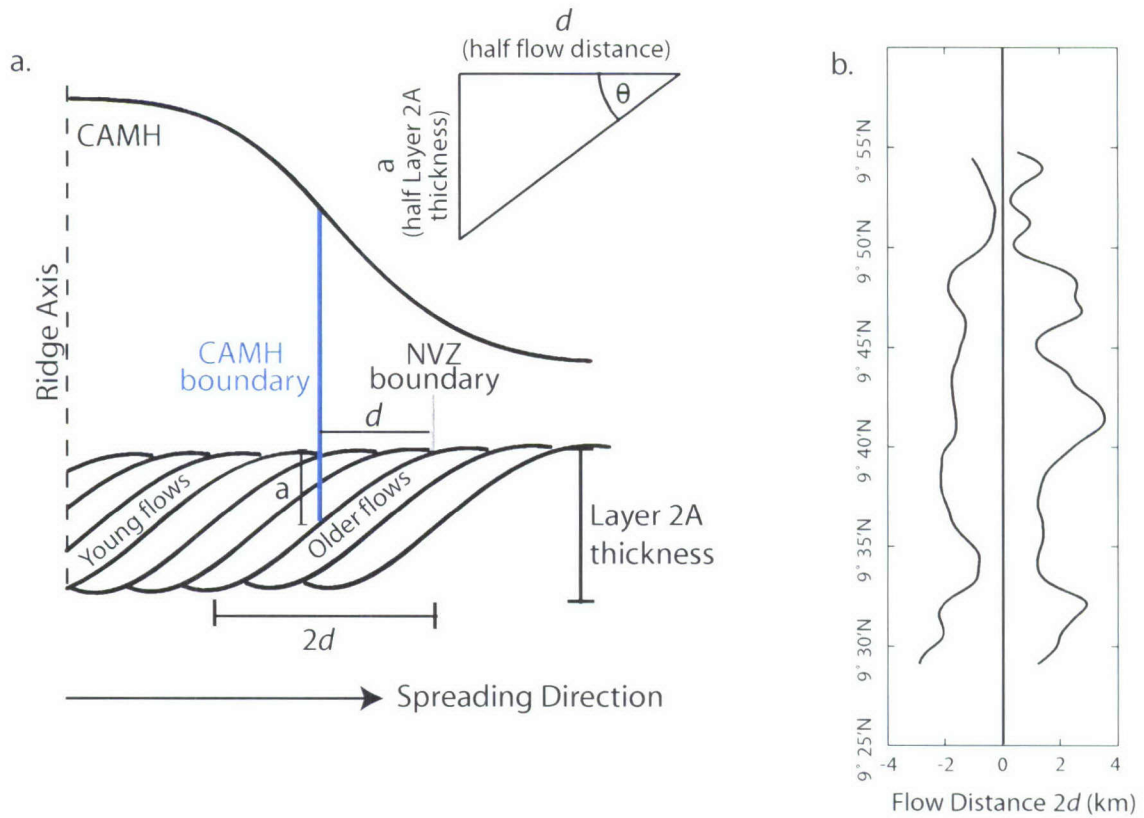
Figure 2-5.a. Cartoon to illustrate the location of the CAMH boundary inside the NVZ due to the dip of lava flows towards the spreading axis. The NVZ and CAMH boundaries are shown by the grey and blue lines respectively. The distance d between the two boundaries represents half the flow distance of the lavas from the spreading axis. The thickness a represents half the Layer 2A thickness. We calculate the dip of the lavas along the four seismic profiles where Layer 2A thickness is known. **b.** Along-axis variations in the flow distance, 2d (these data have been filtered using a 1 km low pass filter).

58
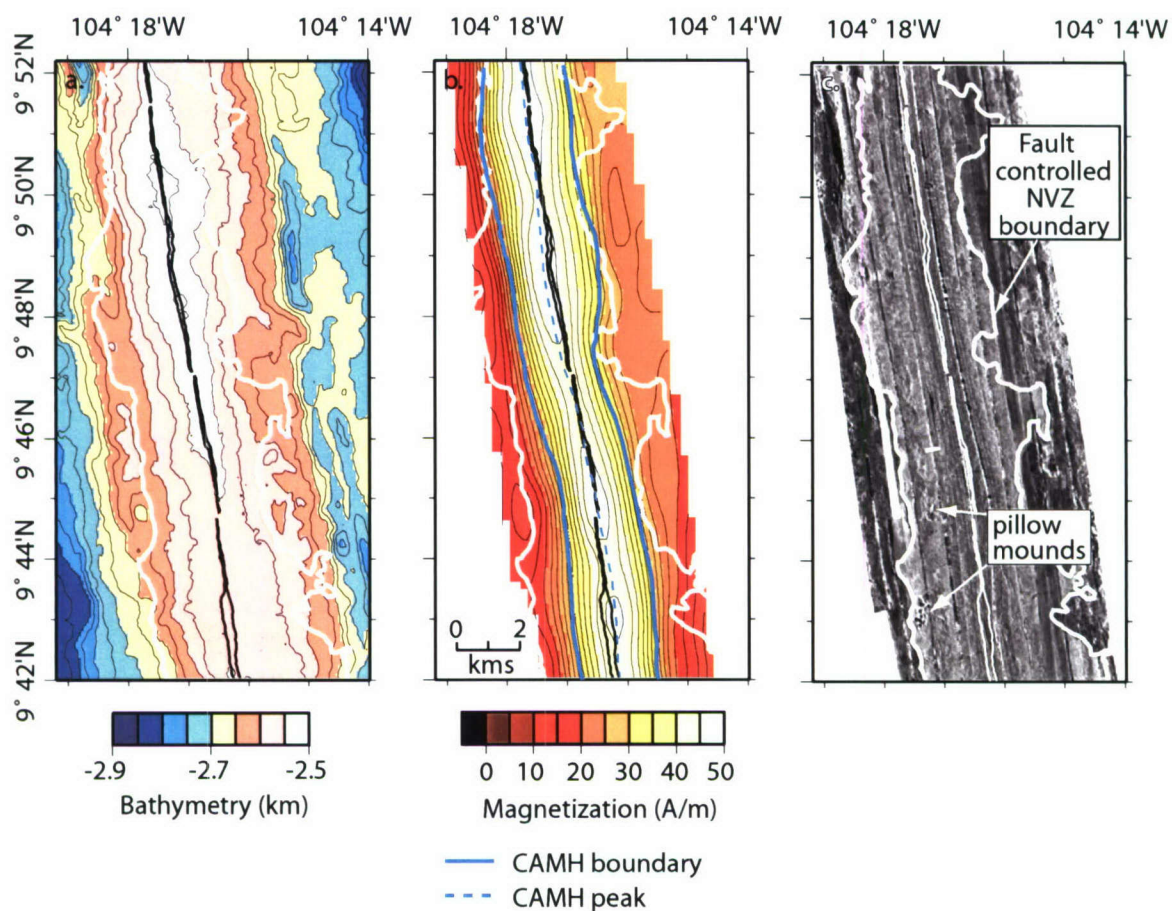
Figure 2-6. The 9° 50-43'N region. **a**. Multibeam bathymetry with NVZ boundaries (white lines). **b**. Near-bottom CAMH magnetization grid with the CAMH boundaries (solid blue lines), CAMH peak (dashed blue line) and NVZ boundaries. **c**. Side scan sonar backscatter data with NVZ boundaries.
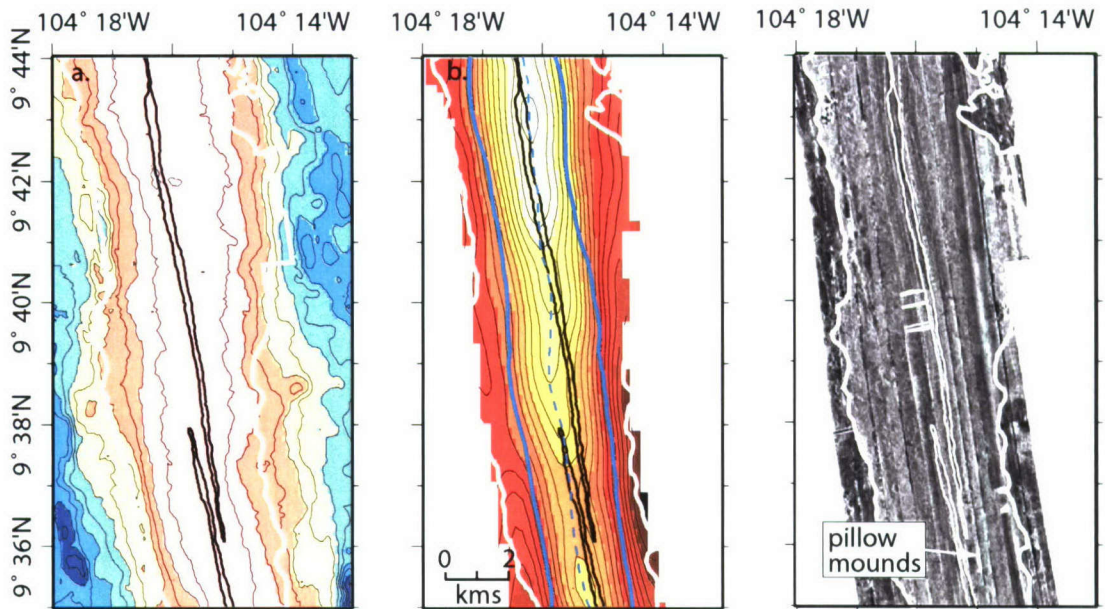
Figure 2-7. The 9° 42-36'N region. Panels and scale bar are the same as those in Figure 2-6.
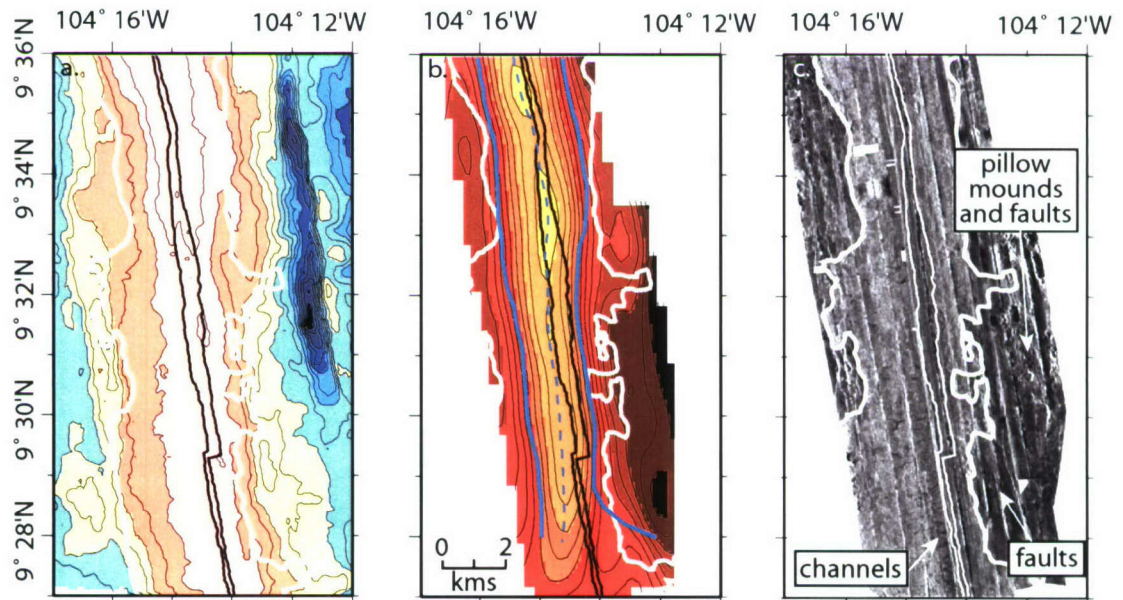
Figure 2-8. Region south of 9° 33'N. Panels and scale bar are the same as those in Figure 2-6.
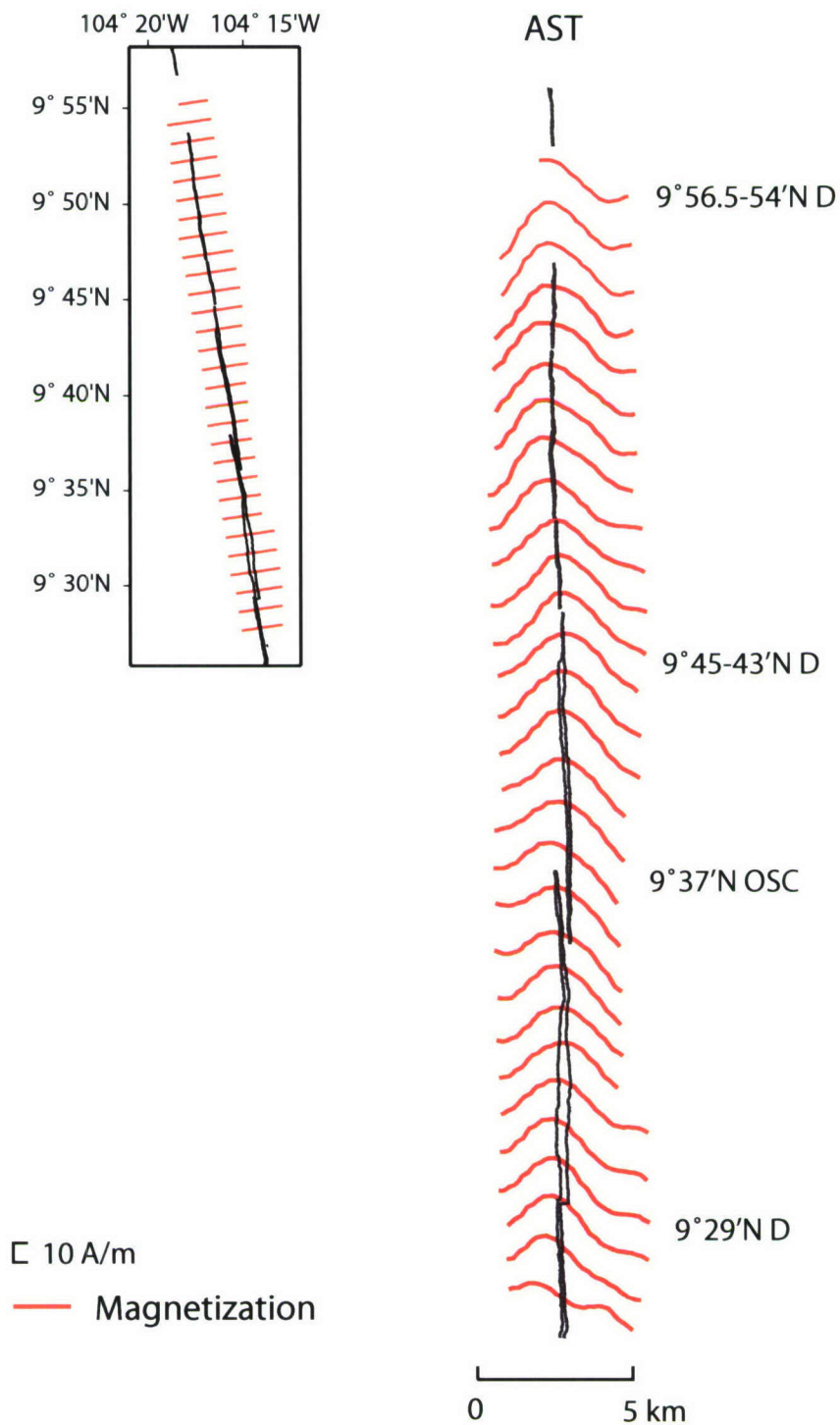
Figure 2-9. Cross axis profiles of the CAMH (approximately every ~1 minute) along the ridge axis. The profiles and AST have been rotated to vertical.
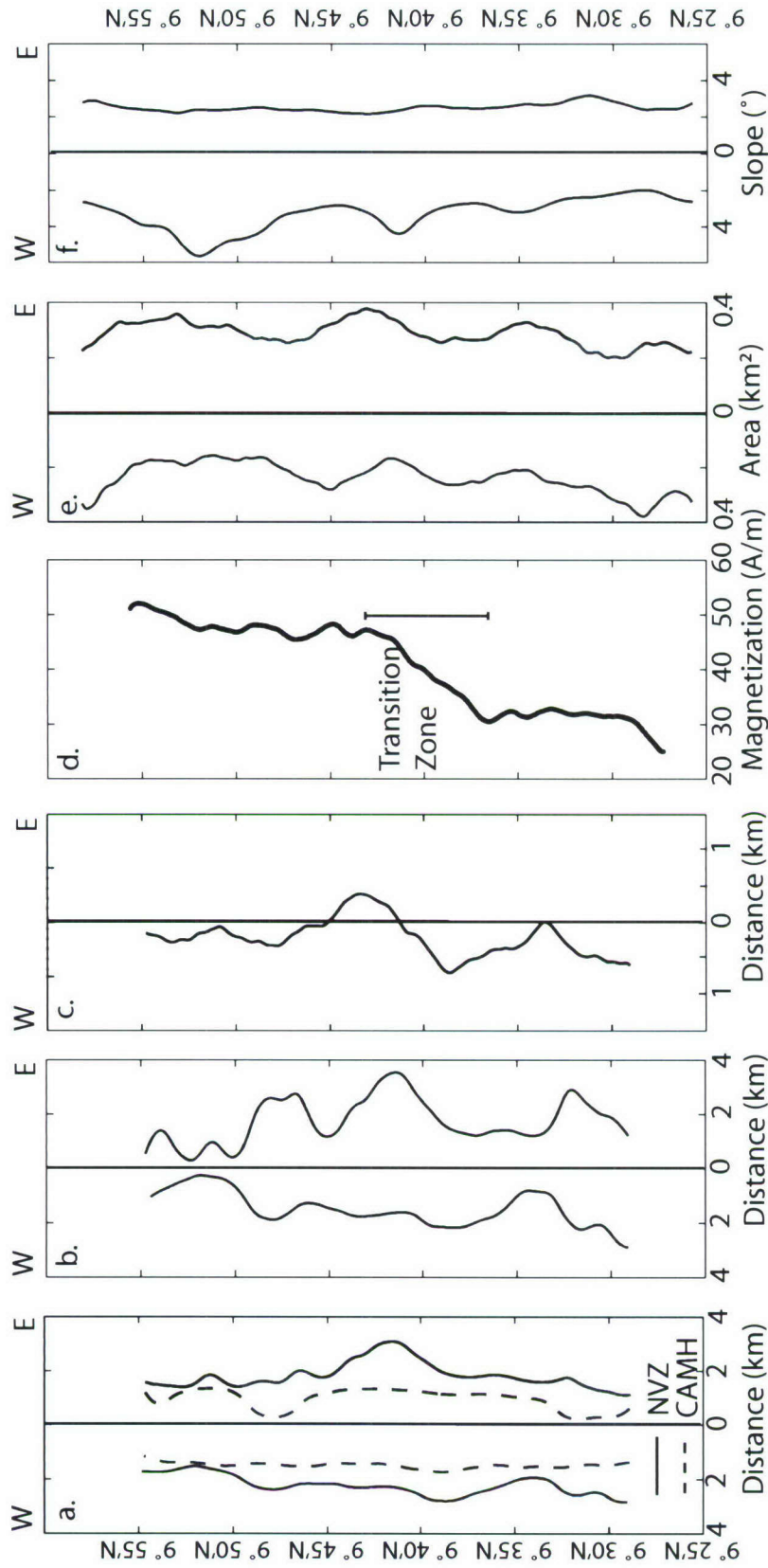
Figure 2-10. Along-axis variations in ridge properties; all data have been filtered using a 1 km low pass filter. **a.** NVZ (solid lines) and CAMH (dashed lines) boundary widths. The light blue boxes coincide with regions of low ridge volume on the eastern flank (Fig. 10e) **b.** Flow distance 2d (twice the distance between the NVZ and CAMH boundaries) **c.** Along-axis CAMH peak location relative to the AST. The resolution threshold of the dataset, 0.75 km, is shown by the grey dashed lines. **d.** Amplitude of along-axis CAMH peak. **e.** The cross-sectional area on both ridge flanks calculated from the top 120 m of the ridge and used as a proxy for ridge volume. The light blue boxes indicate regions of low ridge volume on the eastern flank. **f.** Cross axis slope calculated from the average gradient of the top 120 m of the ridge.
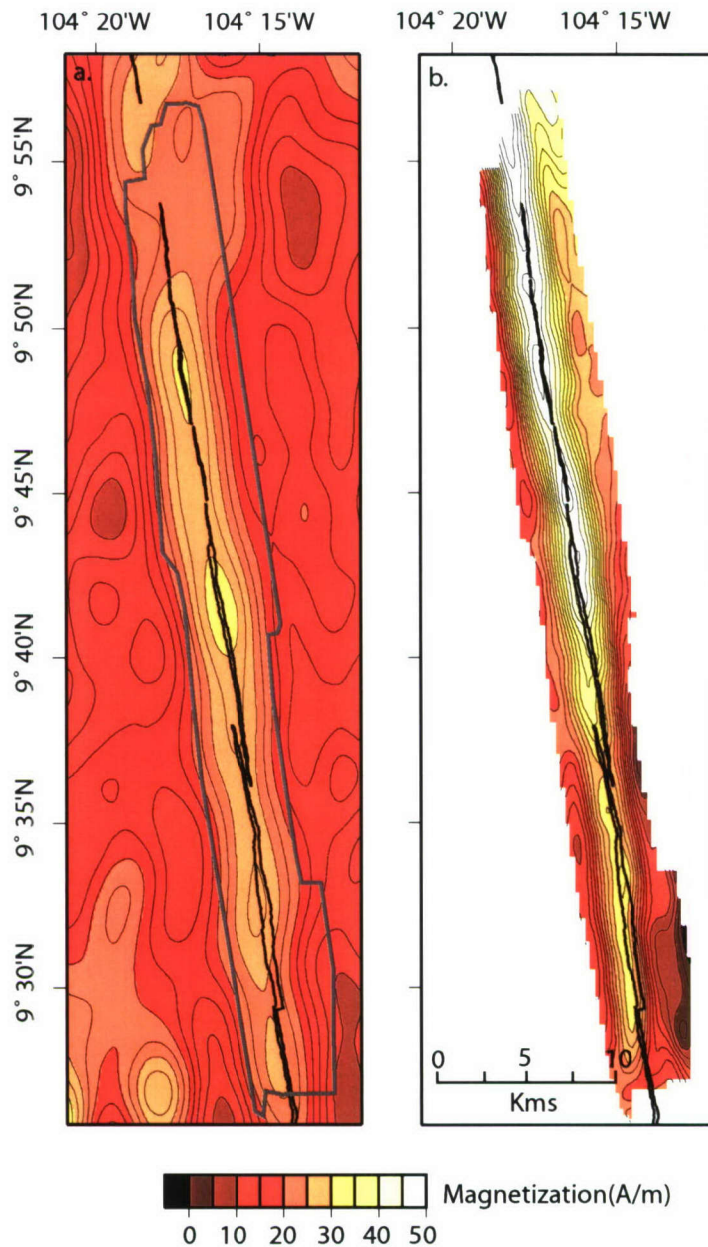
Figure 2-A1. A comparison of a sea surface inversion grid with the near-bottom inversion results. **a**. Sea surface magnetic grid of Carbotte and Macdonald [1992] inverted for a constant source layer thickness of 0.25 km. The area of the DSL-120A survey is shown by the grey outline. **b.** The near-bottom inversion results (same as Fig. 2c). Contour interval is 2.5 A/m in both figures. Eighteen times the annihilator has been added to both grids.
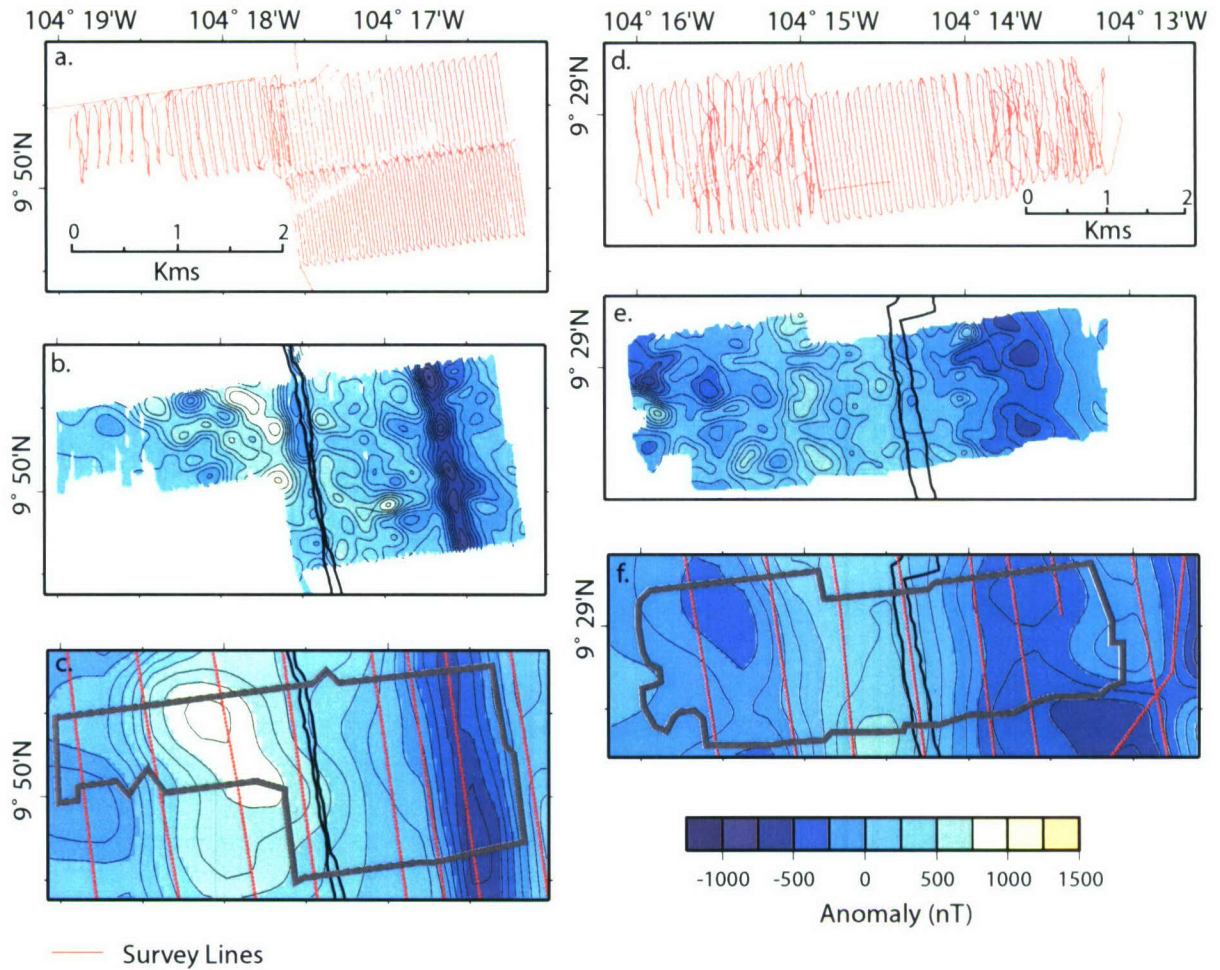
Figure 2-A2. A comparison of two high resolution ABE magnetic grids at 9° 50'N and 9° 29'N with the DSL-120A grid. **a**. Track lines of the ABE grid at 9° 50'N (line spacing < 40 m). **b**. The ABE residual anomaly grid continued upwards to 2.5 km water depth [Schouten et al., 2003]. The boundaries of the AST are shown by the bold black line. **c.** Near- bottom residual anomaly grid continued upwards to 2.5 km water depth, the area of the ABE grid is outlined by the grey solid line. The red dots are data points along the DSL-120A survey lines. **d**. Track lines of the ABE grid at 9° 29'N. **e**. The ABE residual anomaly grid continued upwards to 2.5 km water depth. **f.** Near-bottom residual anomaly grid continued upwards to 2.5km water depth. The contour interval for all the grids in this figure is 125 nT.

CHAPTER 3

Paleomagnetic and rock magnetic measurements of oceanic lithosphere exposed at Kane Megamullion

Abstract

Lower crustal (gabbros) and altered upper mantle (serpentinized peridotites) rocks exposed on the seafloor at the Kane Megamullion record the Chron 2r/2An polarity boundary (2.581 Myrs), indicating that these lithologies are able to preserve a magnetic signal in a coherent manner. Rock magnetic and paleomagnetic results show that both gabbros and serpentinized peridotites could contribute to the magnetic source layer. Serpentinized peridotites have higher mean natural remanent magnetizations (NRM) (4.7 ± 5.8 A/m) than the gabbros (1.5 ± 2.5 A/m), but gabbro NRM is more stable in general (higher median destructive field and Koenigsberger ratio). Ninety percent of the samples have univectoral magnetization direction, implying that the rocks acquired both thermal and/or chemical remanence during one geomagnetic polarity interval. Chron 2A lasted ~ 1 Myrs, therefore the gabbros and serpentinized peridotites likely acquired their remanence within ~ 14 km of the ridge axis. Paleomagnetic data show both normal and reverse polarity samples and the majority of reverse polarity samples are located in anomaly transition zones (Cain and Adam Domes). A reversal test on the samples shows that the antipode of the normal polarity direction lies within the 95 % confidence interval of the mean reverse polarity direction, suggesting we have adequate sampling. Models of the source layer thickness indicate that a 0.5 km serpentinized peridotite layer or 1.75 km gabbro layer with geocentric axial dipole magnetization direction could account for the anomaly amplitude at the chron 2r/2An boundary. Models of rotation about the ridge axis, based on estimates from the paleomagnetic data, suggest that Kane Megamullion has experienced approximately 15° of counter clockwise rotation.

3.1. Introduction

Magnetic anomaly lineations are observed throughout the ocean basins and provide key evidence for seafloor spreading processes and the plate tectonic paradigm [*Morely and Larochelle*, 1964; *Vine and Matthews*, 1963]. Magnetic anomalies are created by polarity reversals in Earth's magnetic field that are recorded by young oceanic lithosphere as a remanent magnetization. An intrinsic problem when inverting magnetic anomaly data for magnetization is the inherent non-uniqueness of the problem because the inversion calculation is not able to distinguish between several variables including magnitude of crustal magnetization, volume of magnetic source layer and direction of magnetization. Consequently, it is essential that magnetic anomaly data are complemented with rock magnetic and paleomagnetic measurements from rock samples in order to interpret the data fully and produce a realistic model of the seafloor magnetic structure. In this paper we present rock magnetic and paleomagnetic data from upper and lower crustal and upper mantle rocks exposed on Kane Megamullion on the Mid-Atlantic Ridge (MAR) (Fig. 3-1). Our dataset represents a detailed magnetic study of seafloor samples from the megamullion, which are used to constrain inversions of magnetic anomaly data in the region [*Williams et al.*, in prep].

The relative contributions of the lithological units in oceanic lithosphere that form the magnetic source layer remain controversial. Easy access to the upper extrusive basalts has resulted in a knowledge bias of crustal magnetization. At this time there is general understanding and agreement regarding the importance of the extrusives and their magnetic properties [*Ade-Hall et al.*, 1971; *Bina and Henry*, 1990; *Gee and Kent*, 1997; *Harrison*, 1987; *Johnson and Hall*, 1978; *Kent and Gee*, 1994]. In contrast, our understanding of how the lower lithologic units, including diabase dikes, gabbros and serpentinized peridotites, relate to the anomaly signal is more uncertain. The manner in which they acquire remanent magnetization and their contribution to the magnetic source layer are also poorly defined in comparison [*Dunlop and Prevot*, 1982a; *Gee and Meurer*,

2002; *Johnson and Salem*, 1994; *Kent et al.*, 1978; *Pariso and Johnson*, 1993a; *Tivey*, 1996].

Certain magnetic characteristics must be considered for a rock to contribute to the magnetic source layer. The rock must be able to record the polarity of the geomagnetic field with reasonable fidelity and preserve this record over geologically significant time periods [*Pariso and Johnson*, 1993a]. The geological processes that control the formation of magnetic minerals in the rock should also be well established. Basalt magnetism is dominated by thermoremanent magnetization (TRM) and titanomagnetites are typically the main magnetic mineral carrying this remanence [see *Harrison* (1980) for review]. In comparison, magnetite tends to be the most significant magnetic carrier in gabbros and serpentinized peridotites [*Bina and Henry*, 1990; *Kent et al.*, 1978; *Nazarova*, 1994; *Oufi et al.*, 2002; *Pariso and Johnson*, 1993b; *Worm*, 2001]. Another important magnetic characteristic to be considered is the acquisition of remanent magnetization. Gabbros frequently have both original TRM and secondary chemical remanent magnetization (CRM) components [*Bina and Henry*, 1990; *Garces and Gee*, 2007; *Pariso and Johnson*, 1993b; *Worm*, 2001]. CRM is dominant in serpentinized peridotites, where serpentinization produces secondary magnetite. If the remanent magnetization of gabbro and serpentinized peridotite is acquired some time later than the basalt TRM signal, then the superposition of these two signals may not be constructive, resulting in reduced amplitude and skewed magnetic anomalies.

Access to lower crustal and upper mantle rocks in marine environments is limited. Modern drilling technology has not allowed for direct drilling through oceanic crust to reach these deeper lithologies until very recently [*Teagle et al.*, 2007]. Sampling has therefore been focused on locations where lower crustal and upper mantle rocks are exposed on the seafloor. These occur in two main tectonic environments; along major fault scarps and at ocean core complexes, both of which are often associated with transform faults and ridge-transform intersections. An ocean core complex, similar to

those described in continental metamorphic core complexes [*Davis and Lister*, 1988; *Wernicke*, 1992], is assumed to be the rotated footwall of a detachment fault that roots in the axial valley of mid-ocean ridges (MORs) [*Blackman et al.*, 1998; *Cann*, 1997; *Cannat et al.*, 1995a; *Escartin et al.*, 2003; *Searle et al.*, 2003; *Tucholke et al.*, 1998; *Tucholke et al.*, 1996]. Long-term slip on the detachment fault exhumes lower crust and upper mantle rocks, thereby removing the upper extrusive sequence from the normal stratigraphic sequence (Fig. 3-2). The Deep Sea Drilling Program (DSDP), Ocean Drilling Program (ODP) and Integrated Ocean Drilling Program (IODP) have cored several ocean core complexes including: 735B at Atlantis Bank (South West Indian Ridge, SWIR) [*Dick et al.*, 1991] sites 1268-1275 between 14°-16° N [*Kelemen et al.*, 2004] and U1309D on the Atlantis Massif [http://iodp.tamu.edu/publications/PR/305PR/305PR.html] (Northern Mid-Atlantic Ridge) and sites 920-924, in the MARK region (Mid-Atlantic Ridge at Kane, Fig. 3-3) [*Cannat et al.*, 1995a]. Major fault scarps frequently bound transform faults,and the scarps are thought to expose the continuation of the detachment fault surface into the transform. Major fault scarps studied include Blanco Transform Fault (Juan de Fuca Ridge) [*Karson et al.*, 2002], Vema Transform Fault and Western Kane Transform Fault [*Auzende et al.*, 1994; *Tivey et al.*, 1998] and Hess Deep [*Francheteau et al.*, 1990a; *Francheteau et al.*, 1990b; *Karson*, 1998; *Karson et al.*, 2002b]. Ophiolites, sections of stratified ocean-type crust thought to form at back arc spreading centers, also provide access to the lower crust and upper mantle. These rocks were obducted onto continental lithosphere and are now sub-aerial. Much of our understanding of oceanic crust is based on ophiolite studies including those exposed in Oman (e.g., *Luyendyk and Day*, [1982]; *Nicolas et al.* [1988]; *Boudier et al.* [1996], *Nicolas et al.* [1996]; *Kelemen et al.*[1997]; *Le Mee et al.* [2004]), Bay of Islands ophiolite (Canada) [*Swift and Johnson*, 1984] and Troodos ophiolite (Cyprus) [*Cann*, 1974; *Gass*, 1968; *Gass and Smewing*, 1973; *Robinson et al.*, 2003]

Previous magnetic studies of gabbros and peridotites show a large range in magnetic properties, which has lead to the low level of consensus concerning their

contribution to the magnetic source layer. Average natural remanent magnetization (NRM) in gabbros range from 0.01 A/m in the Bay of Islands ophiolites [*Swift and Johnson*, 1984], to 4.7 A/m for Fe-Ti oxide gabbros in Hole 735B [*Pariso and Johnson*, 1993a]. Unaltered peridotites are close to paramagnetic and only acquire CRM during alteration processes such as serpentinization, which produce secondary magnetite [*Dunlop and Prevot*, 1982b]. Global serpentinized peridotite NRMs range from 0.02 A/m up to 12 A/m, which are comparable with basalts [*Cannat et al.*, 1995b; *Fox and Opdyke*, 1973b; *Nazarova*, 1994; *Oufi et al.*, 2002]. Understanding how the rocks acquired this magnetic signal is critical for modeling their contribution to the magnetic source layer.

3.1.1 Geological setting

Kane Megamullion is an ocean core complex located ~ 40 km west of the Mid-Atlantic Ridge (MAR) axis at 23° 30'N (Fig. 3-1). The dome-shaped massif is ~ 20 km wide, ~ 35 km long and has a corrugated surface with elongated lineations (mullions) oriented parallel to the spreading direction. The detachment fault initiates at the break-away and dips below the seafloor at the termination, which is the present day contact between the hanging wall and footwall (Fig. 3-2). A linear magnetic anomaly polarity boundary cuts across the eastern side of Kane Megamullion (Fig. 3-3). This polarity boundary is the Chron 2r to Chron 2An transition (age ~ 2.581 Myrs [*Ogg and Smith*, 2004]) [*Williams et al.*, in prep.] and its presence indicates that the lithologies at this location are capable of recording a polarity reversal in a coherent manner. A polarity boundary (C5n.2n/C5An.1n) in lower crustal rocks is also exposed on the seafloor at Atlantis Bank (SWIR) [*Dick et al.*, 1991]. This boundary is estimated to be dipping at ~ 5° away from the ridge axis, after correction for crustal backtilt [*Allerton and Tivey*, 2001]

An extensive bathymetric, magnetic and sea-floor sampling survey of the Kane Megamullion was carried out in 2004, onboard the R/V Knorr (KN180-2). Seafloor samples were collected both in situ by the remotely operated vehicle (ROV) Jason II and

dredged from the seafloor. Over 1600 rocks were collected in total, including basalts, diabases, gabbros and altered peridotites (peridotites make up the largest lithology group, ~ 40 %). There are several topographic highs to Kane Megamullion (Fig. 3-4). Gabbros are found predominantly on Babel Dome to the north and Adam Dome to the south, while peridotites are exposed at Cain and Abel Domes (Fig. 3-4). Two faults, with approximately north-south trends, intersect the surface of the megamullion (East and West Fault) and a linear basalt ridge is located at the northern end of East Fault (Fig. 3-4). Basalts were collected both across the detachment fault surface and from the linear basalt ridge (Fig. 3-4). Diabases were sampled on the detachment fault surface, particularly on Cain Dome and Adam Dome to the southwest (Fig. 3-4).

We present a detailed examination of rock magnetic and paleomagnetic properties from both in situ and dredged samples. The rock samples selected encompass the full range of observed variations in lithology, alteration and geographic location at Kane Megamullion (Fig. 3-4). Our seafloor sample dataset provides reasonable parameters to constrain and model the contribution made by lower crust and upper mantle to the magnetic source layer.

3.2. Methods

Forty eight rock samples were chosen as representative of the rocks collected at Kane Megamullion (Table 3-1). Two 1 inch diameter cores were taken from the larger samples (~ 45 samples) and only one core from smaller samples. All samples were subjected to a suite of magnetic measurements that quantified both their magnetic properties (rock magnetic data) and direction of magnetization (paleomagnetic data). Samples with NRMs of less than 2 A/m were measured using the 2G cryogenic magnetometer at University of Massachusetts, Amherst Paleomagnetic Lab, courtesy of Dr. Laurie Brown. Samples with an NRM > 2 A/m were above the threshold of the 2G magnetometer and were measured instead on a Molspin spinner magnetometer also located at Amherst. The samples were subjected to alternating frequency demagnetization

using a Molspin demagnetizer between 2.5 to 100 mT. The intervals of demagnetization were tailored for each sample (ranging from 2.5 to 20 mT) because of the large range in NRM values for the 48 samples (0.001-26 A/m). The median destructive field (MDF), the field required to reduce the magnetization by half the original value, was calculated from the demagnetization curves. A high MDF value indicates that the magnetization of the sample is stable. Magnetic susceptibility (k) of the samples was measured on a Sapphire Instruments susceptibility bridge at room temperature. The Koenigsberger ratio (Q), the ratio of remanent (NRM) to induced (k) magnetization, was calculated assuming a local geomagnetic field of 30.62 A/m for the Kane Megamullion survey area [*Gee et al.,* 1997]. A high Koenigsberger ratio (Q>1) also indicates that the magnetization of the sample is stable. The final measurement made on all 48 samples was magnetic hysteresis using the Model 2900 Micromag Alternating Gradient Magnetometer at the University of Rochester Paleomagnetic Lab facilities, courtesy of Prof. John Tarduno and Dr. Rory Cottrell. Hysteresis parameters: coercivity, coercivity of remanence, saturation magnetization and magnetization of remanence were measured using an applied maximum field of 500 T (5 KOe) and an averaging time of 200 ms.

A subset of 28 samples was chosen from the original 48 for more detailed analyses: first order reversal curve (FORC) diagrams, thermomagnetic susceptibility curves, anisotropic magnetic susceptibility (AMS), x-ray diffraction and petrographic analyses. The 28 samples encompass the spectrum of NRM and median destructive field (MDF) values observed within each lithology (6 basalts, 3 diabases, 10 gabbros and 9 harzburgites). Thermomagnetic curves were determined using the Kappabridge susceptibility meter (KLY- 4S) at the University of Rochester. Temperature was monitored with a thermocouple in contact with the sample, and the sample chamber was filled with argon to purge the system of oxygen. Both low temperature (-192 ° to 1 °C) and high temperature (40 ° to 700 °C, heating and cooling) susceptibility measurements were made in a background field of 300 A/m, with 3 °C intervals in heating and cooling. AMS measurements were also made on the Kappabridge instrument (15 position setting).

FORC measurements were made using the same Alternating Gradient Magnetometer as the hysteresis measurements. The FORC measurements had a maximum field of 500 T, an averaging time of 500 ms and smoothing factor of 5. The FORC data were processed using the Matlab scripts written by Michael Winklhofer, based on the algorithms of Chris Pike. X-ray diffraction measurements of powdered samples were made on a Philips X-ray diffractometer with CuKα radiation and silica calibration at Woods Hole Oceanographic Institution.

3.3. Magnetic property results

3.3.1 Susceptibility, natural remanent magnetization, median destructive field, Koenigsberger ratio.

Basalts have the highest mean NRM (8.7 A/m), followed by altered peridotites (4.7 A/m) and gabbros (1.5 A/m), while diabases have the lowest values (0.076 A/m) (Fig. 3-5, Table 3-1 and 3-2). The basalts also have the highest Q (102) and MDF (33 mT) values, indicating that their remanent magnetization is the most stable of the four lithologies. However, altered peridotite MDF and Q values are lower than the gabbros, implying that their remanence is less stable (Fig. 3-5). *Swift and Johnson* [1984] proposed that a rock must fulfill the following criteria in order to be considered part of the magnetic source layer: an NRM > 2 A/m, Q > 2 and MDF > 5 mT. The basalts and peridotites fulfill the NRM criteria, but gabbros fall just below this requirement. All four lithologies have mean Q and MDF values greater than 2 and 5 mT respectively. Based on these criteria basalts, altered peridotites and possibly gabbros could all contribute to the magnetic source layer but the diabases likely do not.

A comparison of NRM versus susceptibility shows that basalts follow a separate trend from the serpentinized peridotites and gabbros (Fig. 3-6). Basalts have high NRM and low k compared with the gabbros and serpentinized peridotites, which have relatively low NRM and high k values. The two trends may reflect varying amounts of magnetite in the samples; higher k values are generally interpreted to reflect greater magnetite content

72

or finer grain size in the gabbros and serpentinized peridotites [*Dunlop and Ozdemir*, 1997]. Low NRM values in the gabbros and serpentinized peridotites may be due to extensive low-temperature oxidation of magnetite in the samples [*Smith*, 1987] or differences in effective magnetic grain size, where single domain magnetic grains result in higher NRMs than multidomain grains [*Oufi et al.*, 2002]. The gabbros in Fig. 3-6 can be subdivided into two groups; one with higher NRM and k values, made up of two troctolites and one gabbro mylonite, and a second group with lower NRM and k values that includes mostly olivine gabbros, oxide gabbros and metagabbros (Fig. 3-6).

3.3.2 Thermomagnetic susceptibility curves

Magnetic mineralogy is determined from thermomagnetic susceptibility curves. Curie temperatures (T_c) of magnetic carriers are determined from changes in gradient of susceptibility curves using the differential method, which defines the points of maximum curvature [*Tauxe*, 2002]. Examples of different types of low temperature and high temperature heating and cooling curves observed in each lithology group are shown in Fig.3-7.

Kane Megamullion basalts have several features in common. None of the basalts have a Verwey transition ($T_c \sim -150$ °C) in their low temperature curves (green line Fig. 3-7a, 7b). A Verwey transition indicates the presence of magnetite and occurs when magnetite converts from an electrical insulator to a semi-conductor, due to increased electron mobility [*Dunlop and Ozdemir*, 1997]. However, all the basalts have a small peak or inflection close to 580°C, which is the T_c for magnetite. These two observations appear to conflict but can be explained by either an inversion of titanomaghemite to a multiphase mixture of magnetite and ilmenite during heating [*Dunlop and Ozdemir*, 1997] or the presence of impurities in the magnetite [*Muxworthy and McClelland*, 2000]. Titanomagnetite and titanomaghemite (oxidized titanomagnetite) with ulvopsinel content (χ) ~ 0.6 (TM60) are typical magnetic carriers in oceanic basalts (*Johnson* [1979] and references therein). The inversion of titanomaghemite to magnetite and ilmenite increases

k, resulting in irreversible susceptibility curves (Kane Megamullion samples show ~ 70-300 % increase in susceptibility from their initial values). Alternatively, impurities of ≥ 4% in magnetite cause the Verwey transition to disappear [*Muxworthy and McClelland*, 2000]. Whatever the cause, all the basalts have these features in common but can be divided into two groups based on their average k values and main peak in their heating curves (red lines, Fig. 3-7a, 7b).

Group 1 basalts have lower k (~ 0.050 (x10^3) SI) and the main peak in their high temperature heating curve has a T_c ~ 370° C (samples 11-4, 18-15 and J111-17). Group 2 basalts have much higher k (up to 0.480 (x10^3) SI) and a main peak with T_c ~ 182 °C (samples 9-30, 22-2a and J116-40). The T_c of unaltered titanomagnetite is ~ 180 °C. Impurities lower the T_c, while oxidation raises the T_c. As the main heating peaks in all the Kane Megamullion basalts are > 180° C, we infer that titanomagnetite has oxidized (maghemitized) to titanomaghemite and this is the main magnetic carrier in the basalts. We propose that the difference between the main heating curves in the two basalt groups is due to varying levels of maghemitization. The degree of oxidation is given by the parameter z, which is defined as the ratio of oxidized Fe^{2+} to original Fe^{2+} and ranges from 0 (unoxidized) to 1 (fully oxidized). The 182 °C peak in the Group 2 basalts (Fig. 3-7b) may be relatively fresh titanomaghemite with z ~ 0.02. In contrast, the 370 °C peak in the Group 1 basalts (Fig. 3-7a) is interpreted to be titanomaghemite with z ~ 0.5 [*Dunlop and Ozdemir*, 1997]. The diabase samples all have very low susceptibilities and, like the basalts, show no Verwey transition (Fig. 3-7c). The steepest gradient in the susceptibility curves is located at T_c for magnetite.

Gabbro susceptibility curves range from very high k (~ 1.5 (x10^3) SI) to low k (~ 0.02 (x10^3) SI) samples (Fig. 3-7d and e respectively). In the high k gabbros, magnetite is the main magnetic carrier, indicated by the Verwey transition (T_c -158 °C) and a steep gradient at 578 °C, the T_c of magnetite. Low k gabbros look very similar to diabase (Fig. 3-7c) and are interpreted to have very little primary magnetite. Approximately 70 % (7

samples) of the gabbros are reversible to within 13 % of their original value, indicating little maghemitization of the samples [*Worm*, 2001].

Magnetite is also the main magnetic carrier in the serpentinized peridotite samples, which show a clear Verwey transition and a T_c of 578 °C (Fig. 3-7f and 7g). Unlike the gabbros, two-thirds of the serpentinized peridotite samples have an additional high temperature heating peak at ~ 380 °C (3-7f). Of the nine samples measured, five were within 10 % of their initial susceptibility, again indicating little maghemitization. However, the peridotites differed from the other lithologies in that four samples showed an overall decrease in k of ~ 1-34 % after heating. *Oufi et al.* [2002] also observed that most MAR peridotites were reversible. Those that showed magnetization loss on heating had an inflection point at 350 °C, interpreted to be due to replacement of a significant amount of maghemite by hematite while the sample was brought to temperature above 350°C (e.g. [*Krammer*, 1990]). Maghemite is the oxidized equivalent of magnetite and Kane Megamullion samples with a peak at ~ 380 °C may reflect this replacement process. Secondary magnetite produced by serpentinization could react with seawater or air in the sample tube during thermal cycling to produce maghemite. Maghemite is then replaced by hematite when the sample is heated to temperatures above 350 °C. However, our susceptibility curves differ from *Krammer* [1990] because they observed a ~ 50 % decrease in overall susceptibility during replacement and we observe a decrease of only ~ 1-34%.

3.3.3 Demagnetization and Paleomagnetic directions

Vector component plots (Zijderveld plots) of the four different lithologies show that the large majority of Kane Megamullion samples record a single magnetic vector, after removal of the soft drilling component by ~ 15 mT demagnetizing field (Fig. 3-8a and c). Only three gabbros (20%) and one peridotite have recorded more than one magnetic component, which is defined by a change in gradient in the vector component plots (Fig. 3-8b). As several samples were taken from each rock core, we are able to

confirm that the multicomponent magnetization is present throughout the rock in these four cases. However, three rocks have one sample with multicomponent magnetization, yet additional samples from the same core or second core taken from the same rock are univectoral. This suggests fine-scale heterogeneities in magnetization, behavior that is also observed in the ODP 920-924 gabbros [*Gee et al.*, 1997]. Both straight and curved trajectory plots were observed in these multicomponent cases. The curved trajectories indicate overlapping demagnetization spectra or coercivity spectra of the various magnetization components and require more advanced techniques than those used here to identify the components individually.

All samples with multi-component magnetization are either dredge samples (no orientation information) or unoriented Jason samples. The difference in magnetic vector direction is quantified by averaging the directions for 2-3 samples from each rock [*Fisher*, 1953]. The average direction difference is ~ 60° and ~ 12° in the two planes for the three gabbro samples (Sample 11-1: 053°/8°, 27-70: 050°/13° and 27-86: 074°/14°). However, we do not know which direction is the horizontal plane (declination) and which is the vertical plane (inclination), because the samples are not oriented. The one multicomponent peridotite sample (J113-12) shows a change of 010°/015°.

Nineteen samples collected in situ during Jason dives 113-117 (Fig. 3-9b) are visually-oriented for paleomagnetic measurements. Visually oriented means the original sample orientation was deciphered from video footage of the sample collection, combined with the gyro heading of the ROV at that time. The orientation of the samples is subjective and orientation error is difficult to estimate, but is assumed to be ± 30° in both strike and dip directions. Oriented drill cores collected during submersible dives at Hess Deep Rift [*Varga et al.*, 2004] and MARK area [*Lawrence and Karson*, 1998] using a Geocompass have smaller error estimates of ± 10 ° and ± 15 ° respectively.

Present day declination and inclination at Kane Megamullion is 0°/40°, based on the geocentric axial dipole (GAD). Our results show both normal (positive, down) and reversed (negative, up) paleodirections in samples from the three dive areas (Fig. 3-9 and Table 3-3). There are 8 normal samples and 8 reversed samples in total, with 3 ambiguous samples that lie within 10° of horizontal (Fig. 3-9a). A higher number of reversed samples are observed on Dives 116 (3 samples) and 117 (4 samples), which might be expected as both dives lie within anomaly transition zones (Fig. 3-3a). Reversed and normal samples are located within close proximity (11-500 m) along all three dives (Fig. 3-9b). Paleodirection does not appear to be a function of lithology; gabbros, peridotites and diabase all show reversed and normal paleodirections.

We apply a reversal test to the visually oriented samples, where the average direction of primary NRM for the normal-polarity sites is expected to be antiparallel to the average direction of the primary NRM for the reversed polarity sites [Butler, 1992]. The average direction of Kane Megamullion normal-polarity samples, including the normal ambiguous samples (i.e., n=10), is 044°/53° with a 95 % confidence interval of 32° and the antipode to these samples is located at 244°/-53° (Fig. 3-9a). The average direction of the reverse-polarity samples is 249°/-78° for all the samples (n=9) or 193°/-70° for the reverse samples excluding J114-2 and J117-37 (Table 3-3). The antipode of the normal polarity samples therefore lies within the 95 % confidence limit boundary (45°) of the reverse-polarity boundary (Fig. 3-9a). Our results suggest that the number of Kane Megamullion paleomagnetic samples provides adequate averaging of secular variation during both normal and reversed polarity intervals. Any difference between the GAD direction and the sample mean polarity directions may also reflect a general rotation of Kane Megamullion. The difference in declination ranges from 44° for normal polarity to 13° for reversed polarity, assuming 193° declination for the reversed samples. The effect of rotations on the appearance of the magnetic anomalies is discussed in more detail in section 3.4.4.

3.3.4 Hysteresis loop parameters

Magnetic hysteresis loop parameters provide an assessment of domain state and indirectly the effective magnetic grain size within a sample [*Day et al.*, 1977a]. The effective magnetic grain size can be substantially different from the optical grain size. Saturation magnetization (Ms) is the largest magnetization a sample can have and is thus a measure of the total amount of magnetic mineral. Remanent magnetization (Mr) is the remaining magnetization after the inducing field is reduced to zero. Coercivity (Hc) is a measure of magnetic stability and coercivity of remanence (Hcr) is the magnitude of the reverse field after saturation that results in zero net remanence. The two ratios Mr/Ms and Hcr/Hc are commonly used as indicators of domain state. Magnetic theory predicts Mr/Ms > 0.5 and Hcr/Hc ~ 1 for single domain (SD) grains and Mr/Ms < 0.05 and Hcr/Hc ~ 4 for truly multidomain (MD) grains, with pseudo-single domain (PSD) grains lying between SD and MD [*Day et al.*, 1977; *Dunlop*, 1981; *Rahman et al.*, 1973; *Stoner and Wohlfarth*, 1948]. The effective magnetic grain size of PSD ranges between ~ 0.2-15 µm.

Our results show that the two basalts groups identified from the susceptibility curves plot in two distinct areas in the Day plot; Group 1 in the SD region and Group 2 in the PSD region (Fig. 3-10). Additional basalt samples for which no susceptibility curves were measured all lie in the SD region. The diabases plot in the small-mid sized PSD region (one appears to be similar to the Group 2 basalts).

Gabbro samples span the Day plot from small PSD to MD grain sizes (Fig. 3-10). Kane Megamullion troctolites have small PSD grain sizes in general but larger PSD and MD samples are not limited to one type of gabbro (they include olivine gabbros, gabbros and metagabbros). All serpentinized peridotites lie in the small to mid-sized PSD region, apart from one sample close to the MD region (Fig. 3-10). Our data are compiled with hysteresis data from ODP drill cores in the MARK area and the results discussed in section 4 (Fig. 3-11).

3.3.5 First order reversal curve diagrams

Hysteresis parameters provide a measure of the bulk magnetic properties in a sample, but are limited because they cannot discriminate between different magnetic components in a mixed magnetic mineral assemblage (e.g. they cannot identify true PSD magnetites from mixtures of SD and MD magnetites). First-order reversal curves (FORC) are similar to hysteresis curves but provide more detailed analyses and can be used to discriminate different grain sizes within a sample, based on the distribution of coercivity and interaction energies.

FORC diagrams are constructed by measuring a large number of partial hysteresis curves [*Pike et al.*, 1999; *Roberts et al.*, 2000]. Starting at positive saturation, the applied field is decreased until a specified reversal field (H_a) is reached. A FORC is the magnetization curve measured at regular field steps from H_a back to positive saturation. This measurement procedure is repeated for different values of H_a to obtain a suite of FORC's that fill the interior of a major hysteresis loop (76 FORCs were measured for each of our samples). The magnetization H_b on a FORC with a reversal field H_a is denoted by $M(H_a,H_b)$. Data from consecutive measurement points ($M(H_a,H_b)$) on consecutive reversal curves are used to determine the FORC distribution by fitting a mixed second-order polynomial to a local, moving grid. The size of the local area is determined by a user-defined smoothing factor (SF), where the size of the grid is $(2SF+1)^2$. The data are then transformed into a contour plot or FORC diagram with new coordinates $H_u=(H_a+H_b)/2$, $H_c=(H_b-H_a)/2$. A more complete explanation of the measurement and construction of FORC diagrams is given in *Muxworthy and Roberts* [2006].

As a first approximation, FORC diagrams can be interpreted as the coercivity distribution along the horizontal axis (H_c) and the interaction field distribution along the vertical axis (H_u) [*Muxworthy and Williams*, 2005]. Single domain behavior is identified by contours that close around a single peak and have minimal interaction with the H_u axis

(Fig. 3-12a) [*Pike et al.*, 1999; *Roberts et al.*, 2000]. Unlike SD samples, MD FORC diagrams do not have a single enclosed peak, instead their contours intersect the H_u axis and diverge away from the origin of the FORC diagram (Fig. 3-12d) [*Carvallo et al.*, 2006]. Superparamagnetic (SP) behavior appears to be similar to MD, but the diverging contours due to SP particles are much steeper and lie closer to the origin, at H_c values that are always much less than 10 mT. (Fig. 3-12c). The FORC distributions for MD particles have diverging contours that usually extend beyond 30 mT (higher coercivities) (Fig. 3-12d). Furthermore, contours for SP particles are more pronounced in the lower left-hand portion of the FORC diagram, while MD samples are nearly symmetric. Finally, PSD grains display behavior intermediate between true MD and SD behavior; their inner contours have the closed peak structures observed for SD grains and more open outer contours that become increasingly parallel to the H_u axis with coarser grain size (Fig. 3-12b) [*Roberts et al.*, 2000].

A complete understanding and interpretation of FORC diagrams is evolving at this time and the 28 FORC diagrams in this study contribute a detailed FORC study of oceanic lithosphere. We quantify the full width at half maximum (FWHM) parameter from a profile of magnetic interaction distribution taken through the FORC peak (or peaks), parallel to the H_u axis [*Carvallo and Muxworthy*, 2006; *Muxworthy and Williams*, 2005] (Fig. 3-12a) . This parameter indicates the strength of magnetostatic interactions. We also define the coercivity from the location of the sample peak (or peaks) on the H_c axis. A plot of FWHM versus the peak H_c location is separated into different domains, similar to a Day plot (Fig. 3-13). Multidomain samples, with high interaction energies and low coercivities, reside on the right hand side of the plot (FWHM > 50 mT), while SD and PSD lie at FWHM values < 50 mT (Fig. 3-13a). Coercivities are highest in SD samples and decrease in PSD samples, as the FORC peak moves closer to the H_u axis (Fig. 3-12b). We define the boundary between SD and PSD regions at peak H_c location ~14 mT based on observations of the FORC diagrams (Fig 13). Samples with the lowest coercivities in the PSD region frequently have a secondary peak, interpreted to be a SP

contribution (Fig. 3-12c). It is interesting to note that the boundary between the SD and PSD regions is defined by the coercivity distribution rather than interaction energy, suggesting they have similar effective magnetic grain sizes.

The two basalt groups have distinctly different FORC diagrams. Group 1 basalts have higher peak amplitudes and SD peaks; their contours are separate from the H_u axis (Fig. 3-12a). In contrast, the Group 2 basalts have two peaks; a PSD peak with low coercivity and a second, broader peak near the H_u axis (similar to Fig. 3-12b). The second peak is interpreted to be a SP component, a signal that is not reflected in hysteresis parameters. Interaction energies are similar for the SD and PSD peaks in both basalt groups (6-12 mT), but the SP peaks in the Group 2 basalts have much higher interaction energies (Fig. 3-13b). SP behavior results from thermal relaxation of fine SD grains, which shifts the SD FORC distribution to lower coercivities [*Pike et al.*, 2000]. Superparamagnetism occurs in the temperature interval between the blocking temperature (when the relaxation time is 10^2-10^3 seconds) and Curie temperature. An SP peak will appear in a FORC diagram when the measurement time is comparable to the relaxation time of the majority of particles (500 ms for our measurements) [*Roberts et al.*, 2006].

The signal to noise ratio in the diabase samples is low and the smoothing factor should have been increased for optimal measurements. All diabase samples plot in the PSD region, as in the Day plot. They have larger interaction energies but similar coercivities to Group 2 basalts, suggesting larger and more unstable magnetic grains.

The gabbros plot in all the FORC parameter domains, similar to their appearance in the Day plot. However, the locations of several gabbro samples in the FORC parameter plot are very different from the hysteresis results. The two oxide gabbros 27-70 and 27-86 plot as SD samples in the FORC parameter plot, compared with the PSD region in the Day plot. Furthermore, J117-37 and J114-2 have SD peaks in the FORC parameter plot, but are large PSD in the Day plot. One gabbro sample, 25-1, has a secondary SP peak,

similar to the Group 2 basalts. Unlike the Day plot, different gabbro types plot in separate regions of the FORC parameter plot. Troctolites and oxide gabbros have low interaction energies (FWHM between 4-8 mT), but a range of coercivities (Fig. 3-13b) and plot in the SD and PSD regions. Gabbros and olivine gabbros have lower coercivities in general and larger interaction energies that extend into the MD region.

Serpentinized peridotites exhibit low interaction energies (FWHM between 7-13 mT), indicative of small effective grain sizes, over a large range of coercivities. J113-12 is the only true MD peridotite sample. Two samples have double peaks; 14-45 has both PSD and SP peaks (Fig. 3-12c), while J114-20 is the only sample in our dataset to have an SD and SP peak (Fig. 3-12e). This suggests two possible magnetic carriers in the sample or greater thermal relaxation of the SD grains to SP behavior. The susceptibility curves for J114-20 do not have additional peaks compared with the other peridotites and it has a univectoral magnetization direction, therefore the two possible magnetic carriers must have very similar magnetic properties. Interestingly, the two double peak peridotites we observe (14-45 and J114-20) both plot near the SD-SP mixing lines on the Day plot (from which a SP component might be assumed) unlike the double peak gabbro (25-1) and Group 2 (PSD) basalts, which plot along the SD-MD mixing curve (Fig. 3-10).

In summary, our FORC distributions and FORC parameter plot show that the domain state of the Kane Megamullion samples are fairly consistent with the hysteresis results in general. However, FORC distributions have identified several samples with multiple magnetic components, a result that could not be interpreted from the Day plot alone. We have also shown that FORC parameter plots may be a useful in identifying different basalt and gabbro groups.

3.3.6 Petrographic results

Microscopic observations are used to identify Fe-Ti oxides and to infer the type of remanence they produce, e.g. primary TRM or secondary CRM.

Alteration levels in the basalts are determined based on palagonitization in the hand samples and quantity of clays observed in thin section. The alteration levels are classes as high (H), medium (M) or low (L) in Table 3-1. All the basalts have characteristic acicular/ophitic fabric of plagioclase laths interspersed with clinopyroxene and olivine grains. The laths frequently have swallow-tails, indicating quickly quenched grains. The length of the plagioclase laths tend to be shorter and their grain size more homogenous in the Group 1 (SD) basalts. Group 2 (PSD) basalts have more heterogeneous plagioclase grain sizes . For example, J116-40 has plagioclase grains up to ~ 2 mm in size.

The basalt oxides have skeletal structures that are indicative of rapid cooling due to contact with seawater. Group 2 (PSD) basalts have much larger skeletal oxides (Fig. 3-14a) compared with Group 1 (SD) basalts (Fig. 3-14b), suggesting either faster relative cooling in Group 1 (SD) or the break up of original large skeletal oxides by alteration processes. Skeletal grains indicate primary Fe-Ti oxides, because these crystal types can not be formed by metamorphic processes.

Diabase samples have a green color that is characteristic of chlorite, a low temperature greenschist-facies hydrothermal alteration mineral (300-500° C). We observe the remains of original leached oxide grains as "ghost" structures [*Hall and Muzzatti*, 1999], as well as cracked and anhedral grains, likely to be a result of volume changes during low temperature alteration [*Ade-Hall et al.*, 1976]. This destruction and leaching of the Fe-Ti oxides by hydrothermal alteration explains the significant reduction in NRM within the dikes, compared with the basalts above. We do not observe any ilmenite lamellae that indicate higher temperature alteration (> 300 °C) in either the Kane Megamullion basalts or diabases [*Ade-Hall et al.*, 1971].

Both primary oxides that contribute a TRM and secondary oxides that form during alteration processes and produce a CRM are observed in the gabbros.

Primary oxides are subhedral to anhedral, ranging in size up to 5 mm and are frequently found close to the grain boundaries of altered olivine and plagioclase (Fig. 3-14c and 13d). Zoning is observed within the oxides indicating alteration; light colored oxides, possibly sulphides, are replaced by darker isotropic oxides, likely magnetite. The large size of these primary oxides suggests large effective magnetic grain sizes (e.g. MD), which would not contribute a high NRM to the gabbros. We also observe oxides within brown amphiboles, which form when the water content in the magma is high, i.e., late in the crystallization process when interstitial liquid (mesostasis) crystallizes and therefore has implications for timing of remanence.

Alteration of primary oxides can also produce high stability remanence in the gabbros. Primary magnetites are sub-divided by ilmenite lamellae, which form during initial deuteric (high to low temperature cooling below solidus) oxidation and dramatically reduce the effective magnetic grain size by restricting the movements of domain walls [*Kent et al.*, 1978; *Pariso and Johnson*, 1993b; *Swift and Johnson*, 1984]. We do not observe any ilmenite lamellae in Kane Megamullion gabbros, however they may be below the optical resolution of the microscope.

The gabbros contain evidence of extensive retrograde metamorphism, ranging from upper amphibolite facies down to clay alteration. Alteration phases observed include amphibolite-facies (> 500 °C, e.g. amphibole), greenschist-facies (300-500 °C, e.g. chorite, actinolite), serpentine (< 350 °C) and complete replacement by soapstone in association with metaperidotite. These phases provide a record of several different alteration episodes experienced by the gabbros at varying depths as they were exhumed onto the seafloor.

The source of secondary oxides in the peridotites and troctolite gabbros is hydrous alteration, or serpentinization, of olivine and pyroxene by seawater that penetrates along zones of deformation and produces magnetite. The reaction can be simply written as:

olivine + H_2O =serpentine $\pm$ brucite $\pm$ magnetite

During this process a typical mesh-texture of serpentine-brucite forms around the rims of the olivine and pyroxene grains, followed by replacement of the olivine mesh centers with serpentine and brucite. Fine grained magnetites coalesce in a myriad of small veinlets in serpentite (Fig. 3-14e and 14f) [*Alt and Shanks*, 2003; *Bach et al.*, 2004; *Bach et al.*, 2006; *Pariso and Johnson*, 1993b]. As serpentinization progresses, magnetite is not confined to the mesh rims and we observe abundant magnetite throughout the sample. Samples that have experienced high temperature crystal plastic deformation (mylonites, ~ 600- 1000 °C [*Jaroslow*, 1996]) have well distributed magnetite instead of a distinct meshwork (e.g. Fig. 3-14g).

All of the Kane Megamullion peridotites (mylonites, metaperidotites and serpentinites) are highly serpentinized and have chlorite, tremolite and talc alteration minerals associated with them (greenschist-facies alteration). Reflected light microscopy shows small grained magnetites within the serpentinite mesh-rims, as well as larger oxides in cross-cutting veins of chlorite and tremolite (Fig. 3-14h). Crystallographically oriented needles of magnetite are also observed in pyroxenes (Fig. 3-14i) and likely impart intense and stable remanence in the serpentinized peridotites [*Carvallo et al.*, 2004]. Bright colored lamellae are observed in a highly altered sample; possibly hematite lamellae formed by oxidizing ilmenite (Fig. 3-14j). The presence of several oxide phases suggests the possibility of multiple serpentinization episodes that may have occurred over an extended period of time.

3.3.7 Anisotropy of magnetic susceptibility results

Preliminary results of anisotropy of magnetic susceptibility (AMS) from samples that were not demagnetized show the majority of samples have spherical AMS properties, i.e., linear degree of anisotropy (L) is equal to planar degree of anisotropy (F) (Fig. 3-15). Basalt and diabase samples have lower L/F ratios and lie along L=F, compared with several gabbros and peridotite samples that have higher F values and are therefore more oblate in character (Fig. 3-15). Four of the five samples with F > 1.1 are

85

identified as mylonites, which were deformed in shear zones associated with the detachment fault surface. This deformation explains the origin of the AMS and provides a method of identifying fault surface rocks at Kane Megamullion. The anisotropy in sample 14-45-1B however can not be explained from microscopic observations. Anisotropy of magnetic susceptibility is also defined by the average degree of anisotropy P, which ranges from 1.001-1.468 for the Kane Megamullion samples. *Lawrence et al.* [2002] observed oblate magnetic fabrics in 80% of the peridotite samples from ODP hole 920 and an average P value of 1.2. In these strongly serpentinized veins, the magnetic grains have a preferred orientation that is parallel to the AMS ellipsoid maximum axis, suggesting that the distribution of magnetite within the serpentine veins is largely responsible for the magnetic fabric. In ODP hole 670 the P factor ranges from 1.068-1.261, again indicating oblate AMS fabrics in the peridotites [*Krammer*, 1990].

3.4. Discussion

We now discuss the magnetic properties of the various lithological units sampled at Kane Megamullion and evaluate their potential to contribute to the magnetic source layer.

3.4.1 Basalts

Kane Megamullion basalts fall into two groups with distinct magnetic properties. Group 1 basalts have higher NRM, MDF and Q values, but lower k values relative to Group 2 basalts, suggesting greater stability of remanence and smaller magnetic grain size (Table 3-4). Indeed, they show SD behavior in both the Day plot and FORC parameter plot, while Group 2 basalts lie in the PSD region. A global compilation of drill core and sea sample basalt NRMs range from 0.5 to 81 A/m and plot across both the SD and PSD regions on a Day plot [*Bina et al.*, 1990; *Day et al.*, 1978; *Gee and Kent*, 1995; *Gee and Kent*, 1997; *Prevot et al.*, 1981; *Sempere et al.*, 1988; *Weiland et al.*, 1996].

The theoretical limit for hysteresis parameter Mr/Ms is 0.5 for an assemblage of SD grains with uniaxial anisotropy. *Gee and Kent* [1995] proposed that SD basalts are a result of magnetite dominated by cubic anisotropy. This interpretation was disputed by *Tauxe et al.* [2002] because photomicrographs of fine grained basalts suggest that neither cubes nor parallelpipeds are reasonable approximations for the shapes of the magnetic phases in these rocks. Instead, they suggested that basalts with Mr/Ms > 0.5 could be caused by shapes more complex than simple rods and cubes. Basalts drilled from ODP Hole 648B in the MARK area (south of Kane Megamullion, Fig. 3-1b) all show PSD behavior (Fig. 3-11) and are therefore comparable with Group 2 (PSD) basalts [*Bina et al.*, 1990]. *Bina et al.* [1990a] suggested that the ODP 648B PSD basalts experienced a low degree of maghemitization that had not yet physically divided the titanomagnetite grains into smaller sizes [*Johnson and Hall*, 1978] and/or longer lava cooling times that allows larger grains to form. We interpret Group 2 (PSD) basalts as having lower oxidation parameters (lower maghemization) than Group 1 (SD) basalts, from their susceptibility curves, microscopic observations, and larger oxide grain sizes in general.

In a detailed study of iron oxides in basalts from 12° N on the East Pacific Rise *Zhou et al.* [1997] identified three kinds of magnetic grains; large, micrometer-sized skeletal titanomagnetite grains (similar to those we observe), sub-micron titanomagnetites within the SD range, which they suggest is the main source of NRM, and magnetic oxides that have crystallized from immiscible liquids with grain sizes in the SD and SP range. Similar SP oxides may also be present in the Kane Megamullion samples and would explain the SP FORC behavior in the Group 2 (PSD) basalts. The skeletal oxide grains we observe are unlikely to be the source of the basalts NRM because they are too large (MD grain size). Even though the skeletal grains do not shed much light on the basalt NRM, changes in oxide grain size between Groups 1 and 2 are of interest because they reflect different cooling histories.

Average oxide grain size within a pillow lava decreases from the interior (50 μm) to the pillow rim (nanometer scale)[*Zhou et al.*, 2000]. Group 1 (SD) oxides are similar in size to these interior pillow oxides (Fig. 3-14b), however the Group 2 (PSD) oxides are several orders of magnitude larger (Fig. 3-14a). This suggests that they cooled at a much slower rate and may have been located deeper in the basalt layer, for example within the core of a pillow lava or below the surface of a lobate/sheet flow [*Ade-Hall et al.*, 1976]. The level of maghemitization (oxidation) also agrees with this interpretation as pillow exteriors and lava flow surfaces come into direct contact with seawater (until they are covered by later flows), compared with interior lavas that are maghemitized by seawater in fissures and cracks. Indeed, the thickness of the palagonite crust on the outside of the samples and the palagonitized rim on the interior of the samples are less thick in general in the Group 2 basalts and alteration levels range from low to medium (Table 3-1, Table 3-4).

Our observations therefore agree with *Bina et al.* [1990a]; a combination of both maghemitization levels and lava cooling time control the domain size of the magnetic grains, but we are not able to separate these two variables based on the rocks magnetic properties. Samples with higher maghemitization and/or fast cooling times will plot in the SD region, compared with low maghemitized and/or more slowly cooled lava, which will plot in the PSD region.

Group 2 (PSD) basalts represent an anomalous group of three basalts, based on their magnetic properties compared with the other eight basalt sampled at Kane Megamullion. Kane Megamullion basalts can also be grouped based on differences in their geographical location at the massif; seven basalts are interpreted as being hanging wall debris from the detachment fault surface (samples 11-4, 18-15, 22-1, 22-2a, 9-30, 9-36, J116-40. N.B., all the Group 2 basalts are interpreted to be hanging wall debris) while four are from the basalt ridge at the northern end of the eastern fault (samples 2-1, 2-3, J111-11, J111-17).

Dick et al. [submitted] commented that hanging wall debris was frequently unmetamorphosed and cemented by carbonate with serpentine clasts and diabase chips. In contrast, basalt ridge basalts often had palagonite or glassy rims and had experienced less alteration [*Dick et al.*, 2007]. The eleven basalts in this study do not exhibit such obvious differences in alteration levels. Of the four samples analyzed from the basalt ridge, 2-1 and 2-3 are classed as having low alteration levels, while samples J111-11 and J111-17 both have high alteration (Table 3-4. However, the magnetic properties of the two groups are different; the basalt ridge samples have NRM and Q values almost twice that of the hanging wall debris basalts (Table 3-5). The two groups also plot along different trends in the NRM vs k plot (Fig. 3-6), with the hanging wall debris basalts having a less steep trend (higher k values). These differences between basalt groups may indicate separate basalt sources, which could be investigated further using zeolites, or different levels of alteration.

Dick et al. [submitted] interpret the linear basalt ridge to be an intact volcanic edifice, associated with intersecting outward-facing and transform-parallel normal faults formed by exhumation of Kane Megamullion, most likely at the paleo-inside-corner high as the melt trapped within the footwall was forced to the surface [*Tucholke et al.*, 2001]. *Dick et al.* also cite broad lobes of flow fronts branching down slope on the western flank of the basalt ridge, which they observe in the high resolution ABE bathymetry, and a 'T' shaped orthogonal cross ridge at 23° 36'N as additional evidence of off-axis volcanism. There are no geochemical analyses with which to test this hypothesis at present, but outcrops on the basalt ridge do not show any visual evidence of lavas being emplaced in situ; there are no elongate pillows with their long axis along the slope dip direction, instead the pillows appear to be equant, which suggests deposition on a more horizontal surface, such as near the ridge axis. The difference in magnetic properties between the two geographic regions may be due to increased alteration experienced by hanging wall debris. When these samples were still attached to the hanging wall they could have

experienced low temperature (< 100° C) intense alteration from hydrothermal fluids rising from the detachment fault below.

In conclusion, we see different trends in the basalts related to both maghemitization and cooling rate. It is clear from the high NRMs, MDFs, Q values and quickly quenched oxides that oceanic basalts make excellent recorders of the geomagnetic field. Indeed, the basalt ridge appears as a ~ 4000 nT peak in the near-bottom magnetic anomaly data [*Williams et al.*, in prep]. However, the distribution and volume of basalts is not significant when compared with the gabbros and peridotites at Kane Megamullion and therefore is not a major contributor to the magnetic source layer. Similarly, the diabases have low NRM, k, MDF and other magnetic indicators that suggest that they are also not a significant contributor to the magnetic source in this region.

3.4.2 Gabbros

Kane Megamullion gabbros have a mean NRM of 1.5 A/m (± 2.5), which is very similar to gabbros cored in the nearby ODP holes 921-924 (mean NRM 1.5 A/m (± 2.6)) [*Gee et al.*, 1997]. The Kane Megamullion and ODP 921-924 gabbro values are lower than the ODP 735B gabbro mean NRM of 4.7 A/m [*Pariso and Johnson*, 1993a], but significantly higher than other MAR gabbro studies, e.g., 0.8 A/m [*Kent et al.*, 1978] and 1.0 A/m [*Fox and Opdyke*, 1973a]. Kane Megamullion gabbros can be subdivided based on the type of gabbro: oxide gabbro, olivine gabbro, gabbro mylonite, troctolite and metagabbro. Our results show that two troctolites (primitive gabbros) and one gabbro mylonite (sample 11-1) have the highest NRM and k values. Oxide gabbros are the most stable, with the highest MDF values, even though they have low NRM and k values (Table 3-2). These results agree with the ODP 921-924 gabbros [*Gee et al.*, 1997], which show troctolites have the highest NRMs, followed by gabbros and olivine gabbro, but differ from hole 735B, where oxide gabbros have the highest NRM [*Pariso and Johnson*,

1993b]. We sampled only two oxide gabbros, however, and therefore do not have a good representation of this rock type.

Susceptibility curves show that magnetite is the main magnetic carrier in the Kane Megamullion gabbros, and they have experienced little maghemitization based on the reversibility of their heating and cooling curves. Pure or nearly pure magnetite was found to be the sole magnetic carrier for gabbros from ODP 735B and all the curves were reversible to within 5 % of their initial values [*Worm*, 2001]. The magnetite in the high k troctolites (Fig. 3-7d) may be secondary magnetite due to alteration processes (e.g., serpentinization), which result in a CRM component, or a physical reduction in size of the original oxides (e.g. by ilmenite lamellae). Previous studies have shown that CRM accounts for the majority of gabbro NRM [*Garces and Gee*, 2007; *Pariso and Johnson*, 1993b; *Worm*, 2001], but that TRM may be a more stable source of NRM [*Garces and Gee*, 2007; *Gee et al.*, 1997].

Kane Megamullion gabbros have a higher percentage of large PSD/MD samples compared with gabbros from ODP 921-924 [*Gee et al.*, 1997] (Fig. 3-11) and ODP 735B (average Hcr/Hc=2.6 ± 1.4, Mr/Ms=0.22 ± 0.07) [*Worm*, 2001]. Earlier studies provide little consensus on whether alteration controls the position of a gabbro on the Day plot and its NRM. *Swift and Johnson* [1984] proposed that increasing alteration reduces the effective magnetic grain size. Less altered gabbros have large PSD and MD primary oxides, while more altered samples have smaller secondary oxides that plot in the smaller PSD, and possibly SD regions, and result in higher NRMs. Other studies seem to indicate little systematic change [*Kent et al.*, 1978; *Pariso and Johnson*, 1993b] or even an increase in NRM intensity with increasing alteration [*Kikawa and Ozawa*, 1992].

Percent alteration in the gabbros is defined using hand samples and thin sections, where available (Table 3-1). Alteration minerals vary from amphibolite- to greenschist-facies and serpentine. We do not observe a trend of increasing alteration with decreasing

size of domain state. Alteration levels range from 15-100%, with high levels of alteration observed in both small PSD and large PSD/MD samples. Large PSD and MD samples have lower NRMs in general, but there is no clear relationship between domain size and NRM. The type of alteration experienced by the gabbros does not have a direct control on the grain size or NRM either.

Alteration does appear to be a function of geographical location and stratigraphic distance from the detachment fault surface. As expected, the highest alteration levels were observed in samples collected from the detachment fault surface (Jason Dive 116 on Cain Dome, 100 % alteration). The lowest alteration was found in dredges 25, 27 and Jason Dive 117 from Adam Dome (45 % alteration). *Dick et al.* [submitted] interpret Adam and Eve domes to be a zone of late-stage focused melt delivery based on the large proportion of troctolites and dunites. These samples lie up to 0.9 km below the detachment fault, as indicated by the reduced brittle and crystal-plastic deformation of the rocks in this area, compared with Cain and Abel domes. The gabbros collected further north at Cain, Abel and Babel Domes are more evolved olivine and oxide gabbros, which are associated with peridotites and a large gabbro pluton on Babel Dome [*Dick et al.*, submitted].

The large majority of Kane Megamullion gabbros show stable, univectoral NRM during demagnetization. We identify only three samples with more than one component of magnetization (11-1, 27-70 and 27-86). Similar univectoral behavior has also been observed in other MAR samples and ODP 735B [*Kent et al.*, 1978; *Worm*, 2001]. These results imply that the gabbros acquired their remanence (both TRM and CRM) during a single geomagnetic polarity interval, for example during one of the subchrons that comprise Chron 2A (Fig. 3-3b). Chron 2A lasted for ~ 1 Myrs (2.581- 3. 8 Myrs ago) and subchrons 2An.1n – 2Ar range in duration from 0.091 to 0.591 Myrs [*Ogg and Smith*, 2004]. The gabbros likely cooled (acquiring TRM) and experienced both high and low temperature alteration (acquiring CRM) within ~ 14 km of the ridge axis, based on a

revised spreading rate of 14.5 km/Myrs for the western flank of the MAR at this location [*Williams et al.*, in prep.]. The short duration of several of the subchrons may also explain the reversed and normal paleodirections recorded by samples collected within tens of meters of each other during the Jason dives. *Gee et al.* [1997] also observed normal and reversed polarity gabbros from ODP 921-924, where polarity reversals occur over spatial scales of tens of centimeters to a few meters. They suggest that the gabbros were emplaced and/or cooled through three successive polarity intervals during the last 1.07 Myrs. The complexity and duration of crustal accretion processes and alteration processes may therefore reduce the integrated contribution of the gabbros to the magnetic source layer in oceanic crust.

Kane Megamullion gabbros meet the requirements for a magnetic source layer [*Swift and Johnson*, 1984] and could therefore contribute to the marine magnetic anomalies. The majority of the gabbros record the magnetic field as both a TRM and CRM during a single geomagnetic polarity interval. However, both normal and reverse sample paleodirections suggest that the gabbros acquired their remanence at a time of multiple polarity intervals, such as the subchrons during Chron 2A. This would result in a more complex magnetic signal that contributes to the marine magnetic anomalies. The gabbros have higher stability oxides than the peridotites, but lower average NRMs, implying that the contribution from the gabbros may not be as large as the peridotites, but their magnetic signal is likely more stable over geological time periods. Kane Megamullion gabbros have similar magnetic properties compared with global drill core samples and show that seafloor samples are representative of subsurface rocks and provide useful rock magnetic and paleomagnetic data.

3.4.3 Peridotites

Kane Megamullion serpentinized peridotites have high NRM values, almost comparable with basalts (mean NRM 4.7 A/m ($\pm$ 5.8)) and are close to the median of the global range in peridotites (0.02-12 A/m) [*Luyendyk and Day*, 1982; *Nazarova*, 1994;

Oufi et al., 2002; *Zhao et al.*, 2006]. The Kane Megamullion results are also comparable with the peridotites cored at ODP 670 (mean NRM 3.0 A/m (±3.0) [*Bina and Henry*, 1990]), but are considerably weaker than the ODP 920 peridotites (mean NRM 12.0 A/m (± 3.0)) [*Cannat et al.*, 1995a].

Fresh, unaltered peridotites are known to be mainly paramagnetic [*Dunlop and Ozdemir*, 1997] and typically acquire a CRM through alteration processes. The majority of Kane Megamullion peridotites are heavily serpentinized harzburgites with veining, or metaperidotites that have experienced greenschist facies alteration. The level of alteration does not appear to vary significantly across Kane Megamullion. The most altered peridotites were collected from the eastern side Cain Dome during Jason dive 116 (100 % alteration) and the least altered were found during Jason dive 114 (average ~ 88 % alteration), from the eastern flank of Abel Dome. The difference in alteration between the two locations is likely due to their location relative to the detachment fault surface; Jason dive 116 traversed the surface of the detachment fault, while Dive 114 sampled peridotites below the detachment fault surface in a landslip headwall. These differences in alteration are not as significant as those observed in the gabbro samples, suggesting more extensive alteration of peridotites across Kane Megamullion.

Oufi et al. [2002] proposed that the rate of formation of magnetite varies during serpentinization; ~ 6% iron oxide is formed in the first stages of serpentinization, but this drops to 2-3 % iron oxide as serpentinization proceeds beyond 75%. All of the Kane Megamullion peridotites have experienced > 75 % serpentinization, therefore we cannot make the same comparison, but we do observe iron oxide content ranging from 3-5 %. *Oufi et al.* [2002] also suggests that the large range in serpentinized peridotite remanent behavior is due to differences in the effective magnetic grain size related to the serpentinite texture. Samples with small effective magnetic grain sizes have a well-developed serpentine meshwork, outlined by thin vein-like magnetic concentrations. All the Kane Megamullion peridotites have serpentine meshwork, apart from J113-73, which

has only small oxides within altered pyroxene. This sample has the lowest peridotite NRM and therefore supports *Oufi et al.*'s statement.

As with the gabbros, there is continuing debate as to whether alteration processes control the location of peridotites on a Day plot and their NRM. *Bina and Henry* [1990] showed that on-axis peridotites from ODP 670 in the MARK area plot across the Day plot from small PSD to MD (Fig. 3-11). They hypothesize that samples with a high degree of serpentinization contain mainly large PSD/MD grains and less serpentinized samples exhibit PSD grain behavior [*Bina and Henry*, 1990; *Krammer*, 1990]. In contrast, peridotites from ODP 920 and several other study areas including ODP 895 and DSDP 395 (see *Oufi et al.* [2002] and references therein) [*Zhao et al.*, 2006], have small to mid-sized PSD, similar to the Kane Megamullion samples. Based on these results, *Oufi et al.* [2002] proposed that highly serpentinized peridotites would exhibit PSD behavior and high NRMs.

All Kane Megamullion peridotites are highly serpentinized and altered (78-100 % alteration) and lie in the small-mid PSD region (apart from J113-12, Fig. 3-10). Alteration phases in the peridotites are limited to talc, tremolite and chlorite, implying greenschist-facies alteration. NRM does not appear to increase with reducing domain state, but the range in domain state of our dataset may be too small to observe any trend. Our results, as they stand, therefore favor the hypothesis of *Oufi et al.* [2002]. The FORC parameter plot indicates low interaction energies for the peridotites, but a large range of coercivities. This may be due to different phases of serpentinization that occur as the detachment footwall is exhumed.

All of the serpentinized peridotites, apart from one sample (J113-12), have stable univectoral remanence. This suggests that each peridotite acquired its CRM during a single geomagnetic polarity interval, likely one of the Chron 2A subchrons. Peridotites show both normal and reversed paleodirections (Fig. 3-9a, Table 3-3), indicating that the

peridotites are able to retain a stable magnetic signal over geological time periods (i.e., the signal is not replaced by a significant viscous remanent magnetization (VRM) during a subsequent polarity interval, such as the Brunhes (0.781 Myrs to present)). Reverse polarity peridotites are measured across Kane Megamullion, both on the detachment fault surface (J116) and below the fault surface (J114), in close proximity to other peridotites or lithologies with positive paleodirections (Fig. 3-9b). As with the gabbros, we propose that the peridotites acquired their CRM during the ~ 1 Myr time period of Chron 2A, at least within 14 km of the axis. Consequently, fluid transport and alteration along and near the ridge axis controls the contribution peridotites make to the magnetic source layer and this signal is made more complex by interspersed normal and reverse polarity rocks.

Formation of detachment fault surfaces promotes focused fluid flow along discrete shear zones. Additional faulting associated with the uplift of the ocean core complex (such as synkinematic faulting within the overlying basalts or faulting of the ocean core complex itself) and mass wasting from volume increases due to serpentinization would also promote hydrothermal circulation. For example, pervasive circulation into the Atlantis Massif leads to strongly serpentinized domains on the south wall and appears to be presently active at the Lost City hydrothermal vent fields [*Boschi et al.*, 2006]. Alteration veins in peridotites drilled from ODP holes 920B, 920D and 670A show serpentinization temperatures ranging from > 350-400 °C to 200 °C [*Andreani et al.*, 2007; *Herbert et al.*, 1990]. During the first stage of serpentinization (~ 400 °C) up to 40-50% of the rock can be serpentinized. Anisotropic thermal contraction of olivine can result in cracking along grain boundaries and create an interconnected microcrack network enabling fluid penetration [*de Martin et al.*, 2004]. This process would be limited to the crust above the 400 °C isotherm (~ 4-6 km) and could therefore encompass an increasing proportion of the peridotites as they are exhumed by the detachment fault. Micro-seismicity focal depths beneath the TAG hydrothermal mound show a detachment fault with a steeply dipping interface (~ 70 °) close to the ridge axis, which flattens towards the surface (~ 20 °) [*de Martin et al.*, 2007]. This may explain how

the peridotites move quickly through the temperature interval of serpentinization. The serpentinite alteration front is estimated to extend up to ~ 1 km below the Atlantis Massif detachment fault surface [*Boschi et al.*, 2006]. A seismic reflection survey over Kane Megamullion (Ewing 01-02) shows low seismic-wave velocities (below 5 km/s) that extend to depths of at least 0.7 km. The low seismic velocities are interpreted to reflect serpentinized rocks (*J. P. Canales,* pers. comm.) and therefore a similar alteration zone thickness to Atlantis Massif.

Kane Megamullion serpentinized peridotites fulfill all the rock magnetic criteria to form part of the magnetic source layer. All but one of the peridotites have univectoral magnetization, but their paleodirections show both normal and reversed polarity and could result in reduced amplitude or skewed marine magnetic anomalies. Drilling through Kane Megamullion would provide further information about the alteration front thickness and paleodirections at depth.

3.4.4 Modeling of the magnetic source layer

Our rock magnetic and paleomagnetic data provide parameter constraints that allow us to construct a first-order set of models for the source of the anomalies at Kane Megamullion. Based on our results, we have averaged NRM values and paleodirections for the gabbros and peridotites, which address two of the unknown variables in the inversion. The third variable is the thickness/volume of the magnetic source layer and so here we assume that the serpentinized layer has a minimum thickness of 0.7 km, based on seismic reflection data (*J. P. Canales*, pers. comm.).

A magnetic anomaly profile is taken from the sea-surface anomaly grid over the central region of Kane Megamullion, across Cain and Abel Domes. The amplitude of the observed sea-surface anomaly between Chrons 2r and 2An is ~ 250 nT. A modeled magnetic source layer 0.7 km thick with a magnetization of 4.7 A/m (equivalent to the serpentinized peridotites) and a GAD magnetization direction (0°/40°) produces a ~ 350

nT amplitude anomaly (Fig. 3-16i). This suggests that the peridotites alone are more than able to produce an anomaly of the required amplitude. In fact, a source layer of only 0.5 km is required. In contrast, a modeled magnetic source layer with the same thickness and magnetization direction but magnetization of 1.5 A/m, equivalent to the Kane Megamullion gabbros, only produces a ~ 100 nT amplitude anomaly (Fig. 3-16ii). A source layer with this magnetization would have to be ~ 1.75 km thick to produce an anomaly with the same amplitude as the sea-surface data.

Magnetization direction must be a relict of the direction that was present when the rocks were part of the in situ oceanic crust to be relevant to the model. The model above (Fig. 3-16 i and ii) assumes uniform normal GAD magnetization direction in the source layer, but magnetization direction will change if a body is rotated by tectonic processes. Indeed, previous studies of paleomagnetic vectors from oriented drill cores have shown that ocean core complexes experience rotations ranging from 40° [*Carlut et al.*, 2006] to a maximum of 80° [*Garces and Gee*, 2007]. Averaged normal and reverse declinations for the visually oriented samples at Kane Megamullion range from 13° to 44°, compared with the GAD magnetization directions (Fig. 3-9a). We use the approach of *Verosub and Moores* [1981] to calculate the change in magnetization direction for both clockwise and counter-clockwise rotations, assuming a rotation axis parallel to the ridge axis with a strike of 20° (Fig. 3-17). The range of sample mean declinations from 13° to 44° corresponds to counter clockwise rotations of 15° to 50° (Fig. 3-17a). Model profiles that include these rotations show a change in phase (skewness) of the resulting anomalies (Fig. 3-16iii, iv). A model with 15° of counter clockwise rotation is similar in appearance to the observed profile (Fig. 3-16i), with a larger relative amplitude for the first peak in C2An than the second peak (Fig. 3-16iii). This model requires a source layer thickness of 0.55 km to match the 250 nT difference increase between C2r and C2An. The model results for 50° of counter clockwise rotation show that the relative amplitude between the first and second peaks is slightly different than the observed data, with a larger amplitude

on the second peak (Fig. 3-16 iv). This suggests that 50° of counter clockwise rotation might be an overestimate and the true rotation at Kane Megamullion is closer to ~ 15°.

3.5. Conclusions

Rock magnetic and paleomagnetic measurements of rock samples from the lower crust and upper mantle rocks at Kane Megamullion show several distinct differences. We follow the criteria of *Swift and Johnson* [1984] in identifying a magnetic source rock; a rock that contributes to the magnetic source layer must have an NRM greater than 2 A/m, a Q ratio > 1, an MDF > 5 mT and stable direction. We make the following conclusions:

1. Average basalt and peridotite results fulfill all the criteria for NRM, Q and MDF values to be a magnetic source rock. Diabases have very low NRMs on average (0.079 A/m) and the gabbros fall just below the criteria (1.5 A/m). However, the gabbros appear to be more stable and have increased ability to record remanence than the peridotites.

2. Magnetite is the main magnetic carrier in both the gabbros and peridotites, based on thermomagnetic curves. Remanence is attributed to a combination of thermoremanence (TRM) and chemical remanence (CRM) in the gabbros, and CRM in the peridotites. Titanomaghemite carrying a TRM is the source of remanence in the basalts.

3. The majority of gabbros and peridotites record a single magnetization vector, indicating that they acquired their remanence (both TRM and CRM) during intervals of single geomagnetic polarity, such as subchrons in Chron 2A that range in duration from 0.091 to 0.591 Ma. Chron 2A lasted for ~ 1 Ma, therefore we propose that the gabbros and serpentinized peridotites at Kane Megamullion acquired their remanence within a maximum of ~ 14 km from the ridge axis.

4. Both normal and reverse paleodirections are measured in the gabbros and peridotites across Kane Megamullion. Increased numbers of reversed samples are found in anomaly transition zones along Jason Dives 116 (Cain Dome) and 117 (Adam Dome). Samples with opposite polarities are also located within tens of

meters of each other and could be explained by the short duration subchrons combined with intermittent crustal accretion and fluid transport processes. A reversal test on the Kane Megamullion samples shows that the antipode of the normal polarity direction lies within the 95 % confidence interval of the mean reverse polarity direction.

5. A modeled magnetic source layer thickness of 0.5 km of peridotites or 1.75 km of gabbros with uniform geocentric axial dipole magnetization direction can account for the observed anomaly amplitude across Chron 2r/2An. Counter clockwise rotations of the model, based on estimates from the paleomagnetic data, result in phase changes in the magnetic anomalies. Our results suggest Kane Megamullion has experienced close to 15° of counter clockwise rotation.

6. Magnetic properties of Kane Megamullion samples are comparable to ODP drill core samples from the MARK area

Acknowledgements

References

Ade-Hall, J.M., J.H. Fink, and H.P. Johnson (1976),Petrography of opaque minerals, Leg 34, *Initial Rep. Deep Sea Drill. Proj., 34*, 349-362.

Ade-Hall, J.M., H.C. Palmer, and T.P. Hubbard (1971),The magnetic and opaque petrological responses of basalt to regional hydrothermal alteration, *Royal Astronomical Society Geophysical Journal, 24*, 137-174.

Allerton, S.A., and M.A. Tivey (2001),Magnetic polarity structure of the lower oceanic crust, *Geophys.Res.Letts, 28*, 423-426.

Alt, J.C., and W.C.I. Shanks (2003),Serpentinization of abyssal peridotites from the MARK area, Mid-Atlantic Ridge: Sulfur geochemistry and reaction modeling, *Geochimica et Cosmochimica Acta., 67*, 641-653.

Andreani, M., C. Mevel, A.-M. Boullier, and J. Escartin (2007),Dynamic control on serpentine crystallization in veins: Constraints on hydration processes in oceanic peridotites, *Geochem. Geophys. Geosyst.*, *8*, Q02012, doi:10.1029/2006GC001373.

Auzende, J.-M., M. Cannat, P. Gente, J.P. Henriet, T. Juteau, J.A. Karson, Y. Lagabrielle, C. Mevel, and M.A. Tivey (1994),Observations of sections of oceanic crust and mantle cropping out on the southern wall of the Kane FZ (N. Atlantic), *Terra Research*, *6*, 143-148.

Bach, W., C.J. Garrido, H. Paulick, J. Harvey, and M. Rosner (2004),Seawater-peridotite interactions: First insights from ODP Leg 209, MAR 15° N, *Geochem. Geophys. Geosyst.*, *5*, Q09F26, doi:10.1029/2004GC000744.

Bach, W., H. Paulick, C.J. Garrido, B. Ildefonse, W.P. Meurer, and S.E. Humphris (2006),Unraveling the sequence of serpentinization reactions:petrography, mineral chemistry, and petrophysics of serpentinites from MAR 15° N (ODP Leg 209, Site 1274), *Geophys. Res. Letts.*, *33*, L13306, doi:10.1029/2006GL025681.

Bina, M.M., Y.M. Hamano, K. Krammer, and A. Wooldridge (1990),Paleomagnetism of basalts from ODP hole 648B on the Mid-Atlantic Ridge, *Proc. Ocean Drill. Program Sci. Results*, *106/109*, 291-295.

Bina, M.M., and B. Henry (1990),Magnetic properties, opaque mineralogy and magnetic anisotropies of serpentinized peridotites from ODP Hole 670A near the Mid-Atlantic Ridge, *Physics of the Earth and Planetary Interiors*, *65*, 88-103.

Blackman, D.K., J.R. Cann, B. Janssen, and D.K. Smith (1998),Origin of extensional core complexes: Evidence from the Mid-Atlantic Ridge at Atlantis Fracture Zone, *J. Geophys. Res.*, *103*, 21315-21333.

Boschi, C., G.L. Fruh-Green, A. Delacour, J.A. Karson, and D.S. Kelley (2006),Mass transfer and fluid flow during detachment faulting and development of an oceanic core complex, Atlantis Massif (MAR 30° N), *Geochem. Geophys. Geosyst.*, *7*, Q01004, doi:10.1029/2005GC001074.

Butler, R.F., *Paleomagnetism; magnetic domains in geological terranes*, Blackwell Sci. Publ, Boston, USA, 1992.

Cann, J.R. (1974),A model for oceanic crustal structure developed, *Geophys. J R. Astron. Soc.*, *39*, 169-187.

Cann, J.R.e.a. (1997),Corrugated slip-surface formed at ridge-transform intersections on the Mid-Atlantic Ridge, *Nature*, *385*, 329-332.

Cannat, M., J.A. Karson, D.J. Miller, and a.t.S.S.P.o.O.L. 153, in *Proc. Ocean Drill. Program Init. Repts.*, College Station,TX (Ocean Drilling Program), 1995b.

Cannat, M., C. Mevel, M. Maia, C. Deplus, C. Durand, P. Gente, P. Agrinier, A. Belarouchi, G. Dubuisson, E. Humler, and J.R. Reynolds (1995a),Thin crust, ultrmafic exposures, and rugged faulting paterns at the Mid- Atlantic Ridge (22-24° N), *Geology*, *23*, 49-52.

Carlut, J., C.J. MacLeod, H. Horen, and J. Escartin, Paleomagnetic results from a mid-ocean ridge detachment at the Mid-Atlantic Ridge, 15° 45'N, in *EGU Meeting*, Vienna, 2006.

Carvallo, C., and A. Muxworthy (2006),Low-temperature first-order reversal curve (FORC) diagrams for synthetic and natural samples, *Geochem. Geophys. Geosyst.*, *7*, Q09003,doi:10.1029/2006GC001299.

Carvallo, C., O. Ozdemir, and D.J. Dunlop (2004),First-order reversal curves (FORC) diagrams of elongated single-domain grains at high and low temperatures, *J. Geophys. Res.*, *109* (B04105), doi:10.1029/2003JB002539.

Carvallo, C., A.P. Roberts, R. Leonhardt, C. Laj, C. Kissel, M. Perrin, and P. Camps (2006),Increasing the efficiency of paleointensity analyses by selection of samples using first-order reversal curve diagrams, *J. Geophys. Res.*, *111*, doi:10.1029/2005JB004126.

Davis, G.A., and G.S. Lister (1988),Detachment faulting in continental extension; perspectives from the southwestern U.S. cordillera, *Spec. Pap. Geol. Soc. Am.*, *218*, 133-159.

Day, R., M.D. Fuller, and V.A. Schmidt (1977),Hysteresis properties of titanomagnetities, *Physics of the Earth and Planetary Interiors*, *13*, 260-267.

Day, R., S. Halgedahl, M. Steiner, K. Kobayashi, T. Furuta, T. Ishii, and A. Faller (1978),Magnetic properties of basalts from DSDP Leg 49, *Initial Rep. Deep Sea Drill. Proj.*, *49*, 781-791.

de Martin, B., G. Hirth, and B. Evans, Experimental constraints on thermal cracking of peridotites at ocean spreading centers, in *Mid-Ocean Ridges: Hydrothermal Interactions Between the Lithosphere and Oceans*, edited by C.R. German, J. Lin, and L.M. Parson, pp. 167-185, AGU, Washington D. C., 2004.

de Martin, B.J., R.A. Sohn, J.P. Canales, and S.E. Humphris (2007),Kinematics and geometry of active detachment faulting beneath the TAG hydrothermal field on the Mid-Atlantic Ridge, *in press, Geology*.

Dick, H.J.B., H. Schouten, P.S. Meyer, D.G. Gallo, H. Bergh, R. Tyce, P. Patriat, T.M. Johnson, J. Snow, and A. Fischer (1991),Tectonic evolution of the Atlantis II Fracture Zone, *Proc. Ocean Drill. Program Sci. Results*, *118*, 359-398.

Dick, H.J.B., M.A. Tivey, and B.E. Tucholke (2007),Plutonic foundation of a slow-spread ridge segment: the oceanic core complex at Kane Megamullion, 23° 30'N, 45° 20'W., *submitted to Geochem. Geophys. Geosys*.

Dunlop, D.J. (1981),The rock magnetism of fine particles, *Physics of the Earth and Planetary Interiors*, *26*, 1-26.

Dunlop, D.J., and O. Ozdemir, *Rock-Magnetism, fundamentals and frontiers*, Cambridge University Press, 1997.

Dunlop, D.J., and M. Prevot (1982a),Magnetic properties and opaque mineralogy of drilled submarine intrusive rocks, *Geophys. J. R. Astron. Soc*, *69*, 763-802.

Dunlop, D.J., and M. Prevot (1982b),Magnetic properties and opaque mineralogy of drilled submarine intrusive rocks, *Geophys. J R. Astron. Soc.*, *69*, 763-802.

Escartin, J., C. Mevel, C.J. MacLeod, and A.M. McCaig (2003),Constraints on deformation conditions and the origin of oceanic detachments : The Mid-Atlantic Ridge core complex at 15° 45'N, *Geochemistry, Geophysics, Geosystems, 4*, doi:10.1029/2002GC000364.

Fisher, R.A. (1953),Dispersion on a sphere, *Proc. Roy. Soc. Londo.*, *217*, 295-305.

Fox, P.J., and N.D. Opdyke (1973a),Geology of the Oceanic Crust : Magnetic Properties of Oceanic Rocks, *J. Geophys. Res.*, *78*, 5139-5154.

Fox, P.J., and N.D. Opdyke (1973b),Geology of the oceanic crust: magnetic properties of oceanic rocks, *J. Geophys. Res.*, *78*, 5139-5154.

Francheteau, J., R. Armijo, J.L. Cheminee, R. Hekinian, P. Lonsdale, and N. Blum (1990a),1 Ma East Pacific Rise oceanic crust and uppermost mantle exposed by rifting in Hess Deep (equatorial Pacific Ocean), *Earth Planet. Sci. Letts.*, *101*, 281-295.

Francheteau, J., R. Armijo, J.L. Cheminee, R. Hekinian, P. Lonsdale, and N. Blum (1990b),Dyke complex of the East Pacific Rise exposed in the walls of Hess Deep and the structure of the upper oceanic crust, *Earth Planet. Sci. Letts.*, *111*, 109-121.

Garces, M., and J. Gee (2007),Paleomagnetic evidence of large footwall rotations associated with low-angle faults at the Mid-Atlantic Ridge, *Geology*, *35*, 279-282.

Gass, I.G. (1968),Is the Troodos Massif of Cyprus a fragment of Mesozoic Ocean Floor?, *Nature*, *220*, 39-42.

Gass, I.G., and J.D. Smewing (1973),Intrusion, extrusion and metamorphism at constructive margins: evidence from the Troodos Massif, Cyprus, *Nature*, *242*, 26-29.

Gee, J., and D.V. Kent (1995),Magnetic hysteresis in young mid-ocean ridge basalts: dominant cubic anisotropy, *Geophys. Res. Letts.*, *22*, 551-554.

Gee, J., and D.V. Kent (1997),Magnetization of axial lavas from the southern East Pacific Rise (14°-23°S): Geochemical controls on magnetic properties, *J. Geophys .Res.*, *102*, 24873-24886.

Gee, J., R.M. Lawrence, and S.D. Hurst (1997),Remanence characteristics of gabbros from the MARK area: Implications for crustal magnetization, *Proc. Ocean Drill. Program Sci. Results*, *153*, 429-436.

Gee, J., and W.P. Meurer (2002),Slow cooling of middle and lower oceanic crust inferred from multicomponent magnetizations of gabbroic rocks from the Mid-Atlantic Ridge south of the Kane fracture zone (MARK) area, *J. Geophys. Res.*, *107* (B7), EPM 3, doi:10.1029/2000JB000062,18.

Hall, J.M., and A. Muzzatti (1999),Delayed magnetization of the deeper kilometer of oceanic crust at Ocean Drilling Project Site 504, *J. Geophys. Res.*, *104*, 12,843-12,851.

Harrison, C.G.A. (1987), Marine magnetic anomalies- The origin of the stripes, *Annu. Rev. Earth. Planet. Sci*, *15*, 505-543.

Herbert, R., A.C. Adamson, and S.C. Komor (1990),Metamorphic petrology of ODP leg 109, Hole 670A serpentinized peridotites; Serpentinization processes at a slow spreading ridge environment, *Proc. Ocean Drill. Program Sci. Results*, *106/109*, 103-115.

Jaroslow, G.E. (1996),Abyssal peridotite mylonites: implications for grain-size sensitive flow and strain localization in the oceanic lithosphere, *Tectonophysics*, *256*, 17-37.

Johnson, H.P., and J.M. Hall (1978),A detailed rock magnetic and opaque mineralogy study of basalts from the Nazca Plate, *Geophys. J R. Astron. Soc.*, *52*, 45-64.

Johnson, H.P., and B.L. Salem (1994),Magnetic properties of dikes from the oceanic upper crustal section, *J. Geophys. Res.*, *99*, 21733-21740.

Karson, J.A., Internal Structure of oceanic lithosphere: a perspective from tectonic windows, in *Faulting and Magmatism at Mid-Ocean Ridges*, edited by W.R. Buck, P.T. Delaney, J.A. Karson, and Y. Lagabrielle, AGU, Washington D.C., 1998.

Karson, J.A., E.M. Klein, S.D. Hurst, C.E. Lee, P.A. Rivizzigno, D. Curewitz, and H.D.S. Party (2002b),Structure of uppermost fast-spread oceanic crust exposed at the Hess Deep Rift: Implications for subaxial processes at the East Pacific Rise, *Geochem. Geophys. Geosyst.*, *3*, 2001GC000155.

Karson, J.A., M.A. Tivey, and J.R. Delaney (2002),Internal structure of uppermost oceanic crust along the Western Blanco Transform Scarp: Implications for subaxial accretion and deformation at the Juan de Fuca Ridge, *J. Geophys. Res.*, *107*, doi:10.1029/2000JB000051.

Kelemen, P.B., E. Kikawa, D.J. Miller, and S.S. Party, Ocean Drilling Program, College Station, 2004.

Kent, D.V., and J. Gee (1994),Grain size-dependent alteration and the magnetization of oceanic basalts, *Science*, *265*, 1561-1563.

Kent, D.V., B.M. Honnorez, N.D. Opdyke, and P.J. Fox (1978),Magnetic properties of dredged oceanic gabbros and the source of marine magnetic anomalies, *Geophys. J R. Astron. Soc.*, *55*, 513-537.

Kikawa, E., and K. Ozawa (1992),Contribution of oceanic gabbros to sea-floor spreading magnetic anomalies, *Science*, *258*, 796-799.

Krammer, K. (1990),Rock magnetic properties and opaque mineralogy of selected samples from Hole 670A, *Proc. Ocean Drill. Program Sci. Results*, *106/109*, 269-273.

Lawrence, R.M., and J.A. Karson (1998),Dike orientations, fault-block rotations, and the construction of slow spreading oceanic crust at 22° 40'N on the Mid-Atlantic Ridge, *J. Geophys. Res.*, *103*, 663-676.

Luyendyk, B.P., and R. Day (1982),Paleomagnetism of the Samail ophiolite, Oman,2 , The Wadi Kadir gabbro section, *J. Geophys. Res.*, *87*, 10,903-10,917.

Morely, L.W., and A. Larochelle (1964),Paleomagnetism as a means of dating geological events, *Roy. Soc. Can. Spec. Publ.*, *8*, 39-50.

Muxworthy, A., and E. McClelland (2000),The causes of low-temperature demagnetization of remanence in multidomain magnetite, *Geophys. J. Int.*, *140*, 115-131.

Muxworthy, A., and W. Williams (2005),Magnetostatic interaction fields in first-order-reversal-curve (FORC) diagrams, *J. Appl. Phys.*, *97*, 063905,doi:10.1063/1.1861518.

Nazarova, K.A. (1994),Serpentinized peridotites as a possible source for oceanic magnetic anomalies, *Mar. Geophys. Res.*, *16*, 455-462.

Ogg, J.G., and A.G. Smith, The geomagnetic polarity time scale, in *A geological time scale 2004*, edited by F.M. Gradstein, J.G. Ogg, and A.G. Smith, Cambridge University Press, Cambridge, UK, 2004.

Oufi, O., M. Cannat, and H. Horen (2002),Magnetic properties of variably serpentinized abyssal peridotites, *Journal of Geophysical Research, 107*, 10.1029/2001JB000549.

Pariso, J.E., and H.P. Johnson (1993a),Do layer 3 rocks make a significant contribution to marine magnetic anomalies? In situ magnetization of gabbros from Ocean Drilling Program Hole 735B, *J. Geophys. Res, 98*, 16033-16032.

Pariso, J.E., and H.P. Johnson (1993b),Do lower crustal rocks record reversals of the Earth's magnetic field? Magnetic petrology of oceanic gabbros from ocean drilling program Hole 735B., *J. Geophys. Res, 98*, 16013-16032.

Pike, C.R., A.P. Roberts, and K.L. Verosub (1999),Characterizing interactions in fine magnetic particle systems using first order reversal curves, *J. Appl. Phys., 85*, 6660-6667.

Pike, C.R., A.P. Roberts, and K.L. Verosub (2000),FORC diagrams and thermal relaxation effects in magnetic particles, *Geophys. J. Int., in press*, in press.

Prevot, M., A. Lecaille, and E. Mankinen (1981),Magnetic effects of maghemitization of oceanic crust, *J. Geophys. Res., 86*, 4009-4020.

Rahman, A.A., A.D. Duncan, and L.G. Parry (1973),Magnetization of multi-domain magnetite particles, *Riv. Ital. Geofis., 22*, 259-266.

Roberts, A.P., Q. Liu, C.J. Rowan, L. Chang, C. Carvallo, and C.-S. Horng (2006),Characterization of hematite (a-Fe2O3), goethite (a-FeOOH), greigite (Fe3S4), and pyrrhotite (Fe7S8) using first- order reversal curve diagrams, *J. Geophys. Res., 111*, doi:10.1029/2006JB004715.

Roberts, A.P., C.R. Pike, and K.L. Verosub (2000),First-order reversal curve diagrams: A new tool for characterizing the magnetic properties of natural samples, *J. Geophys. Res., 105*, 28,461-28,475.

Robinson, P.T., J. Malpas, and C. Xenophontos, The Troodos Massif in Cyprus: Its role in the evolution of the ophiolite concept, in *Ophiolite concept and the evolution of geological thought*, edited by Y. Dilek, and S. Newcomb, pp. 295-308, Geologial Society of America, Boulder, 2003.

Searle, R.C., M. Cannat, K. Fujioka, C. Mevel, H. Fujimoto, A. Bralee, and L. Parons (2003),FUJI Dome: A large detachment fault near 64° E on the very slow-spreading southwest Indian Ridge, *Geochemistry, Geophysics, Geosystems, 4* (8), 9105,doi:10.1029/2003GC000519.

Sempere, J.-C., A. Meshkov, M. Thommeret, and K.C. Macdonald (1988),Magnetic properties of some young basalts from the East Pacific Rise, *Mar. Geophys. Res., 9*, 131-146.

Smith, B.M. (1987),Consequences of the maghemitization on the magnetic properties of submarine basalts: Synthesis of previous works and results concerning basement rocks from mainly DSDP Legs 51 and 52, *Physics of the Earth and Planetary Interiors, 46*, 206-226.

Stoner, E.C., and E.P. Wohlfarth (1948),A mechanism of magnetic hysteresis in heterogeneous alloys, *Philos. Trans. R. Soc. London, Ser. A* (240), 599-642.

Swift, B.A., and H.P. Johnson (1984),Magnetic properties of the Bay of Islands ophiolite suite and implications for the magnetization of oceanic crust, *J. Geophys. Res., 89*, 3291-3308.

Tauxe, L., *Paleomagnetic Principles and Practice*, Kluwer, Norwell, MA, 2002.

Teagle, D.A.H., D.S. Wilson, G.D. Acton, and D.A. Vanko, in *Proc. Ocean Drill. Program Sci. Results*, Ocean Drilling Program, College Station, TX, 2007.

Tivey, M.A. (1996),Vertical magnetic structure of ocean crust determined from near-bottom magnetic field measurements, *J. Geophys. Res., 101*, 20, 275-20,296.

Tivey, M.A., A. Takeuchi, and W.S. Party (1998),A submersible study of the western intersection of the Mid-Atlantic ridge and Kane fracture zone (WMARK), *Mar. Geophys. Res., 20*, 195-218.

Tucholke, B.E., K. Fujioka, T. Ishihara, G. Hirth, and H. Kinoshita (2001),Submersible study of an oceanic megamullion in the central North Atlantic, *Journal of Geophysical Research, 106*, 16145-16161.

Tucholke, B.E., J. Lin, and M.C. Kleinrock (1998),Megamullions and mullion structure defining oceanic metamorphic core complexes on the Mid-Atlantic Ridge,, *J. Geophys. Res., 103*, 9857-9866.

Tucholke, B.E., L. Lin, and M.C. Kleinrock (1996),Mullions,megamullions,and metamorphic core complexes on the Mid-Atlantic Ridge, *EOS Trans. AGU, 77* (46), Fall Meet. Suppl., F724.

Varga, R.J., J.A. Karson, and J. Gee (2004),Paleomagnetic constraints on deformation models for uppermost oceanic crust exposed at Hess Deep Rift: Implications for axial processes at the East Pacific Rise, *J. Geophys. Res., 109*, B02104, doi:10.1029/2003JB002486.

Vine, F.J., and D.H. Matthews (1963), Magnetic anomalies over oceanic ridges, *Nature, 199*, 947-949.

Weiland, C.M., K.C. Macdonald, and N.R. Grindlay (1996),Ridge segmentation and the magnetic structure of the Southern Mid-Atlantic Ridge 26° S and 31°-35° S: implications for magmatic processes at slow spreading centers, *J. Geophys. Res., 101*, 8055-8073.

Wernicke, B.P., Cenozoic extensional tectonics of the U. S. Cordillera, in *The Geology of North America; The Cordilleran Orogen: Coterminous U.S.*, edited by B.C. Burchfiel, and e. al, pp. 553-581, Geol. Soc. Am, Boluder, Colorado, 1992.

Worm, H.-U. (2001),Magnetic stability of oceanic gabbros from ODP Hole 735B, *Earth Planet. Sci. Letts., 193*, 287-302.

Zhao, X., P. Riisager, M. Antretter, J. Carlut, P. Lippert, Q. Liu, B. Galbrun, S. Hall, H. Delius, and T. Kanamatsu (2006),Unraveling the magnetic carriers of igneous cores from the Atlantic, Pacific and the southern Indian oceans with rock magnetic characterization, *Phys. Earth Planet. Inter., 156*, 294-328.

Zhou, W., R. Van der Voo, D.R. Peacor, D. Wang, and Y. Zhang (2000),Variable Ti-content and grain size of titanomagnetite as a function of cooling rate in very young MORB, *Earth Planet. Sci. Letts., 179*, 9-20.

Table 3-1 Rock magnetic properties, alteration minerals and deformation results

Sample no.	Lithology	Lon °W	Lat °N	K (x10⁴ SI)	NRM (A/m)	MDF (mT)	Q	Hc (Oe)	Hcr (Oe)	Mr (μemu)	Ms (μemu)	Alteration minerals	Alt %	Deformation crystal/plastic	Deformation brittle
KN180-2-2-1-1a	Basalt	45.3307	23.5418	2.43	12.005	40	161						L	0	0
KN180-2-2-1-1b				2.42	14.786		199								
KN180-2-2-1-2				1.96	9.162	40	153								
KN180-2-2-1-2a				2.63	16.056	38	199	459.9	622.9	310.5	462.4				
KN180-2-2-3-1a	Basalt	45.3307		1.90	8.158	38	140	792.7	978.3	1183.0	158.4		L	0	0
KN180-2-2-3-2a				2.14	7.433	46	114								
KN180-2-9-30-1	Pl-Ol basalt	45.3116	23.6074	12.28	5.207	24	14						L	0	0
KN180-2-9-30-1a				19.65	7.138	18	12								
KN180-2-9-30-2				10.84	4.186		13	74.94	122.1	492.4	2038.0				
KN180-2-9-36-1a	Pl-Ol basalt	45.3116	23.6074	6.05	11.458	26	62						M	0	0
KN180-2-9-36-1b				5.41	12.139	30	73	249.7	325.8	530.8	901.1				
KN180-2-9-36-2				3.74	7.289		64								
KN180-2-11-1-1	Gabbro myn.	45.2308	23.5778	121.00	1.392	8	0					Ab, Cl, gAm	40	3.5	0
KN180-2-11-1-1a				188.00	3.847	7	1	80.22	304	2949.0	37020.0				
KN180-2-11-1-2				58.54	2.546		1								
KN180-2-11-1-2a				47.02	2.436	9	2								
KN180-2-11-4-1a	Pl-Ol basalt	45.2308	23.5778	2.33	11.839	52	166	869.8	1071	323.0	425.3		M	0	0
KN180-2-11-4-2				1.51	5.207	60	113								
KN180-2-11-4-3															
KN180-2-13-1-1a	Diabase	45.2301	23.4803	1.02	0.014	23	0	113.4	335.7	5.7	36.2	Ch	70	0	1
KN180-2-13-1-2				0.98	0.017	19	1								
KN180-2-13-1-3															
KN180-2-13-49-1a	Pl diabase	45.2301	23.4803	1.31	0.236	32	6					Tr, Tc, Srp	70	0.5	2
KN180-2-13-49-2a				1.05	0.185	35	6	260.3	403.3	195.0	523.4				
KN180-2-14-18-1	Ol gabbro	45.3030	23.4638	1.39	0.372	28	9	40.36	194.4	42.2	776.3	Ab, Cl, gAm, Tr	35	0.5	0
KN180-2-14-18-2				1.50	0.958		21								
KN180-2-14-45-1a	Harzburgite myn.	45.3030	23.4638	28.49	0.996	27	1					Cl, Tc, Srp	88	1	0
KN180-2-14-45-1b				15.03	5.506		12								
KN180-2-14-45-2				31.79	1.825	22	2								
KN180-2-14-45-2a				27.29	1.397	22	2								
KN180-2-17-3-1a	Harzburgite	45.3841	23.4856	39.24	2.940	30	2	135.2	290.4	3293.0	11720.0	Tr,Cl,Srp	82	2	0
KN180-2-17-3-2				40.66	3.068	18	2	306.5	454.3	1060.0	2677.0				
KN180-2-18-15-1	Pl-Ol basalt	45.4124	23.4839	1.56	6.012	39	126	657.4	814.4	172.8	226.7		H	0	0
KN180-2-18-15-2a				1.20	4.027	62	110								
KN180-2-21-12-1	Troctolite	45.3739	23.3628	68.58	3.954	21	2	136.9	187.9	3974.0	14350.0	Ab, Cl, Pr,Srp	76	0	0
KN180-2-21-12-1a				82.70	5.659	14	2								
KN180-2-21-12-1b				71.31	5.465		3								
KN180-2-21-12-2a				75.25	11.717	5	5								
KN180-2-21-12-2b				64.16	9.292	7	5								

Sample no.	Lithology	Lon °W	Lat °N	K (x 10⁻³ SI)	NRM (A/m)	MDF (mT)	Q	Hc (Oe)	Hcr (Oe)	Mr (µemu)	Ms (µemu)	Alteration minerals	Alt %	Deformation crystal/plastic	brittle
KN180-2-21-14-1	Troctolite	45.3739	23.3628	58.70	5.721	22	3	212.9	289.2	6417.0	16930.0	Ab,Srp,Ch,gAm	80	0	0
KN180-2-21-14-2a				56.00	5.467	14	3	218.3	282.3	238.5	394.8		M	0	0
KN180-2-22-1-1a	Pl-Ol basalt	45.2607	23.4172	5.21	5.741	21	36						M	0	0
KN180-2-22-1-2				3.51	4.800	21	45								
KN180-2-22-2a	Basalt	45.2607	23.4172	21.18	9.473	19	15	111.9	162.2	834.5	2445.0		M	0	0
KN180-2-22-2a-a				9.55	8.177	17	28								
KN180-2-22-2a-b				25.48	10.829	17	14								
KN180-2-25-1-1	Troctolite	45.4122	23.3999	7.41	0.469		2					Ab, Act, Ch, Cl	25	0	0
KN180-2-25-1-1a				7.22	0.468	9	2	106	160.5	750.7	3057.0				
KN180-2-25-1-1b				5.53	0.419		2								
KN180-2-25-1-2				10.00	0.948	5	3								
KN180-2-27-70-1b	Oxide Ol gabbro	45.4088	23.4112	10.04	0.100	72	0	249.6	757.9	21.8	91.1	bAm,gAm,Ch, Act	35	2	0
KN180-2-27-70-2				1.92	0.133	65	2								
KN180-2-27-70-2a				4.34	0.168		1								
KN180-2-27-86-1	Oxide Gabbro	45.4088	23.4112	1.04	0.084	78	3	217.1	443.6	26.8	91.4	Ab, Act, Ch, gAm	42	0	0
KN180-2-27-86-2a				0.92	0.113	70	4								
Jas111-11-1	Basalt	45.3226	23.5718	1.77	10.203	38	188	347.9	436.5	281.0	433.1		H	0	0
Jas111-11-1a				1.62	7.111	44	143								
Jas111-11-2a				2.38	10.942	38	150								
Jas111-17-1a	Basalt	45.3170	23.5734	2.17	15.655	45	236	424.2	616.7	234.9	387.2		H	0	0
Jas111-17-2				1.67	13.398	28	263								
Jas111-17-2a				2.01	13.990	49	227								
Jas111-17-3															
Jas112-91-1a	Harz. with veins	45.3446	23.4754	63.19	5.107	13	3					Srp,Tr,	78	1	1
Jas112-91-1b				71.27	6.221	11	3	136.1	256.6	1120.0	5311.0				
Jas112-91-2a				52.80	5.957	7	4								
Jas112-103	Harz. with veins	45.3401	23.4793	62.42	3.833	10	2					Srp,Tr	90	1	1
Jas112-103a				93.76	6.662		2								
Jas112-103b				92.10	5.249		2	118.3	214	1669.0	8925.0				
Jas112-107-1	Harz. with veins	45.3471	23.4739	26.54	7.056	30	9	355.2	506	3031.0	7471.0	Srp, Tr	92	1.5	1
Jas112-107-2a				48.87	6.396	33	4								
Jas112-107-2b				50.28	5.832		4								
Jas113-8	Harz. with veins	45.3583	23.4721	36.63	1.772	9	2					Srp,Tr	40	4	0.5
Jas113-8a				42.95	2.086	9	2	110.8	191.4	366.0	2078.0				
Jas113-12-1	Metaperidotite	45.3585	23.4730	16.70	0.273	13	1					Ab, Ch,Tc	95	0	0.5
Jas113-12-1a				14.93	0.364		1	25.22	94.56	1907.0	43110.0				
Jas113-12-2a				24.70	0.556	21	1								
Jas113-12-2b				17.32	0.465	17	1								
Jas113-12-2c				19.48	0.814		1								

Sample no.	Lithology	Lon °W	Lat °N	K (×10³ SI)	NRM (A/m)	MDF (mT)	Q	Hc (Oe)	Hcr (Oe)	Mr (μemu)	Ms (μemu)	Alteration minerals	Alt %	Deformation crystal/plastic	Deformation brittle
Jas 113-20	Ol gabbro myn.	45.3590	23.4745	7.49	0.681	25	3					Ab, Act, Ch	30	2.5	0
Jas 113-20a				9.28	0.760	33	3	221.6	547.5	368.5	1407.0				
Jas 113-20b				1.78	0.200		4								
Jas 113-59	Harzburgite myn.	45.3606	23.4788	154.00	18.107	13	4					Srp,Tr	86	3.5	1
Jas 113-59a				159.00	25.550	19	5	230.4	312.3	45340.0	111400.0				
Jas 113-59b				185.00	25.901	13	5								
Jas 113-59c															
Jas 113-65-1	Harzburgite	45.3603	23.4790	15.31	1.126	21	2	175.7	271.2	4830.0	15910.0			3	0.5
Jas 113-65-1a				18.80	1.858	20	3								
Jas 113-73-1	Harzburgite	45.3603	23.4790	0.28	0.010	17	1	153.3	358.1	11.4	56.3	Tc	100	4	1
Jas 113-73-2a				0.34	0.006	13	1								
Jas 113-73-2b				0.45	0.039		3								
Jas 114-2-1	Gabbro myn.	45.3571	23.4779	0.70	0.000	31	0					Ab, bAm,Ch,Qz	100	3.5	0
Jas 114-2-2a				0.54	0.001	29	0	76.77	336.3	2.0	20.3				
Jas 114-2-2b				0.84	0.001		0								
Jas 114-7-1	Harz. with veins	45.3570	23.4790	23.86	2.142		3					Srp,Tr	98	3	0
Jas 114-7-1a				31.62	3.602	12	4	444.5	603.6	2258.0	4575.0				
Jas 114-17-1	Dunite with veins	45.3597	23.4787	31.11	2.285	22	2					Srp	95	1	0
Jas 114-17-1a				38.89	1.686	22	1								
Jas 114-17-1b				54.12	9.310	23	6	208.7	293.4	7487.0	22960.0				
Jas 114-18-1	Harz. with vein			33.04	3.963		4	411.3	526.4	9010.0	18600.0	Srp,Tr	95	3	0
Jas 114-19-1a	Harz. with vein	45.3597	23.4786	74.42	7.070	15	3	299.5	458.7	1080.0	2832.0	Srp,Tr	95	2	0
Jas 114-19-2				67.25	5.688	15	3								
Jas 114-19-2a				75.34	6.715	15	3								
Jas 114-19-3															
Jas 114-20-1a	Harzburgite myn.	45.3600	23.4792	49.36	3.895	12	3	239.7	484.3	3052.0	8667.0	Srp,Am	100	4	2
Jas 114-20-1b				53.01	8.282	4	5								
Jas 116-3-1a	Metagabbro	45.2840	23.4602	1.56	0.157	23	3					Tc,Ch	100	3	3
Jas 116-3-2a				0.98	0.158	28	5								
Jas 116-3-2b				0.89	0.132	27	5	85.95	354.1	0.3	2.7				
Jas 116-6-1a	Metagabbro	45.2852	23.4608	0.28	0.022	14	3	32.07	214.7	3.5	128.6	Tc,Ch	100	4	5
Jas 116-13-3a	Metaperidotite	45.2863	23.4614	42.82	2.349	14	2	158.1	256.8	2618.0	10070.0	Tc,Ch	100	5	1
Jas 116-13-3b															
Jas 116-18-1a	Soapstone	45.2863	23.4615	7.67	1.007	24	4	198.3	418.2	725.0	3624.0	Tc,Ch	100	-	5
Jas 116-18-2															
Jas 116-40-1	Pl-Ol basalt	45.2794	23.4857	3.82	3.760		32						M	0	0
Jas 116-40-1a				3.87	4.183		35								
Jas 116-40-2a				10.29	5.184	7	16	75.47	115.3	681.1	2263.0				
Jas 116-40-2b				5.19	4.318	12	27								

Sample no.	Lithology	Lon °W	Lat °N	K (x 10³ SI)	NRM (A/m)	MDF (mT)	Q	Hc (Oe)	Hcr (Oe)	Mr (μemu)	Ms (μemu)	Alteration minerals	Alt %	Deformation crystal/plastic	brittle
Jas 117-9-1	Pl- Ol diabase	45.4166	23.3822	0.73	0.022		1					Ch	100	0	1
Jas 117-9-2a				0.90	0.031	32	1	101.4	254	8.3	48.4				
Jas 117-9-2b				0.85	0.030	35	1								
Jas 117-9-3															
Jas 117-32-1a	Ol gabbro	45.4115	23.3805	9.34	0.731	15	3	87.47	418.9	11.5	154.9	Srp,gAm,Tr	15	0	0
Jas 117-32-1b				7.58	0.634	15	3								
Jas 117-32-2				11.30	0.796	15	2								
Jas 117-32-2a				11.75	0.500		1								
Jas 117-37-1	Troctolite	45.4111	23.3803	0.14	0.004	17	1					Ab, Act, gAm, Tc	45	1	1
Jas 117-37-1a				0.23	0.005	20	1	93.63	527.1	16.5	237.3				
Jas 117-37-1b				0.09	0.001		0								
Jas 117-37-2a				0.10	0.001	20	0								
Jas 117-37-2b				0.14	0.003	22	1								
Jas 117-38-1	Ol gabbro	45.4109	23.3802	1.33	0.273	18	6					Ab, Srp,Act	75	1	1
Jas 117-38-2a				0.79	0.047	16	2	91.44	193.8	2.3	14.2				
Jas 117-38-2b				1.05	0.211	22	7								
Jas 117-40-1	Diabase	45.4104	23.3801	0.65	0.034	33	2					Ch	100	0	2
Jas 117-40-1a				0.68	0.035	35	2	123.7	292.6	5.5	28.0				
Jas 117-40-1b				0.69	0.037		2								
Jas 117-40-2a				0.77	0.064	33	3								
Jas 117-40-2b				0.74	0.064	35	3								
Jas 117-57-1a	Troctolite	45.4110	23.3891	7.57	0.435	13	2	212.5	317.2	576.6	1687.0	Ab, Cl, Srp	40	0	0
Jas 117-57-1b				8.79	0.571	14	2								
Jas 117-57-1c				7.80	0.500	15	2								
Jas 117-57-2				7.04	0.389	13	2								
Jas 117-57-2a				7.31	0.391	14	2								
Jas 117-57-2b				7.41	0.431		2								

Pl, plagiocalse, Ol, olivine, Myn., mylonite,Harz,, harzburgite

k, magnetic susceptibility. NRM, natural remanent magnetization, Q, Koenigsberger Ratio, MDF, median destructive field, Hc, coercive force, Hcr, remanent coercive force

Mr, saturation remanent magnetization, Ms, saturation magnetization, Alt, Alteration

Alteration minerals: Ab, albite, bAm, brown amphibole, gAm, green amphibol, Act, actinolite, Cl, clay, Ch, chlorite, Pr, prenite, Qz, quartz, Srp, serpentinite, Tc, talc, Tr, tremolite

Basalts alteration is classified as H(high), M(medium) and L(low). More details are given in Table 3-4

Deformation is catagorized as crystal-plastic or brittle. Each fabric is graded on a scale of 0 to 5, with 0 reflecting no deformation. A value of 5 for crystal-plastic is defined as an ultramylonite and a 5 for brittle deformation describes a rock with > 70% fine-grained matrix.

110

Table 3-2 Average rock magnetic values

Sample no.	Lithology	K (x 10³ SI)	NRM (A/m)	MDF (mT)	Q
KN180-2-2-1	Basalt	2.36	13.002	39	178
KN180-2-2-3	Basalt	2.02	7.795	42	127
KN180-2-9-30	Pl-Ol basalt	12.56	5.510	21	13
KN180-2-9-36	Pl-Ol basalt	5.07	10.295	28	66
KN180-2-11-4	Pl-Ol basalt	1.92	8.523	56	139
KN180-2-18-15	Pl-Ol basalt	1.38	5.020	51	118
KN180-2-22-1	Pl-Ol basalt	4.36	5.270	21	40
KN180-2-22-2a	Basalt	18.74	9.493	18	19
Jas 111-11	Basalt	1.93	9.419	40	160
Jas 111-17	Basalt	1.95	14.348	41	242
Jas 116-40	Pl-Ol basalt	5.79	4.361	10	28
KN180-2-13-1	Diabase	1.00	0.015	21	1
KN180-2-13-49	Pl diabase	1.18	0.210	34	6
Jas 117-9	Pl- Ol diabase	0.83	0.028	34	1
Jas 117-40	Diabase	0.71	0.047	34	2
KN180-2-14-18	Ol gabbro	1.44	0.665	28	15
Jas 113-20	Ol gabbro myn.	6.18	0.547	29	3
Jas 117-32	Ol gabbro	9.99	0.665	15	2
Jas 117-38	Ol gabbro	1.05	0.177	19	5
KN180-2-21-12	Troctolite	72.40	7.217	12	3
KN180-2-21-14	Troctolite	57.35	5.594	18	3
KN180-2-25-1	Troctolite	7.54	0.576	7	2
Jas 117-37	Troctolite	0.14	0.003	20	1
Jas 117-57	Troctolite	7.65	0.453	14	2
KN180-2-11-1	Gabbro myn.	103.64	2.555	8	1
Jas 114-2	Gabbro myn.	0.69	0.001	30	0
KN180-2-27-70	Oxide gabbro	5.43	0.134	69	1
KN180-2-27-86	Oxide Gabbro	0.98	0.098	74	3
Jas 116-3	Metagabbro	1.15	0.149	26	4
Jas 116-6	Metagabbro	0.28	0.022	14	3
KN180-2-14-45	Harzburgite	25.65	2.431	24	4
KN180-2-17-3	Harzburgite	39.95	3.004	24	2
Jas 113-65	Harzburgite	17.06	1.492	21	3
Jas 113-73	Harzburgite	0.36	0.019	15	2
Jas 113-59	Harzburgite myn.	166.00	23.186	15	5
Jas114-20	Harzburgite myn.	51.19	6.089	8	4
Jas 112-91	Harz. with veins	62.42	5.762	12	3
Jas 112-103	Harz. with veins	82.76	5.248	9	2
Jas 112-107	Harz. with veins	41.90	6.428	32	6
Jas 113-8	Harz. with veins	39.79	1.929	9	2
Jas 114-7	Harz. with veins	27.74	2.872	12	3
Jas 114-17	Dunite with veins	41.37	4.427	22	3
Jas 114-18	Harz. with vein	33.04	3.963	-	4
Jas 114-19	Harz. with vein	72.34	6.491	15	3
Jas 113-12	Metaperidotite	18.63	0.494	17	1
Jas 116-13	Metaperidotite	42.82	2.349	14	2
Jas 116-18	Metaperidotite	7.67	1.007	24	4

Table 3-3 Average paleomagnetic direction from partially-oriented samples

Sample no.	Lithology	n	D (°)	I (°)	α95(°)	N/R
Jas 113-59	Harzburgite	3	300	56	10	N
Jas 113-65	Harzburgite	2	72	10	26	N
Jas 113-73	Harzburgite	2	67	53	31	N
Jas 114-2	Gabbro	3	302	-7	9	
Jas 114-7	Harzburgite	2	76	12	36	N
Jas 114-17	Dunite with veins	3	281	53	12	N
Jas 114-19	Harzburgite	4	293	-69	15	R
Jas 114-20	Harzburgite	2	20	7	6	
Jas 116-3	Metagabbro	2	325	3	29	
Jas 116-6	Metagabbro	1	108	-41	-	R
Jas 116-13	Harzburgite	1	61	33	-	N
Jas 116-18	Metaperidotite	1	253	-29	-	R
Jas 116-40	Basalt	4	222	-67	15	R
Jas 117-9	Diabase	2	85	-46	7	R
Jas 117-32	Olivine gabbro	2	246	-15	22	R
Jas 117-37	Troctolite	3	11	-48	14	R
Jas 117-38	Olivine gabbro	1	140	-35	-	R
Jas 117-40	Diabase	2	2	59	48	N
Jas 117-57	Troctolite	5	39	45	3	N

n is the number of samples averaged for the final declination (D) and inclination (I) values

Average vaules calculated using Fisher statistics [*Fisher*, 1953] with 95% (α95) confidence limit

N, normal polarity, R, reversed polarity.

Table 3-4 Basalt Alteration

| Sample | Alteration Level | | Basalt Group | Palagonite crust thickness (cm) | Palagonitization rim thickness (cm) | Manganese crust thickness (cm) |
	T.S.	H.S.				
KN180-2-2-1		L	1	1.5	1	0.1
KN180-2-2-3		L	1	1.5	-	-
KN180-2-9-30	L	-	2	not available	not available	not available
KN180-2-9-36		M	1	removed	1.5	0.1
KN180-2-11-4	M	M	1	0.5	0.5	0.1
KN180-2-18-15	H	H	1	1.5	2.5	-
KN180-2-22-1		M	1	removed	1.5	0.2
KN180-2-22-2a	M	L	2	0.2	0.5	0.1
Jas 111-11		H	1	1.5	pervasive	0.1
Jas 111-17	M	H	1	1	2.5	1
Jas 116-40	M	L	2	0.2	1.5	1

H(high), M(medium) and L(low)

T.S.- thin section, H. S. - hand sample

Table 3-5 Basalt Groups

Basalt Group	K (x10³)	NRM(A/m)	MDF (mT)	Q
1	2 (±1)	10 (±4)	42 (±10)	152 (±57)
2	11 (±7)	6 (±2)	17 (± 5)	24 (±11)
BR	2 (±0.3)	12(±3)	40 (±8)	181 (±43)
HWD	8 (±7)	7 (±3)	28 (±19)	53 (±49)

K, susceptibility, NRM, natural remanent magnetization, MDF median destructive field, Q, Koenigsberger ratio.

Values are arithmetic mean with one standard deviation shown in parenthesis. BR- basalt ridge, HWD- hanging wall debris
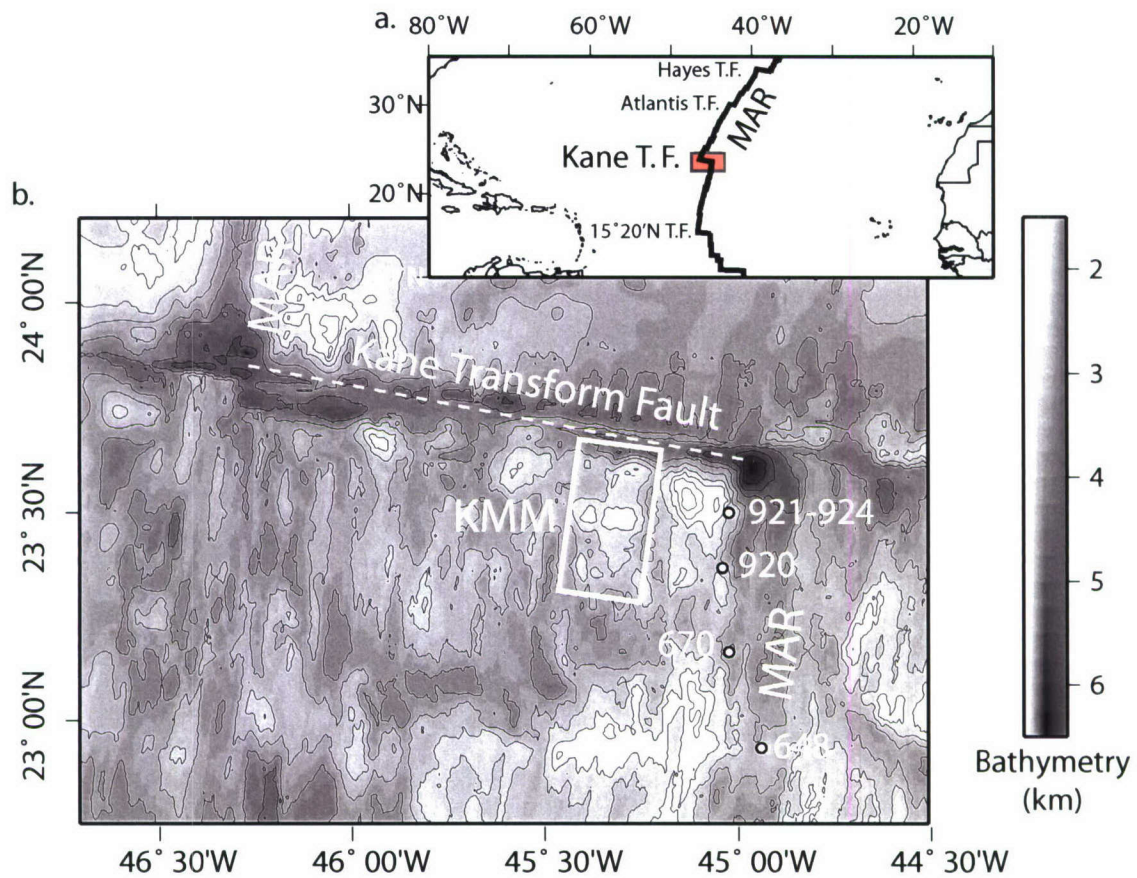
Figure 3-1. a. Location map of the Kane Transform Fault on the Mid-Atlantic Ridge (MAR). **b**. Bathymetric map of the Kane region. Kane Megamullion (KMM) is a massif located to the south of the transform fault, ~ 40 km to the west of the MAR (outlined by the white rectangle). Locations of Ocean Drilling Program (ODP) sites 648B, 670, 920-924 east and south (MARK area) of Kane Megamullion are shown.
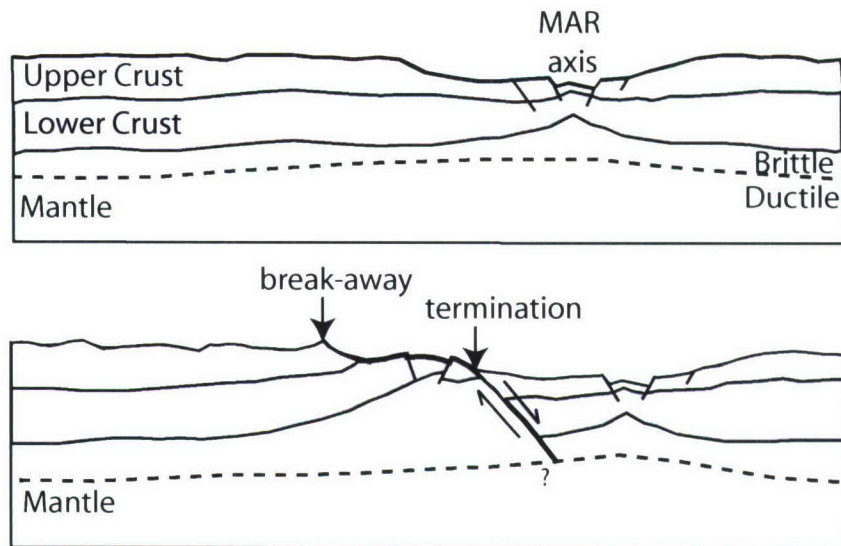
Figure 3-2. Schematic of Kane Megamullion **a**. Normal faults form near the MAR axis. **b**. Large scale detachment fault exhumes lower crust and upper mantle. The detachment fault initiates at the break-away and the fault surface dips below the surface at the termination.
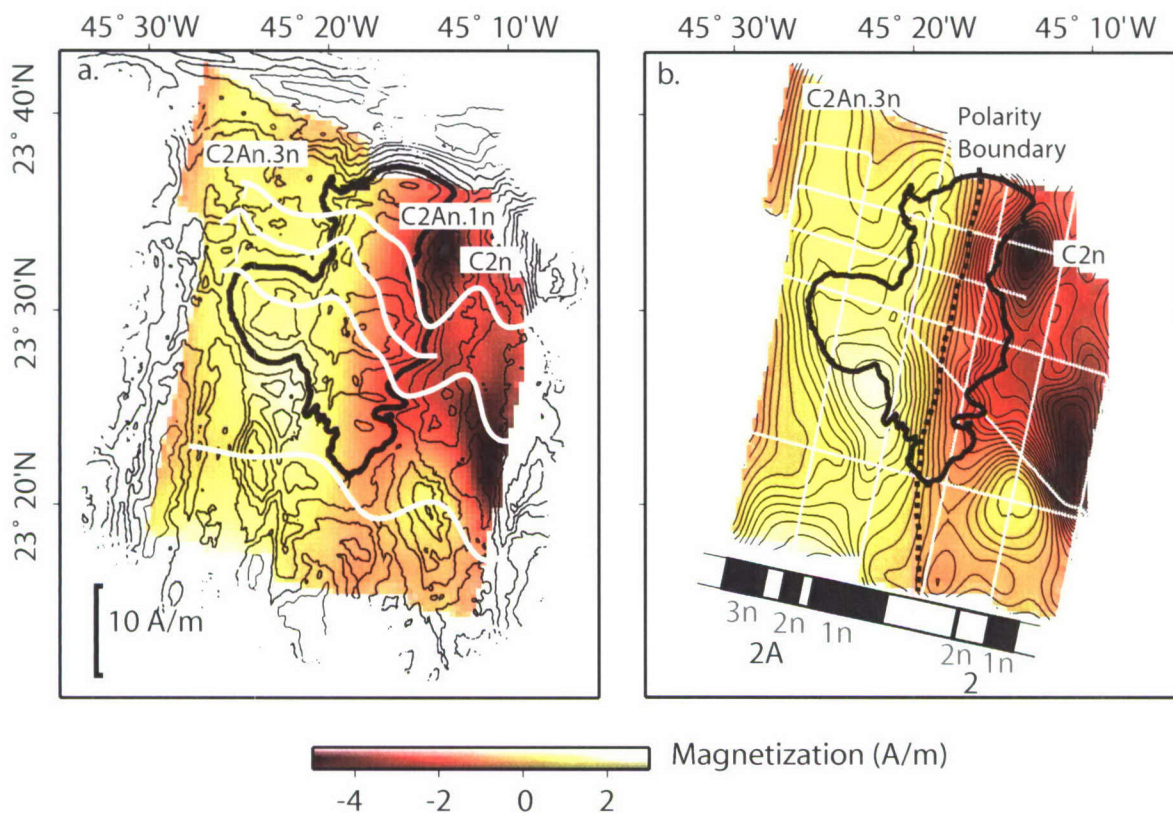
Figure 3-3. a. Inversion results of the sea-surface magnetic anomaly, assuming a constant source layer thickness of 1 km. The contours represent bathymetry and KMM is outlined by the bold black contour. The ridge-parallel magnetic polarity boundary between Chrons 2r and 2An intersects the eastern side of KMM [*Williams et al.*, in prep]. **b**. Contoured inversion results with 0.25 A/m contour interval highlight the linear polarity boundary, defined by the maximum gradient in the grid (dashed black line). Ship tracklines are shown by the white dots. Chrons 2 and 2A are comprised or several normal (black) and reversed (normal) subchrons.
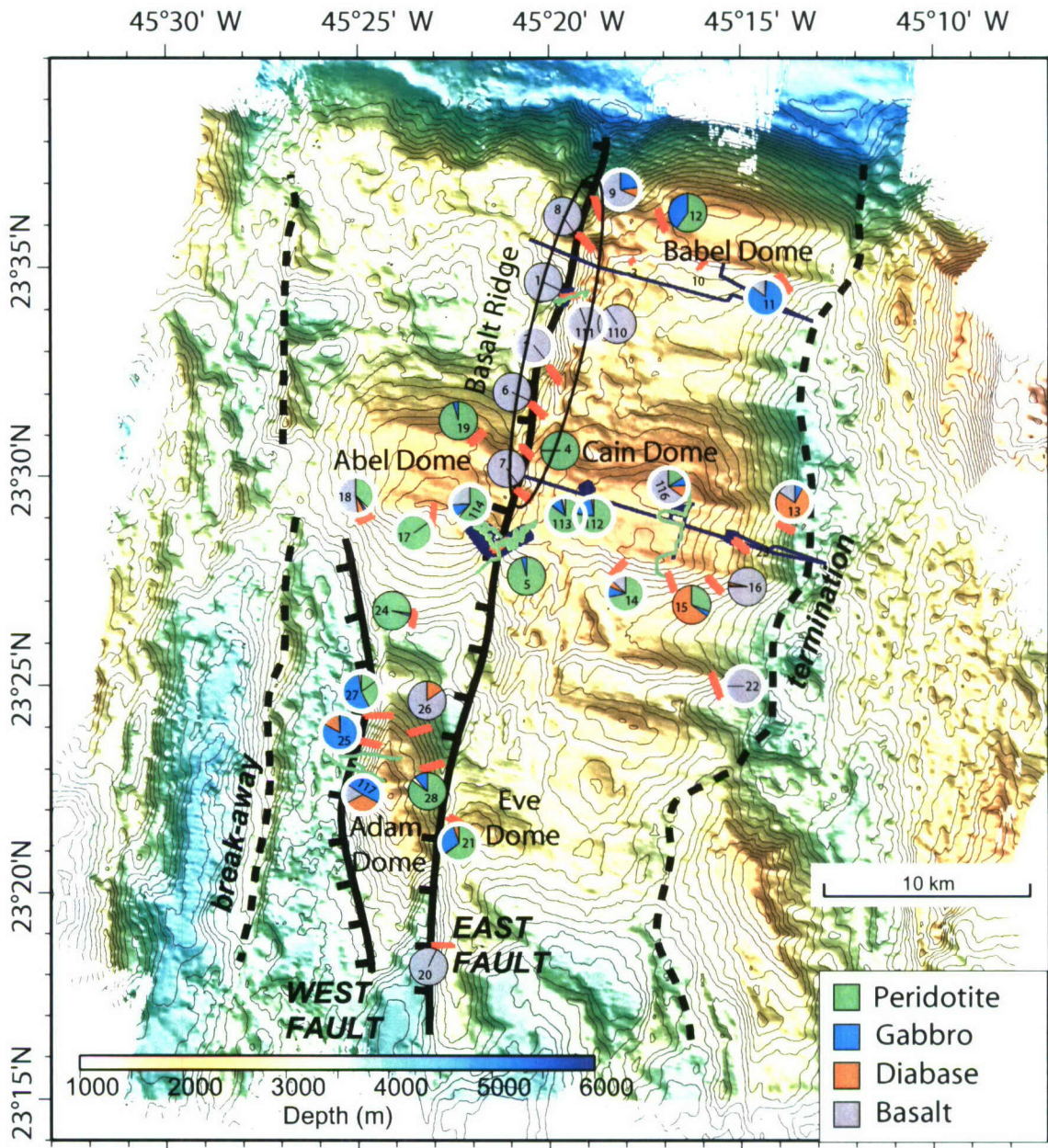
Figure 3-4. Bathymetric color grid of KMM. The detachment fault surface extends from the break-away to the termination. KMM has a smooth, domed appearance with spreading-parallel corrugations. Dredge locations are shown in red, ABE dive profiles in blue and Jason dive locations in green. Numbered pie charts of the rock sample lithologies from each dredge and Jason dive are included. The 48 samples analyzed in this paper were taken from the dredges and dive pie charts outlined in white. Domes and the lineated basalt ridge at the northern end of East Fault are labeled.
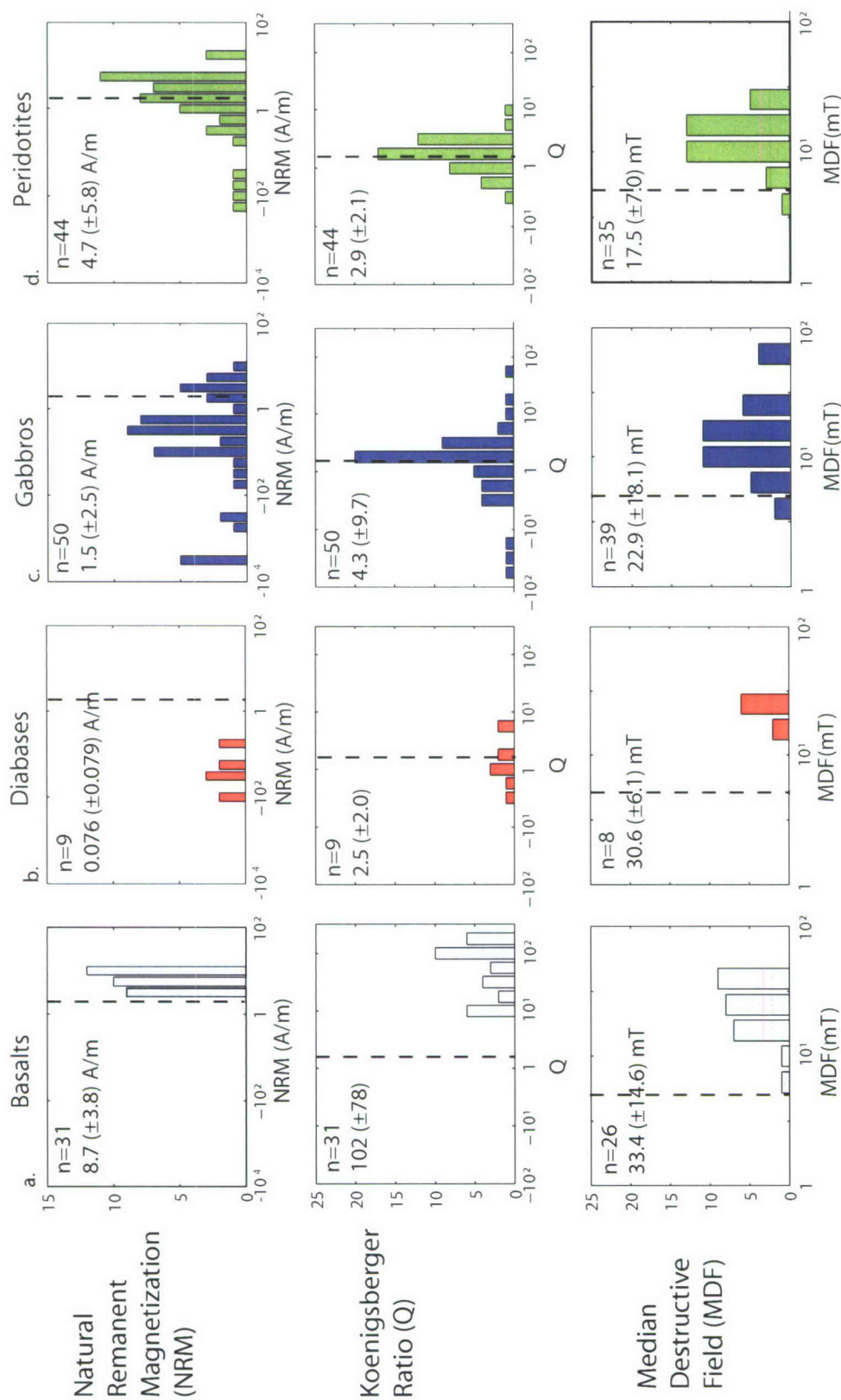
Figure 3-5 - Natural Remanent Magnetization (NRM), Koenigsberger Ratio (Q) and Median Destructive Field (MDF) results for each of the four lithologics. n is the number of samples, the arithmetic mean is shown with one standard deviation in parentheses. The dashed black lines represent the criteria above which a sample may contribute to the magnetic source layer based on *Swift and Johnson* [1984].
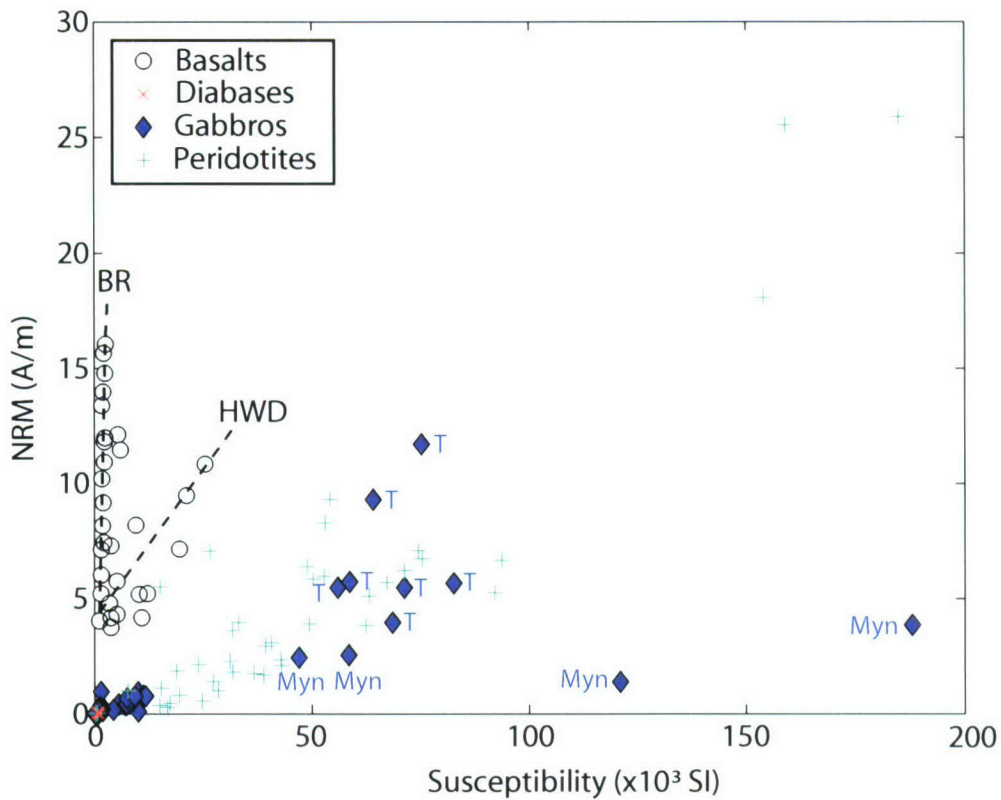
Figure 3-6. NRM versus Susceptibility (k). Basalts, gabbros and peridotites have comparable NRM values, but basalts have much lower susceptibilities in general, as shown by the separate trends in the figure. HWD- hanging wall debris, BR- basalt ridge. Different gabbro types are identified; T- troctolite, Myn- mylonite
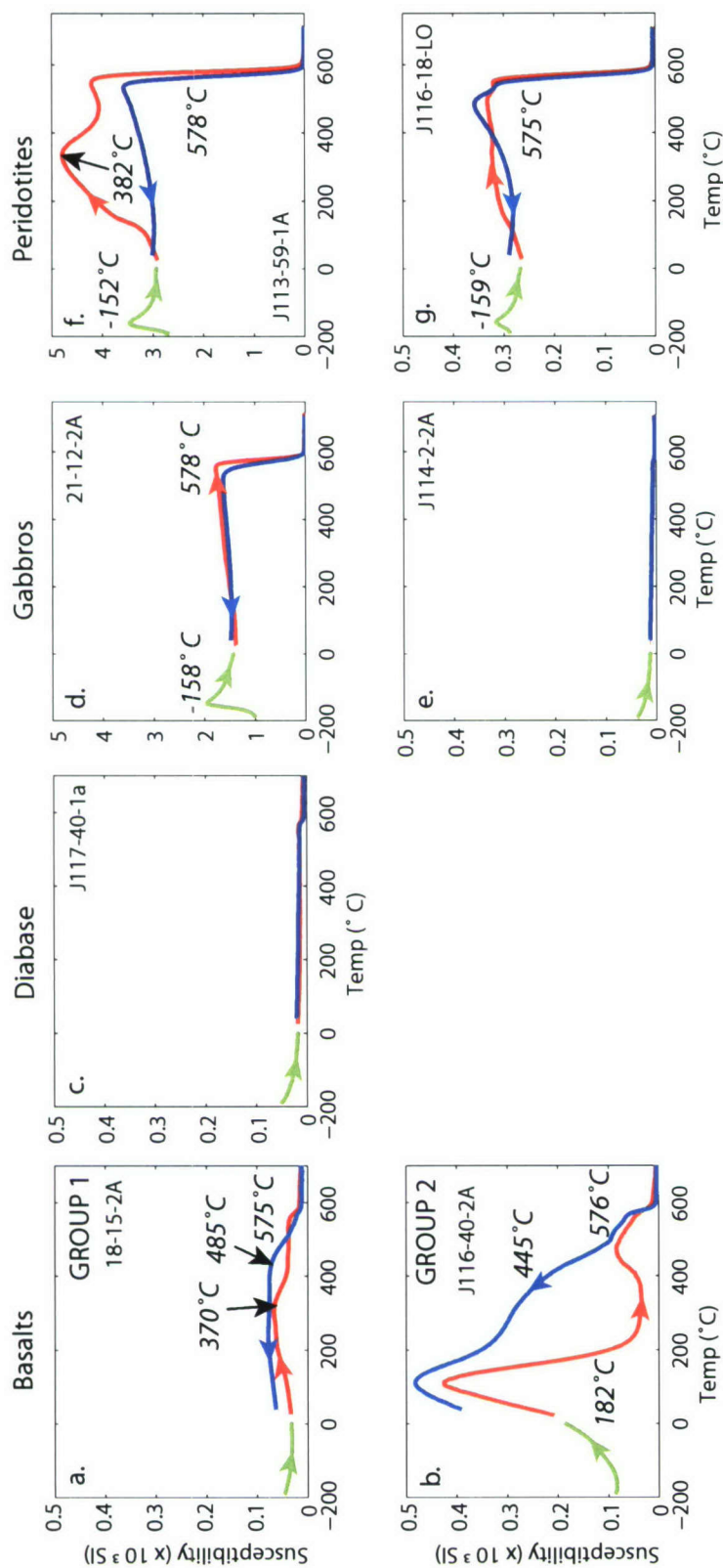
Figure 3-7 - Susceptibility curves; curves shown are low temperature heating (green line), high temperature heating (red line) and high temperature cooling curves (blue lines). **a.** Basalts show inversion of titanomaghemite to magnetite and ilmenite for heated samples. The basalts are divided into two groups; Group 1 has lower k. **b.** Group 2 has higher k **c.** Diabase have low k in general. Gabbros range from; **d.** high k, with distinct Verwey transition (Tc ~ 150 °C) and steep gradient at Tc of magnetite (580 °C) to **e.** low k samples with no evidence of magnetite. **f.** All the peridotites show evidence of magnetite as the main magnetic carrier but fall into two groups with curves that have a high k and a second peak at ~440 °C and **g.** curves that have only a steep gradient at 580 °C.
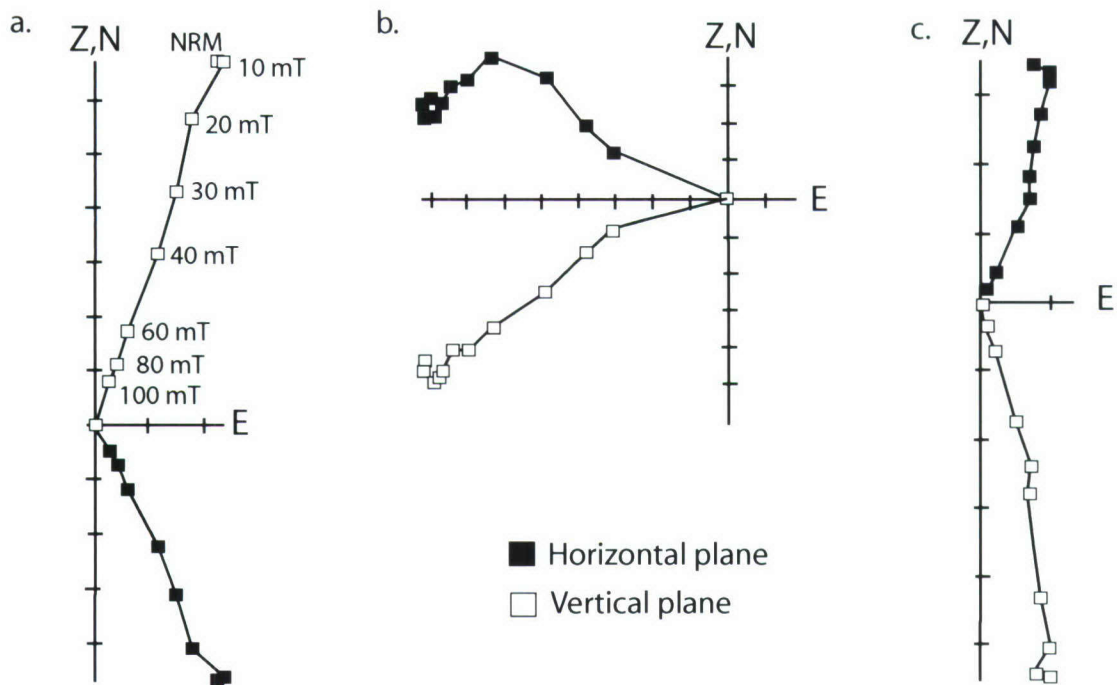
119

Figure 3-8. Vector plots of demagnetization curves. **a.** Univectoral basalt example (not oriented). Soft drilling component is removed by ~ 15 mT. **b.** Two component gabbro example. Approximately 20 % of the gabbro samples have more than one remanent component. **c.** Peridotite univectoral example. Only one peridotite has more than one magnetic component.
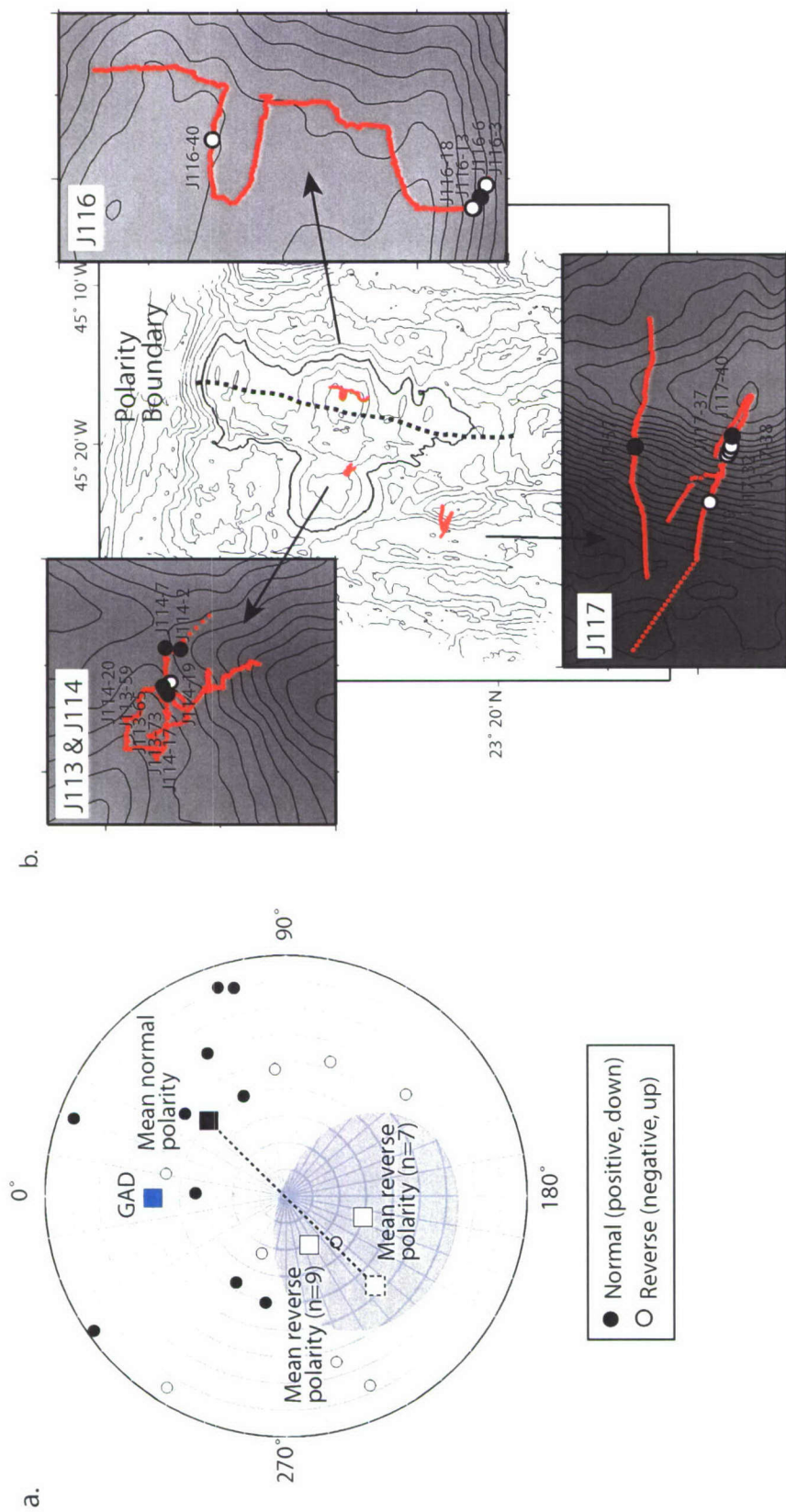
Figure 3-9.a. Equal area projection of visually-oriented samples collected by the ROV Jason. The present day geocentric axial dipole (GAD- solid blue square) at 0° declination, 40° inclination. Solid circles represent the normal direction, open circles are reversed direction. The black solid square represents the average direction for the normal-polarity sites, and its antipode is located 180° from this point (dashed black line). The average directions for the reversed-polarity sites are shown by the white squares, surrounded by the 95 % confidence ellipse in grey (45°). **b.** Location of the visually oriented samples collected on Jason Dives 113, 114, 116 and 117. Again, solid circles represent the normal direction, open circles are reversed direction. Black dashed line is the polarity boundary defined by the maximum gradient in the inversion grid (Fig. 3-3).
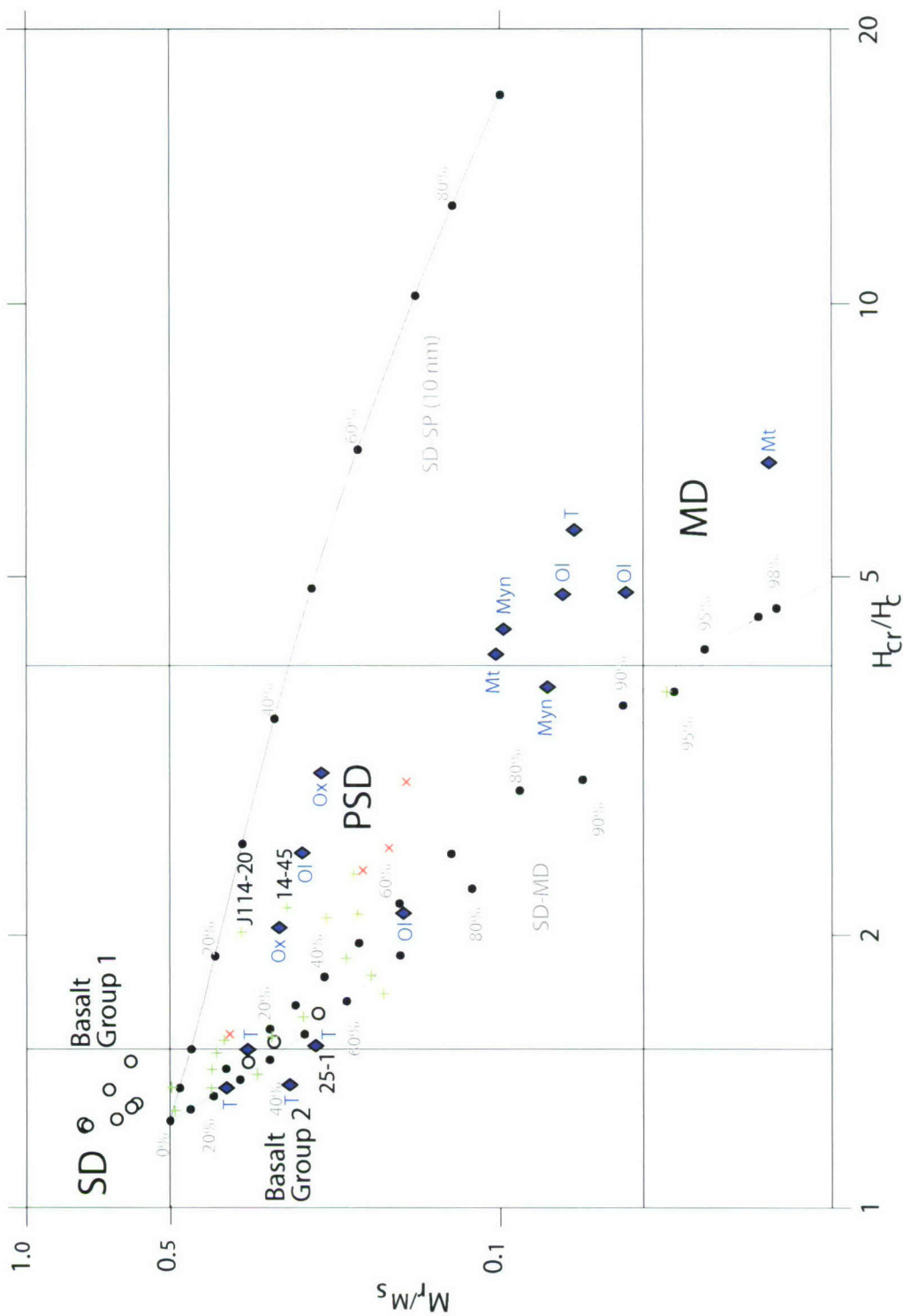
Figure 3-10. Day plot showing domain state and effective magnetic grain size. The two basalt groups plot in separate areas, Group 1 are single domain (SD) and Group 2 are pseudo-single domain (PSD). All diabases plot in the PSD, while the gabbros range from multi-domain (MD) to PSD. The peridotites all lie in the small-medium PSD region. Grey lines show the mixing curves of *Dunlop et al.* [2002a] and the percentage values show the amount of soft component (MD and superparamagnetic curves of *Dunlop et al.* [2002a] and the percentage values show the amount of soft component (MD and superparamagnetic (SP)). Different gabbro types are identified; T-troctolite, Ox-oxide gabbro, Ol-olivine gabbro, Myn-mylonite, Mt-metagabbro

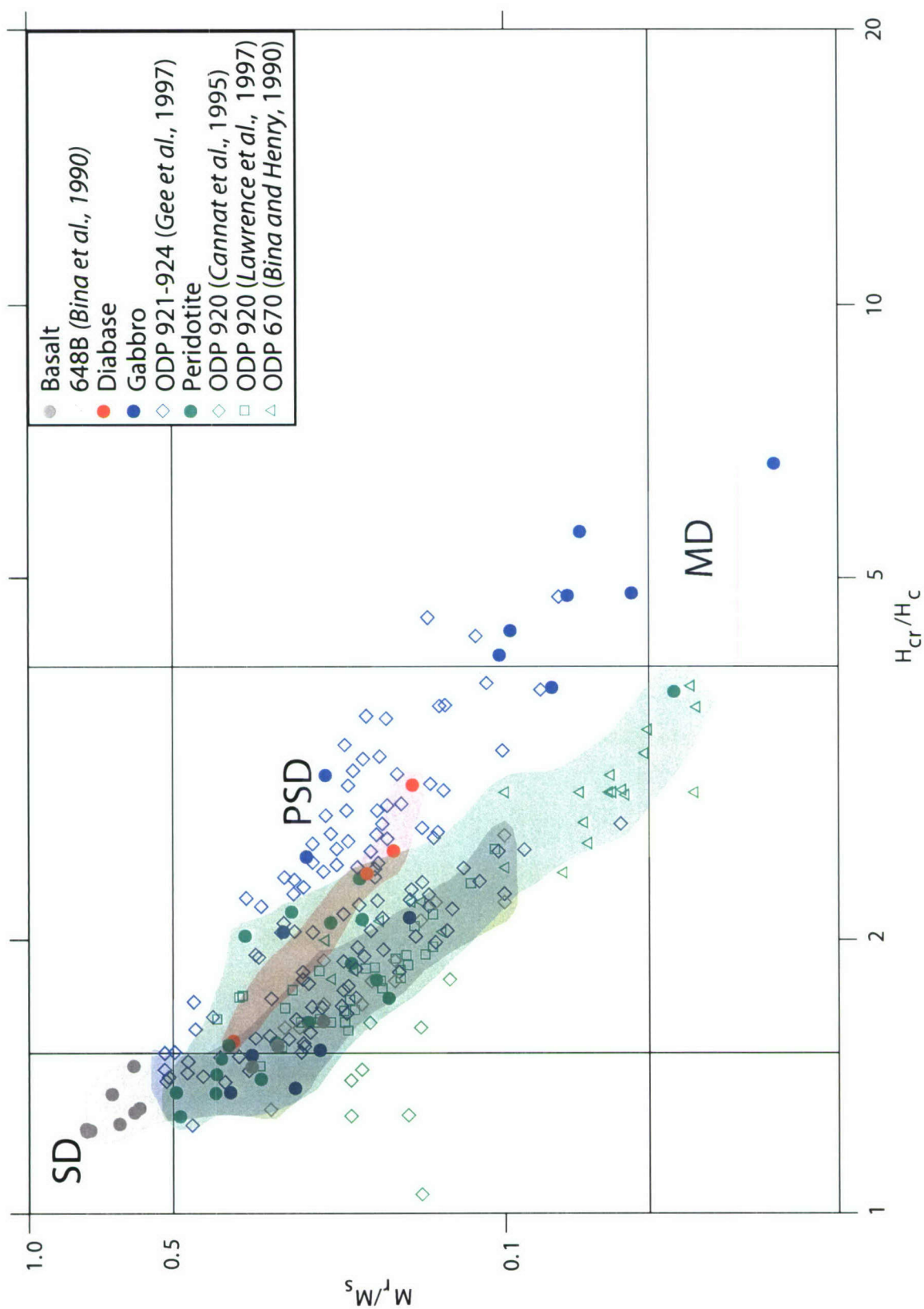**Figure 3-11**- Day plot similar to Figure 3-10 but also includes results from drill cores in the surrounding region. The range of values for each lithology has been defined by the different colored regions.

Figure 3-12. First Order Reversal Curve (FORC) diagram examples of ; **a**. Basalt true SD with single peak, enclosed contours. Full width half maximum (FWHM) parameter is calculated from a profile through the peak of the FORC diagram **b.** Harzburgite PSD example with the peak closer to the Hc, represents lower coercitivies than Fig. 3-12a. **c.** PSD and SP peaks in harzburgite sample. SP is close to the Hu axis. **d**. Gabbro MD sample. The peak extends out to ~ 40 mT and is symmetric about the Hu=0 axis. **e.** Harzburgite sample J114-20 shows two major magnetic components in the sample, a high coercivity SD peak, and a much lower coercivity SP peak.
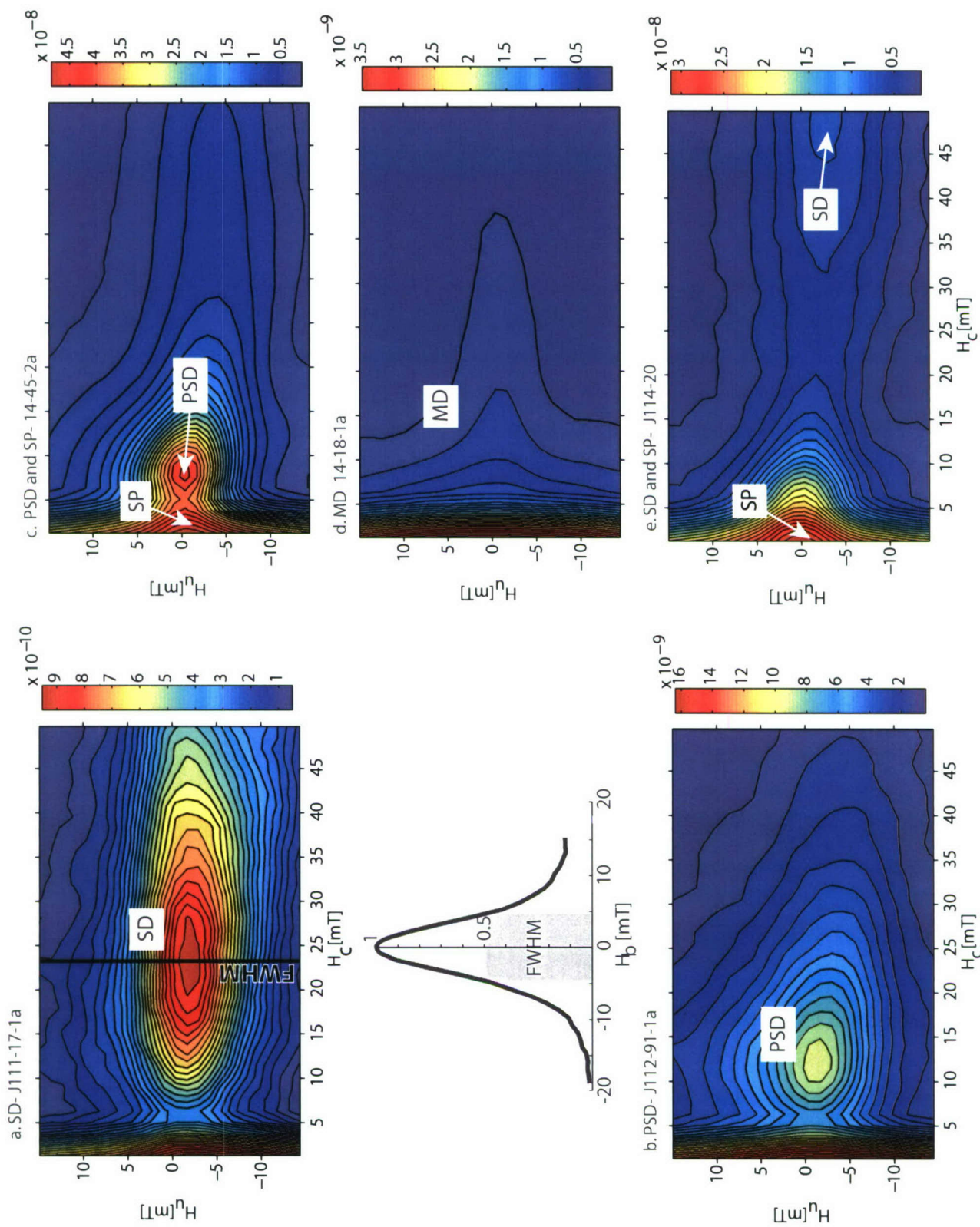
Figure 3-12
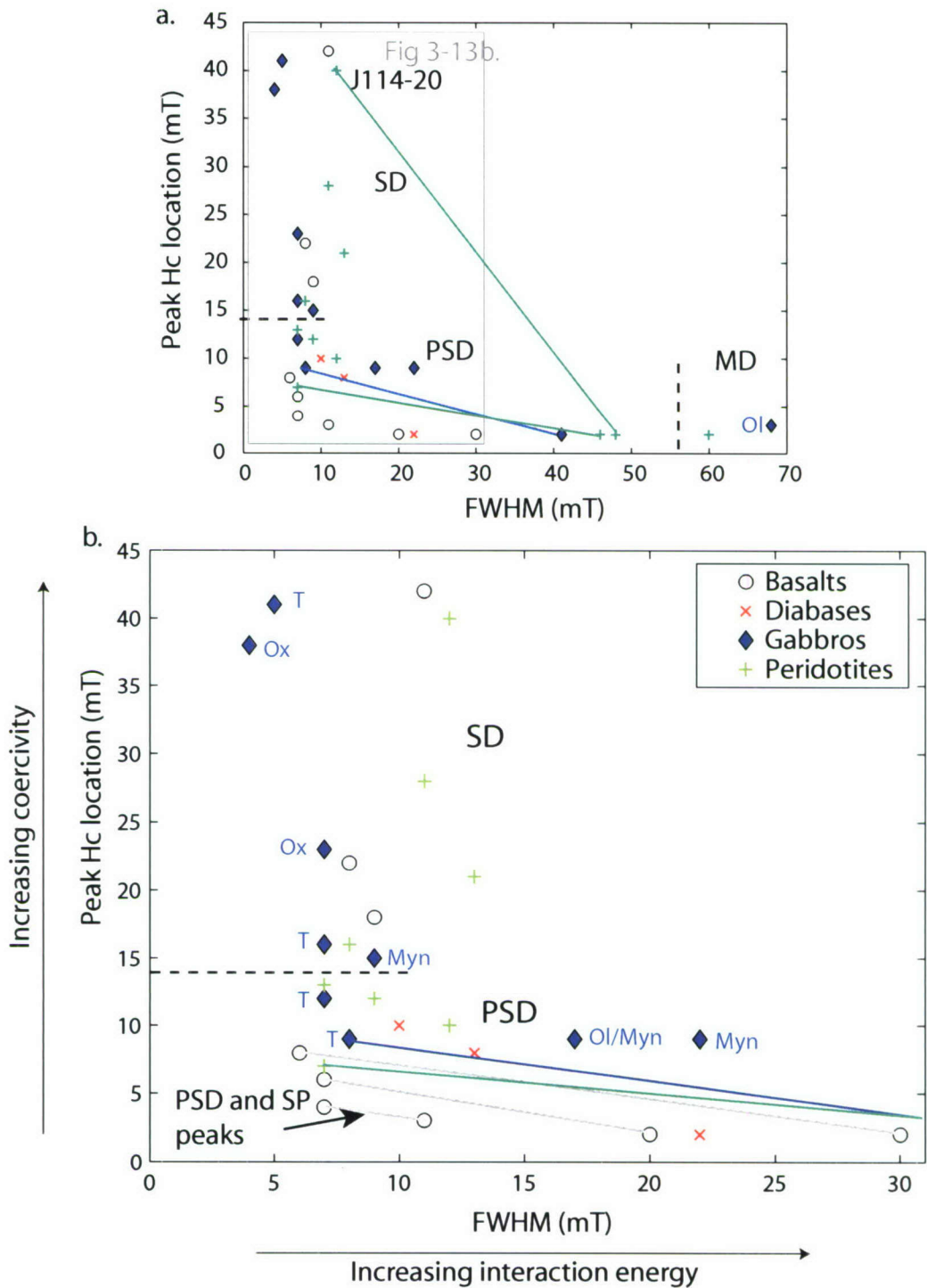
Figure 3-13 a. FORC parameter full width half maximum (FWHM) versus peak Hc location. a. The figure can be broken down into regions which represent SD, PSD and MD domains [*Day et al.*, 1977b]. **b.** Zoom in of Fig. 3-13a. The two basalt groups plot in different regions, with higher peak Hc location values for Group 1. Several samples have multiple peaks and are connected by coloured lines.

a. J111-17 Group 1 basalt
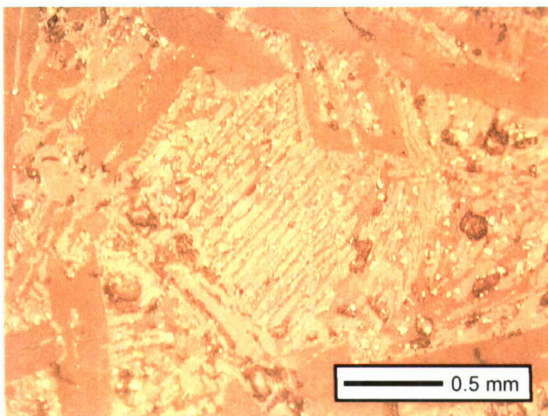
b. 22-2A Group 2 skeletal basalt
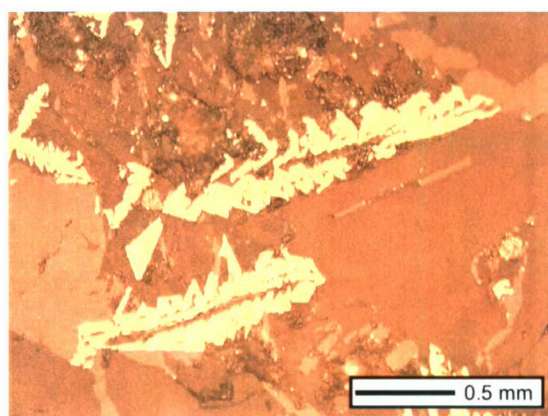
c. 21-12 Troctolite zoned oxide
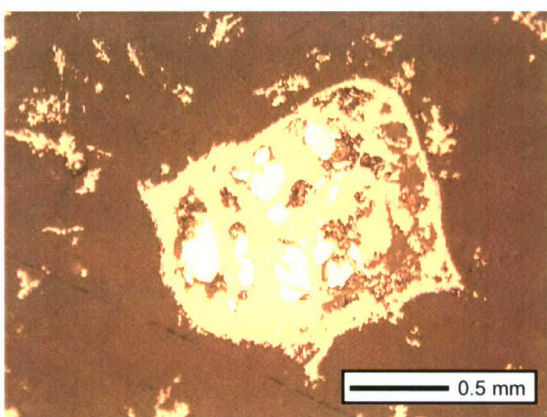
d. 21-14 Troctolite zoned oxide
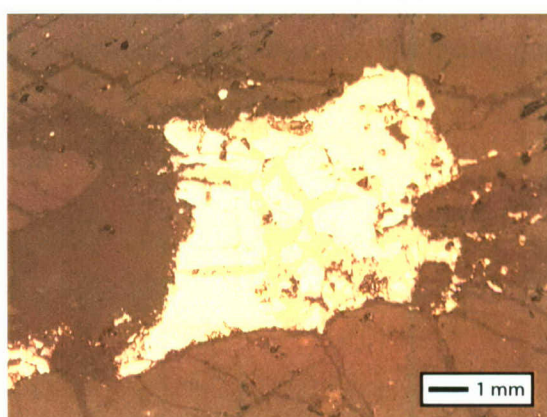
e. 14-45 Harzburgite serpentinite veins
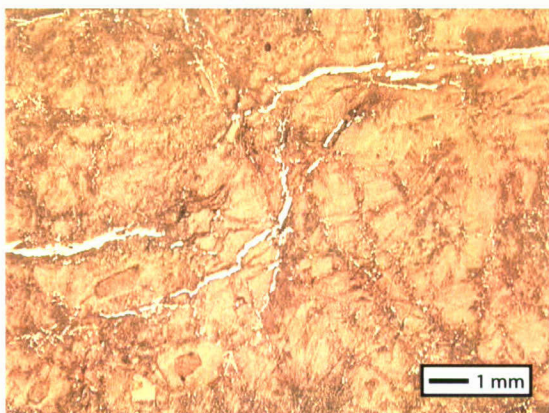
f. 14-45 Serpentinite veins transmitted light

Relict Ol

Figure 3-14

128
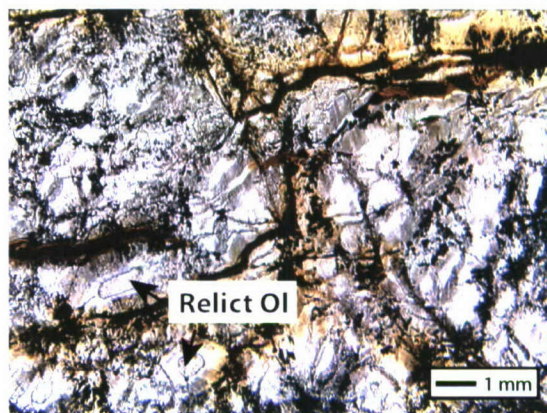
g. 11-1 Gabbro mylonite scattered oxides
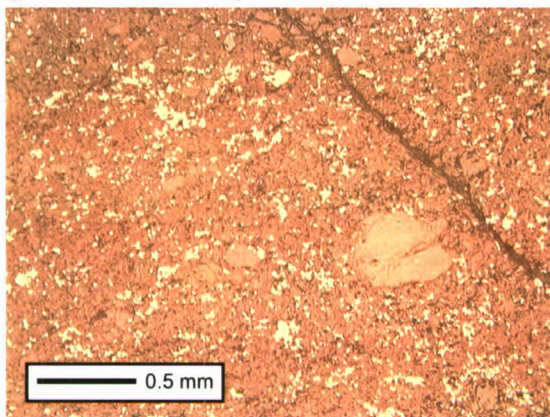
h. J114-20 Harzburgite oxide filled vein
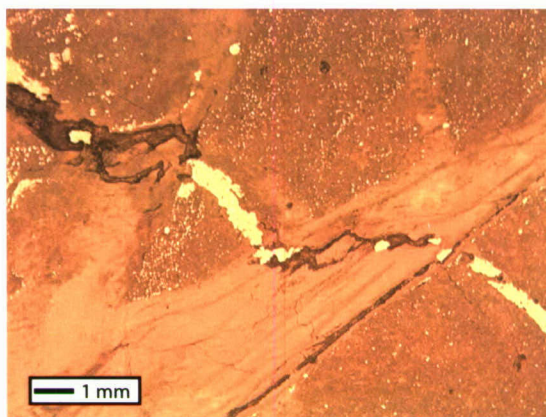
i. J116-18 Soapstone magnetite needles
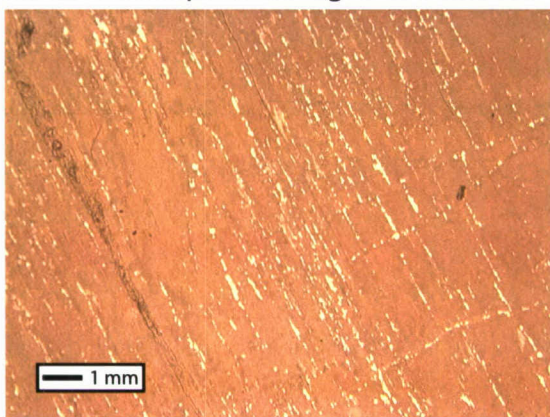
j. J113-12 Metaperidotite lamallae
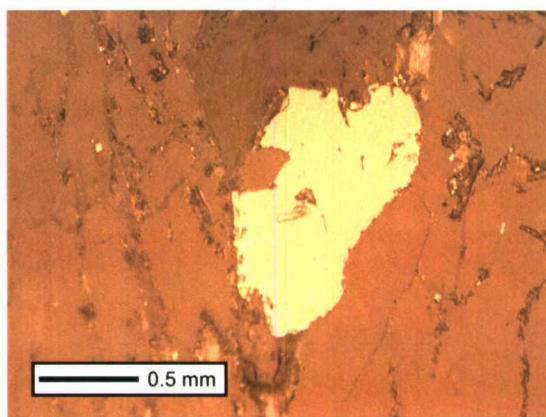
Figure 3-14. Reflected light microscope images of Fe-Ti oxides. **a**. Small skeletal oxides in a Group 1 basalt, **b**. large skeletal (quenched) oxides in a Group 2 basalt. **c**. and **d**. Primary oxides in gabbros that have been zoned due to alteration processes. This reduces the effective magnetic grain size of the oxides, essentially breaking down one oxide into multiple smaller oxides. **e**. Magnetite coalesces in multiple magnetite veins within the serpentinite mesh-texture. **f**. transmitted light image of same veins as Fig. 3-14e. Serpentinite mesh rims surround relict olivine. **g**. Scattered oxides in a gabbro mylonite. **h**. Tremolite vein filled with oxides. **i**. Needle-shaped oxides in the cleavage plans of a cpx grain. **j**. Hematite lamellae within a magnetite grain.
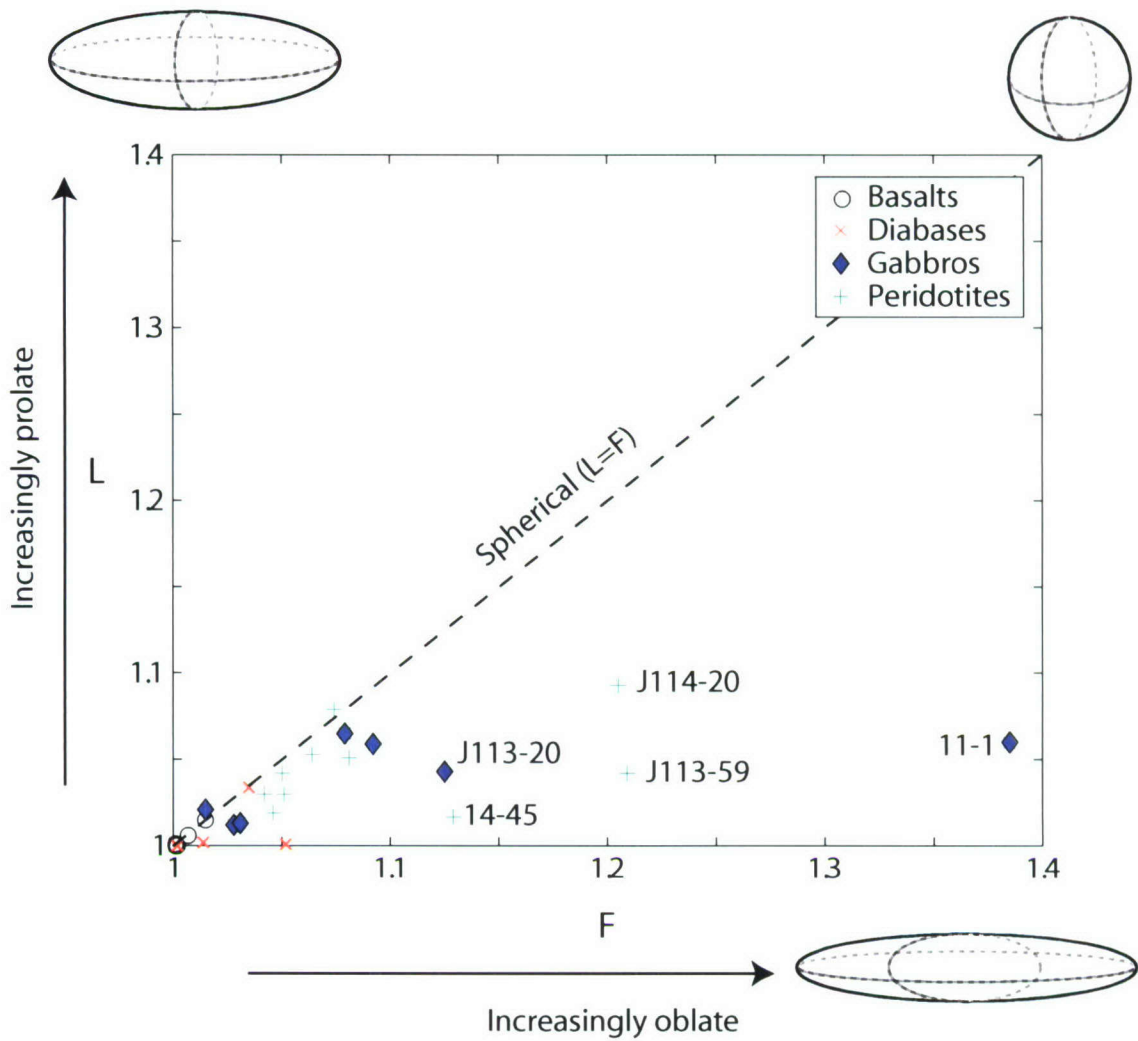
Figure 3-15. Anisotropy of magnetic susceptibility (AMS). F represents planar degree of anisotropy and L is linear degree of anisotropy. When L=F, the susceptibility is spherical. Microscopic observations show that samples 11-1, J114-20, J113-59 and J113-20 are highly deformed mylonites (crystal-plastic deformation) with increasing oblate properties.
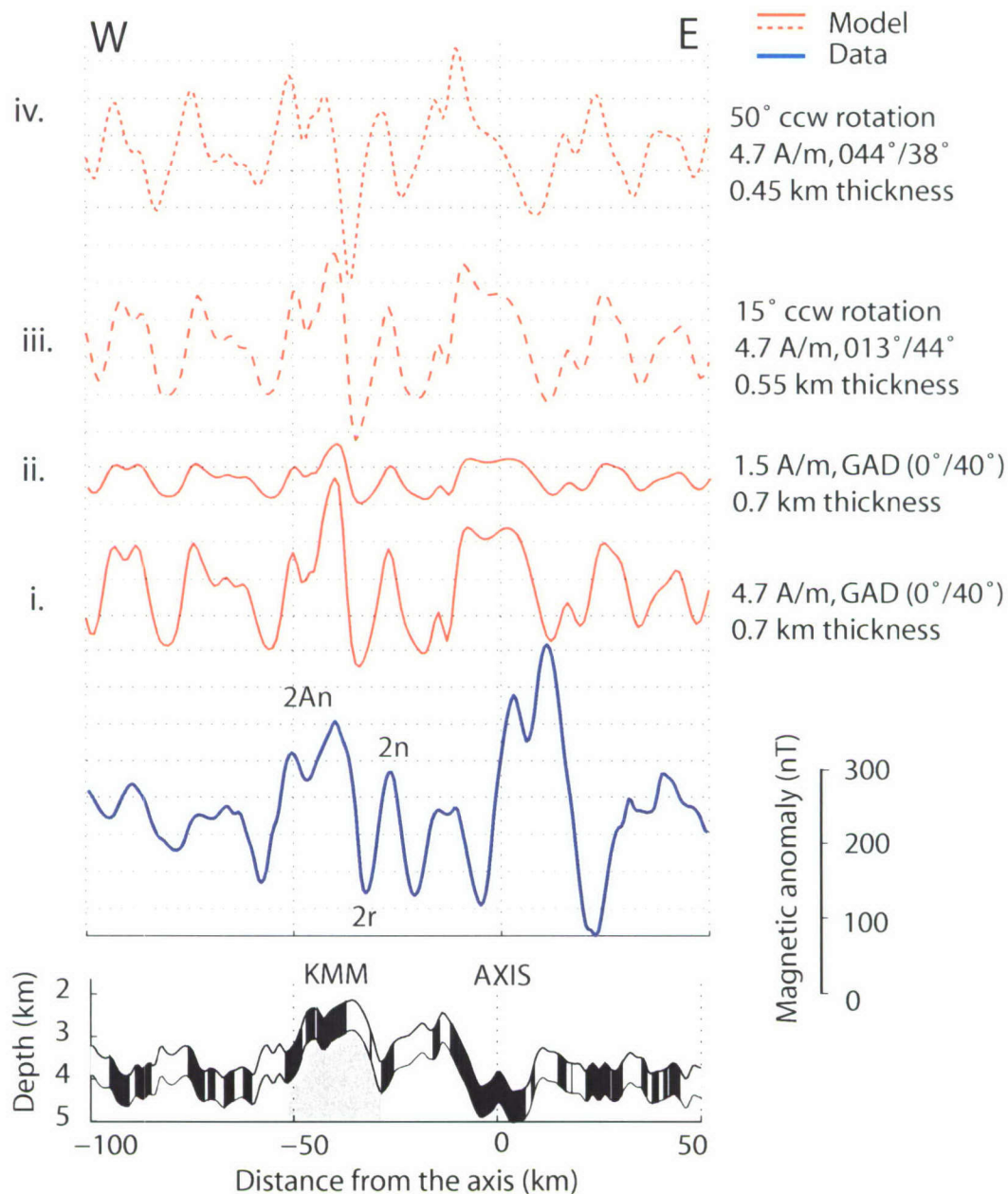
Figure 3-16. Modeling the magnetic source layer using the software package MODMAG [*Mendel et al.*, 2005]. Profile crosses central region of Kane Megamullion. Bottom panel is bathymetry (KMM outlined in grey) with source layer magnetic polarities shown by normal (black) and reversed (white) stripes, based on [*Cande and Kent*, 1992]. A sea-surface observed magnetic anomaly (blue line) has Chrons 2n, 2r and 2An identified. Model spreading rate is assumed to be 23 km/Myrs, with 60% asymmetric spreading to the west. i. Crustal magnetization of 4.7 A/m (equivalent to the average peridotite NRM) and GAD magnetization direction. ii. 1.5 A/m (equivalent to the average gabbro NRM) and GAD magnetization direction. iii. 4.7 A/m and 15° counter-clockwise rotation about a ridge with strike 20° iv. 4.7 A/m and 50° counter clockwise rotation about a ridge with strike 20°.

131
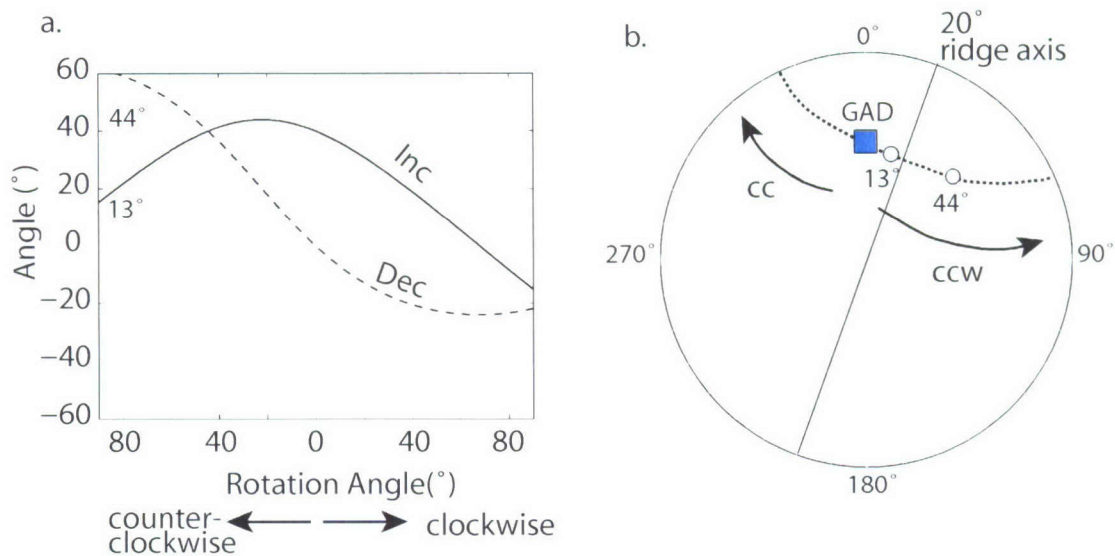
Figure 3-17. a. Changes in magnetization direction due to rotations are calculated based on the approach of *Verosub and Moores* [1981] for a ridge with a strike of 20°. Figure shows inclination and declination values for 90° of clockwise and counter clockwise rotation. The range in declination values for the sample mean normal and reversed polarity directions is shown by the grey region and corresponds to counter clockwise rotations between 15° to 50°. **c.** Equal area projection showing clockwise and counter clockwise rotation, GAD (inclination 40° and declination 0°) and sample mean polarity declinations.

CHAPTER 4

Nature of a magnetic polarity boundary in the lower crust and upper mantle at Kane Megamullion

Abstract

Lower crustal (gabbros) and upper mantle (peridotites) rocks exposed on the seafloor at Kane Megamullion on the southern side of Kane Transform Fault record a polarity boundary (C2r.2r/ C2An.1n , ~2.581 Ma), indicating that these lithologies are able to record a coherent magnetic signal. The geometry of the polarity boundary is estimated from two transform parallel, near-bottom magnetic profiles collected across the northern and central domes of Kane Megamullion. We use the analytic signal approach and calculate a range of dip angle solutions that take into account varying rotations of the magnetic source layer, assuming an initial remanence direction parallel to the geocentric axial dipole. In general, the polarity boundary dips away from the ridge axis along the northern profile and towards the ridge axis on the central profile. The amount of rotation at Kane Megamullion is estimated to be a minimum of ~35° counter clockwise, from the appearance of the anomaly across a basalt ridge in the northern region. Based on this rotation, the dip of the polarity boundary is 134°±14° in the northern region and 41°±17° in the central region. The opposing dip angles in the two regions correspond to observed differences in lithology from seafloor samples. We interpret the polarity boundary in the northern region to be a rotated cooling isotherm in a predominantly gabbroic layer. Two-dimensional modeling of core complex thermal structure indicates that a 580°C cooling isotherm (the Curie temperature of magnetite) with an initial dip of ~165° at the ridge axis can be rotated by up to 45°, to a maximum dip of ~120° after 3 Ma. In contrast, the polarity boundary in the serpentinized peridotites along the central region likely reflects an alteration front Assuming that the serpentinized peridotites experienced the same tectonic rotation as the northern gabbros, the initial dip of the polarity boundary near the ridge axis would be close to vertical (~76°). We suggest that the geometry of the boundary may result from perturbed isotherms that become steeply dipping towards the ridge axis in the footwall of the detachment fault due to seawater penetration. The consistent linearity of the polarity boundary across Kane Megamullion implies that both lithologies acquired their magnetization close to the ridge axis during approximately the same time interval.

4.1. Introduction

The symmetric distribution of marine magnetic lineations about the axes of mid-ocean ridges (MOR) provide key evidence for seafloor spreading processes and the theory of plate tectonics [*Morely and Larochelle*, 1964; *Vine and Matthews*, 1963]. Young oceanic lithosphere at the spreading axis acquires a remanent magnetization in the direction of the ambient geomagnetic field, resulting in stripes of alternating normal and reverse polarity crust that reflect frequent polarity reversals of Earth's magnetic field. However, despite extensive study of marine magnetic anomalies and the magnetic properties of oceanic lithosphere, the source rocks responsible for these magnetic anomalies is still somewhat ambiguous.

The first block models of *Vine and Matthews* [1963] assumed a single magnetic source layer ~15 km thick, whose base was defined by the Curie temperature of magnetite (580 °C), the main magnetic mineral in oceanic crust. In subsequent models the magnetic source layer was revised to include only the upper crustal basalts (~ 0.5 km), because their high initial remanent magnetization and finer grain sized crystals made them the strongest magnetic contributor [*Atwater and Mudie*, 1973; *Irving et al.*, 1970; *Talwani et al.*, 1971]. In contrast, lower crustal gabbros were thought to be less strongly magnetized due to their slowly cooled, coarse grained magnetite crystals, which are intrinsically less magnetic (e.g. *Dunlop and Prevot*, 1982). Fresh peridotites in the upper mantle are weakly ferromagnetic (they are paramagnetic), but become strongly magnetic upon alteration to serpentinized peridotites. It has been assumed that serpentinized peridotites acquire their magnetization too slowly to contribute constructively to the magnetic polarity signal recorded by the crust above and may result in delayed magnetization (e.g. *Sichler and Hekinian* [2002], *Harrison* [1987] and references therein).

More recent work has benefited from an increased number of representative rock samples made possible by advances in deep sea drilling technology and context-sensitive

sampling by submersible and robotic vehicles. From these results, it appears that both lower oceanic crust and upper mantle can have a strong, stable remanent magnetization generated over short enough time intervals to represent significant magnetic sources in slow spreading ridge environments, with proposed gabbro contributions ranging from 25 to 75 % of the overall magnetic anomaly [*Fox and Opdyke*, 1973; *Gee et al.*, 1997; *Gee and Meurer*, 2002; *Harrison*, 1987; *Kikawa and Ozawa*, 1992; *Oufi et al.*, 2002; *Pariso and Johnson*, 1993a; *Pariso and Johnson*, 1993b; *Tivey et al.*, 1998a; *Tivey and Tucholke*, 1998; *Zhao et al.*, 2006]. Models of the magnetic source layer have consequently evolved into a two-layer approximation with an upper basalt layer and a lower intrusive layer [*Dyment et al.*, 1997; *Wilson and Hey*, 1981].

Two-layer models may also help explain the difference in phase, or anomalous skewness, observed in some magnetic anomalies, particularly off-axis [*Cande and Kent*, 1976]. For example, simplified models assumed polarity boundaries to be near vertical in the quickly cooled basalts and sloping boundaries in the gabbros, that follow the curve of a cooling isotherm, such as the Curie temperature of magnetite [*Arkani-Hamed*, 1988; *Cande and Kent*, 1976]. The models therefore suggest that the lateral transition zone between polarity reversals is much wider for the gabbros than the basalts and consequently produces a delayed acquisition of magnetization with depth, thus explaining some of the skewness of the sea surface anomalies. These longstanding polarity boundary assumptions have been tested by very few observational constraints, despite a long history of ocean drilling beginning in the early 1970's [*Talwani et al.*, 1979].

Magnetic surveys at 21°N on the East Pacific Rise [*Macdonald et al.*, 1983a] and Blanco Fracture Zone [*Tivey et al.*, 1998a] showed that boundaries in the basalts are not vertical, but appear to dip towards the ridge axis over a wide range of angles (5°-45°). The dip of the boundary is a consequence of the volcanic emplacement process over a lateral distance typically several kilometers wide [*Kidd*, 1977; *Schouten and Denham*, 1979]. The only study of polarity boundary geometry in lower crust was done at Atlantis Bank

on the South West Indian Ridge (SWIR) and showed the gabbro layer dipping away from the ridge axis at a very shallow angle of 5°, after restoring a back tilt of 20° [*Allerton and Tivey*, 2001].

In this paper we present new observations of a magnetic polarity boundary recorded by both lower crust (gabbros) and upper mantle (peridotites) rocks exposed on the seafloor at Kane Megamullion in the North Atlantic (Fig. 4-1a). The presence of this boundary implies that these two lithologies can record a magnetic reversal in a coherent manner and have the potential to provide new insights into the source and distribution of magnetization in oceanic lithosphere at a slow spreading ridge.

4.1.1 Regional setting

Kane Megamullion is an ocean core complex (OCC) located ~ 40 km west of the Mid-Atlantic Ridge (MAR) axis, on the southern edge of the ~ 150 km long, left stepping Kane Transform Fault (Fig. 4-1b) [*Tucholke et al.*, 1998; *Tucholke et al.*, 1996]. Kane Megamullion is one of many ocean core complexes identified along spreading ridges characterized by a limited magma supply in the Atlantic and Indian Ocean [*Blackman et al.*, 1998; *Cann*, 1997; *Cannat et al.*, 1995a; *Dick et al.*, 2000; *Escartin et al.*, 2003; *Okino et al.*, 2004; *Searle et al.*, 2003; *Smith et al.*, 2006; *Tucholke et al.*, 2007]. Ocean core complexes are inferred to be the rotated footwalls of large detachment faults that root in the axial valley of the MOR (Fig. 4-2). Long term movement on the fault exhumes lower crust and upper mantle rocks on to the seafloor and can potentially accommodate a significant component of plate motion by extension, in the absence of magmatism.

The detachment fault initiates at the break-away and dips below the seafloor at the termination, which is the present day contact between the hanging wall and footwall (Fig. 4-2). At Kane Megamullion gabbros and peridotites are exposed on a dome-shaped massif that is ~ 20 km wide, ~ 35 km long and has a corrugated surface with elongated lineations (mullions) oriented parallel to the spreading direction. There are several

topographic highs to Kane Megamullion. Gabbros are found predominantly on Babel Dome to the north and Adam Dome to the south, while peridotites are exposed at Cain and Abel Domes (Fig. 4-3). Two faults, with approximately north-south trends, intersect the surface of the megamullion (East and West Fault) and a linear basalt ridge is located at the northern end of East Fault (Fig. 4-3).

Exposures of lower crust and upper mantle on the seafloor, like those at Kane Megamullion, provide ideal locations for sampling gabbros and peridotites and defining their potential contribution to the sea surface magnetic lineations, without interference from upper crustal basalts. Kane Megamullion is one of several core complexes located along the southern wall of Kane Transform Fault. We identify three large scale ocean core complexes (OCC) in addition to Kane Megamullion that vary in age from the youngest at the ridge-transform (OCC1) intersection to ~ 7 Ma (OCC4) (Fig. 4-1b). Gabbros and serpentinized peridotites have been sampled from OCC1 and OCC3 during submersible dives [*Auzende et al.*, 1994; *Karson and Lawrence*, 1997] and from drill cores (Ocean Drilling Program (ODP) 670 [*Detrick et al.*, 1990] and ODP 921-924 [*Cannat et al.*, 1995b]). The westernmost massif, OCC4, has not been sampled to date.

Two large scale sea surface magnetic surveys were conducted in the region south of the Kane Transform Fault known as the MARK (Mid-Atlantic Ridge at Kane) area and encompass Kane Megamullion (RC2511[*Detrick et al.*, 1988; *Schulz et al.*, 1988] and SEADMA 1 [*Gente et al.*, 1995; *Pockalny et al.*, 1995; *Schulz et al.*, 1988]). The magnetic lineations identified in these studies indicate asymmetric spreading in the region, with faster spreading rates to the west for at least the last 10 Ma (~ 14 km/Ma to the west and 11 km/Ma to the east [*Schulz et al.*, 1988]). Indeed, asymmetric spreading has characterized this part of the MAR for the last 36 Ma [*Schouten et al.*, 1985]. Magnetic lineations are continuous across all four identified ocean core complexes, where extrusive crust is absent. These studies also identified the polarity boundary C2r/C2An that crosses the eastern side of Kane Megamullion (Fig. 4-4).

Our survey differs from earlier studies by focusing entirely on Kane Megamullion. We acquired multiple datasets, including sea surface and near-bottom magnetic and bathymetry surveys and a large quantity of seafloor samples aboard the R/V Knorr (KN180-2) in 2004. We place the polarity boundary in the context of the regional magnetic anomalies and define the geometry of the boundary from near-bottom magnetic profiles. We test the hypothesis that the boundary represents a cooling isotherm in the lower crust by comparing its geometry with 580° C ridge isotherms that are tracked through the evolution of a core complex in two-dimensional thermal models. The magnetic anomaly data are then combined with paleomagnetic and rock magnetic data from sea floor samples [*Williams et al.*, in prep.] to produce a model of the magnetic structure of Kane Megamullion.

4.2. Methods

Sea-surface survey magnetic data were collected concurrently with Seabeam 2100 multibeam bathymetry along track lines ~4-7 km apart. The survey was conducted using shipboard GPS (Global Positioning System) navigation and data point locations were corrected subsequently for distance between the ship and the magnetometer (~305 m). The IXSEA GEOMAG (model SM-3 overhauser sensor) magnetometer took a reading every second and these were averaged over 1 minute (~ 0.3 km between data points). The residual anomaly at each track line data point was calculated by removing the IGRF for 2004 [*IAGA Division V Working Group, International Geomagnetic Reference Field 2000*, 2000]. The mean IGRF for this area is ~37,500 nT. The residual anomaly data points were interpolated onto an even grid with 0.5 km grid spacing using the minimum curvature algorithm from Generic Mapping Tool (GMT) software [*Wessel and Smith*, 1991] . The grid was then inverted for crustal magnetization using the fast Fourier transform inversion method of *Parker and Huestis* [1974], as adapted by *Macdonald et al.* [1980] for three-dimensional problems. The inversion assumes a source layer thickness of 1 km and uniform geocentric axial dipole magnetization direction (declination of 0° and inclination of 40°). A cosine-tapered bandpass filter with short

wavelength cut-off of 1 km and long wavelength cut-off of 50 km was applied to ensure convergence of the solution. The annihilator, a magnetization distribution that produces no external magnetic field when convolved with the topography of the survey area, is typically used to DC shift the inversion results [*Parker and Huestis*, 1974]. No annihilator was added to the final grid because the amplitude of positive and negative magnetizations is already balanced across the polarity boundary.

We compiled multiple bathymetric and magnetic surveys available in our study area from the National Geophysical Data Center (NGDC) (http://www.ngdc.noaa.gov/), SISMER (Systèmes d'Informations Scientifiques pour la Mer) at the French National Agency for Ocean research (IFREMER) (http://www.ifremer.fr/sismer/index_FR.htm) [*Gente et al.*, 1995], Marine Geoscience Data System (http://www.marine-geo.org/rmbs/) and MODE '94 cruise [*Fujimoto et al.*, 1994]. Average cross-over errors between each dataset and the 2004 Kane Megamullion data were calculated using GMT software. Each dataset was then corrected relative to the new Kane Megamullion data. Cross-over errors were reduced from 490 nT to 23 nT. The corrected compilation magnetic data were then interpolated onto a grid with 0.5 km grid spacing. The area of the compilation grid over Kane Megamullion was masked out and replaced with the 2004 Kane Megamullion survey grid .The two grids were combined using the GMT minimum curvature algorithm. The final grid was then reduced to the pole assuming the geocentric axial dipole magnetization direction (inclination is 40°) (Fig. 4-4).

High resolution near-bottom magnetic and multibeam bathymetry data were collected by ABE (Autonomous Benthic Explorer [*Yoerger et al.*, 2007]) at two locations on Kane Megamullion: along the North profile at ~ 23° 35'N and Center profile at ~ 23° 29'N (Fig. 4-3). Navigation was by acoustic transponder ranging and doppler velocity log. One ABE track line was acquired at an altitude of 20 m above the seafloor along the North profile (ABE Dive 143, ~ 13 km in length), while three ABE track lines were collected along the Center profile at 20 m (ABE Dive 147, ~ 7 km), 60 m (ABE Dive

139

148, ~ 6.5 km) and 250 m (ABE Dive 149, ~ 9 km) above the seafloor. The 3-axis magnetic field data were corrected for the ABE vehicle's magnetic contribution and orientation using a heading correction technique rather than a full vector calibration correction. This was done because the ABE pitch and roll data are not sensitive enough to provide sufficient information for a full vector calibration correction (see Appendix 1). ABE multibeam bathymetry was acquired using a 200 kHz Simrad 2000 multibeam sonar. SeaBeam 2100 sea surface bathymetry was used along ABE Dive 149 because the profile was too far from the seafloor to use the Simrad 2000 system (250 m). We verified that there is no lateral offset between the sea surface and near bottom bathymetry by overlaying the respective bathymetry profiles. We did find a vertical offset between the bathymetry datasets of ~15 m, probably due to differences in algorithms used to calculate depth i.e., pressure (Simrad 2000) versus acoustic (Seabeam 2100) depth. To be consistent with the sea surface multibeam data, all the ABE bathymetry and vehicle depths were adjusted to be 15 m deeper.

The ABE track line data were projected onto profiles perpendicular to the spreading axis (110°) and continued upward to 2.18 km (chosen based on shallowest survey water depth), 2.14 km and 1.95 km water depths for track lines 20 m, 60 m and 250 m above the seafloor respectively. In each case the same tapered cosine filter was used (short wavelength cut-off of 0.25 km and long wavelength cut-off of 30 km) to ensure convergence of the solution and suppression of any noise. The same filter was used on each profile so the near-bottom profiles could be compared with the seasurface data. The profiles were then inverted assuming a 1 km source layer thickness and cosine-tapered bandpass filter with short wavelength cut-off of 0.9 km and long wavelength cut-off of 100 km, to ensure convergence of the solution. As with the sea surface data, no annihilator was added to the ABE inversion results.

4.3. Results

4.3.1 Sea surface data

On a regional scale the identified magnetic isochron patterns are coherent and indicate asymmetric spreading throughout the region south of the Kane Fracture Zone, with faster spreading to the west (Fig. 4-4b). Spreading rate asymmetry is calculated from the age of the magnetic lineations and their distance from the ridge axis. We update previous estimates of chron age using lineation age from the Geomagnetic Polarity Time Scale of *Ogg and Smith* [2004] (Table 4-1). The start and end of each normal polarity chron is defined by the maximum gradient at the edge of the picked magnetic anomaly lineation.

Spreading rates are calculated along four transform parallel profiles, three of which cross the North, Center and South regions of the core complex region (the first two also correspond to the ABE North and Center profiles). A fourth profile crosses an area of apparent normal seafloor at 22° 50'N (Fig. 4-4b). Figure 4-5 shows all four magnetic profiles as well as the bathymetry and model results for the South and the 22° 50'N profiles. The models are calculated using the software package MODMAG [*Mendel et al.*, 2005], from which we identify the lineations.

Full spreading rate along the North, Center and South profiles average 23.4 km/Ma, with ~ 62-61 % asymmetry to the west, where 50 % means symmetrical spreading (Table 4-2 and Fig. 4-6). Average half spreading rates for the two flanks are calculated from a least squares fit to the data and show rates of 14.4 km/Ma to the west and 9.0 km/Ma to the east (Table 4-2). These values update previous published values of *Schulz et al.* [1988]. Spreading rates for normal seafloor along the 22° 50'N profile show only ~ 57 % asymmetry to the west (Table 4-2). There is a step-like increase in asymmetry from 52% to 62 % at 6 Ma (Chron 3A) on the 22° 50'N profile (Table 4-2, Fig. 4-6h), which also coincides with an observed decrease of several percent in asymmetry for the North, Center and South profile between 6-10 Ma (Table 4-2).

We calculate the spreading rate within each chron by subtracting the distance from the ridge axis at the beginning and end of the chron and taking into account the time interval between. Spreading rates are not constant along the profiles and asymmetry within each chron ranges from 42-78% to the west (Fig. 4-6 e-h). We observe a significant increase in asymmetry during Chron 2An on the North, Center and South profiles (72-75 %), which coincides with the location of Kane Megamullion (Fig. 4-6 e-h). No increase in asymmetry is observed during the same time interval on the 22° 50'N profile over normal seafloor (Fig. 4-6). Other core complexes east and west of Kane Megamullion (OCC1, OCC3 and OCC4) also appear to be associated with periods of increased asymmetry (Fig. 4-6 e-g). We note that intervals of increased asymmetry, are often preceded by periods of reduced asymmetry, well below the average asymmetry value for the whole profile. This is particularly apparent on the Center profile, which shows decreased asymmetry (42-49 %) before both Chrons 3 and 2A, which coincide with OCC3 and Kane Megamullion respectively (Fig. 4-6f).

The North, Center and South profiles all appear to have complex lineations between Chrons 1 and 2, which make these chrons and their subchrons difficult to identify. We therefore assume a constant spreading rate between present day (0 Ma) and the first identified chron along each profile (dashed grey lines in Fig. 4-6 e-g). The North profile has no C1r.1n or C2n lineations on the eastern flank, but appears to have an extra lineation between C1r.1n and C2n on the western flank (Fig.4-5a). On the Center profile we were not able to identify any lineations before C2An on the eastern flank (i.e. C2n is missing) (Fig. 4-5b), yet C2n is present on both flanks in the South profile (Fig. 4-5c).

The sea surface inversion results over Kane Megamullion clearly show a ridge parallel polarity boundary that cuts through the eastern side of the massif (Fig. 4-7b,7c). Based on the regional magnetic lineations, the boundary represents the reversal between C2An.1n and C2r.2r (~ 2.581 Ma). The boundary is linear in appearance at Kane Megamullion, but becomes less well defined south of 23° 20'N (Fig. 4-7c). This change

in character also coincides with a narrowing of the C2An anomaly and the presence of a positively magnetized feature located at 23° 20'N/45° 15'N, to the south-east of Kane Megamullion (Fig. 4-7b,7c). Chron 2A is composed of 3 normal subchrons (Table 4-1), but our inversion results indicate that only two subchrons, possibly the longer ones C2An.1n (2.581-3.032 Ma) and C2An.3n (3.33-3.596 Ma), are resolved by our sea surface data. The two subchrons merge when the lineation narrows to the south at 23° 25'N (Fig. 4-7c). Our crustal magnetization inversion solution across the survey area ranges between ~ -4 to 2 A/m for a nominal 1 km thick source layer. Magnetization increases from the northern end of Kane Megamullion to the highest amplitude located at 23° 26'N (just south of Abel Dome, Fig. 4-3), and then decreases again south of Kane Megamullion (Fig. 4-7c). The polarity transition zone is approximately 5 km (± 2 km) wide and absolute magnetization increase between C2r.2r and C2A.1n ranges from ~ 5 A/m along the North profile, to ~ 3 A/m along the Center profile, assuming a 1 km thick source layer and geocentric axial dipole direction (inclination is 40°, declination is 0°).

4.3.2 ABE profiles

Crustal magnetization amplitude and anomaly shape vary significantly between ABE profiles along the North and Center profiles. ABE 143, collected at 20 m altitude along the North profile, crosses the polarity boundary and extends west across the southern flank of Babel Dome, ending at the East Fault (Fig. 4-8, 4-3). Inversion results, which assume a 1 km thick source and geocentric axial dipole magnetization direction, show several individual magnetic anomalies along the profile (Fig. 4-9a). The polarity transition has an amplitude of ~ 14 A/m. We identify the C2An.1n anomaly, which forms the end of the transition zone and a second peak to the west that may represent subchron C2An.2n (Fig. 4-9a). The final peak at the west end of the line coincides with a basalt block or ridge along the northern end of East fault (Fig. 4-3). It should be kept in mind however, that our inversion assumes geocentric axial dipole magnetization direction for the entire magnetic source layer. Any rotation of KMM will change the magnetization

directions and introduce a phase shift in the inversion results. Issues associated with rotation are discussed later in section 4.4.1.

The three ABE profiles acquired along the Center profile (ABE 147, ABE 148 and ABE149) cross Cain Dome, which is the widest section of the massif (Fig. 4-3, 4-8). The polarity transition zone at the eastern end of the three profiles has an amplitude ranging from of 4-6 A/m, approximately one third the amplitude at ABE 143. The polarity boundaries also have a double peaked appearance, which differs from the smooth transition in ABE 143. The shortest profiles, ABE 147 and ABE 148 (collected at 20m and 60 m altitude respectively), show only the C2An.1n anomaly and possibly the C2An.2n anomaly at their western ends (Fig. 4-9b). ABE 149 extends as far as the East fault, which cuts between Cain and Abel Domes at this location (Fig. 4-3). At the western end of ABE 149 there is an anomaly associated with the basalt block, similar to that observed on ABE 143. However, there are two additional peaks between the basalt block and C2An.2n, which may represent cryptochrons (polarity transitions < 30 ka) (Fig. 4-9b).

4.4 Discussion

We discuss the appearance of the near bottom and sea surface magnetic anomalies and application of the information contained in the anomalies to investigate the geometry of the C2r.2r/C2An.1n polarity boundary in lower crust and upper mantle rocks at Kane Megamullion.

4.4.1 Geometry of the polarity boundary

Macdonald et al. [1983] observed an offset in the location of the Brunhes/Matayama boundary (C1n, 0.781 Ma) between magnetic anomaly profiles collected at varying altitudes near 21° N on the East Pacific Rise. A near-bottom profile tends to be more sensitive to the shallow polarity boundary while profiles higher in the

water column and/or at the sea surface will reflect the average polarity boundary location over a deeper section of the subsurface [*Blakely*, 1995].

We construct a forward model to illustrate the effect of a dipping polarity boundary on anomaly appearance. The model uses a prism [*Telford et al.*, 1990] to represent a dipping contact and assumes a strike of 0° (profiles run west to east), geocentric axial dipole magnetization direction (inclination is 40°) and magnetization contrast of 10 A/m. The contact boundary has a dip of 45° (measured clockwise from the eastern end of the profile) and anomaly profiles are calculated at 0.05 km, 0.25km and 2 km altitude (Fig. 4-10a).

We test the approach of *Macdonald et al.* [1983] to calculate the dip of the boundary using our forward model. *Macdonald et al.* [1983] define the dip of the boundary based on the lateral offset of the maximum vertical gradient between profiles at varying altitudes. Assuming a simple trigonometric relationship, the dip of the boundary is calculated from the lateral offset and relative difference in water depth between profiles. Our results show that the lateral offset between the 0.05 km and 0.25 km profiles is 0.09 km and the offset between the 0.25 km and 2 km profiles is 0.85 km. The calculated dip of the polarity boundary based on these offsets is 66° and 64° respectively. The *Macdonald et al.*, approach therefore tends to over estimate the dip of the boundary.

An alternative method to calculate the dip is a data enhancement technique known as the analytic signal, which is based on both the horizontal and vertical derivatives of the anomaly.[*Nabighian*, 1972; *Thurston and Smith*, 1997]. This approach requires only the information contained in a profile nearest to the seafloor, rather than a comparison between profiles, as with the *Macdonald et al.* approach. The first horizontal and vertical derivatives are calculated using the Fast Fourier Transform along the profiles (Fig. 4-10b). The complex analytic signal (Fig. 4-10c) is then defined from the vertical and horizontal derivatives,

$$A(x,z) = \frac{\partial M(x,z)}{\partial x} - i\frac{\partial M(x,z)}{\partial z} \tag{4.1}$$

the analytic amplitude (Fig. 4-10d),

$$|A| = \sqrt{\left(\frac{\partial M}{\partial x}\right)^2 + \left(\frac{\partial M}{\partial z}\right)^2} \qquad (4.2)$$

and analytic phase (Fig. 4-10e),

$$\Theta = \tan^{-1}\left[\frac{\partial M}{\partial z} \Big/ \frac{\partial M}{\partial x}\right] \qquad (4.3)$$

The analytic amplitude is represented by a symmetric function that peaks at the location of contact or boundary on the seafloor, defined as $x=0$, for a semi-infinite contact (Fig. 4-10d). The dip, d, of the boundary can be estimated from the analytic phase at $x=0$ using

$$d = \Theta + 2I' - 90 \qquad (4.4)$$

where the effective inclination angle I' is

$$I' = \arctan\left[\frac{\tan I}{\sin a}\right] \qquad (4.5)$$

I is the inclination of the ambient magnetic field, and α is the angle between the strike of the magnetic feature and magnetic north, measured clockwise from north. Magnetization is assumed to be in the same direction as the ambient field. The result from the 0.05 km model profile is a dip of 48° (d=-42+180-90), which agrees well with our input model dip of 45°. Dip angles were calculated for additional test models ranging from 30-90° and had a maximum error of ± 6°.

Our forward model does not take rotation of the magnetic body into account. Analytic amplitude is independent of inclination, declination, remanence direction or dip of the boundary, provided the source is two-dimensional [*Thurston and Smith*, 1997]. The

146

location of the polarity boundary identified by the maximum in the analytic amplitude will therefore not change for a rotated body. The analytic phase will also remain constant, but the effective inclination will reflect any rotation. We take rotation into account in the analytic signal approach by expanding the effective inclination term into two parts: the effective inclination of the remanent magnetization direction (I'_r) and the effective inclination of the geomagnetic field (I'_h)

$$d = \Theta + I'_h + I'_r - 90 \qquad (4.6)$$

I'_h is the present day direction and Θ is measured from the analytic phase, therefore the unknown variables are the dip, d, and I'_r. Gathering the unknown variables on the left-hand side we have

$$d - I'_r = \Theta + I'_h - 90 \qquad (4.7)$$

The effective remanent inclination (I'_r) will change based on the amount of rotation, which also changes the boundary dip angle. We construct a second forward model with the same 45° dipping boundary, but parameters similar to the ABE profiles to show the effect of rotation on I'_r and the dip angle. The forward model assumes a profile azimuth of 290°, present day geomagnetic field direction (inclination 41°, declination 344°) and initial remanent magnetization in the direction of the geocentric axial dipole (GAD, inclination 40°, declination 0°) (Fig. 4-11a). The body is rotated from 0° to 90° counter clockwise by changing the remanent magnetization inclination and declination using the approach of *Verosub and Moores* [1981] for a ridge with a strike of 20°. At zero rotation the effective remanent inclination (I'_r) has an initial value of 112° and for a dip angle of 45° and results in a phase (Θ) of 102° (Fig. 4-11b). Counter clockwise rotation decreases I'_r and the dip angle to minimum values of 22° and 135° (45° west) respectively for 90° rotation (Fig. 4-11b). By using the estimate of Θ from the profiles we can estimate the combined effect of I'_r and dip, but without addition constraints we cannot distinguish their respective values.

The analytic signal approach was applied to both low-pass filtered version of the observed profiles (filter cutoff of 0.1 km) and the upward continued near-bottom ABE profiles. We assume present day geomagnetic field direction, 20° for the rotation axis and a profile azimuth of 290° for all the ABE profiles analyzed (Fig. 4-11a).

On the northern Babel Dome (ABE 143) the analytic amplitude locates the boundary of the polarity transition zone on the seafloor at 20.23±0.1 km (Fig. 4-12aiii, 45° 14.9' W, 23° 34.2'N ±0.06') and the analytic phase at this location is -18°±10° for the upward continued profile (Fig. 4-12aiv). These values are similar to those for the filtered observed profile, which locates the boundary at 20.3±0.1 km (45° 14.9' W, 23° 34.2'N ±0.06') and has a phase of -25°±12°. The average polarity boundary location and phase angle from the two profiles are 20.27±0.13 km (45° 14.9' W, 23° 34.2'N) and -22°± 14° respectively.

At central Cain Dome (ABE 147) the analytic amplitude locates the contact boundary at ~18.2±0.1km (Fig. 4-12biii, 45° 17.1' W, 23° 29.1'N ±0.06') and the analytic phase is 64°±12° for the upward continued profile (Fig. 4-12biv). The values for the filtered observed profile are 17.9±0.1km (45° 17.3' W, 23° 29.1'N ±0.06') for the polarity boundary location and 78°±12° for the phase angle. The average polarity boundary location and phase angle from the two profiles are 18.1±0.17 km (45° 17.2' W, 23° 29.1'N) and 71°±18° respectively. Comparing the two profiles shows that, while the polarity boundaries locations have a similar longitude, the phase angles are very different at the two domes.

We can calculate the combined value of I'_r and the dip angle (i.e., $d - I'_r$) from the Θ estimates. At Babel Dome, ABE 143 gives a value for $d - I'_r = 57 \pm 14$, which translates into a range of solutions for I'_r and the dip angle from 169°±14° for no rotation (dipping away from the ridge axis) to 79°±14° (dipping towards the ridge axis) for 90° rotation (Fig. 4-13a, b), assuming the initial remanent direction at zero rotation was

GAD. At Cain Dome, ABE 147 gives a value of $d - I_r' = -36 \pm 17$, which results in a range of solutions of 76°±18° (dipping towards the ridge axis) for no rotation to -14°±18° (dipping away from the ridge axis) for 90° rotation (Fig. 4-13c & d), again assuming the initial magnetization at zero rotation was GAD. Our data therefore show that the dip of the polarity boundary at Babel Dome is in the opposite direction to the polarity boundary at Cain Dome, assuming both domes have experienced the same amount of rotation.

Another interesting result is that, if we assume the initial magnetization direction is GAD, then the Θ at zero rotation could be used to estimate the initial dip of the boundary before any rotation occurred at Kane Megamullion. At Babel Dome the initial dip would be 169° (Fig. 4-13a, b) for ABE 143 i.e. dipping away from the ridge axis, which is consistent with a cooling isotherm. In contrast, the zero rotation initial dip at Cain Dome would be 76° (Fig. 4-13c, d), which, as we discuss later, may parallel the young detachment fault zone.

The direction of dip can also be inferred from offsets between anomalies at different altitudes, as discussed by *Macdonald et al.* [1983]. The westward lateral offset of C2An.1n and the location of the polarity boundary defined by the analytic amplitude between the ABE and sea surface profiles on Babel Dome indicates that the boundary is dipping away from the ridge axis (Fig. 4-14a). The opposite is true when comparing the offset between ABE profiles and the sea surface at Cain Dome, indicating a dip towards the axis (Fig. 4-15a). This independently confirms our analytic dip results above. The location of the boundary contact, based on the maximum peak in the analytic amplitude, can also give some indication of the dip direction. The boundary is near the base of the transition zone on Babel Dome (ABE 143, Fig. 4-14a), but near the top of the transition zone on Cain Dome (ABE 147 (Fig. 4-15a). As the polarity boundary is the cause of the magnetic anomaly in both locations, we would expect the transition zone to extend in the dip direction.

4.4.2 Rotation of Kane Megamullion

Two end-member models exist to describe the subsurface geometry of the detachment fault surface. One model envisages constant slope low-angle faults cutting through the magmatic zone under the ridge axis (30°) [*Karson and Winters*, 1992; *Reston et al.*, 2002]. The other model suggests fault steepening with depth and rooting under the spreading axis at either the brittle/ductile transition [*Tucholke et al.*, 1998] or soling out along weak serpentinization fronts [*Escartin et al.*, 2003]. A recent microseismicity study by *deMartin et al.* [2007] from the TAG hydrothermal vent field at 26°N at the MAR shows a detachment fault surface that dips steeply at ~ 70° between 3-7 km depth and shallows to ~ 20° at depths less than 3 km. Another observation is linear basalt ridges associated with core complexes similar to the basalt ridge on the East Fault at Kane Megamullion (Fig. 4-3, 4-14). Basalt ridges at 13° N on the MAR have steep inward and outward facing slopes interpreted to be associated with rotations of up to 30°, suggesting that they were formed close to the axis by flexural rotation of steep (50°- 60°) normal faults [*Smith et al.*, submitted].

Rotation angles have also been estimated based on paleomagnetic vectors from oriented drill cores. *Garces and Gee* [2007] used the remanence vector in core complex gabbros from the 15° 20'N region as a measure of the rotations, assuming that the samples acquired their magnetization prior to deformation and their vectors remained as passive markers during subsequent rotation of the footwall. Their results suggest rotations of 50°- 80° in 1 Ma old crust. A similar study by *Carlut et al.* [2007] from footwall samples at 15° 45'N show rotations of ~ 40°.

The previous studies discussed above suggest a range of possible rotation angles between 30° to 80° associated with exhumation of ocean core complexes. If we assume the same range for Kane Megamullion, solutions for the dip angle of the polarity boundary at Babel and Cain domes are 139° (30° ccw) to 89° (80° ccw) (Fig. 4-13b) and 76° (30° ccw) to -4° (80° ccw) (Fig. 4-13d) respectively, assuming that the initial

remanent direction was GAD. Additional structural information is required to know which of these solutions is reasonable for Kane Megamullion. As yet there are no oriented drill cores from our study area for detailed paleomagnetic analyses and the small number of samples collected by submersible, which are only visually oriented, have large estimated errors of ±30°.

One possible source of information about crustal rotations at Kane Megamullion is the anomaly generated by the lineated basalt ridge located at the northern end of East fault (Fig. 4-3). ABE 143 profile at Babel Dome crosses the ridge at its western end (Fig. 4-8, 4-14) and has a short wavelength anomaly associated with the ridge, indicative of a shallow source rather than a long wavelength polarity transition (Fig. 4-14a). The basalt ridge is similar to the linear basalt ridges with steep inward and outward facing slopes observed in the 13-15°N area of the MAR [*Smith et al.*, submitted]. *Smith et al.* [submitted] propose that these ridges form close to the axis and are rotated sections of the valley floor that became entrained in the footwall. Any rotation experienced by the footwall after entrainment of the basalts will be reflected in the shape or phase of its magnetic anomaly. However, *Dick et al.* [submitted] suggest that the presence of the basalt ridge at Kane Megamullion may be due to off-axis volcanism [*Dick et al.*, submitted]. The basalt ridge may be an intact volcanic edifice associated with intersecting outward-facing and transform-parallel normal faults formed by exhumation of Kane Megamullion, most likely at the paleo-inside-corner high as the melt trapped within the footwall was forced to the surface [*Tucholke et al.*, 2001]. Based on this latter hypothesis, the basalt ridge should have experienced little, if any, rotation.

We can estimate the amount of rotation experienced by the basalt ridge and test the two hypotheses for the origin of the ridge using a simple block model to simulate the magnetic anomaly along ABE 143 and average rock magnetic parameters for Kane Megamullion samples (Table 4-3). The profile is modeled as a small, high magnetization (8.7 A/m) block within a larger, lower magnetization (1.5 A/m) block, both with normal

polarity to simulate a basalt body within the gabbros (Fig. 4-16d). The model was run for a range of rotation angles between 50° clockwise to 50° counter clockwise with an initial remanent direction of GAD. We focus on just fitting the basalt ridge anomaly. The model profile and ABE 143 magnetic profile are compared by calculating the RMS misfit (Fig. 4-16b). Our results show the model profile that has been rotated 35° counter clockwise has the best fit with the observed data (Fig. 4-16a). This suggests that the basalt ridge may indeed be an entrained block of hanging wall that has been back tilted during later exhumation of the core complex. The estimated counter clockwise rotation does not support the hypothesis that the basalt ridge formed by off-axis volcanism. Indeed, the western slope of the basalt ridge is dipping at ~ 24° away from the ridge axis (Fig. 4-14b). If we assume that this was the original, horizontal top surface of the basalts at the axis and has experienced some amount of erosion, a counter clockwise rotation of ~ 35° at Kane Megamullion is reasonable and compares well with studies at other core complexes. It must be kept in mind, however, that this may represent a minimum rotation angle because the core complex could have experienced some rotation before the basalt block was entrained.

A counter clockwise rotation of 35° at Babel Dome (ABE 143) results in a polarity boundary dipping at 134°±14° (i.e., away from the ridge axis) (Fig. 4-13a,b). The same rotation at Cain Dome (ABE 147) results in a polarity boundary dipping at 41°±17° (i.e., towards the ridge axis) (Fig. 4-13c,d). This significant difference in orientation of the polarity boundary implies that these two locations on Kane Megamullion acquired their remanent magnetization, and thus recorded the polarity boundary, through different processes or have experienced different tectonic rotations.

Dick et al. [submitted] suggest that Babel Dome is a gabbro pluton, based on the amount of gabbros sampled on the flanks of the dome and gabbro geochemistry. In contrast, peridotites were sampled extensively on Cain and Abel Domes and gabbros were very scarce (Fig. 4-3). The two sets of ABE profiles therefore traverse regions

dominated by different lithologies, at least defined by the surficial sampling. Opposing dip directions at Babel and Cain Domes could reflect different processes by which gabbros and peridotites acquire their magnetization. The underlying subsurface structure is also likely different too, with a potentially thicker source layer beneath Babel Dome compared with Cain Dome, where the gabbros are scarce.

We can estimate the source layer thickness in the two areas using simple trigonometry based on the width of the polarity reversal transition zone and our estimate of the dip of the polarity boundary. The polarity transition zone width on ABE 143 (Babel Dome) is ~ 4.01 km and results in a source layer thickness of 5.04±2.1 km, assuming simple trigonometric relationships and a dip of 134°±14° (Fig. 14-7a). This is quite thick and thus would imply that the source layer at Babel Dome may include either a thick gabbro layer or a gabbro layer and some portion of the altered peridotites below. In contrast, the source layer thickness along ABE 147 (Cain Dome), where the transition zone is ~3.03 km wide, is estimated to be 2.63 ±1.1 km, which likely includes only serpentinized peridotites (Fig. 4-17b).

Models of gabbro polarity boundaries assume they have the curved shape of conductively cooled isotherms, dipping away from the ridge axis [*Cande and Kent*, 1976; *Dyment et al.*, 1997; *Wilson and Hey*, 1981]. This dip direction agrees with the dip of the polarity boundary along ABE 143 (Babel Dome), in the gabbro pluton region. The polarity boundary in the altered peridotites may result from serpentinization processes whereby the peridotites acquire a chemical remanence due to secondary magnetite formation. Serpentinization processes are controlled by temperature and access to seawater at appropriate temperature and pressure. As access to seawater is governed by permeability, the distribution of serpentinization is likely controlled to a first order by faulting. Thus, the serpentinization front likely parallels the detachment fault surface or related faults that provide a major conduit of hydrothermal fluids.

For Babel Dome we test the hypothesis that a cooling isotherm reflects the dip of the polarity boundary in the gabbros by tracking a 580 °C isotherm in a ridge thermal model over a time interval of ~ 3 Ma. The initial and final dips of the isotherms are compared with the range of ABE 143 polarity boundary dip angles to assess whether it is reasonable to interpret the boundary as a rotated isotherm.

4.4.2.1 Thermal modeling

Deformation and thermal evolution are modeled in a 2-D visco-elastic-plastic layer using the fast Lagrangian analysis of continua (FLAC) technique. Material behavior is a function of temperature, strain-rate and accumulated plastic strain throughout the model space and a detailed description of the model can be found in *Tucholke et al.* [2007]. The numerical domain is 60 km wide by 20 km deep, with a maximum grid resolution of 0.25 km x 0.25 km at the ridge axis, which gradually coarsens to 2 km with distance from the ridge. Deformation is driven by applying a uniform rate of far-field extension along the sides of the model space corresponding to a half-rate of 12 mm/yr. The model runs for 3 Ma in time steps of ~ 25 ka. Magma injection is imposed by kinematically widening a vertical column of elements at the center of the model space. The rate of injection is described by the parameter M, which is defined as the ratio of the rate of dike opening to the rate of far-field extension (i.e. when M=0 all the plate motion is taken up by extension and when M=1 the extension is taken up by magmatism).

Our models are calculated for M values 0.3, 0.4 and 0.5, which *Tucholke et al.* [2007] have shown to be optimal values for detachment fault formation in the model (i.e, 30-50 % of plate motion is taken up magmatically). The injection zone extends from the surface of the model space to a depth of 5 km. Heat is added to the ridge axis during dike emplacement due to the injection temperature of the magma and the latent heat of crystallization. The effect of hydrothermal circulation on temperature is simulated by increasing the thermal conductivity by a factor (Nusselt number, Nu) above a threshold

depth of 7 km where the temperature is also <600°. In the models presented here, each M value is run with Nu of 2, 4 and 8 (total of 9 models).

The thermal models produce a detachment fault that continuously roots at the brittle-plastic transition, near the base of the emplacement dike (~ 5 km). The conjugate plate takes up the remaining plate separation by melt accretion at shallow levels and from rising asthenosphere at deeper levels. Figure 4-18 shows an example model with input parameters of M=0.4 and Nu=4 at time steps of 1, 2 and 3 Ma.

The tracking process is run several times for each model, beginning at three different origin times of 0.25, 0.5 and 0.75 Ma, to allow the model to equilibrate and also represent a range of time over which the gabbros passed through the Curie temperature and acquired their magnetization (Fig. 4-18d shows an example of tracking an isotherm which originates at 0.5 Ma). The dips of the initial and final isotherms are calculated from the top ~3 km of the model. The results show isotherm rotations ranging from 6-47° counter clockwise, with a mean value of 23°. The amount of rotation varies depending on the origin time of the isotherm, Nusselt number and M value of the model (Table 4-4). High Nusselt numbers represent efficient cooling of the crust through hydrothermal circulation. The isotherms are therefore depressed at the ridge axis and have more shallow dips at the beginning of the model. Rotations for 0.5 Ma and 0.75 Ma origin isotherms are similar, showing that the model equilibrates at around 0.5 Ma. Rotations angles do not vary systematically with M values, however M=0.4 models do have the largest rotations and average ~40 °, a result that is similar to the paleomagnetic rotation angles from the 15° N region of the MAR [*Carlut et al.*, 2006; *Garces and Gee*, 2007].

The dip of the polarity boundary along ABE 143 is 134°±14°, assuming 35° of counter clockwise rotation (Fig 4-13 a, b). Thermal modeling shows that the isotherms in four of the nine models have average rotations of 32° to 43° counter clockwise (M 0.3 Nu 2, M 0.4 Nu 4, M 0.4 Nu 8 and M 0.5 Nu 4) (Table 4-4). The dip of the initial isotherms

in these four models ranges from 155° to 176°, a result that is very similar to dip angle solution for no rotation at ABE 143 (169°±14°, Fig. 4-13a). The model results also agree well with the 580 °C isotherm in the *Cande and Kent* [1976] thermal model, which has a dip of ~ 165° within 10 km of the ridge axis. Isotherms from the *Phipps Morgan and Chen* [1993] model are significantly steeper; ~ 135° for a 600° C isotherm at a ridge spreading rate of 30 mm/yr, however this is within 2 km of the axis and the models assume M=1, i.e., all the plate motion is taken up by magmatism. Our thermal modeling results therefore imply that ~35° of counter clockwise rotation is reasonable during the evolution of an ocean core complex over 3 Ma. The dip of the polarity boundary along ABE 143 is consistent with the hypothesis that it is a rotated cooling isotherm that had an initial dip of ~169° at the ridge axis.

The polarity boundary at Cain Dome (ABE 147) dips at 41°±17° towards the ridge axis (Fig. 4-13b,d), if we assume that the serpentinized peridotites have experienced the same amount of counter clockwise rotation as the gabbros at Babel Dome and the initial remanence direction was GAD. The dip of the polarity boundary with no rotation is 76°±17° and this value could reflect the initial boundary dip angle close to the ridge axis, before rotation occurred. Such a steep boundary requires a very localized alteration process by which the peridotites acquire their remanence. A near-vertical polarity boundary may be explained by the peridotites passing through a zone of intense hydrothermal activity close to the ridge axis into an adjacent, less active zone. Alteration veins in peridotites from ODP holes 920B, 920D and 670A in the MARK area show serpentinization temperatures ranging from 200-400° C [*Andreani et al.*, 2007; *Herbert et al.*, 1990]. A significant reduction in cooling rates off axis may be fast enough so the peridotites were able to move through the temperature interval of serpentinization and acquire the majority of their remanence over a very short time interval, resulting in the coherent polarity reversal we observe. Fast cooling rates due to hydrothermal circulation have been estimated in the gabbros at Atlantis Bank (SWIR)[*John et al.*, 2004]. However, these cooling rates were associated with mantle temperatures that are much higher than

the 200-400° C required for serpentinization and is it unlikely that a rapid cooling rate process can explain the initial dip of the polarity boundary.

An alternative explanation for the steep polarity boundary is the depression of isotherms around the location of the detachment fault surface, which acts as a conduit for cold seawater penetrating the seafloor. Isotherms between ~200-400° C could dip steeply towards the ridge axis on the footwall side of the detachment fault (Fig. 4-19), resulting in a steeply dipping polarity boundary. The top 380 m of core recovered from IODP holes U1309B and U1309D at Atlantis Massif shows an alteration profile characteristic of pervasive infiltration of seawater, compared with restricted alteration in haloes adjacent to veins, fractures and lithological contacts in deeper core sections [*Ildefonse et al.*, 2007]. Samples from the south wall of Atlantis Massif also show both focused fluid flow along detachment fault shear zones and pervasive circulation that has led to strongly serpentinized domains, such as presently below the Lost City hydrothermal field [*Boschi et al.*, 2006].

Identifying the dip of the polarity boundaries in both the gabbros and serpentinized peridotites and quantifying the amount of rotation that has occurred are critical parameters for understanding the crustal structure at Kane Megamullion. Our results suggest Kane Megamullion has experienced at least 35° of counter clockwise rotation during its evolution. The polarity boundary in the gabbros at Babel Dome (ABE 143), which dips away from the ridge axis, is consistent with a rotated cooling isotherm. In contrast, the polarity boundary in the serpentinized peridotite dominated Cain Dome (ABE 147) dips towards the ridge axis. The initial dip of this boundary may have been close to vertical, if we assume that both Babel and Cain Domes have experienced 35° of rotation, and we propose that the boundary reflects a serpentinization alteration front associated with the detachment fault.

4.4.3 Modeling the magnetic structure of Kane Megamullion

We can use our magnetic anomaly calculations and thermal modeling results, along with rock magnetic and paleomagnetic data from Kane Megamullion samples, to constrain models of the magnetic structure at the megamullion. Average values of natural remanent magnetization (NRM) and susceptibility (k) measured from seafloor samples collected at Kane Megamullion in 2004 are given in Table 4-3[*Williams et al.*, in prep]. We use the software package GM-SYS (Northwest Geophysical Assoc.), which requires input profiles of bathymetry, fish depth and residual anomaly, to model the subsurface magnetic structure along ABE 143 (Babel Dome) and ABE 147 (Cain Dome).

4.4.3.1 North Profile at Babel Dome

The dominant magnetic anomalies on ABE 143 are the polarity boundary to the east and basalt block to the west (Fig. 4-9, Fig. 4-14). Gabbros from Kane Megamullion have an average NRM of ~ 1.5 A/m, which is significantly less than the basalt ridge basalts with NRM of 8.7 A/m (Table 4-3, *Williams et al.*, in prep). The proposed counter clockwise rotation of ~35° at Kane Megamullion about an axis with a strike of 20° clockwise from north would result in a phase shift of the initial geocentric axial dipole magnetization direction (0° declination and 40° inclination) to an inclination of 43 ° and declination of 32° [*Verosub and Moores*, 1981]. These magnetic property parameters are combined with our estimated source layer thickness and location of the boundary contact at the surface to create a cross section through Babel Dome.

Our model results show that the basalt ridge anomaly can easily be resolved assuming an NRM of 8.7 A/m. In contrast, the amplitude of the polarity transition zone anomaly along the ABE 143 profile (Fig. 4-20a) cannot reasonably be generated by a gabbro source layer with an NRM of 1.5 A/m (Fig. 4-20b). Figure 4-20b shows that even for a gabbro source layer over 7 km thick (greater than the total thickness of normal oceanic crust), the amplitude is significantly less than the observed anomaly. Instead, we assume a model with two gabbro layers; a upper layer with Kane Megamullion values of

1.5 A/m that forms a skin < 200 m thick above a lower layer with NRM of 4.7 A/m, which is the average NRM for oxide gabbros drilled at ODP 735B on Atlantis Bank (SWIR) [*Pariso and Johnson*, 1993a] (Fig. 4-20c). This type of gabbro was found to increase upsection in hole 735B [*Dick et al.*, 2000] and may well underlie the surficial gabbros at Babel Dome [*Dick et al.*, submitted]. Our two layer gabbro model shows a better fit with the observed data (Fig. 4-20a). The model source layer thickness 1.5 km is required to match the anomaly amplitude, which is much thinner than our minimum estimated source layer thickness of ~2.94 km (5.04-2.1 km) for Babel Dome.

4.4.3.2. Center profile at Cain Dome

Pervasive serpentinized peridotite exposure [*Dick et al.*, submitted] along the ABE 147 profile suggests that peridotites are the most significant lithology at Cain Dome and gabbros may not be present even at depth. The residual mantle bouguer anomaly (RMBA) is also lower at Babel Dome than the central region of Kane Megamullion, implying that the crust is thicker at Babel Dome [*Maia and Gente*, 1998]. A thin serpentinized peridotite magnetic source layer only ~ 0.8 km thick produces an anomaly with an amplitude comparable to the observed anomaly (Fig. 4-21). This result compares well with shallow seismic reflection data from Kane Megamullion (Ewing 01-02). The seismic data images the upper 0.7 km of the crust and is characterized by low velocities associated with serpentinization (< 5 km/s) [*J.P. Canales*, pers. comm.]. The seismic data are therefore consistent with the magnetic data, which suggests that the magnetic source layer has a minimum thickness of 0.7 km. Our estimate of the source layer thickness from the polarity transition width is 2.63±1.1 km, therefore the model source layer is thinner than the minimum estimated thickness. This discrepancy may result from alternating polarities in the serpentinized peridotites, which may reduce the overall average NRM of the source layer to a value less than 4.7 A/m.

While there are an infinite number of possible subsurface structure models that would agree with the observed anomaly, we can use measured rock magnetic properties

and estimates of the polarity boundary dip, rotation and source layer thickness from the observed magnetic anomalies to provide constraints on the parameters for Kane Megamullion magnetization and crustal structure. Our models of the subsurface structure along ABE 143 and ABE 147 highlight the different lithologies in the two regions and their affect on the magnetic source layer and polarity boundary. ABE 143 at Babel Dome requires a gabbro layer with higher mean NRM than the values measured from the Kane Megamullion samples to match the change in anomaly amplitude across the polarity boundary. The resulting magnetic source layer that provides a good fit with the data is ~4 km thick, which lies within our estimate from the width of the polarity transition zone . ABE 147 at Cain Dome requires only a peridotite layer 0.8 km thick to account for the change in amplitude.

4.4.4 Regional magnetic isochrons

We move from our focused study of the polarity boundary at Kane Megamullion to the regional anomalies and patterns of crustal accretion. Our compilation of sea surface magnetic data shows that asymmetric spreading to the west has persisted in the region for at least 10 Ma (start of Chron 5) [*Gente et al.*, 1995; *Pockalny et al.*, 1995; *Schulz et al.*, 1988]. The asymmetry has resulted in a compressed sequence of reversals on the eastern flank, such that only magnetic chrons of duration longer than 0. 3 Ma can be identified (e.g., Chron 3B is not resolved on the eastern flank, Fig. 4-4 and 4-5).

Average spreading rate asymmetry is similar (62-61%) between the North, Center and South profiles in the core complex region and decreases to 57 % along the 22° 50'N profile for normal seafloor over the last 10 Ma (Fig. 4-6, Table 4-2). The difference in asymmetric spreading is more significant during the last 6 Ma; 52 % on 22° 50'N profile and 65-60 % along the North, Center and South profiles (Table 4-2). *Baines et al.* [2007] suggest that the calculated spreading rate is not a record of the slip rate along the detachment fault, but rather the apparent rate of plate spreading. The apparent rate may include a component of extension on the detachment fault following denudation. The ~

10 % increase in observed asymmetry between the core complex region and normal seafloor to the south over the last 6 Ma may result from this type of late-stage extension. We predict that the 10 % asymmetry increase results from ~ 9 km of additional seafloor on the western ridge flank compared with the eastern flank in the core complex region.

The presence of the core complexes does not break the continuity of the magnetic lineations between Chron 5 and 2A in our study area. A similar lack of lineation disruption in core complex regions was also observed on Atlantis Bank (SWIR) [*Dick et al.*, 1991; *Hosford et al.*, 2003], FUJI Dome (SWIR) [*Searle et al.*, 2003] and the west MARK area [*Tivey et al.*, 1998b]. The lineation patterns therefore imply that the lower crust and upper mantle acquired their magnetization close to the ridge axis over a similar, short time interval. The presence of the core complexes becomes more apparent in the magnetic data when the spreading rates are calculated between chrons.

The North, Center and South profiles all show greater spreading rate asymmetry during Chron 2A (72-75%), which coincides with the location of Kane Megamullion (Fig. 4-6 e-g). Again, similar rates of asymmetry have been recorded at other core complex locations including 77 % at FUJI Dome (SWIR) [*Searle et al.*, 2003], 80 % at Atlantis Bank (SWIR) [*Baines et al.*, submitted] and 75 % on the Australian-Antarctic Discordance (SEIR) [*Okino et al.*, 2004]. *Baines et al.* [submitted] attribute the asymmetry to the detachment fault acting as the primary plate boundary in the upper crust, with the majority of magmatic accretion occurring on the footwall.

We also observe a significant decrease in asymmetry in the time interval before KMM and OCC3 on the Center profile (Fig. 4-6f). *Smith et al.* [submitted] identified a significant reduction in spreading rate on the western side of the ridge axis that coincides with the location of Logachev massif, a core complex located at ~ 14 °40'N on the MAR. They interpret this to be the time at which the core complex initiated, when the magmatic spreading center remained active but at a reduced rate. In the Kane area, the majority of

plate motion may have been taken up by magmatism on the eastern flank until the core complex became more developed, or a further reduction in magmatism could have initiated accelerated extension along detachment fault.

Continuous and easily identified lineations between Chron 5 and 2A contrast markedly with the disrupted anomalies between Chron 2A and Chron 1 in our study area. Absent lineations on the eastern flank and extra lineations on the western flank have been attributed to recent ridge jumps by *Schulz et al.* [1988]. *Fujiwara et al.* [2003] and *Smith et al.* [submitted] also describe a similar pattern of organized lineations off axis and complex near-axis anomalies that are difficult to interpret at the 15° 20'N Transform Fault and 13° N segment of the MAR. The similarity between the three regions suggests that the process is not unusual, and the transition from chaotic to systematic patterns of lineations may be typical.

4.5. Conclusions

Our detailed study of Kane Megamullion provides new insights into the source layer of marine magnetic anomalies. We suggest that the polarity boundary in the peridotites may be close to vertical near the ridge axis. This hypothesis could help explain why polarity transition zones are narrow and suggests that the contribution of peridotites to the magnetic source layer is significant. We also suggest that the continuous linear appearance of the polarity boundary across Babel and Cain Domes indicates that the gabbros and peridotites acquired their magnetization during the same time interval. The lack of disruption in magnetic lineations across the core complex region shows that the crustal magnetization recorded by gabbro and serpentinized peridotite can be as significant as the magnetization recorded by the extrusive layer. We make the following conclusions:

1. The polarity transition that crosses Kane Megamullion is the C2n.2r\C2An.1n boundary (~ 2.581 Ma). The boundary is continuous and linear in appearance,

indicating that the lower crust and upper mantle recorded the signal in a coherent manner.

2. The dip of the polarity boundary is calculated from near-bottom magnetic profiles using the analytic signal approach, which provides a range of solutions for varying crustal rotations at Kane Megamullion. Our results show that the polarity boundary in the northern region of Kane Megamullion (interpreted to be a gabbro pluton) is dipping away from the ridge axis, while the boundary is the central region is dipping towards the ridge axis.

3. We estimate that a minimum of ~35° of counter clockwise rotation has taken place at Kane Megamullion from the appearance of the anomaly across the basalt ridge at the northern end of East Fault. Based on this rotation, the resulting boundary dip angle in the northern region is 134°±14° and 41°±17° in the central region, assuming that the initial remanent magnetization was in the direction of the geocentric axial dipole.

4. Two-dimensional ridge thermal models show that a cooling isotherm tracked through the evolution of the core complex can be rotated up to ~45° counter clockwise, from an initial dip angle of ~165° (dipping away the ridge axis) to ~120°. The dip of the polarity boundary in the northern gabbro region is therefore consistent with a rotated cooling isotherm.

5. The polarity boundary in the serpentinized peridotite layer may reflect an alteration front. Assuming that the serpentinized peridotites experienced the same amount of counter clockwise rotation as the gabbros, the initial dip of the boundary was close to vertical at the ridge axis. We propose that this geometry is due to perturbed 200°- 400° C isotherms, which dip steeply towards the ridge axis in the footwall of the detachment fault due to penetration of seawater along the fault plane.

6. The presence of ocean core complexes results in increased asymmetric spreading rates (~ 76 %) compared with normal seafloor south of the core complexes.

7. A basalt ridge at the western edge of Babel and Cain Domes is interpreted to be a piece of hanging wall that has been rafted off and incorporated into the footwall and rotated, rather than a volcanic feature that has been erupted off-axis.

Acknowledgements

References

Allerton, S.A., and M.A. Tivey (2001),Magnetic polarity structure of the lower oceanic crust, *Geophys.Res.Letts*, *28*, 423-426.

Andreani, M., C. Mevel, A.-M. Boullier, and J. Escartin (2007),Dynamic control on serpentine crystallization in veins: Constraints on hydration processes in oceanic peridotites, *Geochem. Geophys. Geosyst.*, *8*, Q02012, doi:10.1029/2006GC001373.

Arkani-Hamed, J. (1988),Remanent magnetization of the oceanic upper mantle, *Geophys. Res. Letts.*, *15*, 48-51.

Atwater, T., and J.D. Mudie (1973),A detailed near-bottom geophysical study of the Gorda Rise, *J. Geophys. Res.*, *78*, 8865-8886.

Auzende, J.-M., M. Cannat, P. Gente, J.P. Henriet, T. Juteau, J.A. Karson, Y. Lagabrielle, C. Mevel, and M.A. Tivey (1994),Observations of sections of oceanic crust and mantle cropping out on the southern wall of the Kane FZ (N. Atlantic), *Terra Research*, *6*, 143-148.

Baines, A.G., M. Cheadle, B. John, and J.J. Schwartz (submitted),The rate of oceanic detachment faulting at Atlantis Bank, SW Indian Ridge, *submitted to Geology*.

Blackman, D.K., J.R. Cann, B. Janssen, and D.K. Smith (1998),Origin of extensional core complexes: Evidence from the Mid-Atlantic Ridge at Atlantis Fracture Zone, *J. Geophys. Res.*, *103*, 21315-21333.

Blakely, R.J., *Potential Theory in Gravity and Magnetic Applications*, Cambridge University Press, Cambridge, UK, 1995.

Boschi, C., G.L. Fruh-Green, A. Delacour, J.A. Karson, and D.S. Kelley (2006),Mass transfer and fluid flow during detachment faulting and development of an oceanic core complex, Atlantis Massif (MAR 30° N), *Geochem. Geophys. Geosyst.*, *7*, Q01004, doi:10.1029/2005GC001074.

Cande, S.C., and D.V. Kent (1976),Constraints imposed by the shape of marine magnetic anomalies on the magnetic source, *J. Geophys.Res.*, *81*, 4157-4162.

Cann, J.R.e.a. (1997),Corrugated slip-surface formed at ridge-transform intersections on the Mid-Atlantic Ridge, *Nature*, *385*, 329-332.

Cannat, M., J.A. Karson, D.J. Miller, and a.t.S.S.P.o.O.L. 153, in *Proc. Ocean Drill. Program Init. Repts.*, College Station,TX (Ocean Drilling Program), 1995b.

Cannat, M., C. Mevel, M. Maia, C. Deplus, C. Durand, P. Gente, P. Agrinier, A. Belarouchi, G. Dubuisson, E. Humler, and J.R. Reynolds (1995a),Thin crust, ultrmafic exposures, and rugged faulting paterns at the Mid- Atlantic Ridge (22-24° N), *Geology*, *23*, 49-52.

Carlut, J., C.J. MacLeod, H. Horen, and J. Escartin, Paleomagnetic results from a mid-ocean ridge detachment at the Mid-Atlantic Ridge, 15° 45'N, in *EGU Meeting*, Vienna, 2006.

Detrick, R.S., P.J. Fox, N.J. Schulz, R.A. Pockalny, L. Kong, L. Mayer, and W.B.F. Ryan (1988),Geologic and tectonic settings of the MARK area, leg 106/109, *Initial Rep. Deep Sea Drill. Proj.*, 15-22.

Detrick, R.S., J. Honnorez, W.B. Bryan, T. Juteau, and e. al. (1990),*Proc. Ocean Drill. Program., Init. Repts.*, *106/109*.

Dick, H.J.B., J.H. Natland, J.C. Alt, W. Bach, D. Bideau, and e. al. (2000),A long in situ section of the lower crust: results of ODP Leg 176 drilling at the Southwest Indian Ridge, *Earth. Planet. Sci. Letts.*, *179*, 31-51.

Dick, H.J.B., H. Schouten, P.S. Meyer, D.G. Gallo, H. Bergh, R. Tyce, P. Patriat, T.M. Johnson, J. Snow, and A. Fischer (1991),Tectonic evolution of the Atlantis II Fracture Zone, *Proc. Ocean Drill. Program Sci. Results*, *118*, 359-398.

Dick, H.J.B., M.A. Tivey, and B.E. Tucholke (submitted),Plutonic foundation of a slow-spread ridge segment: the oceanic core complex at Kane Megamullion, 23° 30'N, 45° 20'W., *submitted to Geochem. Geophys. Geosys.*

Dyment, J., J. Arkani-Hamed, and A. Ghods (1997),Contribution of serpentinized ultramafics to marine magnetic anomalies at slow and intermediate spreading centers: Insights from the shape of the anomaly, *Geophys. J. Int.*, *129* (691-701).

Escartin, J., C. Mevel, C.J. MacLeod, and A.M. McCaig (2003),Constraints on deformation conditions and the origin of oceanic detachments : The Mid-Atlantic Ridge core complex at 15° 45'N, *Geochemistry, Geophysics, Geosystems*, *4*, doi:10.1029/2002GC000364.

Fox, P.J., and N.D. Opdyke (1973),Geology of the oceanic crust: magnetic properties of oceanic rocks, *J. Geophys. Res.*, *78*, 5139-5154.

Fujimoto, H., W.B. Bryan, and e. al. (1994),A geophysical survey of the Mid-Atlantic Ridge around the western Kane Transform Fault, *EOS Trans. AGU*, *75*, Fall Meet. Suppl. ,656.

Garces, M., and J. Gee (2007),Paleomagnetic evidence of large footwall rotations associated with low-angle faults at the Mid-Atlantic Ridge, *Geology*, *35*, 279-282.

Gee, J., R.M. Lawrence, and S.D. Hurst (1997),Remanence characteristics of gabbros from the MARK area: Implications for crustal magnetization, *Proc. Ocean Drill. Program Sci. Results*, *153*, 429-436.

Gee, J., and W.P. Meurer (2002),Slow cooling of middle and lower oceanic crust inferred from multicomponent magnetizations of gabbroic rocks from the Mid-Atlantic Ridge south of the Kane fracture zone (MARK) area, *J. Geophys. Res.*, *107* (B7), EPM 3, doi:10.1029/2000JB000062,18.

Gente, P., R.A. Pockalny, C. Durand, C. Deplus, M. Maia, G. Ceuleneer, C. Mevel, M. Cannat, and C. Laverne (1995),Characteristics and evolution of the segmentation of the Mid-Atlantic Ridge between 20° N and 24° N during the last 10 million years, *Earth Planet. Sci. Letts.*, *129*, 55-71.

Harrison, C.G.A. (1987), Marine magnetic anomalies- The origin of the stripes, *Annu. Rev. Earth. Planet. Sci*, *15*, 505-543.

Herbert, R., A.C. Adamson, and S.C. Komor (1990),Metamorphic petrology of ODP leg 109, Hole 670A serpentinized peridotites; Serpentinization processes at a slow spreading ridge environment, *Proc. Ocean Drill. Program Sci. Results*, *106/109*, 103-115.

Hosford, A., M.A. Tivey, T. Matsumoto, H.J.B. Dick, H. Schouten, and H. Kinoshita (2003),Crustal magnetization and accretion at the Southwest Indian Ridge new the Atlantis II fracture zone, 0-25 Ma, *J. Geophys. Res.*, *108*, 2169, doi:10.1029/2001JB000604.

Ildefonse, B., D.K. Blackman, B. John, Y. Ohara, D.J. Miller, and C.J. MacLeod (2007),Oceanic core complexes and crustal accretion at slow-spreading ridges, *Geology*, *35*, 623-626.

Irving, E., W.A. Robertson, and F. Aumento (1970),The Mid-Atlantic Ridge near 45° N VI, Remanent intensity, susceptibility, and iron content of dredge samples, *Can. J. Earth Sci.*, *7*, 226-238.

John, B., D.A. Foster, M.J. M., M. Cheadle, A.G. Baines, C.M. Fanning, and P. Copeland (2004),Determining the cooling history of in situ lower oceanic crust- Atlantis Bank, SW Indian Ridge, *Earth Planet. Sci. Letts.*, *222*, 145-160.

Karson, J.A., and R.M. Lawrence (1997),Tectonic window into gabbroic rocks of the middle oceanic crust in the MARK area near sites 921-924, *Proc. Ocean Drill. Program Sci. Results*, *153*, 61-76.

Karson, J.A., and A.T. Winters, Along-axis variations in tectonic extension and accommodation zones in the MARK area, Mid-Atlantic Ridge 23° N latitude, in *Ophiolites and their modern oceanic analogues*, edited by L.M. Parson, B.J. Murton, and P. Browning, pp. 107-116, Geological Society Special Publication, 1992.

Kidd, R.G.W. (1977),A model for the process of formation of the upper oceanic crust, *Geophys. J R. Astron. Soc.*, *50*, 149-183.

Kikawa, E., and K. Ozawa (1992),Contribution of oceanic gabbros to sea-floor spreading magnetic anomalies, *Science*, *258*, 796-799.

Macdonald, K.C., S.P. Miller, B.P. Luyendyk, T.M. Atwater, and L. Shure (1983a),Investigation of a Vine-Matthews magnetic lineation from a submersible: The source and character of marine magnetic anomalies,, *J. Geophys. Res*, *88*, 3403-3418.

Maia, M., and P. Gente (1998),Three-dimensional gravity and bathymetry analysis of the Mid-Atlantic Ridge between 20° N and 24° N: flow geometry and temporal evolution of the segmentation., *J. Geophys. Res.*, *103*, 951-974.

Mendel, V., M. Munschy, and D. Sauter (2005),MODMAG, a MATLAB program to model marine magnetic anomalies, *Computers and Geoscience*, *31*, 589-597.

Morely, L.W., and A. Larochelle (1964),Paleomagnetism as a means of dating geological events, *Roy. Soc. Can. Spec. Publ.*, *8*, 39-50.

Nabighian, M.N. (1972),The analytic signal of two-dimensional magnetic bodies with polgonal cross-section: its properties and use for automated anomaly interpretation, *Geophysics*, *37* (3), 507-517.

Okino, K., K. Matsuda, D.M. Christie, Y. Nogi, and K. Koizumi (2004),Development of oceanic detachment and asymmetric spreading at the Australian-Antarctic Discordance, *Geochemistry, Geophysics, Geosystems*, *5*, doi:10.1029/2004GC000793.

Oufi, O., M. Cannat, and H. Horen (2002),Magnetic properties of variably serpentinized abyssal peridotites, *Journal of Geophysical Research*, *107*, 10.1029/2001JB000549.

Pariso, J.E., and H.P. Johnson (1993a),Do layer 3 rocks make a significant contribution to marine magnetic anomalies? In situ magnetization of gabbros from Ocean Drilling Program Hole 735B, *J. Geophys. Res*, *98*, 16033-16032.

Pariso, J.E., and H.P. Johnson (1993b),Do lower crustal rocks record reversals of the Earth's magnetic field? Magnetic petrology of oceanic gabbros from ocean drilling program Hole 735B., *J. Geophys. Res*, *98*, 16013-16032.

Parker, R.L., and S.P. Huestis (1974),The inversion of magnetic anomalies in the presence of topography, *J. Geophys. Res.*, *79*, 1587-1594.

Pockalny, R.A., A. Smith, and P. Gente (1995),Spatial and temporal variability of crustal magnetization of a slowly spreading ridge: Mid-Atlantic Ridge (20° - 24°), *Mar. Geophys. Res.*, *17*, 301-320.

Reston, T.J., W. Weinrebe, I. Grevemeyer, E. Flueh, N.C. Mitchell, L. Kirstein, C. Kopp, and H. Koop (2002), A rifted inside corner massif on the Mid-Atlantic Ridge at 5° S, *Earth Planet. Sci. Letts.*, *200*, 255-269.

Schouten, H., S.C. Cande, and K.D. Klitgord, Magnetic Anomaly Profiles South (22° N to 28° N), in *Ocean Margin Drilling Program Regional Data Synthesis Series, Atlas 11, Mid- Atlantic Ridge between 22° and 38° N*, Marine Science International, Woods Hole, MA, 1985.

Schouten, H., and R. Denham, Modeling the oceanic magnetic source layer, in *Implications of deep drilling results in the Atlantic Ocean*, edited by M. Talwani, and M. Ewing, pp. 151-159, AGU, 1979.

Schulz, N.J., R.S. Detrick, and S.P. Miller (1988),Two and three-dimensional inversions of magnetic anomalies in the MARK area (Mid-Atlantic Ridge 23°N), *Mar. Geophys. Res.*, *10*, 41-57.

Searle, R.C., M. Cannat, K. Fujioka, C. Mevel, H. Fujimoto, A. Bralee, and L. Parons (2003),FUJI Dome: A large detachment fault near 64° E on the very slow-

167

spreading southwest Indian Ridge, *Geochemistry, Geophysics, Geosystems, 4* (8), 9105,doi:10.1029/2003GC000519.

Smith, D.K., J.R. Cann, and J. Escartin (2006),Widespread active detachment faulting and core complex formation near 13° N on the Mid-Atlantic Ridge, *Nature, 442,* 440-443.

Talwani, M., C.G.A. Harrison, and D.E. Hayes, *DSDP results in the Atlantic Ocean: Ocean crust Maurice Ewing Ser.*, 431 pp., AGU, Washington D. C., 1979.

Talwani, M., C.C. Windisch, and M.G. Langseth (1971),Reykjanes ridge crest:a detailed geophysical study, *J. Geophys. Res., 76,* 473-517.

Telford, W.M., L.P. Geldart, and R.E. Sheriff, *Applied Geophysics*, 92-96 pp., Cambridge University Press, Cambridge, UK, 1990.

Thurston, J.B., and R.S. Smith (1997),Automatic conversion of magnetic data to depth, dip and susceptibility contrast using the SPI (TM) method, *Geophysics, 62* (3), 807-813.

Tivey, M.A., H.P. Johnson, C. Fleutelot, S.A. Hussenoeder, R.M. Lawrence, C. Waters, and B. Wooding (1998a),Direct measurement of magnetic reversal polarity boundaries in a cross-section of oceanic crust, *Geophys. Res. Letts., 25,* 3631-3634.

Tivey, M.A., A. Takeuchi, and W.S. Party (1998b),A submersible study of the western intersection of the Mid-Atlantic ridge and Kane fracture zone (WMARK), *Mar. Geophys. Res., 20,* 195-218.

Tivey, M.A., and B.E. Tucholke (1998),Magnetization of 0-29 Ma ocean crust on the Mid-Atlantic Ridge, 25° 30'N to 27° 10'N, *J. Geophys. Res., 103* (B8), 17807-17826.

Tucholke, B.E., M.D. Behn, W.R. Buck, and J. Lin (2007),The role of melt supply in detachment faulting and the formation of oceanic core complexes, *submitted to Geology*.

Tucholke, B.E., K. Fujioka, T. Ishihara, G. Hirth, and H. Kinoshita (2001),Submersible study of an oceanic megamullion in the central North Atlantic, *Journal of Geophysical Research, 106,* 16145-16161.

Tucholke, B.E., J. Lin, and M.C. Kleinrock (1998),Megamullions and mullion structure defining oceanic metamorphic core complexes on the Mid-Atlantic Ridge,, *J. Geophys. Res., 103,* 9857-9866.

Tucholke, B.E., L. Lin, and M.C. Kleinrock (1996),Mullions,megamullions,and metamorphic core complexes on the Mid-Atlantic Ridge, *EOS Trans. AGU, 77* (46), Fall Meet. Suppl., F724.

Verosub, K.L., and E.M. Moores (1981),Tectonic rotations in extensional regimes and their paleomagnetic consequences for oceanic basalts, *Journal of Geophysical Research, 86,* 6335-6349.

Vine, F.J., and D.H. Matthews (1963), Magnetic anomalies over oceanic ridges, *Nature, 199,* 947-949.

Wessel, P., and W.H.P. Smith (1991),Free software helps map and display, *EoS Trans. AGU, 72,* 44.

168

Wilson, D.S., and R.N. Hey (1981),The Galapagos axial magnetic anomaly: evidence for the Emperor event within the Brunhes and for a two-layer magnetic source, *Geophys. Res. Letts.*, *8*, 1051-1054.

Yoerger, D., A. Bradley, M. Jakuba, C.R. German, T. Shank, and M.A. Tivey (2007),Autonomous and remotely operated vehicle technology, *Oceanography*, *20* (1), 152-161.

Zhao, X., P. Riisager, M. Antretter, J. Carlut, P. Lippert, Q. Liu, B. Galbrun, S. Hall, H. Delius, and T. Kanamatsu (2006),Unraveling the magnetic carriers of igneous cores from the Atlantic, Pacific and the southern Indian oceans with rock magnetic characterization, *Phys. Earth Planet. Inter.*, *156*, 294-328.

Table 4-1 Geomagnetic Polarity Timescale

Polarity Chron	Top (Ma)	Base (Ma)	Polarity Chron Name
1n	0.000	0.781	Brunhes/ Matayama
1r.1n	0.988	1.072	Jaramillo
1r.2n	1.173	1.185	Cobb Mountain
2n	1.778	1.945	Olduvai
2r.1n	2.128	2.148	Reunion
2An.1n	2.581	3.032	Gauss
2An.2n	3.116	3.207	
2An.3n	3.330	3.596	
3n.1n	4.187	4.300	Cochiti
3n.2n	4.493	4.631	Nunivak
3n.3n	4.799	4.896	Sidufjall
3n.4n	4.997	5.235	Thvera
3An.1n	6.033	6.252	
3An.2n	6.436	6.733	
3Bn	7.140	7.212	
3Br.1n	7.251	7.285	
3Br.2n	7.454	7.489	
4n.1n	7.528	7.642	
4n.2n	7.695	8.108	
4r.1n	8.254	8.300	
4An	8.769	9.098	
4Ar.1n	9.312	9.409	
4Ar.2n	9.656	9.717	
5n.1n	9.779	9.934	

Table 4-2 Spreading rates and asymmetry referenced to the west

Profile	Spreading rate (km/Ma) West	East	Total	% Asym (0-6 Ma)	% Asym (6-10 Ma)	% Asym (0-10 Ma)
North	14.5	8.8	23.3	65	58	62
Central	14.3	9.0	23.3	60	56	61
South	14.4	9.1	23.5	60	57	61
22° 50'N	13.4	10.1	23.5	52	62	57

Table 4-3 Magnetic property parameters

Lithology	K (x 10^3 SI)	NRM (A/m)
Basalts	5.28	8.70
Diabases	0.93	0.08
Gabbros	18.39	1.50
Peridotites	45.33	4.70

170

Table 4-4 Thermal modeling results

M 0.3 Nu 2

Time (Ma)	Initial Dip (°)	Final Dip (°)	Rotation (°)
0.25	174	124	-50
0.5	165	135	-30
0.75	155	138	-17
		Average Rotation	-32

M 0.3 Nu 4

Time (Ma)	Initial Dip (°)	Final Dip (°)	Rotation (°)
0.25	174	154	-20
0.5	167	140	-27
0.75	169	159	-10
		Average Rotation	-19

M 0.3 Nu 8

Time (Ma)	Initial Dip (°)	Final Dip (°)	Rotation (°)
0.25	177	150	27
0.5	176	157	-19
0.75	173	154	-19
		Average Rotation	-4

M 0.4 Nu 2

Time (Ma)	Initial Dip (°)	Final Dip (°)	Rotation (°)
0.25	164	134	-30
0.5	158	139	-19
0.75	149	137	-12
		Average Rotation	-20

M 0.4 Nu 4

Time (Ma)	Initial Dip (°)	Final Dip (°)	Rotation (°)
0.25	170	142	-28
0.5	167	123	-44
0.75	164	119	-45
		Average Rotation	-39

M 0.4 Nu 8

Time (Ma)	Initial Dip (°)	Final Dip (°)	Rotation (°)
0.25	176	138	-38
0.5	175	128	-47
0.75	173	130	-43
		Average Rotation	-43

M 0.5 Nu 2

Time (Ma)	Initial Dip (°)	Final Dip (°)	Rotation (°)
0.25	159	148	-11
0.5	163	157	-6
0.75	160	149	-11
		Average Rotation	-9

M 0.5 Nu 4

Time (Ma)	Initial Dip (°)	Final Dip (°)	Rotation (°)
0.25	170	141	-29
0.5	166	130	-36
0.75	166	124	-42
		Average Rotation	-36

M 0.5 Nu 8

Time (Ma)	Initial Dip (°)	Final Dip (°)	Rotation (°)
0.25	Model stopped before 3 Myrs		
0.5			
0.75			
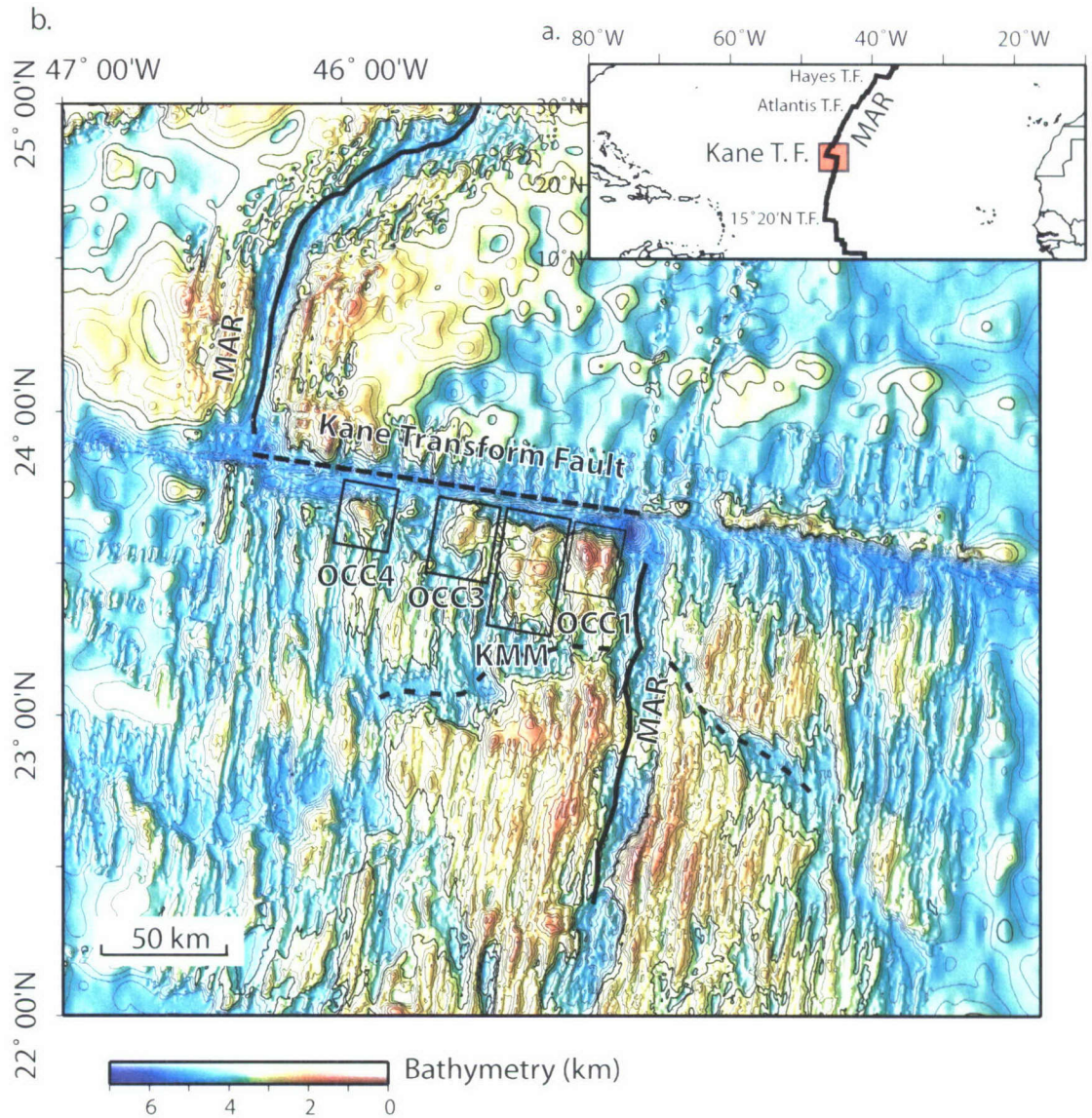
Figure 4-1. a. Regional location map of the northern Atlantic Ocean showing the Mid-Atlantic Ridge (MAR) and transform faults. Our study area, outlined by the red box, is located in the region of the Kane Transform Fault. **b**. Bathymetric map of the Kane Transform Fault area showing the location of Kane Megamullion (KMM) south of the Kane Transform Fault and ~ 40 km to the west of the MAR. Additional shallow seafloor features (possibly other ocean core complexes (OCC)) also located on the south side of the transform fault (OCC1, OCC3 and OCC4) are highlighted by the black rectangles. The ridge south of the Kane Transform is separated into two segments by a ridge discontinuity at 23° 10'N. The region to the north of the discontinuity is dominated by core complexes on the western flank, compared with normal seafloor to the south.
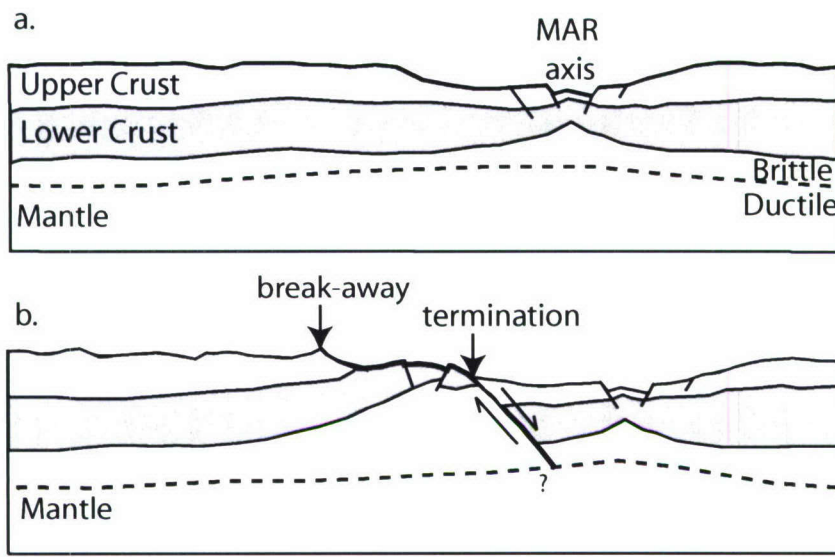
Figure 4-2. Schematic of the formation of Kane Megamullion. **a.** Normal faults form near the MAR axis. **b.** Large scale detachment fault exhumes lower crust and upper mantle. The detachment fault initiates at the breakaway and the fault surface extends as far as the termination, where it dips below the surface. The dip of the fault surface and depth at which the fault soles out are not well understood at this time.
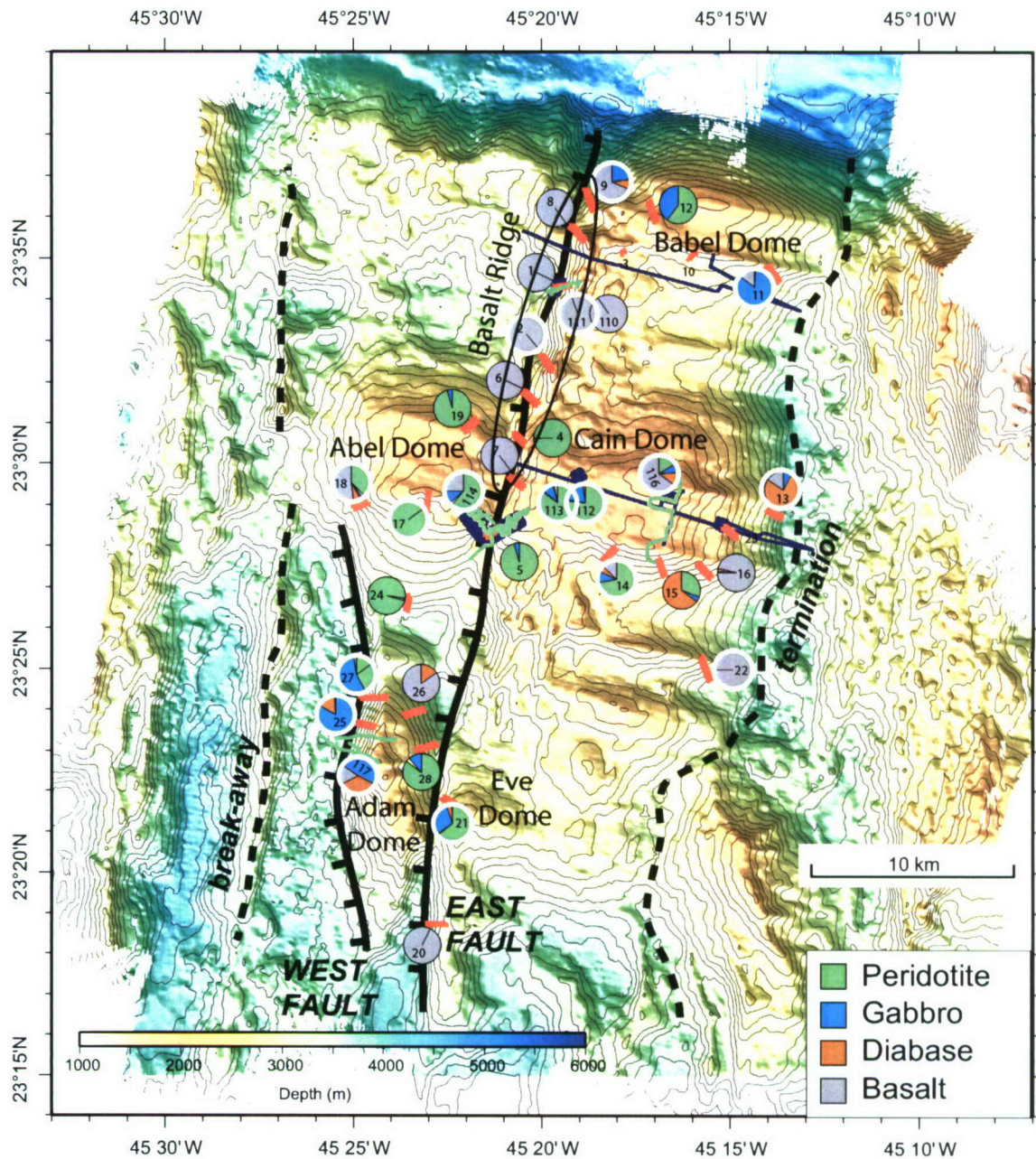
Figure 4-3. Bathymetric color grid of Kane Megamullion. The detachment fault surface extends from the break-away to the termination. Kane Megamullion has a smooth, domed appearance with spreading-parallel corrugations. Dredge locations are shown in red, ABE dive profiles in blue and Jason dive locations in green. Numbered pie charts are included of the rock sample lithologies from each dredge and Jason dive. Rock magnetic and paleomagnetic analyses were carried out on 48 samples taken from the dredges and dive pie charts outlined in white [*Williams et al.* ,in prep]. Domes and a lineated basalt ridge are labeled.

174
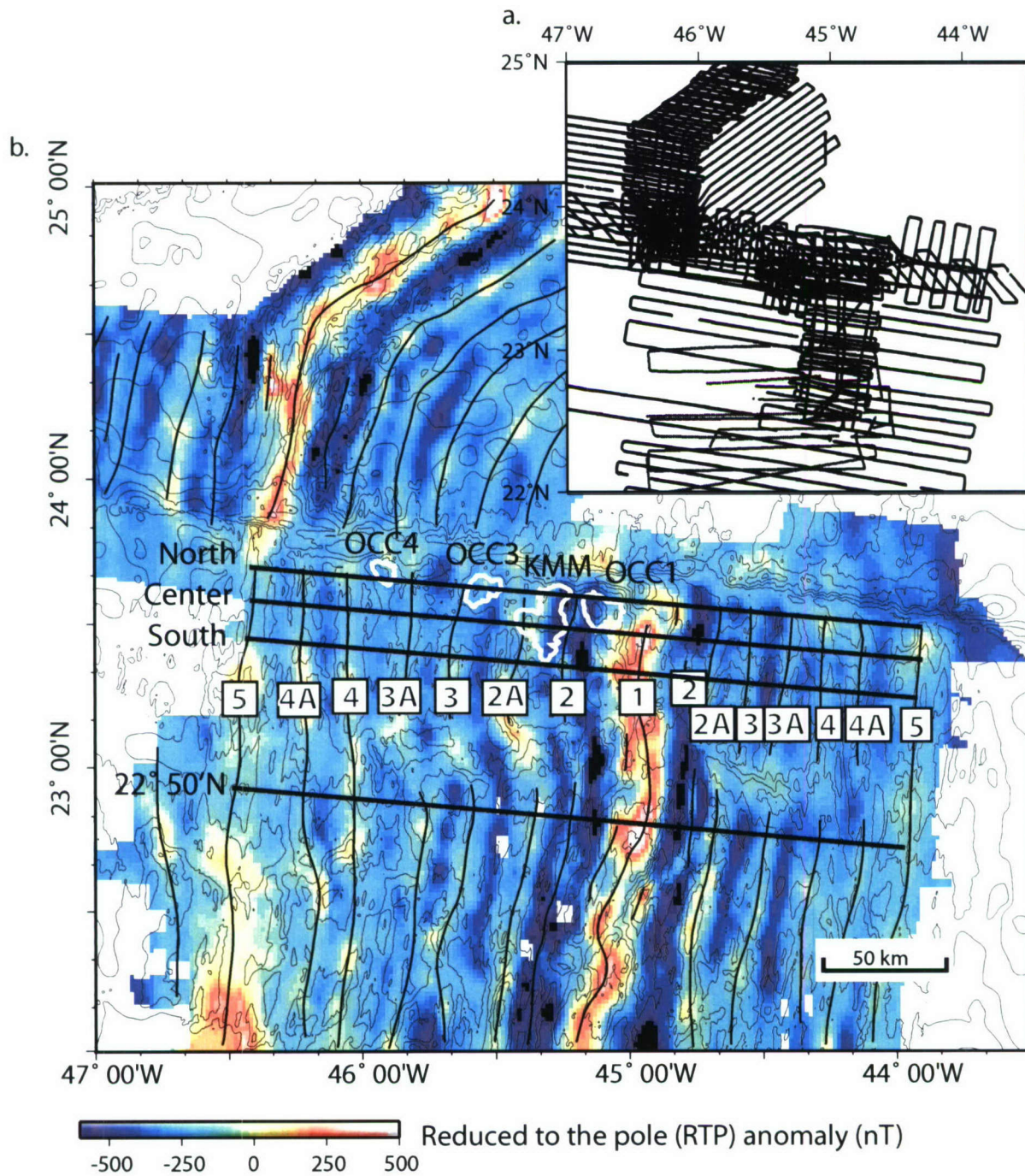
Figure 4-4. Regional RTP sea surface magnetic anomaly grid. **a.**Tracklines of surveys compiled to create the magnetic grid. **b**. Reduced to the pole magnetic anomaly grid. Polarity Chrons 1 through 5 are labeled (0 ~ 10 Myrs). Four profile locations across the northern, central and southern portions of KMM and 22° 50'N are shown by solid black lines.
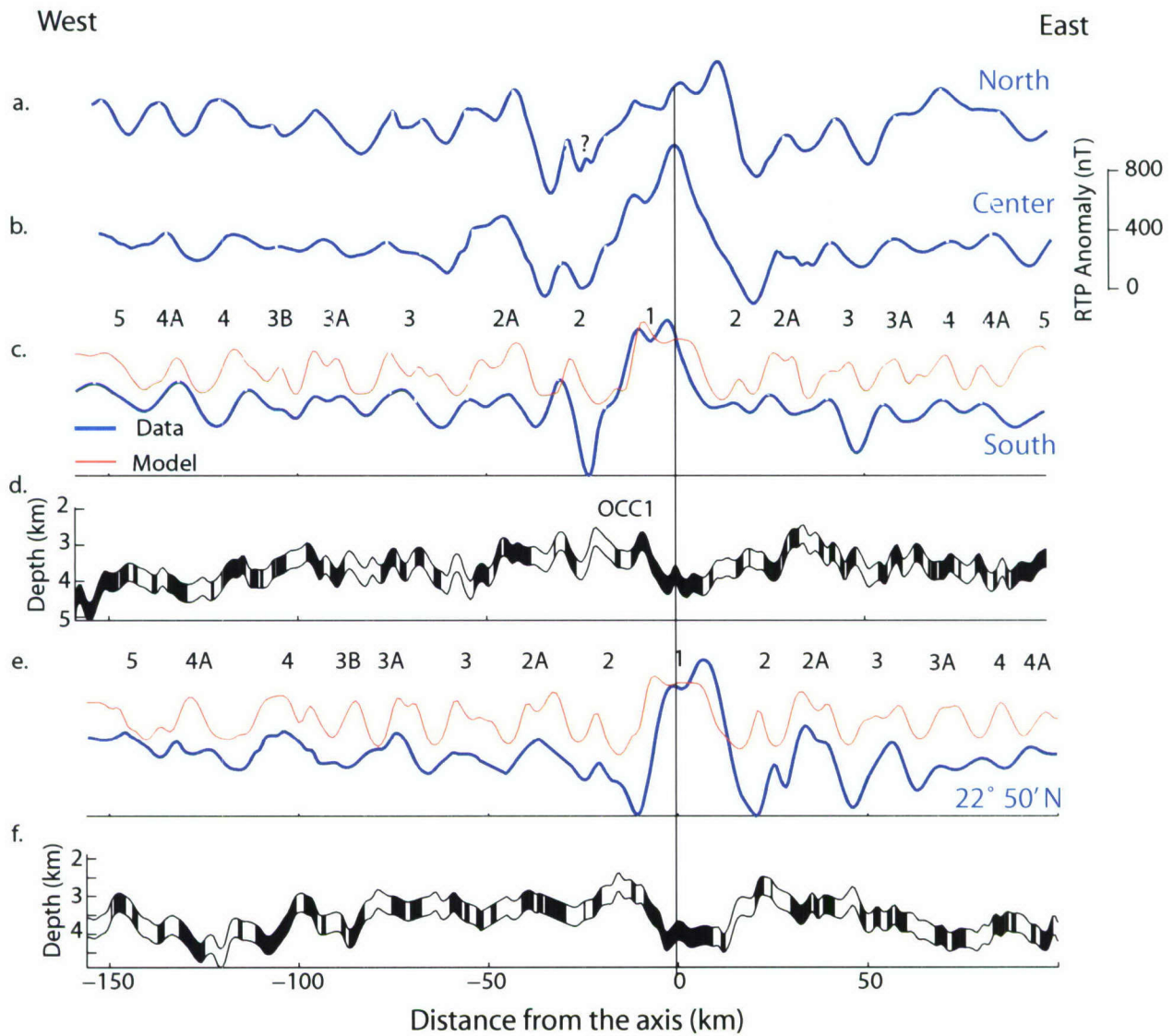
Figure 4-5. Reduced to the pole magnetic anomalies along the **a.** North, **b.** Center and **c.** South profiles (blue lines, see Fig. 4-4 for locations) and model results (red line) using the software MODMAG [*Mendel et al.*, 2005]. Chrons 1 though 5 are labeled. **d.** Bathymetry along the south profile with normal (black) and reverse (white) magnetic polarities and 1 km source magnetic layer thickness. **e.** 22° 50'N magnetic profile (blue line) and model (red line) results, and **f.** 22° 50'N bathymetry profile.
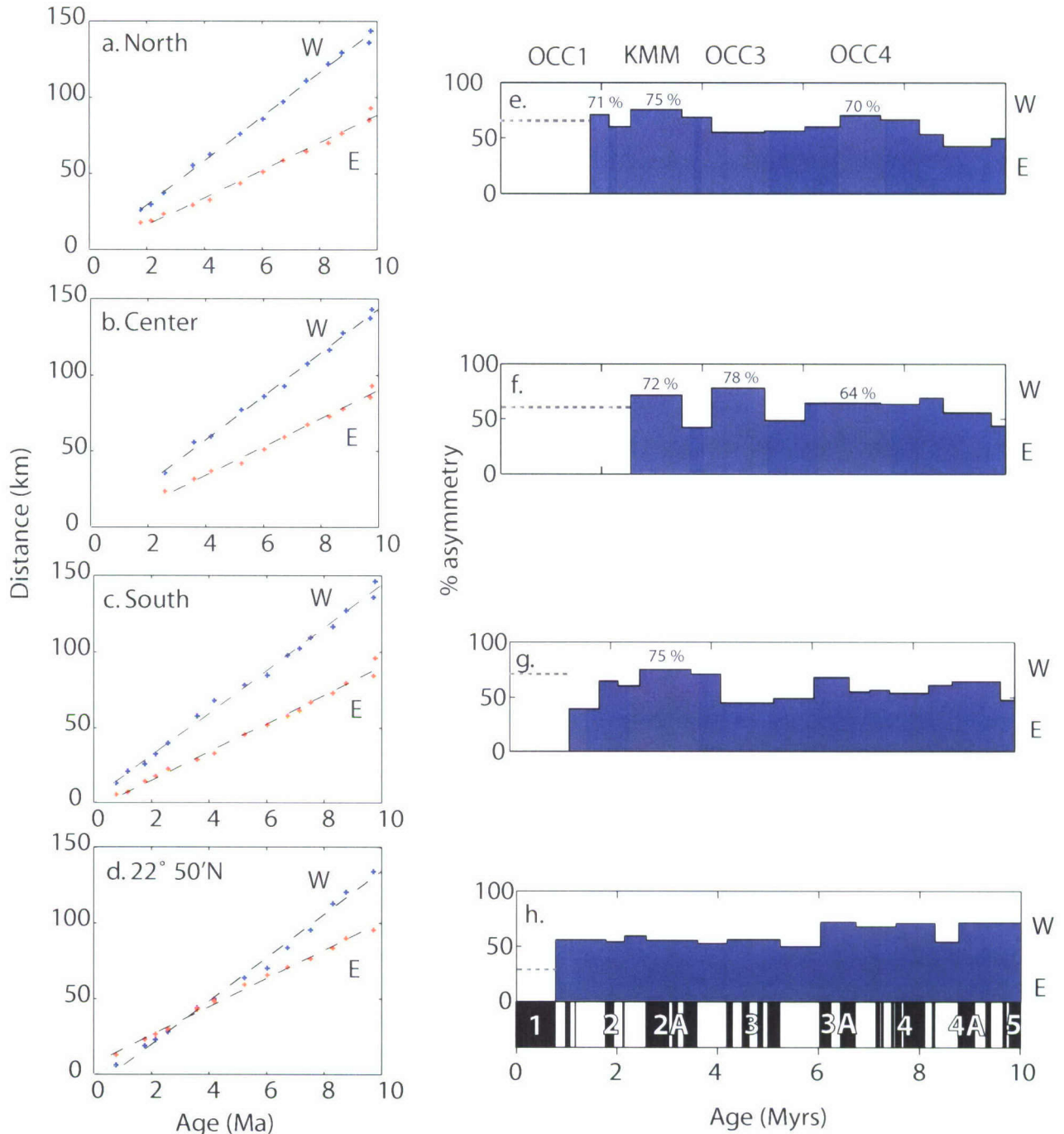
Figure 4-6. Plots show spreading rates along **a.** North **b.** Center **c.** South and **d.** 22° 50'N Profiles. Black dashed lines are least squares best fit, blue crosses are picks on the western flank, red crosses the eastern flank. Bar charts represent percent asymmetry of spreading rate during each identified chron, where 50 % is symmetric spreading. **e.** North **f.** Center **g.** South and **h.** 22° 50'N Profiles. Grey regions represent the locations of KMM and the other OCC's. Grey dashed lines show average asymmtery from 0 Myrs to the first isochron pick
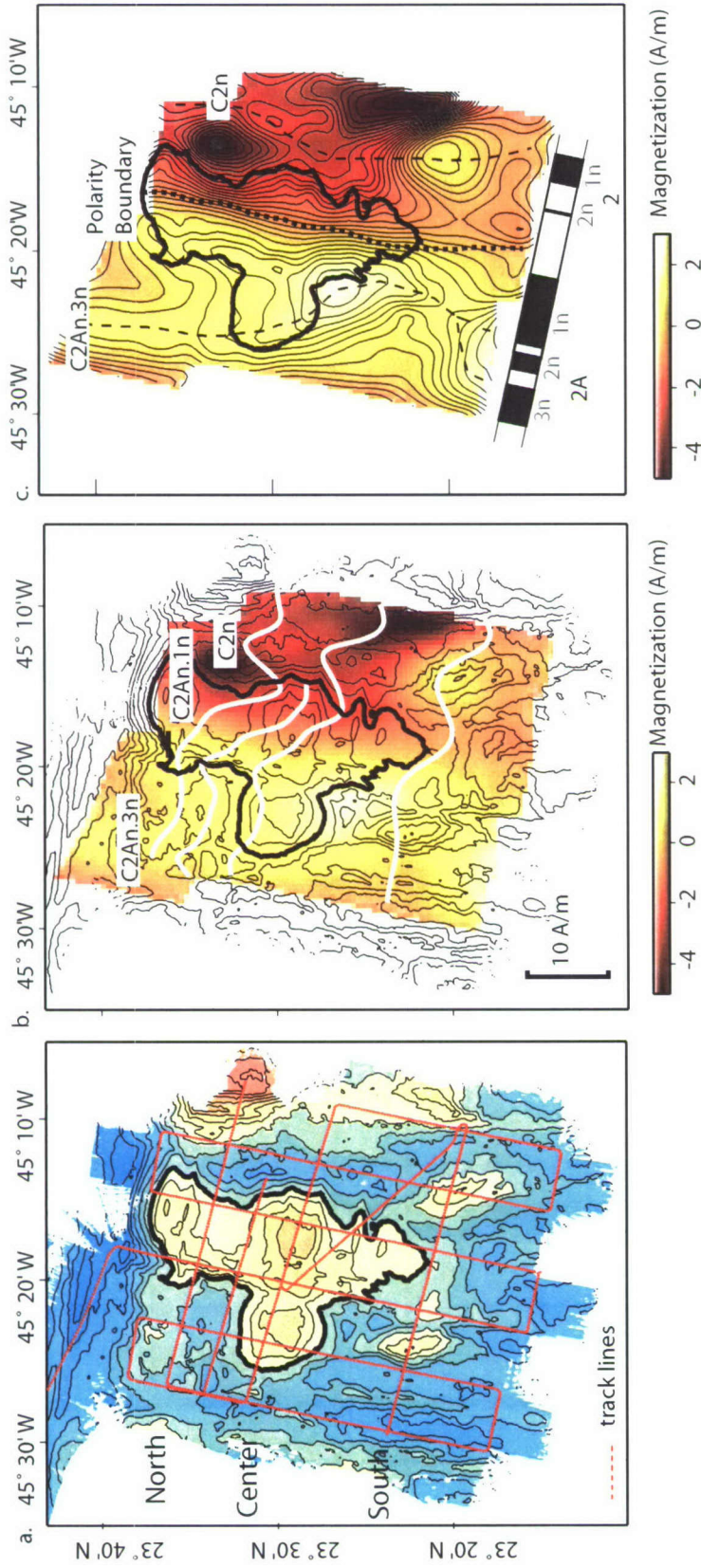
Figure 4-7. Kane megmullion sea surface magnetic anomaly grid. **a.** Bathymetry with sea surface survey tracklines shown in red. **b.** Inversion of the sea surface grid assuming a 1 km source layer and geocentric axial dipole magnetization direction. Contours are bathymetry. **c.** Contoured inversion results with 0.25 A/m contour interval. Location of KMM is shown by the black outline. Chrons 2 and 2A are made up of several subchrons. C2r.2r/C2An.1n polarity boundary is shown by the thick dashed black line.

179
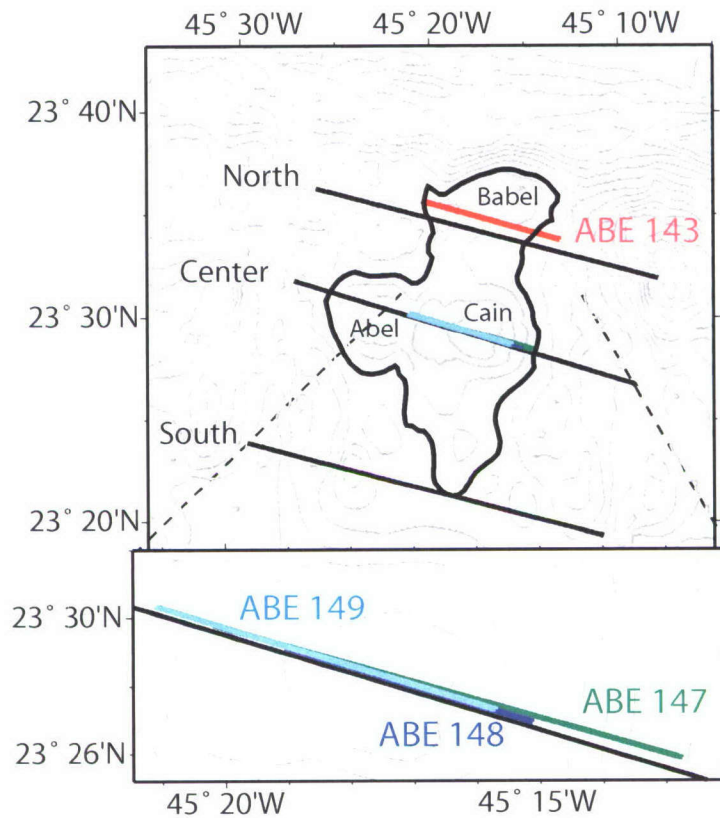
Figure 4-8. Location map of the sea surface (solid black lines) and ABE profiles (colored lines) collected across Kane Megamullion. Contours are bathymetry. Profiles ABE 143 and ABE 147 were collected at 20 m above the seafloor, ABE 148 at 60 m and ABE 149 at 250 m.

a. North profile- Babel Dome

West   basalt block   C2An.2n   C2An.1n   East

ABE143- 20 m

A/m 5 / 0 / −5

Polarity transition zone

10 12 14 16 18 20 22 24
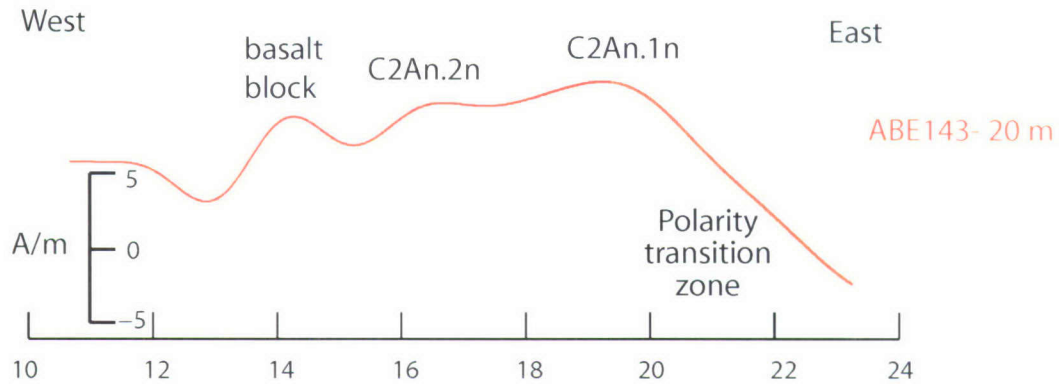
b. Center profile- Cain Dome

West   C2An.2n?   C2An.1n   East

ABE149- 250 m

ABE148- 60 m

A/m 2.5 / 0 / -2.5

Polarity transition zone

ABE147- 20 m

C2r.2r

12 14 16 18 20 22

Distance (km)
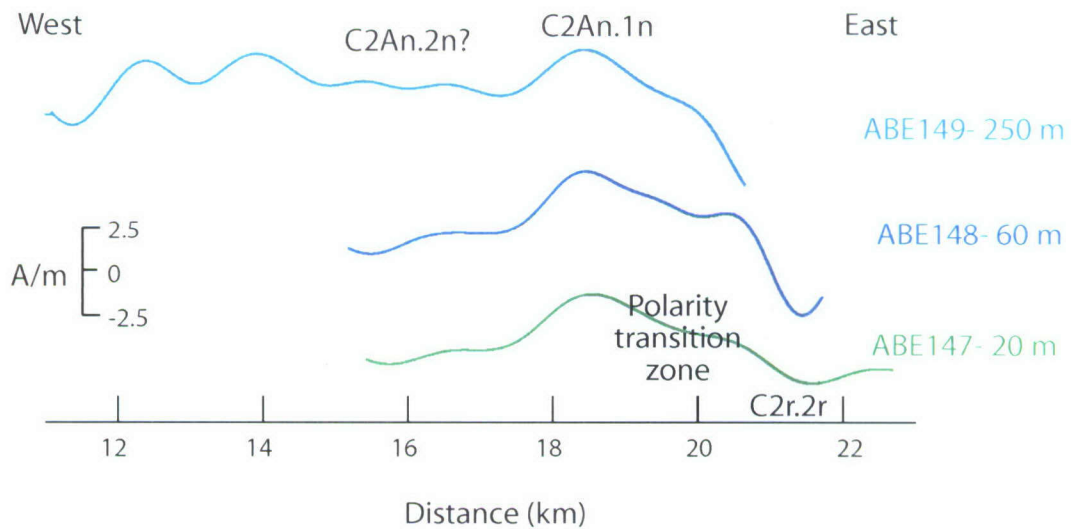
Figure 4-9. ABE inversion results **a**. North profile (ABE 143) and **b**. Center profile (ABE 147, ABE 148 and ABE 149). Inversion assumes geocentric axial dipole magnetization direction and a source layer thickness of 1 km. The first subchron C2An.1n, possible location of second subchron C2An.2n and anomaly due to the basalt ridge are labeled The polarity transition zone between C2r.2r and C2An.1n is defined by the grey box.

a. Anomaly

2 km

0.25 km

0.05 km

b. Analytic signal

— dM/dx
— dM/dz

c. Analytic amplitude

d. Analytic phase

e.

45°

N   R

2 km

Distance (km)
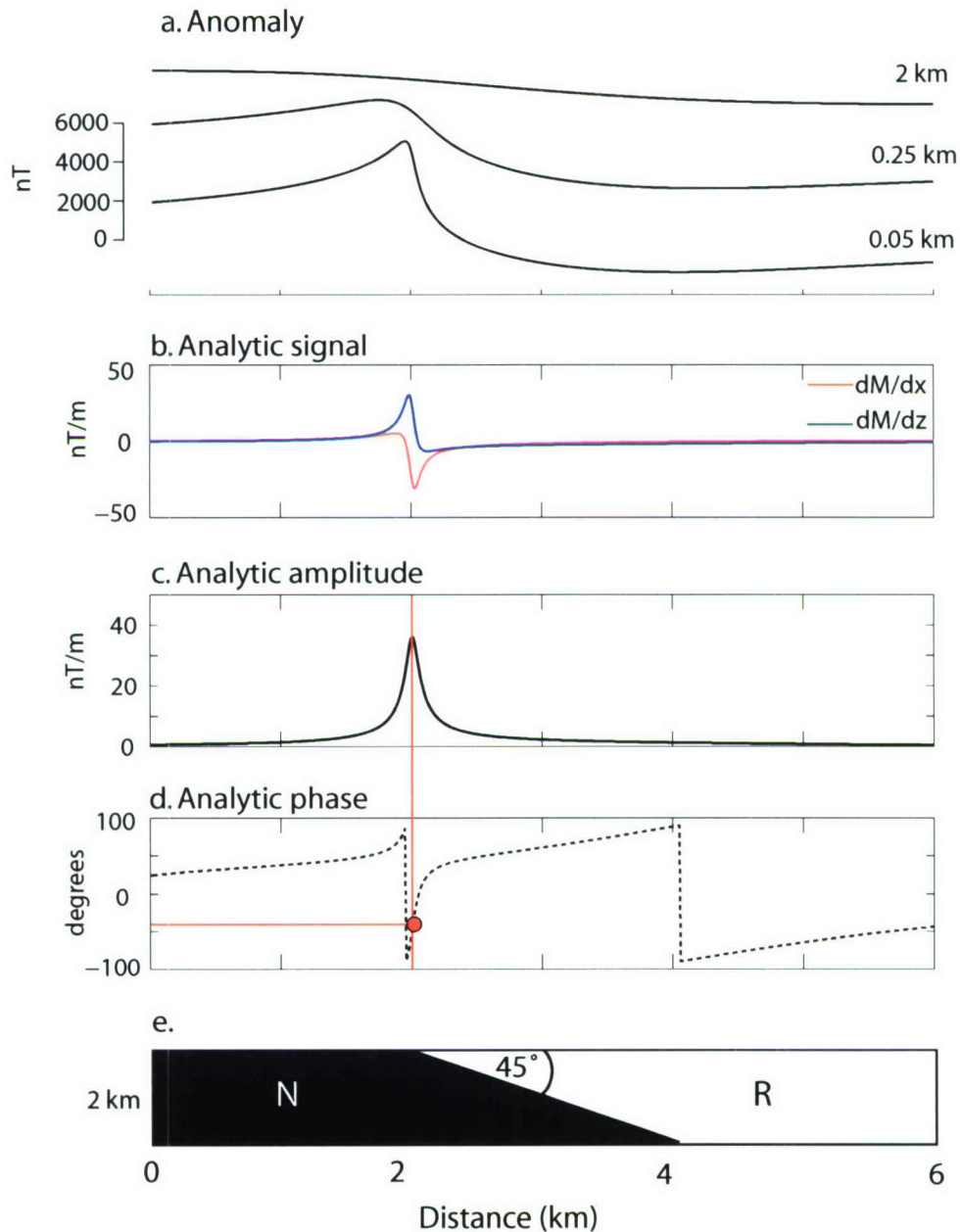
Figure 4-10. a. Anomaly calculated at 2 km, 0.25 km and 0.05 km above the model with a 45° dipping contact. The 0.05 km altitude anomaly is then used to calculate the dip of a contact boundary with the analytic signal approach. **b.** Analytic signal showing real (horizontal derivative, red) and imaginary parts (vertical derivative, blue). **c.** Analytic amplitude and **d.** analytic phase. The analytic amplitude is symmetric about the contact and its peak defines the edge of the contact boundary (x=0) for a semi-infinite contact. The analytic phase (Θ) at x=0 is used to calculate the dip of the contact where d=Θ+2I'-90.
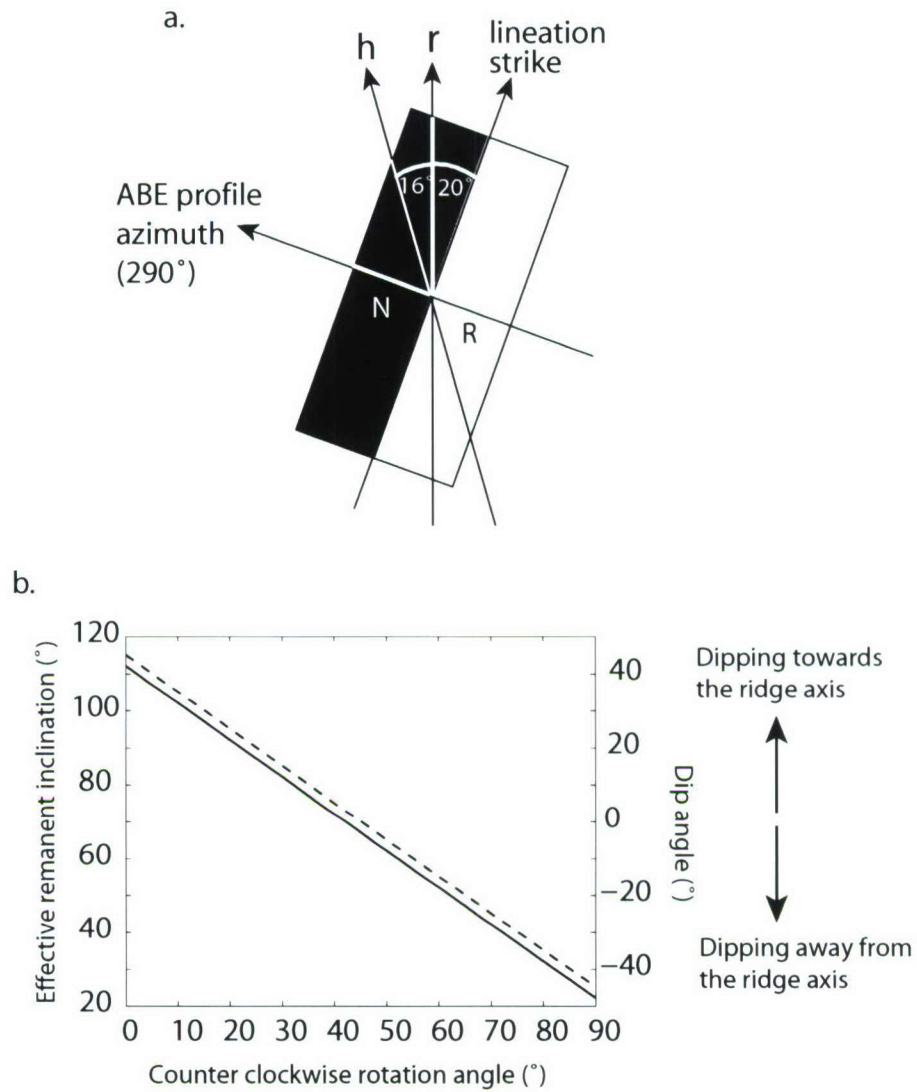
Figure 4-11 a. Model parameters. Remanent magnetization direction r (geocentric axial dipole direction, inclination 40° and declination 0°) and present day geomagnetic field h (inclination 41° and declination 344°). The strike of the magnetic lineations is ~20° clockwise of north and the azimuth of the ABE profiles is 290° (approximately east to west). **b.** Effective remanent inclination (solid black line) and dip angles (dashed black line) for a 45° dipping boundary model that has been rotated counter clockwise between 0° to 90°. Both variables decrease with increasing rotation angle.
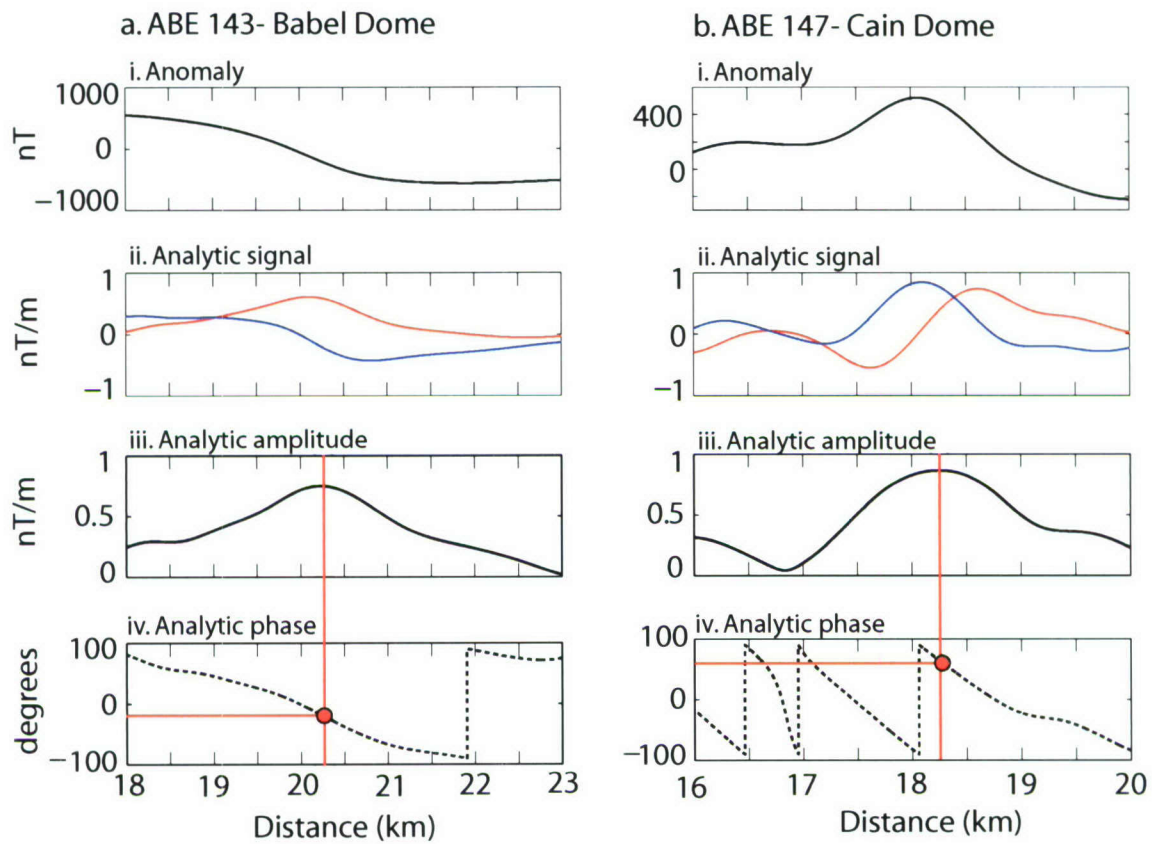
Figure 4-12. Analytic signal approach for the polarity transition zone along **a**. ABE 143 and **c.** ABE 147 profiles continued to 2.18 km water depth. Sequence of panels is the same as Fig. 4-10. The polarity boundary is located at ~20.3±0.1 km along ABE 143 and has a phase value of -18°±10°. The polarity boundary along ABE 147 is located at ~18.2± 0.1 km and has a phase value of 64°±12°. Grey regions define the errors in the polarity boundary location and phase values.
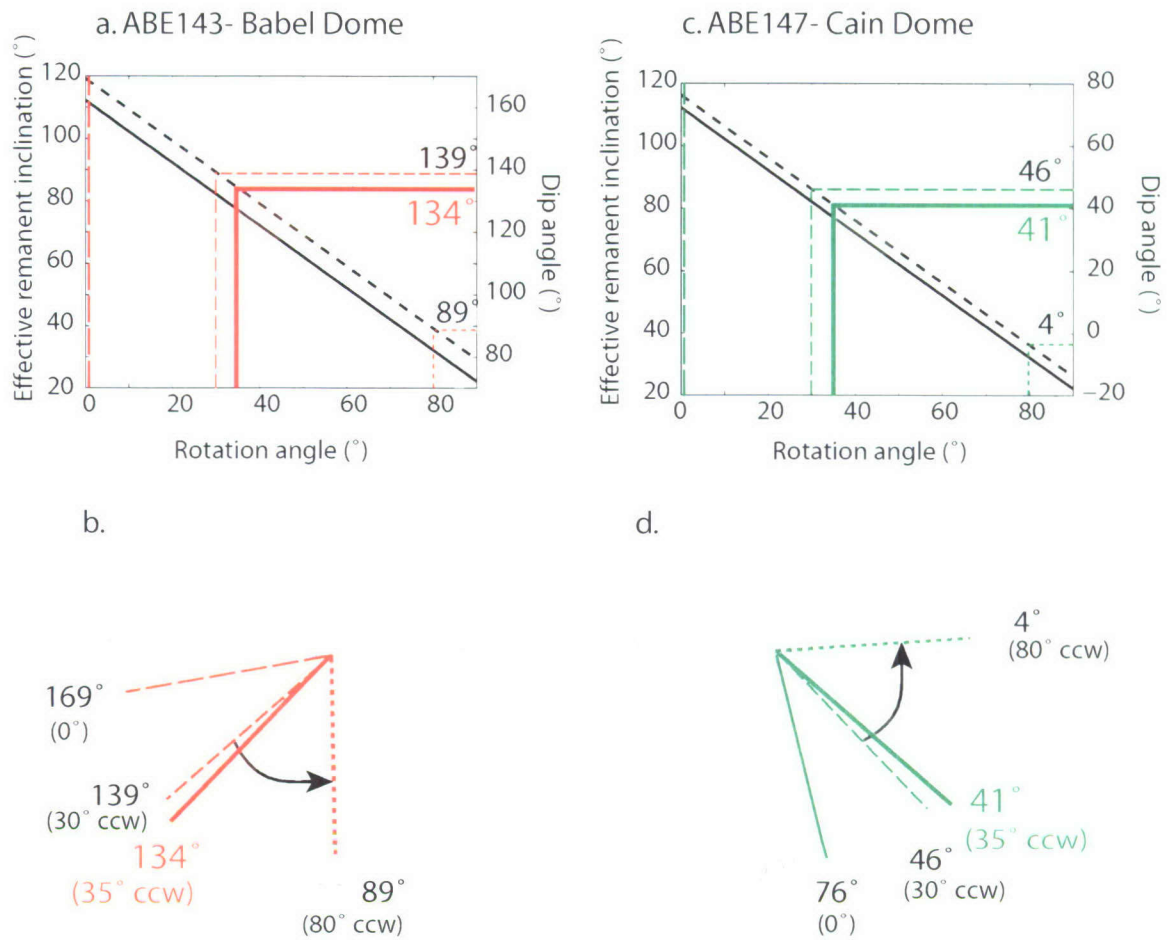
Figure 4-13. Counter clockwise rotation of the polarity boundary through changing effective inclination angle (solid black line) and resulting change in dip angles (dashed black line) assuming an intial remanent direction of GAD (inclination of 40°) and rotation axis of 20°.**a**. ABE 143 at Babel Dome and **c**. ABE 147 at Cain Dome . Grey regions represent the range of calculation errors. Dip values for rotation angles of 0° (broad dashed line), 30°(medium dashed line) and 80°(fine dashed line) are plotted for **b**. ABE 143 and **d**. ABE 147. We estimate the minimum rotation angle to be 35°, based on the appearance of the basalt ridge at the northern end of East Fault (Fig. 4-16). This rotation angle results in dip angle of 134°±14° at Babel Dome and 41°±17° at Cain Dome.

a. Anomaly profiles

Sea surface
(v.e. x 5)

ABE143-2.18 km

C2An.1n

ABE143- observed

C2r.2r

b. Bathymetry

ABE143- 2.18 km

ABE143- 20 m
observed

basalt
ridge
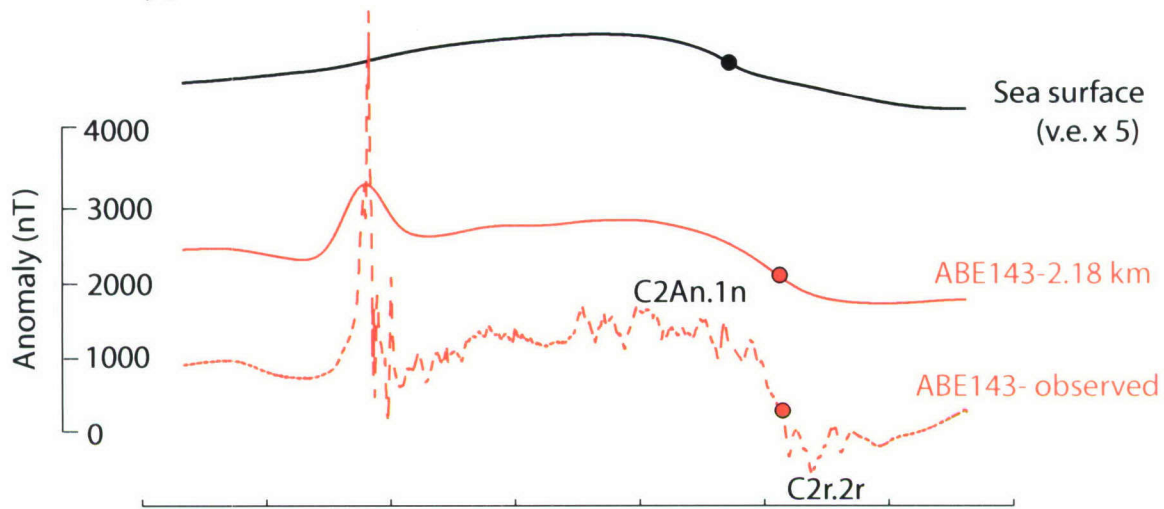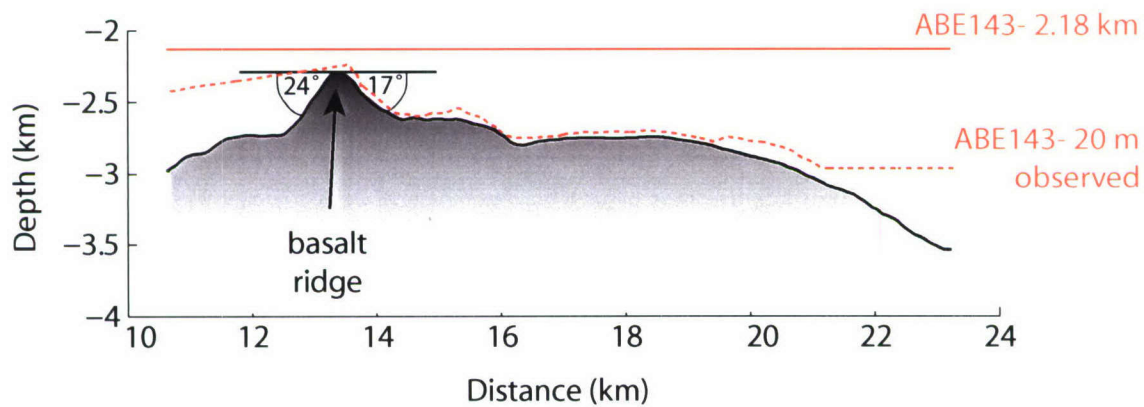
Figure 4-14. North profiles at Babel Dome. **a.** Sea surface profile (solid black line), ABE 143 continued to 2.18 km (solid red line) and ABE 143 at 20 m above the seafloor (dashed red line). Solid dots indicate the location of the polarity boundary contact along each profile from the peak in the analytic amplitude. **b.** Bathymetry along the profile. The basalt ridge is located at ~ 13 km along the profile and correlates with the short wavelength, high amplitude peak in the ABE 143 profiles. Basalt ridge slope angles from horizontal are labeled.

a. Anomaly profiles

Sea Surface

ABE149- 1.95 km

ABE148- 2.14 km

ABE 147- 2.18 km

ABE147- 20 m

C2An.1n

C2r.2r

Anomaly (nT)

1000
750
500
250
0

10 12 14 16 18 20 22 24

b. Bathymetry

1.95 km
2.14 km
2.18 km

ABE 147- 20 m
observed level

Depth (km)

-2
-2.4
-2.8

10 12 14 16 18 20 22 24

Distance (km)
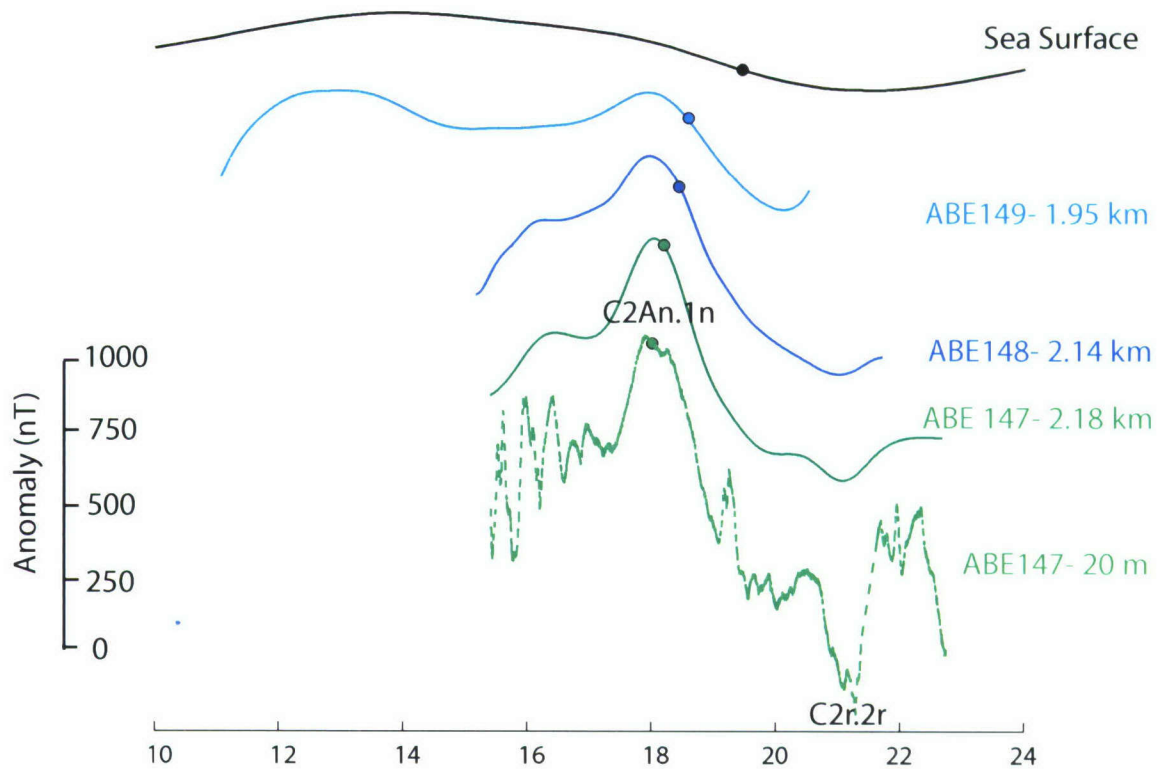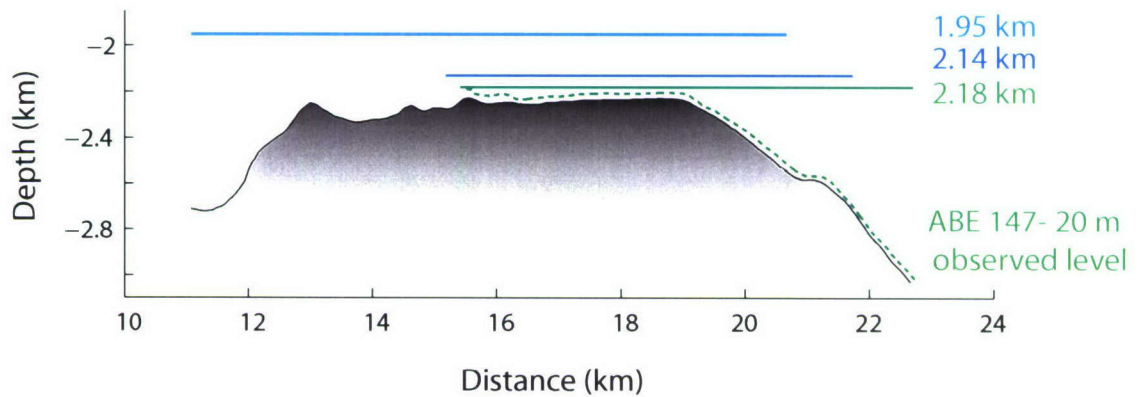
Figure 4-15. Center profiles **a**. Sea surface profile (solid black line), ABE 149 continued to 1.95 km (solid light blue line), ABE 148 continued to 2.14 km (solid dark blue line), ABE 147 continued to 2.18 km (solid green line) and ABE 147 at 20 m above the seafloor (dashed green line). Colored dots indicate the location of the polarity boundary, based on the peak in the analytic amplitude for each profile .**b**. Bathymetry along the profile.
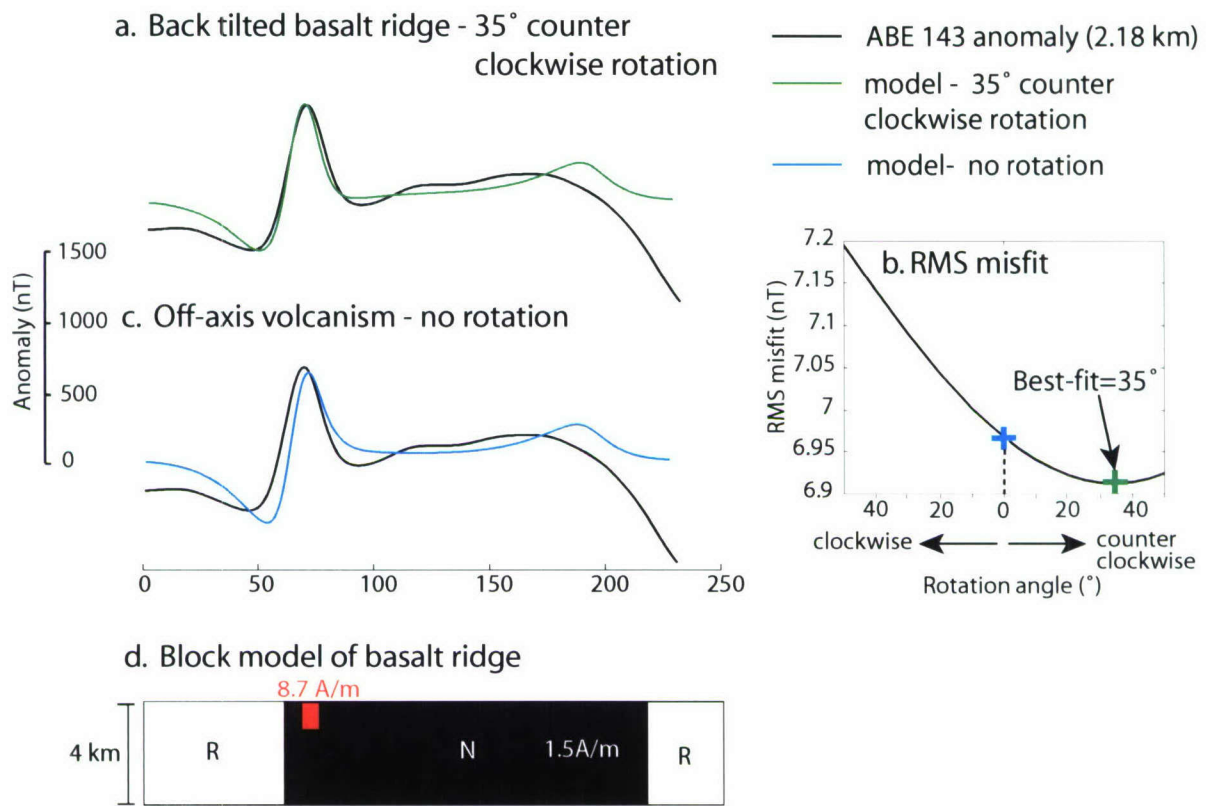
Figure 4-16. Basalt ridge block model. The basalt ridge has an NRM of 8.7 A/m, while the surrounding gabbros have NRM of 1.5 A/m. The model assumes geocentric axial dipole magnetization direction and basalt ridge is rotated by changing the phase value of the anomaly. We focus on fitting the anomaly at the basalt ridge .**a**. North profile across Babel Dome (ABE 143) continued to 2.18 km water depth (black line) and best-fit model profile, which has a rotation of 35° counterclockwise (green line). The model results therefore suggest that the basalt ridge has been back tilted **b**. RMS misfit between the ABE 143 profile and the block model profile. **c**. Model profile assumes no rotation of the basalt ridge, which may be expected if the basalt ridge was formed by off-axis volcanism.**d**. Parameters used in block model. Gabbros with normal polarity are shown in black and the basalt ridge in red.
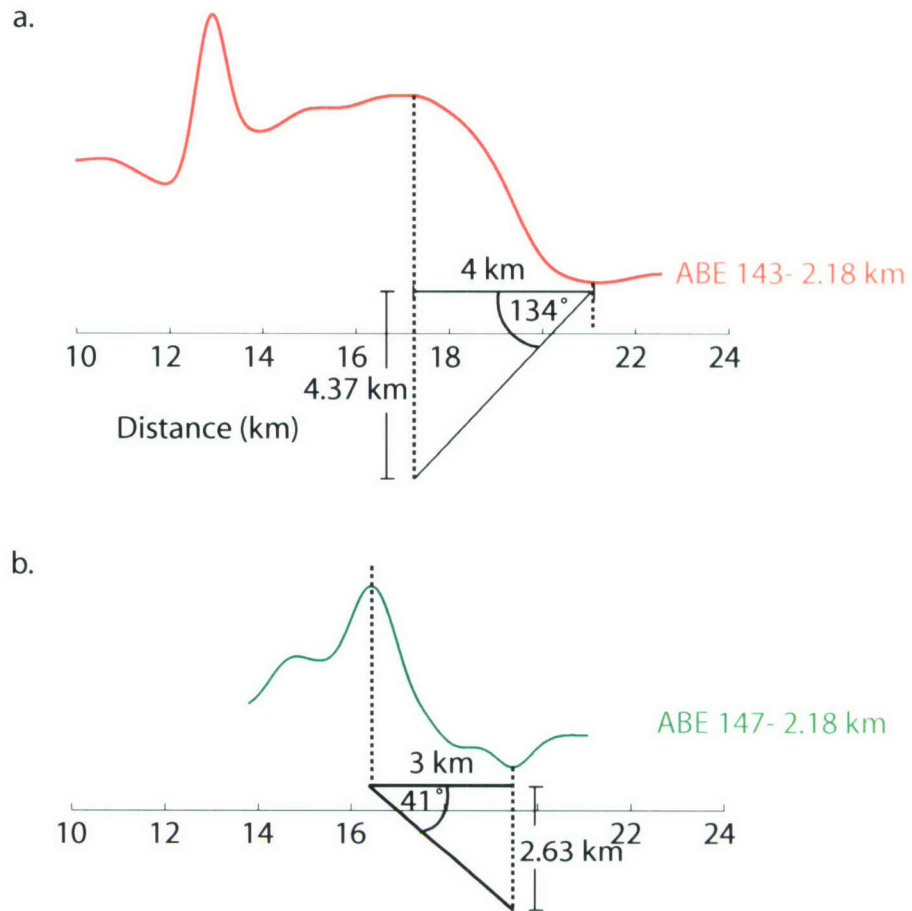
Figure 4-17. Source layer thickness calculation for **a**. Babel Dome (ABE 143) and **b**. Cain Dome (ABE 147). The layer thickness is calculated using simple trigonometry based on the transition zone width and the known dip of the polarity boundary
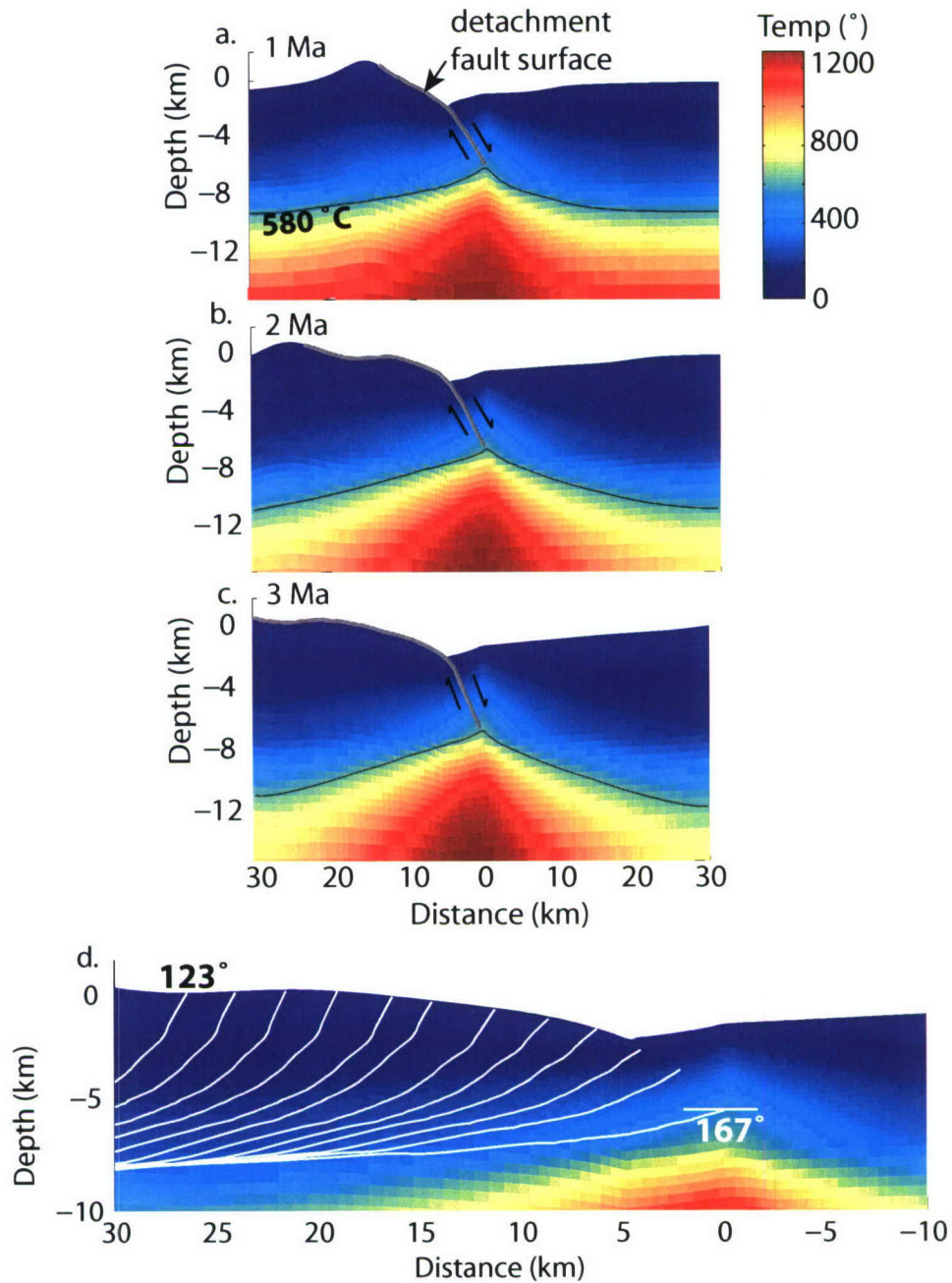
Figure 4-18. Example of two dimensional thermal model perpendicular to the ridge axis. In this example the model is shown at **a.** 1 Ma, **b.** 2 Ma and **c.** 3 Ma time steps and illustrates the development of a long lived detachment fault on the western flank. The 580 °C isotherm (Curie temperature of magnetite) is highlighted by the black solid line. **d.** The 580 °C isotherm at time 0.5 Ma is "frozen" into the subsurface and tracked through the evolution of the detachment fault over the next 2.5 Ma. The angle of the frozen isotherm increasing from ~ 167 ° at 0.5 Ma to ~ 5123 ° at 3 Ma. The core complex therefore experienced ~ 44° of counter clockwise rotation during its evolution.
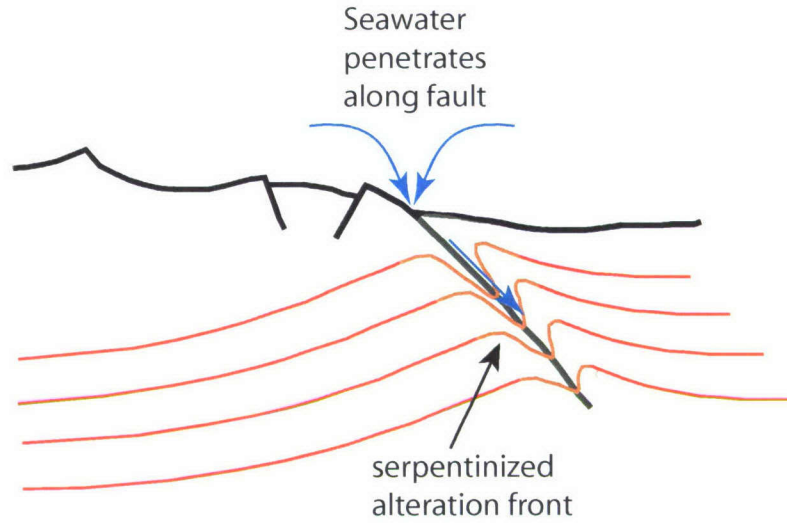
Figure 4-19. Cartoon of depressed isotherms at the detachment fault surface. Seawater penetrates the seafloor along the detachment fault, creating a serpenitized alteration zone in the peridotites (green shaded area). Isotherms (solid red lines) near the surface will be deflected to a greater extent than the deeper isotherms and may explain the steep polarity boundary at Cain Dome.
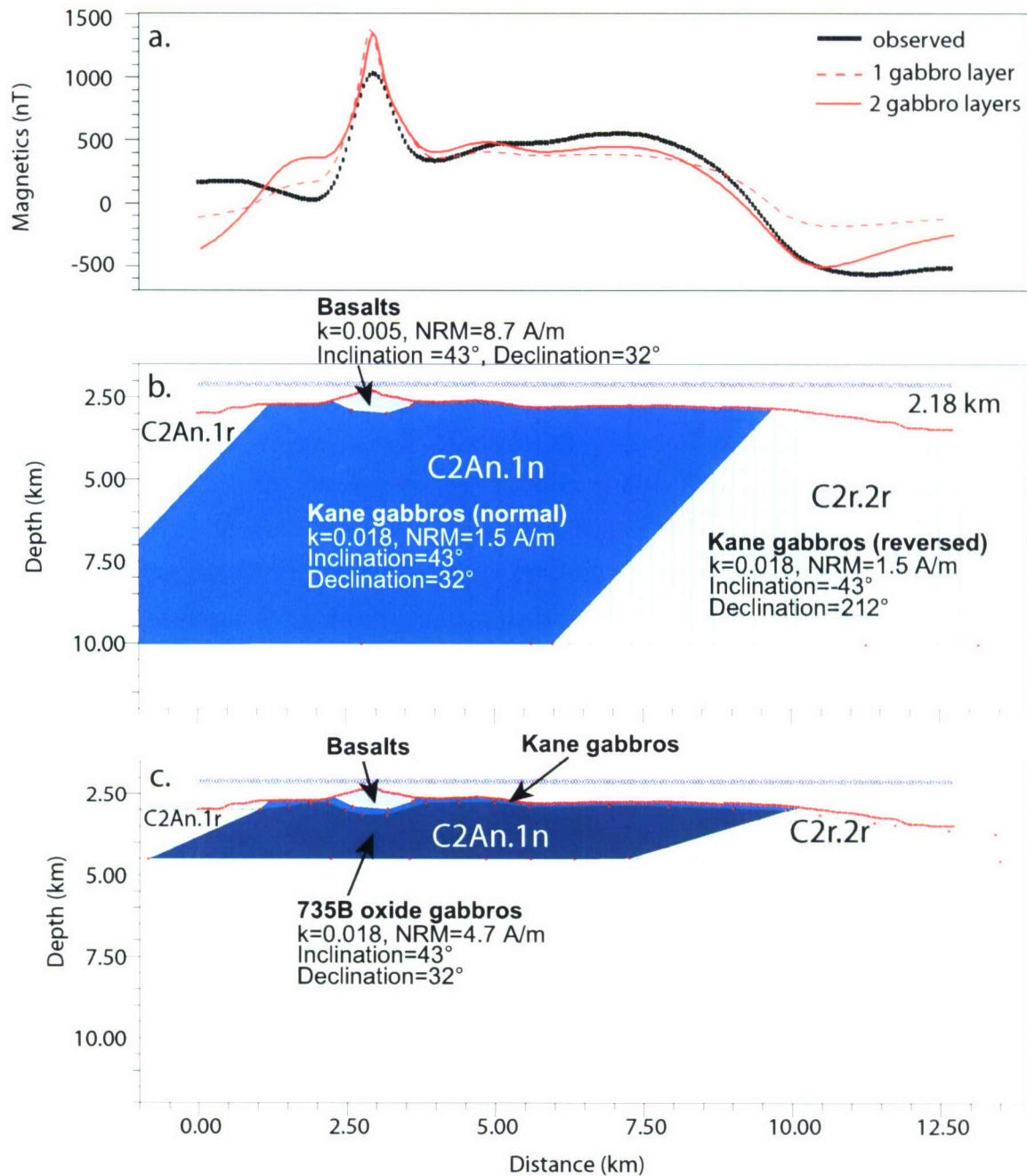
Figure 4-20. Model of subsurface structure along continued ABE 143 profile. **a.** Observed anomaly (black solid line) and calculated anomalies (red lines). **b**. Model of subsurface with a gabbro source layer (blue) and entrained basalt block (grey). We assume the Kane NRM and k values from Table 4-4. Inclination is 43° and declination is 32° for ~35° of counter clockwise rotation about a 20° ridge axis [*Verosub and Moores,* 1981], assuming an initial remanent direction of GAD. Solid colored blocks are normal polarity and dashed areas are reversed. **c.** Model with two gabbro layers and entrained basalt block. The Kane gabbros form a thin skin (< 200 m) over the surface of a deeper gabbro layer that has NRM of 4.7 A/m, which is the average NRM value for oxide gabbros from ODP 735B at Atlantis Bank [*Pariso et al.,* 1993a]
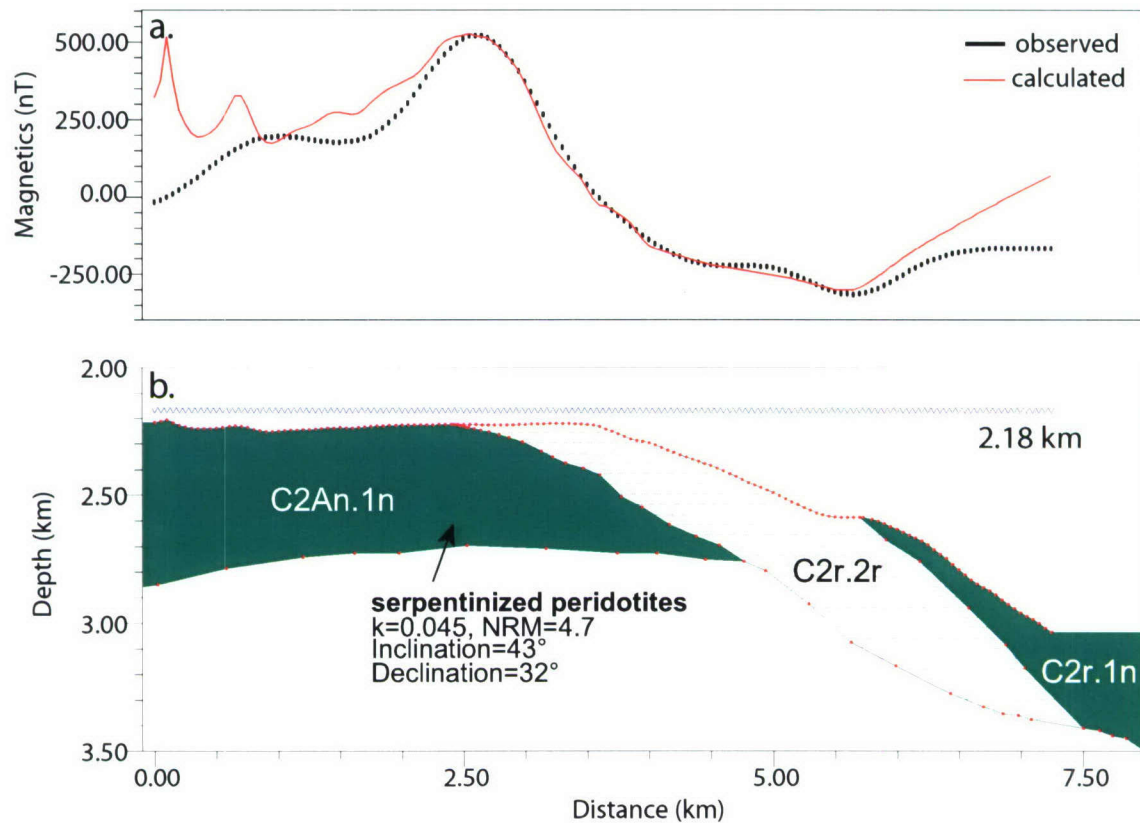
Figure 4-21. Model of subsurface structure along continued ABE 147 profile. **a.** Observed anomaly (black) and calculated anomaly (red). **b.** Model of subsurface showing only a thin peridotite layer is required to match the amplitude of the anomaly (~ 0.8 km) . Solid colored blocks are normal polarity peridotites and dashed blocks are reversed. We assume the NRM and k values from Table 4-4 [*Williams et al.*, in prep].

CHAPTER 5

Hydroacoustic events located at the intersection of the Atlantis (30°N) and Kane (23° 30'N) Transform Faults with the Mid-Atlantic Ridge[*]

Clare M. Williams, Ralph A. Stephen and Deborah K. Smith

Abstract

We investigate the characteristics of T-phase events located at the ends of two segments of the Mid-Atlantic Ridge. Our motivations for the study were to understand whether T-phase locations represent earthquake epicenters (and thus whether accurate geological inferences can be made from their spatial patterns) and to understand further the relationship between T-phase event characteristics and earthquake properties. We examine the characteristics of 158 T-phase events with respect to both event location water depth and source to receiver distance. The propagation paths of the T-phases are also modeled to study the effects of encountering seafloor topography. We find that existing models for T-phase excitation and propagation cannot explain adequately all of our observations. The amplitudes (Received Levels) of T-phases at the hydrophones show no dependence on event water depths, in contrast to current excitation models which predict a decrease in event magnitude with increasing water depth. The Received Levels are observed to decrease with increasing source to receiver distance, and events from the two study areas exhibit different trends in relative Received Levels between hydrophones, once attenuation is taken into account. Our acoustic ray trace model is able to reproduce similar trends in relative amplitudes at the hydrophones based on 1-D topography between the event and each hydrophone, but the variances in both the observed data and model are high. We observe a pattern of short T-phase onset times for shallow water events and long onset times for deep water events, where onset time is defined as the time interval between the appearance of the T-phase envelope above the ambient noise and its first peak. This suggests that the onset time may be a function of several variables, including efficiency of energy conversion based on local topography, efficiency of propagation based on event water depth, and hypocentral depth in the crust. The results of this study underscore the complexity of T-phase excitation and propagation and argue that current models of T-phase excitation and propagation need to be improved to explain the observed characteristics of T-phase data.

Reprinted with permission of American Geophysical Union

Hydroacoustic events located at the intersection of the Atlantis (30°N) and Kane (23°40′N) Transform Faults with the Mid-Atlantic Ridge

Clare M. Williams

MIT/WHOI Joint Program in Oceanography, Department of Geology and Geophysics, Woods Hole Oceanographic Institution, 360 Woods Hole Road, Woods Hole, Massachusetts 02540, USA (cwilliams@whoi.edu)

Ralph A. Stephen and Deborah K. Smith

Department of Geology and Geophysics, Woods Hole Oceanographic Institution, 360 Woods Hole Road, Woods Hole, Massachusetts 02540, USA

[1] We investigate the characteristics of T-phase events located at the ends of two segments of the Mid-Atlantic Ridge. Our motivations for the study were to understand whether T-phase locations represent earthquake epicenters (and thus whether accurate geological inferences can be made from their spatial patterns) and to understand further the relationship between T-phase event characteristics and earthquake properties. We examine the characteristics of 158 T-phase events with respect to both event location water depth and source to receiver distance. The propagation paths of the T-phases are also modeled to study the effects of encountering seafloor topography. We find that existing models for T-phase excitation and propagation cannot explain adequately all of our observations. The amplitudes (Received Levels) of T-phases at the hydrophones show no dependence on event water depths, in contrast to current excitation models which predict a decrease in event magnitude with increasing water depth. The Received Levels are observed to decrease with increasing source to receiver distance, and events from the two study areas exhibit different trends in relative Received Levels between hydrophones, once attenuation is taken into account. Our acoustic ray trace model is able to reproduce similar trends in relative amplitudes at the hydrophones based on 1-D topography between the event and each hydrophone, but the variances in both the observed data and model are high. We observe a pattern of short T-phase onset times for shallow water events and long onset times for deep water events, where onset time is defined as the time interval between the appearance of the T-phase envelope above the ambient noise and its first peak. This suggests that the onset time may be a function of several variables, including efficiency of energy conversion based on local topography, efficiency of propagation based on event water depth, and hypocentral depth in the crust. The results of this study underscore the complexity of T-phase excitation and propagation and argue that current models of T-phase excitation and propagation need to be improved to explain the observed characteristics of T-phase data.

1. Introduction

[2] The T-phase (T-wave or Tertiary Wave) from an earthquake in the oceanic crust and upper mantle is a hydroacoustic wave that travels at the speed of sound in water (~1.5 km/s) and consequently arrives at an oceanic or coastal sensor after the faster traveling P- (Primary) and S- (Secondary) body waves, which propagate through the earth [*Tolstoy and Ewing*, 1950; *Johnson et al.*, 1963]. The origin time and seafloor location of T-phase generating events can be obtained from the data recorded by sparse arrays of single hydrophones moored in the ocean sound channel. Catalogs of T-phase events have become increasingly comprehensive and accessible as the networks of hydrophone arrays deployed in the world's oceans expand [e.g., *Fox et al.*, 1994, 2001; *Smith et al.*, 2002]. Long term monitoring of seismicity in remote areas of the oceans using hydrophone arrays has proven to be very successful over the last decade. This is especially true at mid-ocean ridges where T-phase data are providing information on the overall seismicity of the ridge axis and are helping to constrain models of mid-ocean ridge crustal structure [e.g., *Dziak and Fox*, 1999a, 1999b; *Dziak et al.*, 1995, 2004; *Schreiner et al.*, 1995; *Fox et al.*, 1994, 1995, 2001; *Bohnenstiehl and Tolstoy*, 2003; *Bohnenstiehl et al.*, 2002, 2003, 2004; *Smith et al.*, 2002, 2003]. T-phase data are also an important source of information for studying hydroacoustic wave propagation in the oceans [*Johnson et al.*, 1968; *Pulli et al.*, 1999; *Pulli and Upton*, 2002; *Harben et al.*, 2003].

[3] When a submarine earthquake occurs within the crust or upper mantle, seismic energy insonifies an area of the seafloor. The seismic energy at the seafloor couples with the water column to form acoustic energy which then propagates as a T-phase. However, there is much still to understand about the fundamental processes of T-phase excitation and propagation, a situation which limits the extent to which geological inferences can be made from T-phase characteristics. For example, because the area of seafloor that is significantly insonified by the seismic energy may be large, with a diameter up to a few tens of kilometers, it is not known whether the location estimated for the T-phase event is the same as the earthquake epicenter. We do not understand the coupling mechanism which converts seismic energy at the seafloor to acoustic energy in the sound channel. Consequently we do not understand the relationship between T-phase event characteristics and earthquake properties
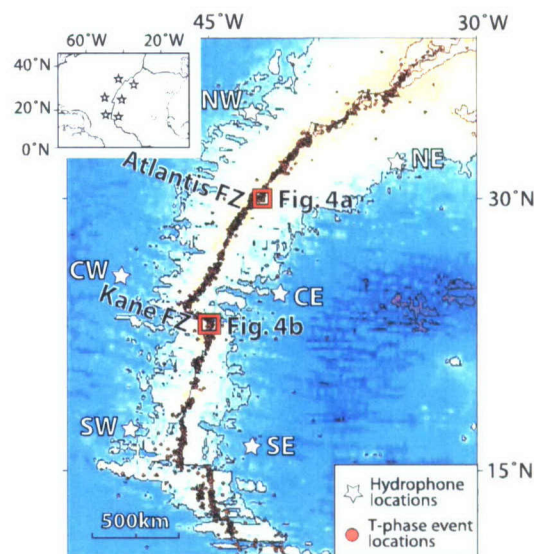
Figure 1. Location map of the North Atlantic Hydrophone Array (NAHA) and the two study areas at the eastern intersection of the Atlantis (30°N) and Kane (23°40′N) Transform Faults (red boxes) on the northern Mid-Atlantic Ridge (MAR). The red dots represent the locations of all the T-phase events recorded between February 1999 and February 2001 (~3500 events). Each of the six hydrophones is identified by its location in the array (white stars labeled NE, NW, CE, CW, SE, and SW). The hydrophones are positioned ~1000 km apart.

such as magnitude, event depth and focal mechanism. Also we do not understand how seafloor bathymetry effects the propagation of the T-phase.

[4] Motivated by the deficit in our understanding of T-phases we address some of these fundamental issues by investigating the characteristics of T-phase events recorded from two study areas on the Mid-Atlantic Ridge (MAR) by the North Atlantic Hydrophone Array (NAHA) [*Smith et al.*, 2002] (Figure 1). The study areas are located at the eastern end of the Atlantis Transform Fault (TF) (30°N) and at the eastern end of the Kane TF (23°40′N). The two areas were chosen on the basis of their comparable geological setting, their geological relevance to ocean ridge processes, their dramatic bathymetric relief, and their similar number and spatial distribution of T-phase events.

[5] Within these study areas, we examine the spatial distribution of T-phase event locations as a function of water depth and geologic setting. We assess whether the amplitudes of the T-phase events are dependent on water depth at the event
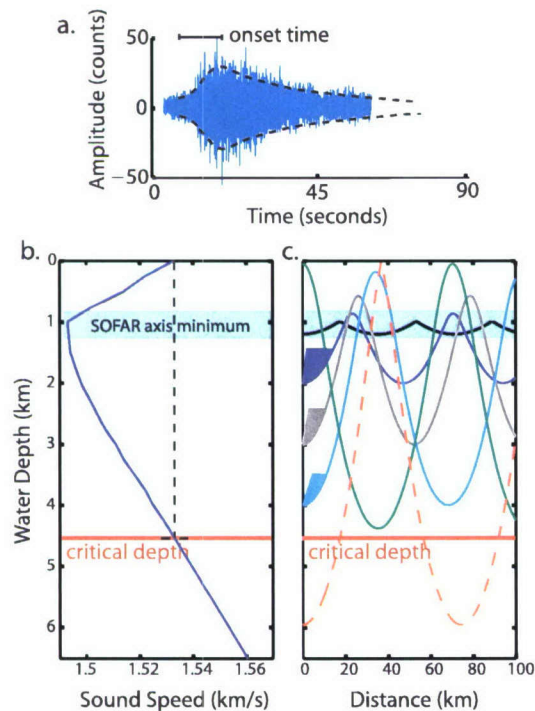
Figure 2. (a) An example of a T-phase time series. The T-phase is composed of a lens or envelope of energy less than 90 seconds in duration. The T-phase has a short onset time, measured from its appearance above the ambient noise to its maximum amplitude, and then gradually decays back to ambient noise levels. (b) Example of a sound velocity profile for the North Atlantic. The SOFAR channel extends from the sea surface to the critical depth (red line), and the sound axis minimum is shown by the darker blue rectangle. (c) Ray trace modeling for events that occur by excitation scattering at the seafloor at varying event water depths. Events in the SOFAR channel will propagate great distances (green, black, blue, gray, and cyan rays). However, those events below the critical depth will be severely attenuated by scattering at the seafloor (red dashed ray) and will not propagate far. The rays plotted represent only the ray path of a horizontally traveling ray from each event. All rays with emergent angles that lie within the colored cones will propagate through the SOFAR channel. As water depth increases, the width of the cone decreases to zero at and below the critical depth. We define the process of decreasing energy with increasing depth as event location water depth dependence.

location and on source to receiver distance. We also quantify and study the significance of the onset time of the T-phase events, which is defined as the time interval between the appearance of the T-phase and the first peak in the T-phase envelope (Figure 2a). Finally, we model bathymetric block-

age along the inferred propagation path on the basis of known topography and ray trace theory and compare the model results to the observed data.

[6] This work is a first step in comparing hydro-acoustic modeling results with data. Quantifying the differences between predictions and observations will guide the future development of acoustic propagation models which, in turn, will extend the applicability of T-phase data to the study of oceanic crustal processes.

2. Acoustics Background

[7] T-phase energy appears in the frequency band of 1–100Hz. The time series of a T-phase usually resembles a lens or envelope of energy where the wave amplitude increases to a maximum and then slowly decays to ambient noise levels (Figure 2a). The T-phases in this study are typically less than 90 seconds in duration. The maximum amplitude of the T-phase lens is assumed to correspond to the point on the seafloor with the maximum conversion of seismic to acoustic energy in the T-phase excitation region [*Slack et al.*, 1999]. Models of T-phases generally consider two regions: a relatively short excitation region where the T-phase characteristics are established and a propagation region where the T-phase energy is totally trapped in the ocean sound channel. Since scattering of some kind is usually invoked in one or both regions we distinguish them by region as excitation scattering and propagation scattering.

[8] The waveguide that traps the T-phase propagation is defined by the sound velocity structure of the water column. A typical sound velocity profile for the North Atlantic is shown in Figure 2b. The depth at which the sound velocity is equal to the sea surface sound velocity is called the critical depth and the water column from the surface to the critical depth is defined as the Sound Fixing and Ranging (SOFAR) channel. The axis of the channel is at the sound velocity minimum, normally located around 1 km water depth in the tropics and midlatitudes (Figure 2b). Steeply emergent rays (i.e., rays with a low incidence angle, which is measured from the vertical) and any energy originating below the critical depth will reflect and scatter from the sea surface and the seafloor and will not travel far horizontally before being attenuated by propagation scattering processes (red dashed ray, Figure 2c). In contrast, low grazing angle (high incidence angle) energy will become
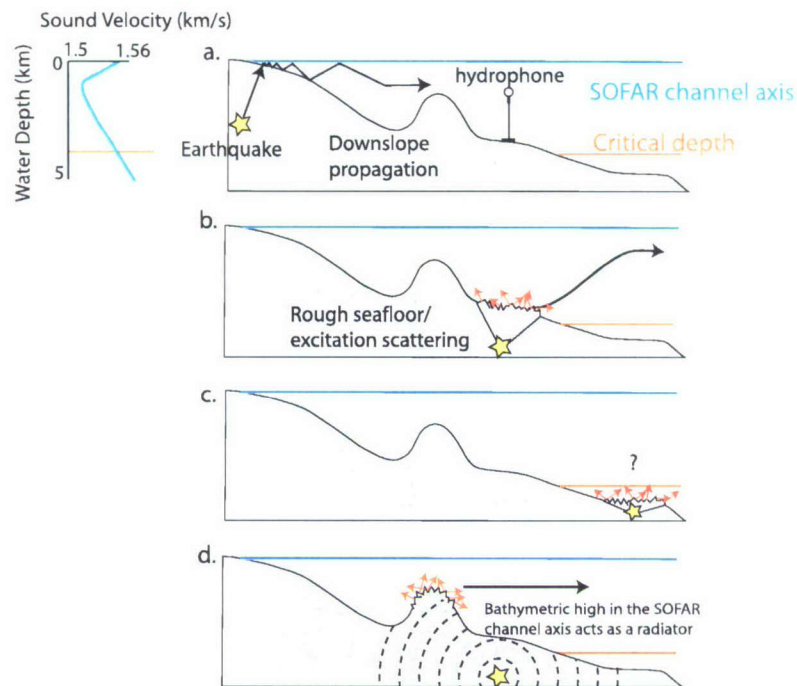
Figure 3. Illustrations of coupling mechanisms that may generate T-phases. (a) Downslope propagation and (b) rough seafloor scattering. (c) Events that occur below the critical depth should not be able to propagate in the SOFAR channel based on ray trace theory (Figure 2c). (d) A local bathymetric high located in the SOFAR channel axis may act as a radiator, where acoustic energy from a deep water event enters the SOFAR channel efficiently and results in T-phase event locations that are not epicenters.

totally trapped in the SOFAR channel. This energy will then propagate efficiently because the anelastic attenuation in the water column is practically negligible [*Talandier and Okal*, 1998] and energy divergence in the channel is cylindrical, compared with spherical divergence for body waves (r^{-1} compared with r^{-2} respectively). The colored cones in Figure 2c represent the effective energy or range of ray angles which will be totally trapped in the water column from omnidirectional scattering at various seafloor depths. The effective energy decreases with increasing water depth to zero at the critical depth and below. Earthquakes that occur in regions where the water depths are below the critical depth should have strongly attenuated T-phases (Figure 3c).

[9] The "T-phase problem" is that models of T-phase excitation produce acoustic energy with low incidence angles, due to the sound velocity contrast between the seafloor and water column. Several mechanisms have been proposed for the conversion from low incidence to high incidence energy. For earthquakes which insonify sloping seafloor, the T-phase energy is converted into high incidence

angles through multiple reflections and downslope propagation [*Johnson et al.*, 1963; *Chiu*, 1994; *Talandier and Okal*, 1998] (Figure 3a). In deep water, scattering from the rough seafloor [*Walker et al.*, 1992; *de Groot-Hedlin and Orcutt*, 1999, 2001; *Park et al.*, 2001; *Yang and Forsyth*, 2003] (Figure 3b), sea surface [*Johnson et al.*, 1968], or the underside of sea ice [*Keenan and Merriam*, 1991] may excite high incidence angle energy. It has also been suggested that scattering (or mode coupling) at internal waves and SPICE (density neutral thermohaline variations) [*Butler*, 2004; *Colosi*, 2004], can excite high incidence angle propagation [*Park et al.*, 2001] and these processes may cause propagation scattering as well.

[10] The complexity of T-phase excitation makes it difficult to infer hypocenter locations, magnitudes and focal mechanisms from the characteristics of the T-phase. For example, the peak of a bathymetric high may act as a radiator of acoustic energy for local seismic events (Figure 3d). As a result, the T-phase location does not coincide with a point on the seafloor directly above the earthquake hypocenter. There have been several efforts to derive a
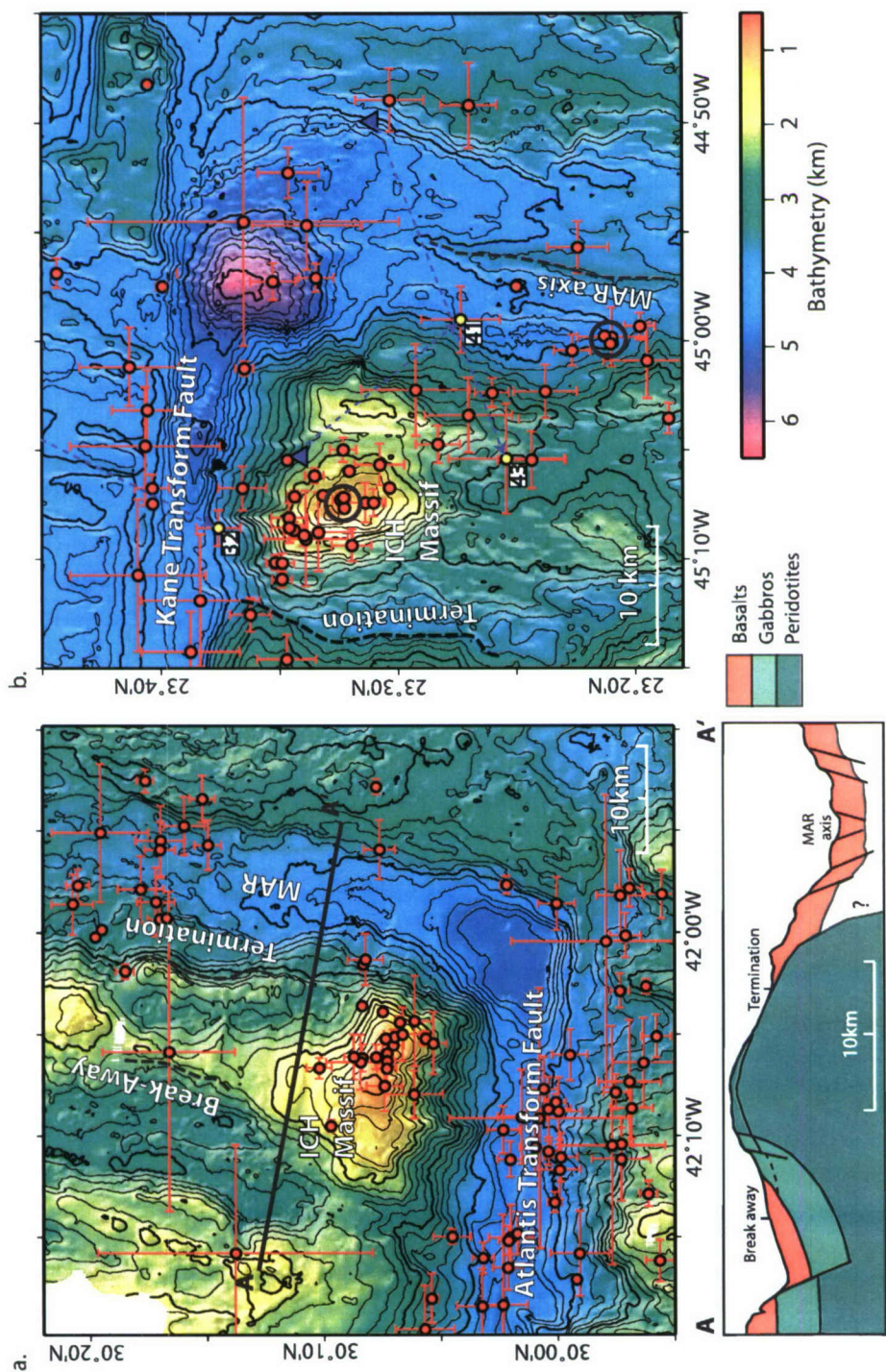
Figure 4

relationship between seismic magnitude and acoustic magnitude [*Dziak et al.*, 1997; *Dziak*, 2001; *Fox et al.*, 2001; *Bohnenstiehl*, 2001; *Pulli and Upton*, 2002; *Yang and Forsyth*, 2003; *Pan and Dziewonski*, 2005]. There are several problems, however, because in the past large magnitude earthquakes were clipped by the hydrophone sensors ($m_b > 4.7$ [*Fox et al.*, 2001]) making the estimate of T-phase magnitude unreliable (this problem is being eliminated with the larger dynamic range in more recent hydrophone systems). Another problem is that small magnitude events ($m_b < \sim 4$) recorded by the hydrophones are not recorded by land-based seismometers and therefore do not have a calculated seismic magnitude. Understanding the relationship between seismic magnitude and acoustic magnitude will require a concurrent hydrophone and ocean bottom seismometer (OBS) study.

[11] In addition to quantifying acoustic magnitude, variations in risetimes have been used for geological interpretation of T-phase events. Risetime is defined as the time between the appearance of the T-phase and its maximum peak and it has been related to the focal depth of the earthquake [*Norris and Johnson*, 1969]. For example a shorter risetime may reflect a shallower earthquake and longer risetime may mean a deeper earthquake. The combined observations of migration in seismic activity, a decrease in risetime and acoustic magnitude of T-phase events were interpreted as a shallowing magma dike intrusion at Axial [*Dziak and Fox*, 1999b] and CoAxial [*Schreiner et al.*, 1995] segments of the Juan de Fuca Ridge and the Lucky Strike segment of the MAR [*Dziak et al.*, 2004].

[12] Finally, T-phases are commonly assumed to be blocked by bathymetry along the propagation path [e.g., *Fox et al.*, 2001], but little work has been

done to quantify and model the effect. *Pulli and Upton* [2002] investigated a T-phase event recorded by the Diego Garcia hydroacoustic array which was associated with a continental earthquake and its aftershocks in India. T-phase acoustic magnitudes in the blocked (or shadow) region of the islands were reduced by ~ 40 dB confirming a transmission loss along the propagation path but not total blockage. Modeling and accurate assessment of bathymetric blockage is hindered by a lack of high-resolution bathymetry over large areas of seafloor [*Harben et al.*, 2003].

3. Study Areas

[13] The MAR between 35°N and 15°N is a slow spreading (~ 12 mm/yr, average half spreading rate) mid-ocean ridge (MOR) separated into multiple segments by large offset transform faults and nontransform offsets (Figure 1). Both of our study areas are located at a ridge-transform intersection (RTI): the eastern intersection of the MAR with the Atlantis TF (Atlantis study area, Figure 4a) and the eastern intersection of the MAR with the Kane TF (Kane study area, Figure 4b).

[14] The typical features of a RTI include a deep valley at the intersection of the ridge and transform (known as a nodal basin), a high massif located at the corner of the RTI toward the offset ridge axis (the inside corner high (ICH)), and relatively lower topography on the other side of the ridge segment (the outside corner high (OCH)) [*Severinghaus and Macdonald*, 1988]. It is thought that the ICH is composed of lower crust and upper mantle rocks that have been unroofed along a low-angle detachment fault [*Mutter and Karson*, 1992; *Tucholke and Lin*, 1994; *Escartin and Lin*, 1995; *Tucholke et al.*, 1996, 1998; *Cann et al.*, 1997; *Blackman et al.*,

Figure 4. Locations of the maps in Figures 4a and 4b are shown in Figure 1. (a) Bathymetric map of the Atlantis study area with T-phase events represented by the red circles and the error in their locations (provided in the T-phase catalog) shown by the red bars. The ICH massif may have formed by movement on a low angle detachment fault that first nucleated along the break-away. The termination is the present-day contact between the footwall and the hanging wall of the fault. The cross section through the ICH massif illustrates the inferred low angle detachment fault and the unroofing of lower crustal (gabbros) and upper mantle (peridotites) rocks to form the summit. Volcanic seafloor (basalts) makes up the hanging wall and covers the axial zone. (b) Bathymetric map of the Kane study area with T-phase event locations and errors as in Figure 4a. The locations of 2 teleseismic events recorded by land-based networks that occurred during the period of this study are indicated by blue triangles. A third teleseismic event is located to the north, but its T-phase is located within our study area. Teleseismic locations and corresponding T-phase event locations are connected by dashed blue lines. The three T-phases associated with these teleseismic events are labeled with their event number and shown by the yellow circles. The black open circles surround two clusters of three T-phase events which are shown in Figure 7. The bathymetry data for both study areas were obtained from the Ridge Multibeam Synthesis Project Web site (http://ocean-ridge.ldeo.columbia.edu/general/html/home.html). The bathymetry contour interval is 200 m in both Figures 4a and 4b.

1998, 2002; *Canales et al.*, 2004]. Both study regions have approximately the same spatial area (~56 by 50 km) and are centered on the ICH massif.

3.1. Atlantis Study Area

[15] The Atlantis TF is a 75 km long, left lateral offset fault (Figure 4a). The ICH massif, located at the eastern end of the RTI, has a smooth domed shape and a corrugated surface and rises to ~0.7 km water depth at its southern edge [*Cann et al.*, 1997; *Blackman et al.*, 1998, 2002]. The nodal basin has water depths of ~4.6 km, on average. This results in a change in water depth of ~4 km over ~20 km lateral distance from the summit of the ICH to the valley of the nodal basin. Serpentinized upper mantle rocks (serpentinized harzburgites) have been sampled from the summit of the Atlantis ICH massif and along its eastern slope [*Blackman et al.*, 1998]. Extensive mass wasting has shaped the south slope of the massif leaving large scarps and talus slopes [*Blackman et al.*, 1998]. The southern slope is associated with hydrothermal activity. A serpentinite-hosted, carbonate vent field, "Lost City", is located near the top of the steep south slope [*Kelley et al.*, 2001].

3.2. Kane Study Area

[16] The Kane TF is a 150 km long, right lateral offset fault (Figure 4b). The nodal basin has water depths that exceed ~6 km and the top of the ICH rises to a water depth of ~1.2 km (~4.8 km difference in water depth over ~20 km lateral distance). Gabbroic rocks have been sampled from the top of the Kane ICH and along the eastern slopes [*Karson*, 1998]. Serpentinite has not been sampled at the Kane study area and there are no corrugations on the summit of the Kane ICH. In addition, no hydrothermal activity has been found, to date, associated with the Kane ICH. The closest known hydrothermal activity is the "Snake Pit" sulphide vent field located on the neovolcanic ridge within the valley floor (<5 kyr old crust) [*Brown and Karson*, 1989; *Lalou et al.*, 1993].

3.3. Seismicity

[17] Both study areas have a large number of T-phase events located on the summit and flanks of the ICH compared with the nearby ridge axis, transform fault, and OCH (Figures 4a and 4b). Previous seismicity studies of mid-ocean ridge transform and nontransform offsets have observed clustering of earthquakes on the ICH (nontransform offset at 29°N [*Wolfe et al.*, 1995], Oceanographer TF (35°N [*Rowlett*, 1981]), St Paul's TF (0°40′N, [*Francis et al.*, 1978]) and Vema TF (10°45′N [*Rowlett and Forsyth*, 1984]) on the MAR and Rivera TF (19°N [*Reid*, 1976]) on the East Pacific Rise (EPR)). The source of the seismicity may be associated with movement on the inferred detachment fault, along which the lower crustal and upper mantle rocks have been exposed (cross section shown in Figure 4a). Oblique faults with normal [*Rowlett*, 1981] and reverse focal mechanisms [*Engeln et al.*, 1986; *Behn et al.*, 2002], and faults which form in response to continuous rotation of the footwall of the detachment fault [*Tilmann et al.*, 2004] might also play a role in generating seismicity. At the Atlantis ICH seismicity may be associated with the increase in volume and heat generation during the process of serpentinization, which may cause flexing and brittle failure as well as fluid expulsion events [*Kelley et al.*, 2001].

4. Hydrophone-Recorded and Teleseismic Data

[18] The NAHA consists of six autonomous hydrophone moorings that straddle the MAR from 35°N–15°N, as shown in Figure 1 [*Smith et al.*, 2002, 2003]. We refer to the hydrophones as Northeast (NE), Northwest (NW), Central East (CE), Central West (CW), Southeast (SE), and Southwest (SW), reflecting their relative positions within the array. The moorings are anchored to the seafloor and the hydrophones float in the SOFAR channel. The hydrophones continuously and autonomously record low frequency energy propagating through the SOFAR channel and the data are retrieved annually when the hydrophones are recovered and redeployed. The National Oceanic and Atmospheric Administration (NOAA) Pacific Marine Environmental Laboratory (PMEL) processes the data to produce a T-phase catalog containing event time, number and identity of the hydrophones that recorded the event, location in latitude and longitude (and errors) and acoustic magnitude (and error). The data are available at http://www.pmel.noaa.gov/vents/data/index.html, and detailed descriptions of the hydrophones and PMEL processing methods are given by *Fox et al.* [2001], *Dziak* [2001], and *Smith et al.* [2003].

[19] The NAHA was first deployed in February 1999 and was recovered in 2005. The data used in

Table 1. Atlantis Study Area T-Phase Events

Event Number	Year	Day	Hour	Min	Secs x10	No. of Hyd[a]	Hyd ID[b]	Lon, °E	Lat, °N	Source Level, dB re: 1μPa@1m	Error Time	Error Lon, °E	Error Lat, °N	Error Source Level
1	1999	63	8	55	55	5	56243	−42.1	30.12	202.06	0.375	0.01	0.01	2.6
2	1999	70	21	10	237	6	156243	−42.14	30	227.2	0.624	0.01	0.02	3
3	1999	73	10	47	180	6	156243	−42.27	29.93	211.69	0.432	0.01	0.01	9.2
4	1999	73	21	28	515	6	156243	−42.2	29.91	210.99	0.46	0.01	0.01	5.7
5	1999	83	7	54	454	4	1564	−42.09	30.12	209.11	0.049	0	0	4.5
6	1999	85	18	53	146	5	56243	−42.06	30.14	210.48	0.34	0.01	0.01	4.2
7	1999	100	22	55	197	5	56243	−42.09	30.12	204.67	0.346	0.01	0.01	2.4
8	1999	115	7	44	308	5	15243	−42.03	30.31	205.85	0	0	0	4.1
9	1999	117	16	20	69	6	156243	−42	30.33	203.3	0.5	0.01	0.01	2.9
10	1999	118	19	32	137	6	156243	−41.96	30.34	211.61	1.102	0.02	0.03	3.1
11	1999	119	15	59	318	5	15624	−42.31	30.05	201.37	2.087	0.03	0.06	2.2
12	1999	190	7	35	106	5	15643	−41.92	30.33	205.19	0.452	0.01	0.01	1.6
13	1999	200	18	41	554	6	156243	−42.05	29.96	211.32	0.33	0.01	0.01	4.2
14	1999	205	2	20	351	3	564	−42.11	30.12	202.24	5.899	0.07	0.12	0.8
15	1999	209	17	29	30	5	15624	−42.01	29.97	206.15	0.481	0.01	0.01	2.6
16	1999	209	19	8	215	5	15624	−42.17	29.95	202.55	0.525	0.01	0.01	2.4
17	1999	218	17	6	381	5	15624	−42.2	29.91	215.08	1.35	0.02	0.04	2
18	1999	230	7	20	160	6	156243	−42.11	29.94	208.27	0.796	0.01	0.02	4.3
19	1999	230	11	43	475	6	156243	−42.08	30.11	223.36	0.185	0	0.01	12.6
20	1999	230	12	15	87	6	156243	−42.03	30.14	208.61	0.191	0	0.01	6.8
21	1999	231	15	43	11	6	156243	−42.07	30.11	219.39	0.406	0.01	0.01	4.3
22	1999	231	22	36	355	5	15624	−42.1	30.14	208.47	0.801	0.01	0.02	2.8
23	1999	231	22	46	355	5	15624	−41.98	30	208.29	0.915	0.02	0.03	6.4
24	1999	233	17	32	223	6	156243	−41.97	29.91	232.75	0.731	0.01	0.02	2.4
25	1999	233	20	17	327	6	156243	−42.18	30	212.83	0.417	0.01	0.01	3.8
26	1999	233	21	36	76	6	156243	−42.18	30.01	212.42	0.305	0.01	0.01	4.1
27	1999	234	9	28	145	5	15643	−42.22	30	207.13	0.748	0.01	0.02	10.3
28	1999	234	9	28	264	6	156243	−42.18	30.02	205	0.971	0.02	0.03	9.7
29	1999	239	0	11	368	6	156243	−42.25	30.03	211.74	0.642	0.01	0.02	6.3
30	1999	240	18	45	227	6	156243	−42.09	29.93	221.51	0.767	0.01	0.02	7.7
31	1999	240	19	45	307	6	156243	−42.02	30.14	224.05	0.22	0	0.01	5.2
32	1999	259	11	42	467	4	1564	−42.09	30.09	211.32	1.214	0.02	0.04	5.5
33	1999	261	1	24	512	4	5243	−42.15	30.03	202.62	0.915	0.01	0.01	4.7
34	1999	263	5	30	265	4	1564	−42.25	30.08	208.18	0.764	0.01	0.02	9.5
35	1999	266	3	33	22	6	156243	−41.93	30.13	209.87	1.014	0.02	0.03	3.9
36	1999	279	15	31	259	5	56243	−42.18	29.91	200.88	0.5	0.01	0.01	1.6
37	1999	314	17	51	19	5	15624	−42.11	30.17	208.15	0.911	0.02	0.03	3.7
38	1999	314	17	51	19	5	15624	−42.2	30	208.15	0.911	0.02	0.03	3.7
39	1999	319	19	54	51	6	156243	−42.2	30	204.54	0.424	0.01	0.01	2.8
40	1999	322	15	13	497	6	156243	−42.11	30.12	215.39	0.372	0.01	0.01	5.3
41	1999	323	15	6	275	6	156243	−42.1	30.13	209.73	0.004	0	0	3.6
42	1999	337	18	45	583	6	156243	−42.07	30.12	203.07	0.671	0.01	0.02	1.8
43	1999	341	22	30	410	6	156243	−42	29.95	214.72	0.71	0.01	0.02	4.2
44	1999	347	8	24	60	6	156243	−42.16	30.04	210.63	0.92	0.02	0.03	4.6
45	1999	349	17	31	494	6	156243	−42.14	29.95	210.08	0.994	0.02	0.03	7.3
46	1999	350	23	25	120	6	156243	−41.96	30.3	219.39	0.538	0.01	0.02	5.4
47	1999	359	12	40	442	6	156243	−42.19	30.03	212.52	1.288	0.02	0.04	3
48	2000	10	1	11	218	6	156243	−42.33	30.1	206.11	1.015	0.02	0.03	2.7
49	2000	18	17	39	118	6	156243	−42.15	30	219.43	1.081	0.02	0.03	5.9
50	2000	35	2	32	369	5	56243	−41.97	29.92	217.01	1.336	0.02	0.02	5.4
51	2000	45	9	5	593	6	156243	−42.11	30.14	225.61	0.649	0.01	0.02	6.2
52	2000	47	4	38	373	4	1524	−42.28	30.04	220.41	0.705	0.01	0.03	12.8
53	2000	63	8	59	507	5	56243	−42.09	30.09	212.59	5.384	0.1	0.09	2.7
54	2000	90	5	11	472	6	156243	−42.26	30.23	224.22	1.277	0.02	0.04	3.3
55	2000	91	11	41	286	6	156243	−42.26	29.98	227.39	1.262	0.02	0.03	5.4
56	2000	91	15	26	401	6	156243	−42.19	29.95	231.28	3.921	0.06	0.11	4.8
57	2000	92	6	7	56	5	15624	−42.15	30.01	211.48	0.383	0.01	0.01	1.8
58	2000	105	19	23	507	4	1524	−42.21	29.94	206.41	2.735	0.04	0.1	3.5
59	2000	121	3	9	308	5	15243	−42.18	29.96	209.11	3.726	0.05	0.13	1.1
60	2000	144	8	2	383	4	5624	−42.1	30.28	212.76	1.153	0.02	0.02	3.4

Table 1. (Continued)

Event Number	Year	Day	Hour	Min	Secs x10	No. of Hyd[a]	Hyd ID[b]	Lon, °E	Lat, °N	Source Level, dB re: 1μPa@1m	Error Time	Error Lon, °E	Error Lat, °N	Error Source Level
61	2000	157	6	56	16	6	156243	−42.13	30.1	221.04	0.766	0.01	0.02	5.8
62	2000	173	11	41	220	4	1562	−42.13	30.12	209.69	0.501	0.01	0.01	4
63	2000	173	11	57	544	5	15624	−42	30.33	206.42	1.067	0.02	0.03	2.4
64	2000	188	3	4	91	6	156243	−41.93	30.28	218.1	0.228	0	0.01	3.4
65	2000	173	11	57	495	5	15624	−41.99	30.28	207.69	0.905	0.02	0.03	2.3
66	2000	173	11	57	516	5	15624	−41.98	30.35	207.33	0.004	0	0	2.7
67	2000	234	19	38	532	4	1524	−41.88	30.13	199.42	0.51	0.01	0.02	3.5
68	2000	237	6	53	175	6	156243	−42.1	30.15	221.49	0.53	0.01	0.01	3.2
69	2000	255	11	28	400	5	15624	−42.13	29.96	210.98	0.971	0.02	0.03	2.5
70	2000	256	3	28	0	4	1564	−42.14	30.01	206.86	0.182	0	0.01	2.3
71	2000	256	16	34	10	4	1564	−42.04	29.94	203.93	1.588	0.02	0.05	2.1
72	2000	256	16	35	174	4	1564	−42.12	29.95	204.59	1.155	0.02	0.04	1.8
73	2000	285	3	11	373	6	156243	−41.97	29.96	210.43	0.725	0.01	0.02	3.4
74	2000	287	4	45	260	4	1524	−41.97	29.93	202.44	0.026	0	0	0.5
75	2000	288	21	20	389	4	1564	−41.99	30.28	209.54	0.647	0.01	0.02	2.7
76	2000	288	22	2	380	4	1564	−41.93	30.25	207.83	0.614	0.01	0.02	2.1
77	2000	288	22	3	498	4	1564	−41.88	30.25	206.31	0.898	0.01	0.03	1.5
78	2000	289	17	32	389	6	156243	−41.97	30.29	216.48	0.353	0.01	0.01	4.5
79	2000	289	20	38	170	4	1564	−41.88	30.29	202.12	0.733	0.01	0.02	2.8
80	2000	296	0	20	196	5	15624	−41.93	30.28	209.29	0.433	0.01	0.01	1.4
81	2000	297	6	10	166	4	1543	−42.25	30.04	214.65	0.319	0.01	0.02	4.3
82	2000	297	6	10	398	4	1543	−42.3	30.09	215.81	1.163	0.02	0.07	1.7
83	2000	297	12	59	251	5	15624	−42.31	30.04	205.88	0.641	0.01	0.02	1.6
84	2000	298	5	38	32	4	1524	−42.25	30.03	202.71	1.019	0.01	0.04	1.1
85	2000	299	21	16	333	5	15624	−42.07	30.1	205.91	0.875	0.01	0.02	2.8
86	2000	320	3	58	259	5	15624	−41.91	30.27	202.6	0.769	0.01	0.02	2.3
87	2000	320	9	24	368	5	15624	−42.1	29.99	205.21	0.567	0.01	0.02	1.5
88	2000	323	19	47	377	5	15624	−41.96	29.95	202.47	0.002	0	0	1.8
89	2000	337	18	45	145	6	156243	−42.29	29.99	207.25	0.467	0.01	0.01	1.8
90	2000	348	3	11	542	6	156243	−42.27	30.05	203.79	0.27	0	0.01	1.8
91	2001	14	11	11	351	6	156243	−41.96	30.04	205.65	0.344	0.01	0.01	1.4
92	2001	19	19	23	540	6	156243	−41.99	29.9	202.96	0.129	0	0	1.3
93	2001	39	2	0	281	4	1524	−42.09	30.12	204.49	0.724	0.01	0.03	2.3
94	2001	39	7	15	164	6	156243	−42.13	30.01	204.69	0.19	0	0.01	1.5
95	2001	39	7	15	164	6	156243	−42.16	30.16	204.69	0.19	0	0.01	1.5

[a] No. of Hyd: total number of hydrophones that recorded the event.
[b] Hyd ID: identity of the hydrophones (1-NW, 2-CW, 3-SW, 4-SE, 5-CE, 6-NE).

this report were recorded between 25 February 1999 and 9 March 2001. During this period all six instruments in the array functioned properly. The NW hydrophone results were removed from our analyses, however, because this hydrophone experienced high ambient noise levels due to strumming of the mooring line. As a result, many of the T-phase events cannot be distinguished in the time series or the spectrogram.

[20] In total 95 events were located in the Atlantis study area and 63 in the Kane study area during the two year period. Tables 1 and 2 list the T-phase catalog information for all the events at Atlantis and Kane, respectively. We make the following assumptions about the T-phase catalog event locations for this study: (1) the T-phase event locations

are accurate, and (2) the locations represent earthquake epicenters.

[21] Searches for all teleseismic events at the two locations during the two year time period were made on the Harvard Centroid Moment Tensor (CMT) Catalog (http://www.seismology.harvard.edu/CMTsearch.html), the National Earthquake Information Center (NEIC) Database (http://neic.usgs.gov/neis/epic/epic_rect.html) and the International Seismology Center (ISC) which includes data from the International Database Center (IDC)/European International Data Center (EIDC) (http://www.isc.ac.uk/Bulletin/arrivals.htm). Three events were large enough to be recorded both as teleseisms and T-phases. All three teleseimic events were located in the Kane study area

Table 2. Kane Study Area T-Phase Events

Event Number	Year	Day	Hour	Min	Secs x10	No. of Hyd[n]	Hyd ID[b]	Lon, °E	Lat, °N	Source Level, dB re: 1μPa@1m	Error Time	Error Lon, °E	Error Lat, °N	Error Source Level
1	1999	58	9	5	580	5	52346	−45.169	23.586	204.1	0.006	0.006	0.3	6.6
2	1999	66	12	2	509	4	2346	−45.124	23.523	205.54	0.012	0.015	0.72	4.2
3	1999	66	18	1	92	5	52346	−44.997	23.349	203.55	0.024	0.023	1.15	5.1
4	1999	68	1	28	521	5	52346	−45.121	23.54	206.67	0.006	0.005	0.26	9.5
5	1999	74	12	43	545	5	52346	−45.128	23.538	209.15	0.003	0.003	0.14	13.1
6	1999	87	6	50	12	4	2341	−44.82	23.45	203.57	0.02	0.033	1.42	2.3
7	1999	109	18	35	456	5	52346	−45.007	23.377	219.58	0.013	0.012	0.6	6.1
8	1999	109	18	37	383	5	52346	−44.989	23.33	215.96	0.011	0.01	0.51	8.1
9	1999	111	4	34	214	5	52346	−45.12	23.539	207.42	0.005	0.005	0.23	4.3
10	1999	125	21	15	330	5	52346	−44.871	23.577	212.63	0.022	0.019	0.99	5.1
11	1999	143	20	55	45	4	2346	−45.124	23.517	207.73	0.008	0.01	0.5	12.5
12	1999	151	4	33	97	5	52346	−45.17	23.582	211.31	0.009	0.008	0.4	8.9
13	1999	152	6	41	86	4	5234	−45.156	23.533	205.06	0.014	0.012	0.65	4.7
14	1999	159	3	12	554	5	52346	−45.079	23.472	206.3	0.016	0.014	0.74	2.1
15	1999	166	0	28	465	4	5346	−45.179	23.683	209.71	0.048	0.058	2.57	8
16	1999	197	0	20	457	4	5346	−44.958	23.417	209.28	0.001	0.002	0.07	1.5
17	1999	212	3	7	498	4	5346	−45.053	23.676	203.64	0.025	0.03	1.32	4
18	1999	215	3	6	304	4	5346	−45.146	23.556	208.24	0.024	0.03	1.3	9.7
19	1999	247	3	55	252	5	52346	−45.094	23.513	207.44	0.017	0.016	0.82	3.9
20	1999	265	0	31	504	5	52346	−45.04	23.434	204.13	0.012	0.011	0.56	0.9
21	1999	280	2	3	280	4	5346	−45.151	23.565	207.91	0.03	0.037	1.57	5.2
22	1999	280	2	3	324	5	52346	−45.112	23.506	201.89	0.001	0.001	0.05	3.3
23	1999	303	6	2	10	5	52346	−44.954	23.588	215.75	0.016	0.014	0.74	2.3
24	1999	305	13	41	339	5	52346	−45.182	23.582	202.24	0.007	0.006	0.33	2.5
25	1999	322	23	24	237	6	523416	−45.083	23.539	210.93	0.009	0.009	0.46	8.1
26	1999	335	3	32	16	5	52346	−45.243	23.579	210.59	0.021	0.019	0.98	4.3
27	1999	335	20	27	411	5	52346	−45.148	23.566	211.7	0.009	0.008	0.42	8.6
28	1999	340	23	8	441	5	52346	−45.103	23.559	203.33	0.006	0.006	0.3	2.1
29	1999	352	18	33	83	4	5234	−45.091	23.578	205.68	0.003	0.003	0.14	4.1
30	2000	3	17	40	161	6	523416	−44.816	23.506	217.31	0.024	0.024	1.19	4.4
31	2000	10	22	33	434	6	523416	−45.119	23.573	218.09	0.005	0.005	0.23	6.7
32	2000	13	14	26	10	6	523416	−45.113	23.61	234.12	0.017	0.017	0.84	6.8
33	2000	31	10	26	598	5	52346	−45.209	23.604	207.8	0.014	0.013	0.67	5
34	2000	33	3	27	106	5	52346	−44.929	23.373	205.67	0.021	0.02	1.01	3.3
35	2000	52	14	35	394	6	523416	−45.124	23.673	222.93	0.003	0.003	0.16	4.7
36	2000	70	16	48	571	4	5234	−45.02	23.689	209.07	0.035	0.03	1.6	3.5
37	2000	88	23	30	495	4	5234	−44.909	23.608	203.01	0.109	0.095	5.04	3.8
38	2000	89	20	5	597	4	5234	−45.08	23.678	204.65	0.053	0.045	2.42	2.9
39	2000	90	2	33	180	5	52346	−45.237	23.646	205.03	0.035	0.031	1.6	3.7
40	2000	96	16	6	125	5	52346	−45.038	23.488	219.88	0.038	0.035	1.8	1.7
41	2000	96	16	15	350	5	52346	−44.984	23.456	221.89	0.028	0.025	1.3	3.3
42	2000	96	17	24	384	4	5234	−45.039	23.396	211.77	0.022	0.02	1.06	2.3
43	2000	98	4	26	546	6	523416	−45.09	23.424	222.13	0.041	0.042	2.06	6.2
44	2000	98	5	12	286	4	5234	−45.091	23.406	208.98	0.024	0.022	1.14	3.3
45	2000	102	7	46	463	4	5234	−44.912	23.564	206.26	0.039	0.034	1.79	2.4
46	2000	128	0	26	89	4	5234	−44.958	23.666	209.81	0.004	0.004	0.2	4.6
47	2000	154	12	17	554	3	526	−45.059	23.31	199.66	0.105	0.012	3.92	1.9
48	2000	164	19	50	502	5	52346	−45.143	23.626	210.54	0.015	0.014	0.72	2.4
49	2000	188	3	25	432	4	5234	−45.144	23.573	206.72	0.007	0.006	0.33	1.9
50	2000	227	19	7	14	5	52346	−45.057	23.45	206.36	0.031	0.028	1.45	2.2
51	2000	233	5	55	10	5	52346	−45.015	23.325	213.08	0.031	0.029	1.46	3.7
52	2000	258	13	55	392	4	5346	−45.198	23.639	209.8	0.041	0.051	2.23	2.2
53	2000	287	7	3	445	5	52346	−45.135	23.577	205.12	0.013	0.012	0.6	3.5
54	2000	287	7	13	153	3	526	−44.948	23.74	204.97	0.085	0.011	2.74	2.1
55	2000	287	7	52	272	6	523416	−45.118	23.553	209.88	0	0	0	5.5
56	2000	310	6	54	253	5	52346	−45.143	23.577	205.28	0.013	0.011	0.59	1.9
57	2001	11	8	24	217	5	52346	−45.099	23.535	209.31	0.003	0.003	0.13	8
58	2001	13	11	26	260	5	52346	−44.996	23.355	202.78	0.002	0.002	0.11	2.3
59	2001	16	11	36	367	5	52346	−45.021	23.608	204.99	0.006	0.006	0.29	2.5
60	2001	26	2	41	297	4	5234	−44.952	23.557	203.01	0.012	0.011	0.58	2.4

Table 2. (Continued)

Event Number	Year	Day	Hour	Min	Secs x10	No. of Hyd[a]	Hyd ID[b]	Lon, °E	Lat, °N	Source Level, dB re: 1μPa@1m	Error Time	Error Lon, °E	Error Lat, °N	Error Source Level
61	2001	37	9	34	542	5	52346	−45.002	23.351	207.47	0.002	0.001	0.07	2.6
62	2001	63	12	54	401	5	52346	−45.112	23.673	204.88	0.012	0.011	0.55	3
63	2001	68	7	30	258	4	5234	−44.804	23.676	202.22	6E-04	5E-04	0.03	1.8

[a] No. of Hyd: total number of hydrophones that recorded the event.
[b] Hyd ID: identity of the hydrophones (1-NW, 2-CW, 3-SW, 4-SE, 5-CE, 6-NE).

(Figure 4b) but no focal mechanism solutions are available for these events from the Harvard CMT catalog.

5. Results and Interpretation

[22] In the following section, the T-phase data from the Atlantis and Kane study regions are compared by geological setting (e.g., top of massif, transform valley, ridge axis). The data for each study area are also combined to allow for more robust comparison with the ray trace modeling results and to assess trends in T-phase character with varying event water depths, source to receiver distances and onset time. Details of the data processing, picking of events, modeling and curve fitting are provided in Appendices A–D.

5.1. Spatial Distribution of the T-Phases

[23] The average number of events per unit area has been calculated for each of the study areas and normalized to 1000 km². At the Atlantis study area

there are ~35 events/1000 km² and at Kane there are ~22 events/1000 km². By comparison, the MAR segments adjacent to our study areas, segment 34 for Atlantis and 17 for Kane (as defined by *Smith et al.* [2003]) both fall within the "medium" T-phase activity group (~10 events/1000 km²) over the same two year time period [*Smith et al.*, 2003]. This difference in the density of the T-phase events implies that there are significantly more seismic events associated with the RTIs in our two study areas compared with the ridge axis.

[24] The spatial density of T-phase events in the study areas was also examined as a function of the event location water depth. Water depth of an event was obtained by sampling a multibeam bathymetry grid (data spacing 150 m) at the latitude and longitude of the event location. Event water depths for those events with T-phase location errors <0.03° were sorted into 1 km sized bins and the seafloor surface area calculated within each bin (81 events from Atlantis and 48 events from Kane). The normalized number of T-phase events per 100 km²
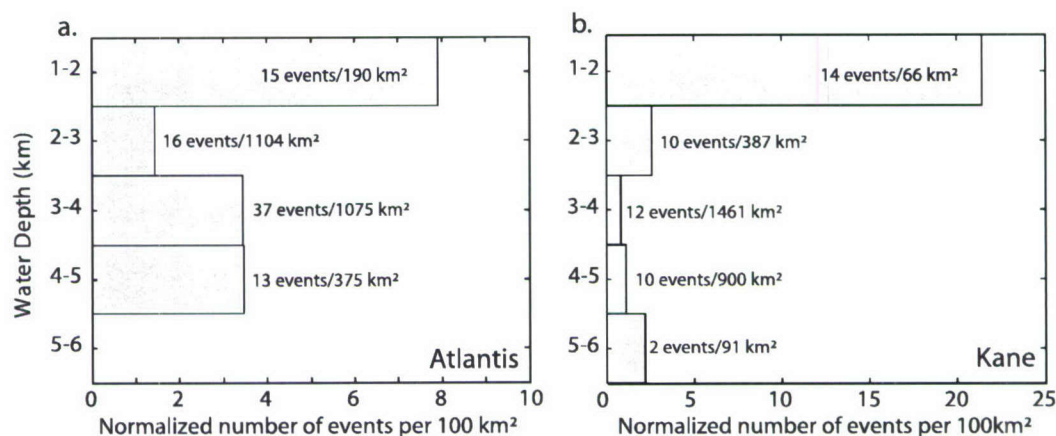

Figure 5. Histograms of the T-phase spatial density with increasing water depth for (a) Atlantis and (b) Kane study areas. Note the greater number of events located on the summit and flanks of the ICH massif (between 1 and 2 km water depth) compared with all other water depths at both study areas.

for each bin shows that a greater number of events are located in water depths shallower than 2 km (i.e., the shallow summit and flanks of the ICH) compared with deep water events along the transform and ridge axis in both survey areas (Figure 5). We suggest three possible reasons that could explain the large number of events located on the ICH:

[25] 1. The ICH acts as a radiator of seismic energy from events located beneath the ridge axis or transform fault (Figure 3d). Seismic energy from the events propagate through the ICH crust and couples with the water column at the ICH summit, which intercepts the axis of the SOFAR channel in both study areas.

[26] 2. The same number of events occur at all water depths, but a larger number of events are recorded from the summit and the shallow flanks of the ICH because the energy couples more easily into the SOFAR channel, as in (1) above.

[27] 3. A greater number of seismic events occur at shallow water depths compared with deep water depths and are associated with the building and maintenance of the ICH massif.

5.2. Amplitude of the T-Phases

[28] The amplitude of a T-phase event is the first characteristic we quantify from the T-phase time series. Our definition of the amplitude of a T-phase is different from the T-phase catalog. The value of acoustic magnitude (called Source Level) provided in the T-phase catalog measures the amplitude of the broadest band portion of the T-phase spectrogram. This amplitude, recorded by the hydrophone, is corrected for instrument gain and transmission loss over the source to receiver distance to give a magnitude ~1 m above the seafloor at the event location. The Source Levels for all the hydrophones that record the T-phase are averaged to give a mean Source Level for each event. The range in Source Level for the Atlantis study area is 199.42–232.75 dB re: 1μPa @ 1m and 199.66–234.12 dB re: 1μPa @ 1m for the Kane study area.

[29] In this study we calculate the Received Level, which is the Root Mean Square (RMS) of a 90 second window of the time series containing the T-phase event. Ambient noise levels are quantified from the RMS of the first 10 seconds of each 90 second window of the time series, with the assumption that this is "quiet time" before the arrival of the T-phase. We then select T-phase events with locations errors <0.03° and a RMS Signal >1 dB re: counts (72 events from Atlantis and 39 events

from Kane, see Appendix A). One value of Received Level is calculated for each event at each hydrophone. The Received Level calculation was done in counts and the results converted to decibels (decibel conversion, dB re: counts = 20 log$_{10}$ (Amplitude)). The variability in Received Level between hydrophones for the same event is expressed by the horizontal range in values for each event in Figure 6. To summarize, the difference between the Received Level (used here) and Source Level (given in the T-phase catalog) is that Source Level is the magnitude of the T-phase ~1 m above the seafloor at the event location while the Received Level is the magnitude at the hydrophone (with no range correction).

[30] A comparison of hydrophone catalog Source Level, mean Received Level (a geometric mean calculated in dB re: counts), and seismic event magnitude (m_b), for the three teleseismic events recorded at the Kane study area is shown in Table 3 and the event locations are labeled in Figure 4b. The results highlight a difference between seismic body wave magnitudes and T-phase amplitudes: Event 32 has a significantly higher mean Received Level (and Source Level) than events 41 and 43 but the lowest mean body wave magnitude of the three events. The discrepancy between the magnitude values may be due to different water depths and topography at the event locations. Event 43 is the shallowest of the three (water depth of 2.96 km) and is located on the broad southern side of the ICH. Event 32 is at a water depth of 3.36 km and located on the steep northern side of the ICH. Event 41 is the deepest with a water depth of 4.18 km and located within the inner valley floor. The comparison between the seismic magnitude and Received Level for the three teleseismic events suggests that the relationship between seismic and Received Level is more complex than we currently understand. However, the small number of events makes it difficult to draw conclusions from our comparison. It is surprising that there were no teleseismic events located in the Atlantis study area because seven events have a mean Received Level greater than Event 41 in the Kane area. This suggests that the relationship between seismic and acoustic magnitude may be location specific.

5.3. Received Level of T-Phases Versus Event Location Water Depth

[31] Ray trace theory predicts that the range of ray angles that can propagate through the SOFAR channel decreases with increasing water depth,
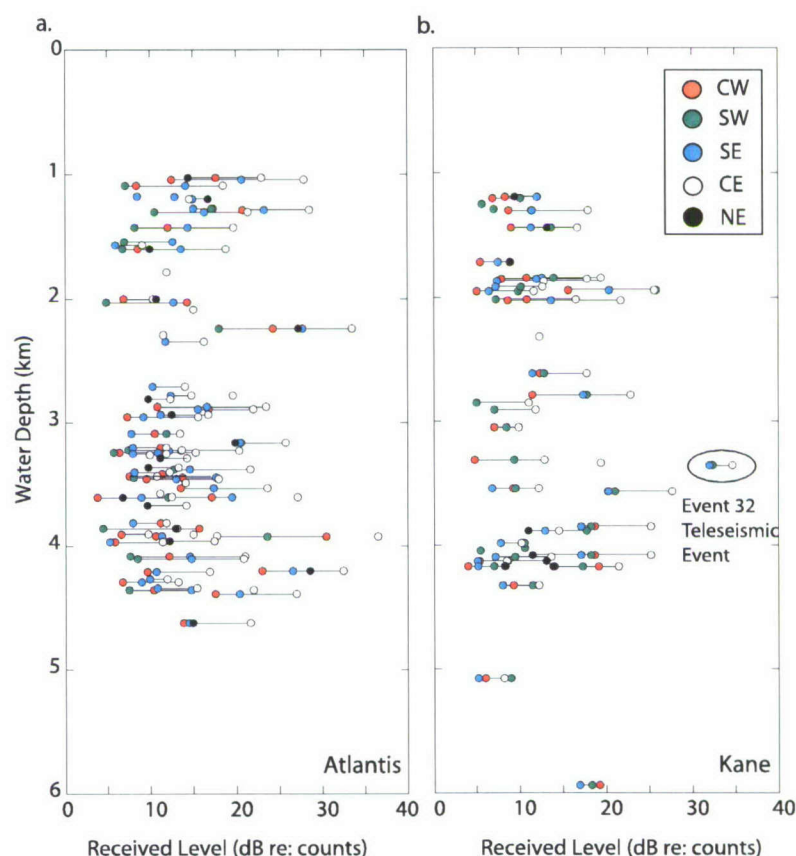
Figure 6. Plot of T-phase Received Level versus event location water depth for events at (a) Atlantis and (b) Kane. The different colored circles represent the 5 different hydrophones. The range in Received Level is ~5–30 dB re: counts for all water depths at both study areas. This result is contrary to ray trace theory which predicts decreasing Received Level with increasing water depth.

approaching zero at the critical depth (Figure 2c). If we assume that the range of ray angles can be related to the T-phase Received Level we would expect the Received Level to decrease with increasing water depth. However, this trend is not observed at either study region (Figures 6a and 6b). Instead, the spread in Received Levels recorded by the hydrophones for one event appears to remain fairly constant, ~5–30 dB re: counts for both study

areas, at all water depths (a similar trend is observed for Source Level as well). We assume that all hydrophone-recorded events have magnitudes <4.0 m_b, (except the 3 teleseismic events at Kane) because they were not listed in the teleseismic earthquake catalogs. We also assume that most of the T-phase events have magnitudes >3 m_b because 3 m_b is the level of completeness for the NAHA [*Bohnenstiehl et al.*, 2002]. Therefore the range of

Table 3. Teleseismic Events From the Kane Study Area

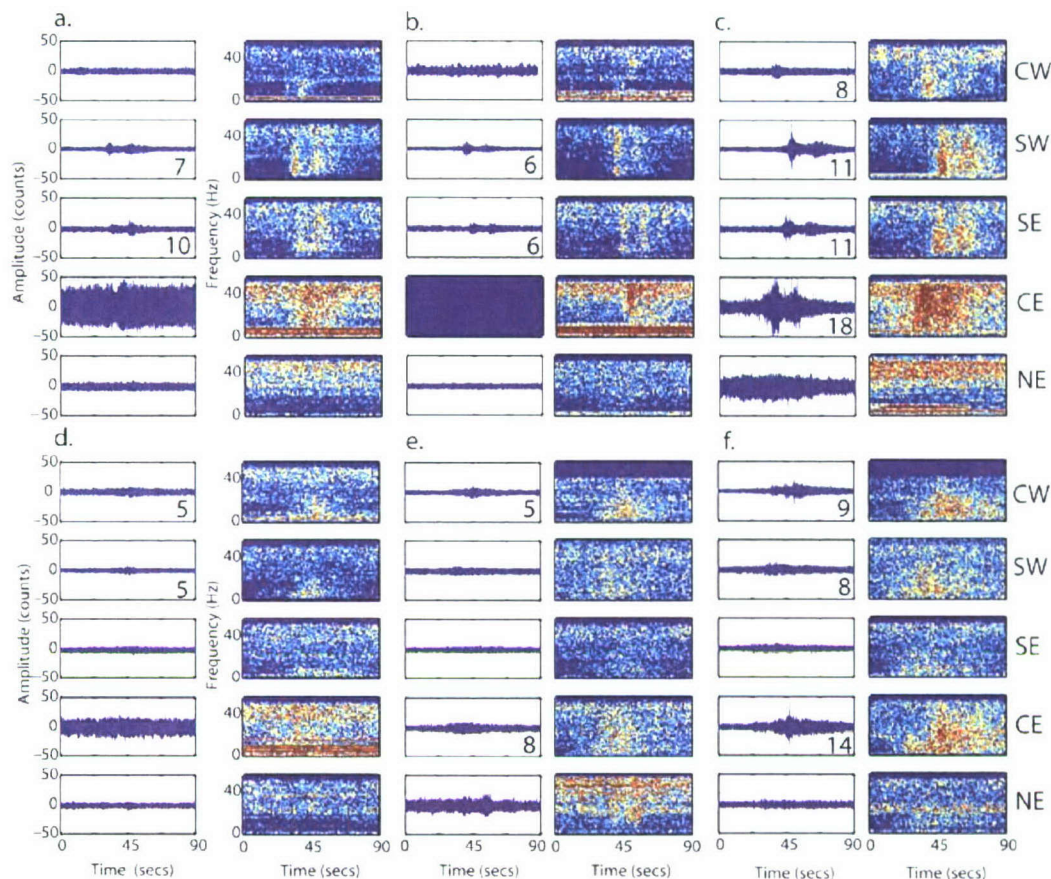| Event Number[a]	ISC, m_b	IDC/EIDC, m_b	NEIC, m_b	Mean m_b	Mean Received Level, dB re: counts	Source Level, dB re: 1μPa @ 1m	Event Location Water Depth, km
32	4.1	4.0	4.0	4.03	27.78	234.15	3.358
41	4.2	3.9	4.4	4.17	17.66	221.89	4.177
43	4.1	3.9	4.5	4.17	18.3	222.13	2.966

[a] See Figure 4b for locations.

Figure 7. Time series and spectrograms of the two clusters of events identified by the open black circles in Figure 4b. All six columns show data for the CW-SW-SE-CE-NE hydrophones from top to bottom. (a–c) Time series and spectrograms for events 4, 5, and 9 located at the top of the ICH massif at ~1.2 km water depth. The T-phase Received Level at the hydrophones (in dB re: counts, labeled by black text) varies for the three events, but the appearances of their T-phase time series and spectrogram are similar. All three have short onset times (defined as the time interval between the appearance of the T-phase envelope above the ambient noise and its first peak). (d–f) Time series and spectrograms for events 3, 58, and 61 located near the neovolcanic zone at ~4 km water depth. These events also have varying Received Levels, but the T-phases have longer onset times than events 4, 5, and 9 above.

earthquake magnitudes for all our events has relatively small scatter (between ~3–4 m_b) and variable earthquake magnitudes are unlikely to be the source of the range of Received Levels between T-phase events. We confirm this assumption by comparing groups of events with similar Received Level and Source Level but no trends with changing water depth were observed. To highlight the variability in Received Level for T-phase events located at the same water depth we compare the spectrograms from two clusters of 3 events located at ~1.2 km (Figures 7a–7c) and ~4 km water depth at Kane (Figures 7d–7f). The locations of these two clusters are outlined by the open black circles in Figure 4b. Within each of the two clusters

the T-phase event time series and spectrograms look similar but the hydrophones record a range of Received Levels (dB re: counts values shown in the large black text in Figure 7).

[32] Ray trace theory also predicts that energy from events which occur at water depths below the critical depth will not propagate to the hydrophones in the SOFAR channel (Figure 2c), however several T-phase events are located below the average critical depth in both our study areas (~4.5 km water depth). One explanation for the hydrophones recording these deep water events may be insonification of large areas of seafloor by earthquakes. Ray trace modeling of an earth-
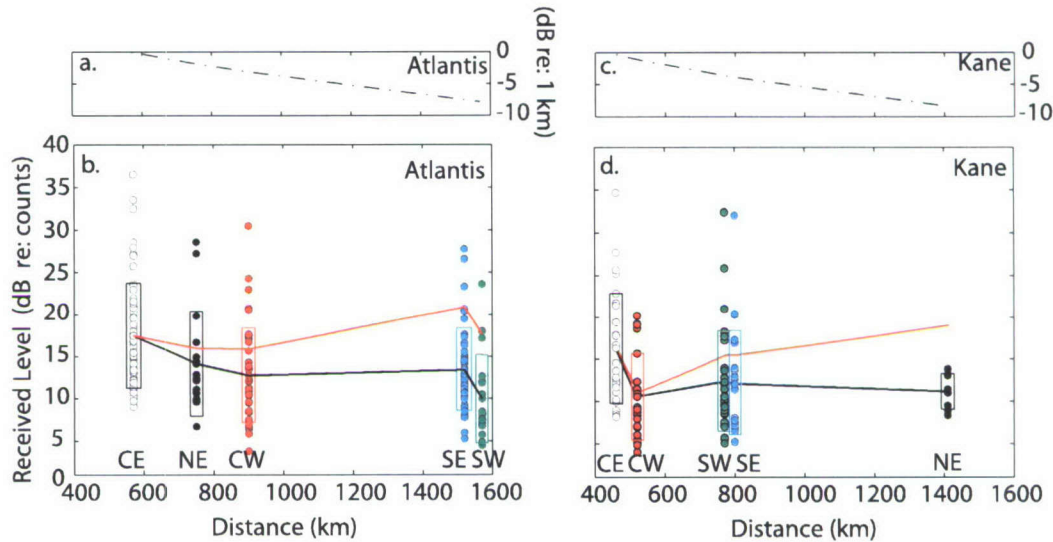
Figure 8. (a and c) Plots show transmission loss curves due to cylindrical spreading and intrinsic attenuation from each study area to the hydrophones. We define the transmission loss to be zero at the hydrophone closest to the event and a maximum at the furthest hydrophone. (b and d) Received Level versus distance from the event to the hydrophones for the Atlantis and Kane study areas respectively. The solid black line represents the mean Received Level (in dB re: counts) for each hydrophone. The mean Received Level is corrected for transmission loss and shown by the red line. The vertical colored bars at each hydrophone represent one standard deviation from the mean Received Level. Events from the Atlantis region have the highest Received Level at the CE and SE hydrophones and the lowest at the CW and NE. Events from the Kane region have the highest Received Level at the CE and NE hydrophones and the lowest at the CW hydrophone.

quake with a hypocenter at 4 km depth in the crust shows that energy insonifies a seafloor area of ~20 km radius [*Stephen et al.*, 2002]. The source of the T-phase therefore may be a large area of the seafloor that includes water depths above and below the critical depth (a broad area of insonification is also discussed by *de Groot-Hedlin and Orcutt* [1999, 2001] and *Yang and Forsyth* [2003]). Until the mechanisms of seismic energy coupling into the water column and conversion to acoustic energy are understood (whether it can be explained by ray or wave theory) this problem will remain.

5.4. Received Level of T-Phases Versus Distance From Event to Hydrophone

[33] Received Levels decrease with increasing source to receiver distance, as shown by the mean Received Level (black solid line) in Figures 8b and 8d. This result is expected because T-phase energy is reduced by transmission loss, attenuation and scattering along the propagation path. Transmission loss curves are calculated for each study region by summing attenuation due to cylindrical spreading and intrinsic attenuation in the water column (Figures 8a and 8c; see Appendix B).

The curves are then used to correct for transmission loss at each hydrophone relative to the hydrophone closest to the event (i.e., the transmission loss at the furthest hydrophone is maximum and zero at the closest hydrophone). The mean Received Level (black line in Figures 8b and 8d) is then corrected for transmission loss so as to reduce the number of processes that affect the T-phase as a function of distance from the event to the hydrophones. The correction flattens the trend of mean Received Level versus distance (red solid line in Figures 8b and 8d) and highlights the relative differences in mean Received Level recorded by each hydrophone.

[34] We believe the corrected mean Received Level (red solid line in Figures 8b and 8d) may reflect bathymetric blockage along the propagation path for different source and receiver pairs. The trend of the corrected mean Received Level is different for each study area. Events from the Atlantis study area have a corrected mean Received Level which varies by ~5 dB re: counts between hydrophones (Figure 8b). The CW hydrophone records events that have the lowest magnitudes, closely followed by the NE hydrophone. The SE hydrophone
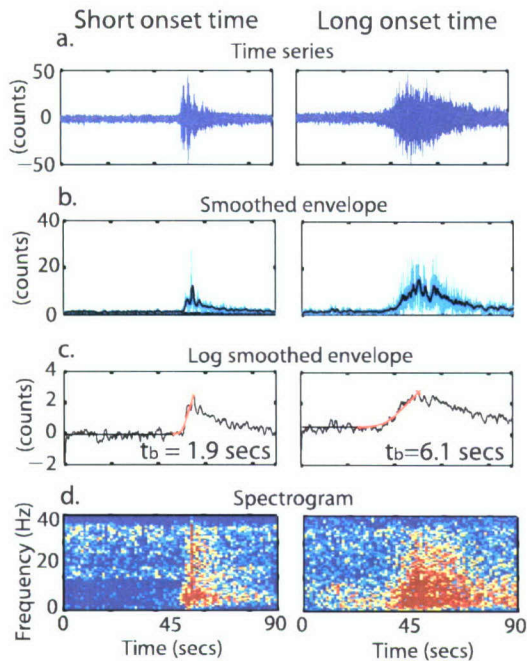
Figure 9. Examples of the curve fitting process used to calculate the onset time of the T-phases (the time interval between the appearance of the T-phase envelope above the ambient noise and its first peak). A short onset time event in shown in the left column, and a long onset time event is shown in the right column. (a) Time series of an event recorded at one hydrophone. The time series is band pass filtered in an octave centered on 16 Hz. (b) A complex envelope of the time series is calculated and smoothed with a one second running average (black line). (c) The log of the smoothed complex envelope with a fitted curve (red line). The value of the onset time, t_b, is shown in seconds. (d) Spectrogram of the event.

records events with the highest magnitudes and the CE and SW are intermediate. The greatest difference in magnitude is between the two southern hydrophones, which have only 50 km difference in the length of the propagation path but have an average difference of ~4 dB re: counts. The corrected mean Received Level from the Kane study area varies by ~8 dB re: counts between hydrophones (Figure 8d). As with the Atlantis events, the CW hydrophone records the lowest magnitudes for the Kane events but the NE hydrophone records the highest (however, there are few data points for the NE hydrophone). Unlike the Atlantis events, the Kane events have approximately equal magnitudes at the two southern hydrophones. These results and their significance for bathymetric

blockage are discussed in more detail in section 5.6.

5.5. Onset Time

[35] The onset time is defined as the time interval from when the T-phase envelope or lens emerges above the ambient noise to the first peak in the T-phase (Figure 2a). We quantify the onset time following the curve fitting method of *Yang and Forsyth* [2003] (details can be found in Appendix C). The onset time was only calculated for those events with a signal-to-noise ratio (SNR) >2 and with latitude and longitude errors <0.03° (27 events at Atlantis and 17 events at Kane) so as to exclude those events with anomalously high ambient noise levels.

[36] The first peak in many of the events in our study area is not the maximum peak of the T-phase time series, and thus the onset time differs from the "risetime" [*Schreiner et al.*, 1995; *Dziak and Fox*, 1999b] which is defined as the time from the emergence of the T-phase to its maximum peak. T-phase locations are traditionally based on either the arrival time of the largest amplitude of the smoothed envelope of the time series or on the arrival time of the broadest spectral content in a spectrogram. For simple lens-shaped arrivals these are usually at the same time (for example the two events shown in Figure 9). For more complicated arrivals with multiple peaks (for example, events 4, 5 and 9 shown in Figures 7a–7c) the broadest spectrum may not correspond to the peak of the envelope or multiple peaks may have indistinguishable amplitude and spectral content. As we do not understand the mechanism for multiple peaks we focus only on the first peak in the T-phase.

[37] We quantify the onset time by fitting a curve to the log of the complex envelope of the event (Figure 9, Appendix C). We then select and empirically define a critical onset time, t_c, based on our visual inspection of the T-phase coda. A T-phase event that has onset times <t_c, for all the hydrophones which record the event are termed "short onset" and onset times >t_c "long onset" events. The t_c is 4 seconds for the Atlantis and 6 seconds for the Kane study areas. Those events with hydrophone onset times that bridge the critical onset time are termed "mixed onset".

[38] Our results show that all of the short onset events in both study areas are located on the top and slopes of the ICH in water depths <2 km
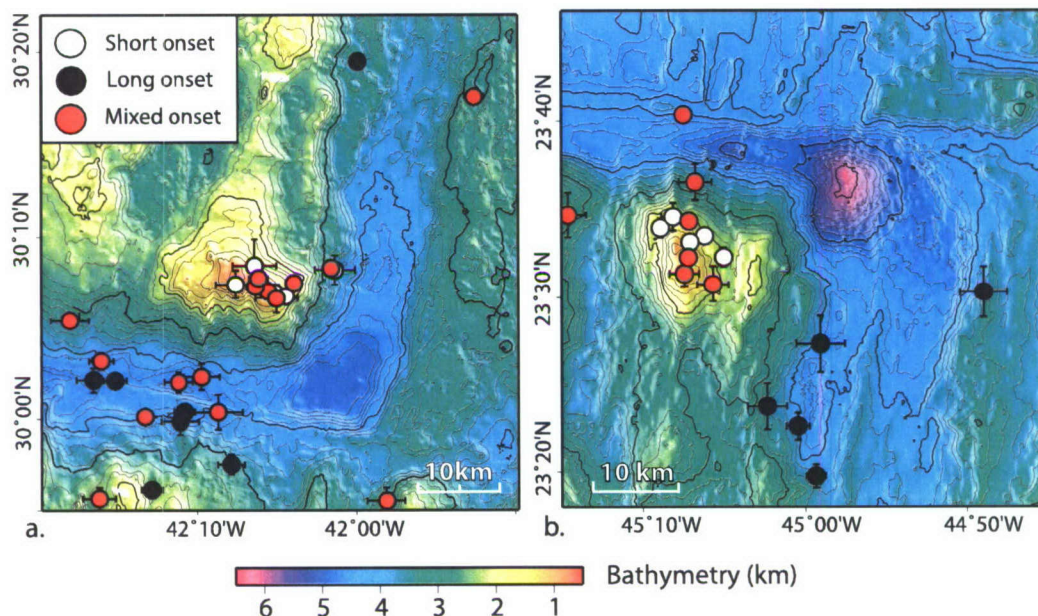
Figure 10. Map showing the spatial distribution of onset times for (a) Atlantis and (b) Kane. The critical onset times at Atlantis and Kane are 4 seconds and 6 seconds, respectively. The white circles represent events for which arrivals at all the hydrophones were shorter than the critical onset time, and the black circles represent all arrivals longer than the critical time. Those events that have arrivals which bridge the critical onset time are shown in red. The general trend in the two study areas is short onset events at water depths <2 km and long onset events at water depths >2 km. Only those events with SNR >2 are shown in this figure. The bathymetry contour interval is 200 m in both Figures 10a and 10b.

(Figure 10). All of the long onset events are located on the seafloor in water depths >2 km. The mixed onset events occur in both shallow and deep water. This is strictly an empirical observation but the correlation between onset time and event water depth is remarkable. At this time we do not have a physical explanation for this correlation. It is interesting to note that all of the events with mixed onset at the Kane were due to a long onset time recorded by the CE hydrophone alone. Only two of the mixed onset events at Atlantis, located at the top of the massif, were due to a long onset time for the CE hydrophone alone. The CE hydrophone is the closest hydrophone to the Kane study area (~460 km) and the second closest to the Atlantis study area (~560 km). We therefore conclude from this that length of the propagation path does not influence the onset time of the event.

[39] Variations in risetime of T-phases have been noted prior to this study [*Johnson et al.*, 1968, *Schreiner et al.*, 1995; *Dziak and Fox*, 1999b; *de Groot-Hedlin and Orcutt*, 2001; *Yang and Forsyth*,

2003]. *Schreiner et al.* [1995] interpret the change in risetime to reflect the crustal depth of the seismic source: a deep crustal event will insonify a larger surface area of the seafloor and have a long risetime. The opposite is true for a shallow crustal event which may have a tighter wave packet and shorter risetime. However, our onset time could also be a function of other variables apart from hypocenter depth, such as efficiency of energy conversion from shallow topography and efficiency of propagation based on water depth of the event (Figure 2c).

[40] Onset times can vary depending on the T-phase excitation process. Downslope propagation on a steep slope requires few reflections (Figure 3a) and may be considered a more efficient coupling mechanism than rough seafloor and sea surface scattering, where only a small percentage of the acoustic energy can propagate in the SOFAR channel [*Johnson et al.*, 1968; *Talandier and Okal*, 1998]. *Johnson et al.* [1968] suggested that downslope propagation and seafloor scattering excite
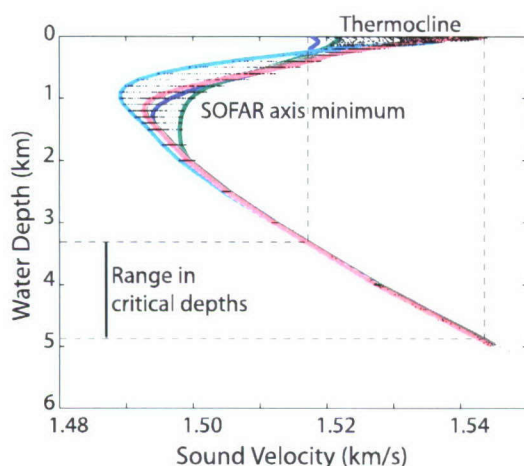
215

Figure 11. Two hundred and forty sound velocity profiles between each of the six hydrophones and the Kane study area are shown by the black dots. The data were acquired from the Generalized Digital Environmental Model (GDEM) for four times of year (March, June, September, and December). The five colored lines represent the five profiles used in the ray trace modeling to represent all the variability in the water column sound velocity. We assume that the sound velocity profile is constant from the event to the hydrophone. The critical depth of the five profiles varies greatly (3.35–4.85 km, shown by black dashed line) due to the large variation in sound velocity in the thermocline.

different types of T-phases: (1) Slope T-phase, generated by downslope propagation, and (2) Abyssal T-phase, generated by excitation scattering processes. The Slope T-phase has a short onset time and low frequencies compared with the Abyssal T-phase which has a long onset and high frequencies. *de Groot-Hedlin and Orcutt* [2001] also observed differences in the onset times of T-phases, excited by scattering alone, at different water depths. Their synthesized T-phases show deep water events have higher frequencies, shorter durations and are near-symmetrical compared with shallow T-phase events generated on slopes. If we compare shallow and deep water events in our study areas (Figure 7 and Figure 10) the deep events have long onset times and lower frequencies compared with the shallower events (Figure 7). Therefore our results do not reflect the same frequency or duration characteristics as seen by *Johnson et al.* [1968] and *de Groot-Hedlin and Orcutt* [2001]. This suggests that the T-phases generated at RTI locations (average slopes $>\sim10°$) are different from Abyssal and Slope type T-phases.

[41] Efficiency of propagation based on water depth over the event is the same hypothesis discussed in section 5.1. An event at the depth of the SOFAR channel axis will propagate more efficiently because the majority of its energy will enter the waveguide and propagate with little attenuation [*Pulli et al.*, 1999].

5.6. Ray Trace Model

[42] A ray trace model was used to investigate bathymetric blocking of T-phase energy assuming a coupling mechanism of rough seafloor scattering. The model assumes Snell's Law and takes into account 1-D topography along the propagation path (for details see Appendix D). The model was run five times for each event, each time with a different sound velocity profile. The five profiles were used to encompass the seasonal variability observed in the water column (Figure 11). They were obtained from the Generalised Digital Environmental Model (GDEM) [*Davis et al.*, 1986; *Teague et al.*, 1990]. The range in critical depth for the five profiles is 3.35–4.85 km (average ~4.1 km, Figure 11). In the ray trace model, ninety rays are emitted from each T-phase event at 1° increments from horizontal to vertical (Figure 12). When a ray intersects the seafloor or sea surface it is terminated. The number of rays that reach the range of each hydrophone for an event is averaged over the five runs of the model and this value is used for the rest of our analyses. We find that only 1–9 rays reach each of the hydrophones from events in the Atlantis study region (Figure 13a) and 1–12 rays from events in the Kane study region (Figure 13b). These numbers represent a maximum of 10% of the original energy of the T-phase (assuming omnidirectional scattering). Note that the model results show that no rays should have reached the hydrophones for ~65% (61 events) of the events that were recorded by the hydrophones from the Atlantis area and ~33% (21 events) of the events from the Kane area because they encounter the high relief of the transform and median valley walls (e.g., MAR location shown by gray box in Figure 12). The ray trace model also predicts that rays should have reached one or more hydrophones for 9 events from Atlantis and 6 events from Kane that were not included in the hydrophone catalog. Of the 9 events from the Atlantis area, the data from 5 of them have noise from air guns and other unidentified noise sources which mask the T-phase to some extent. The data from 2 events from the Kane area also have noise from air guns. The large percentage of events for
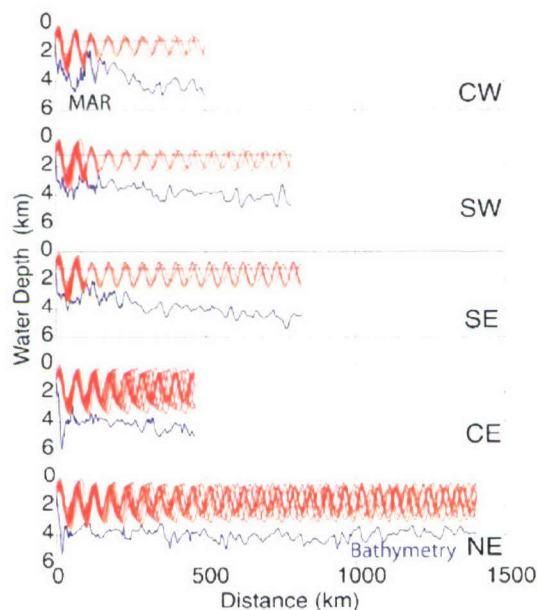
Figure 12. Example of the ray trace model output for one event located on the top of the Kane massif. The blue line is bathymetry, and the red curves are the ray traces. Ninety rays emerge from the event on the left-hand side of the plot, and any ray that intersects the bathymetry is terminated. We assume the number of rays that reach the hydrophone on the right-hand side of the plot are a proxy for the amount of energy that propagates to the range of each hydrophone. Each source to receiver path encounters very different topography; some cross the MAR axis (marked by gray column on CW hydrophone), while others travel only along the deeper water of the ridge flanks (NE).

which no rays should have reached the hydrophones implies that this model is not a good predictor of acoustic energy levels. To identify where and why the ray trace model does not work we consider sound velocity profile variations, source location water depth, and distance from the event to the hydrophones.

[43] We find that the model results for the number of rays that reach a hydrophone are strongly dependent on the sound velocity profiles used. As an example, for one T-phase event at the Atlantis study region, the number of rays that reached the range of the NE hydrophone varies between 2–12 rays depending on the sound velocity profile used. The standard deviation from the average number of rays that reach the range of the hydrophones is largest for the shallow events and generally decreases with increasing event location water depth. Our results may be influenced by the

large variation in the SOFAR channel sound velocities observed around the same depths as these shallow events (~10 m/s difference over 0.5–1.5 km water depth, Figure 11). This variation in the sound velocity profile may be caused by changes in Antarctic Intermediate Water [*Roemmich and Wunch*, 1985] or possibly high salinity Mediterranean Eddies ("Meddies"), both of which lie around this depth in the water column [*Richardson et al.*, 1988, 1991]. Whatever the source, future T-phase propagation models should take sound velocity variations into account.

[44] The ray trace model results combine two processes: the event location depth dependence from ray trace theory (see Figure 2c) and bathymetric blockage along the direct line propagation path from the source to the receiver. We have included all T-phase events at all hydrophones, apart from those with large location errors (> 0.03°), for the ray trace model so as to take into account events that may not have been recorded due to bathymetric blockage (79 events at Atlantis and 43 events at Kane). Therefore there are more T-phase events shown in Figures 13 and 14 than in Figures 6 and 8.

[45] In this model we use the number of rays that travel unblocked to the hydrophone range as a proxy for the energy arrival at each hydrophone. Admittedly this is a simple model but the results have shown it is applicable. We take the same approach as the observed data and compare the number of rays that reach the range of the hydrophones with the event location water depth and source to receiver distance. When we compare the number of rays with event water depth we observe a decrease in the number of rays with increasing water depth, approaching zero rays as the average critical depth (4.1 km) is reached for the five sound velocity profiles (Figure 13). This is the relationship we expected to observe in the Received Levels. However, Received Levels remain fairly constant at all water depths (Figure 6) suggesting that omnidirectional scattering combined with the event location water depth dependence does not describe the process of coupling at the seafloor. The process of T-phase generation is more complex and does not appear to be strictly bounded by the sound velocity profile.

[46] The ray trace model results (Figures 14b and 14d) show two different trends in the mean number of rays versus distance from the event for the two study areas and there is some correlation between the model trend and the observed data trend
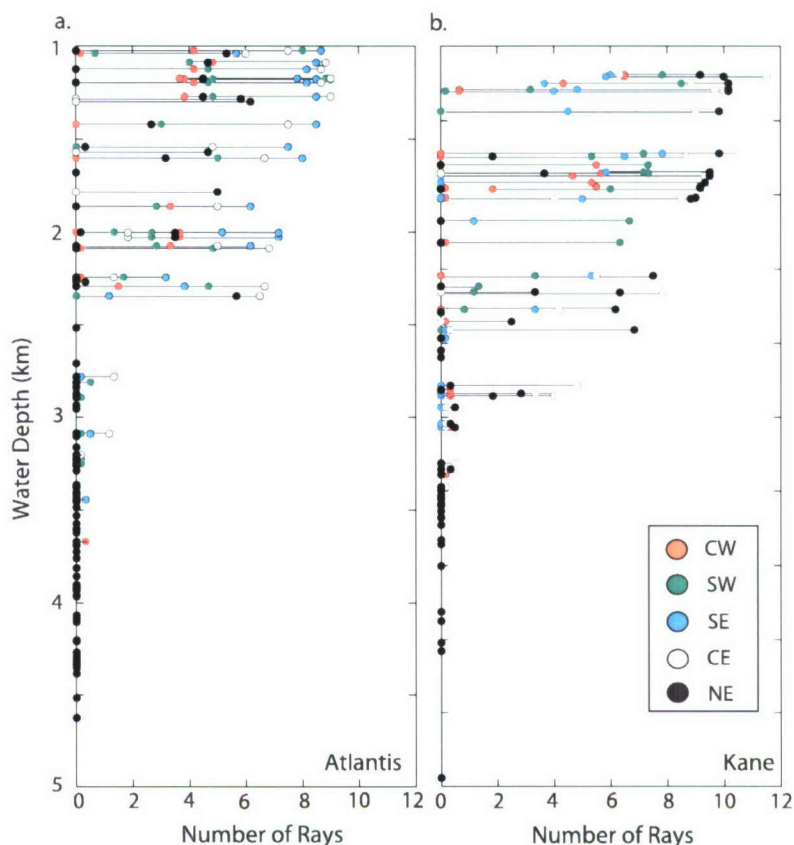
Figure 13. Ray trace model results versus water depth for events from (a) Atlantis and (b) Kane. The results are a combination of an event location depth dependence (from Figure 2) and bathymetric blockage. Those events which appear to have only one black circle represent events where no rays made it to any of the 5 hydrophones and the five colored dots are stacked at zero, with the NE hydrophone (black circle) on the top. The overall trend is decreasing number of rays with increasing event water depth at both study locations. The CE and SE hydrophones receive the highest number of rays relative to all the other hydrophones from the Atlantis region, and the CE and NE hydrophones receive the highest from the Kane study region.

(Figures 14a and 14c). For events from the Atlantis region, the model has a minimum mean number of rays at the CW hydrophone and maximum mean number of rays at the CE and SE hydrophones. The maximum values at the CE and SE hydrophones may be due to the rays entering deep water more quickly along the first 50 km of the propagation path, compared with propagation paths to the NE and SW hydrophones. The minimum at the CW hydrophone is most likely due to the shallow MAR axis topography between the source and the hydrophone.

[47] For Kane events the model shows the CE and NE hydrophones have the maximum mean number of rays and the CW hydrophone the minimum. Again, the rays enter deeper water more quickly

along propagation paths to the CE and NE hydrophones which may explain why more rays, in general, make it to these hydrophones (Figure 12). Even though the CW hydrophone is located close to the Kane region (~500 km), the T-phases must propagate out of the transform fault and over the MAR axis, resulting in much interaction with the topography and disruption of the T-phases before they reach the CW hydrophone.

[48] The high standard deviation of the observed data and the model results makes it difficult to interpret the results extensively. We conclude that the ray trace model under predicts the amount of energy that propagates from deep water events, and the model condition that the rays terminate when they intersect the bathymetry is likely too rigorous.
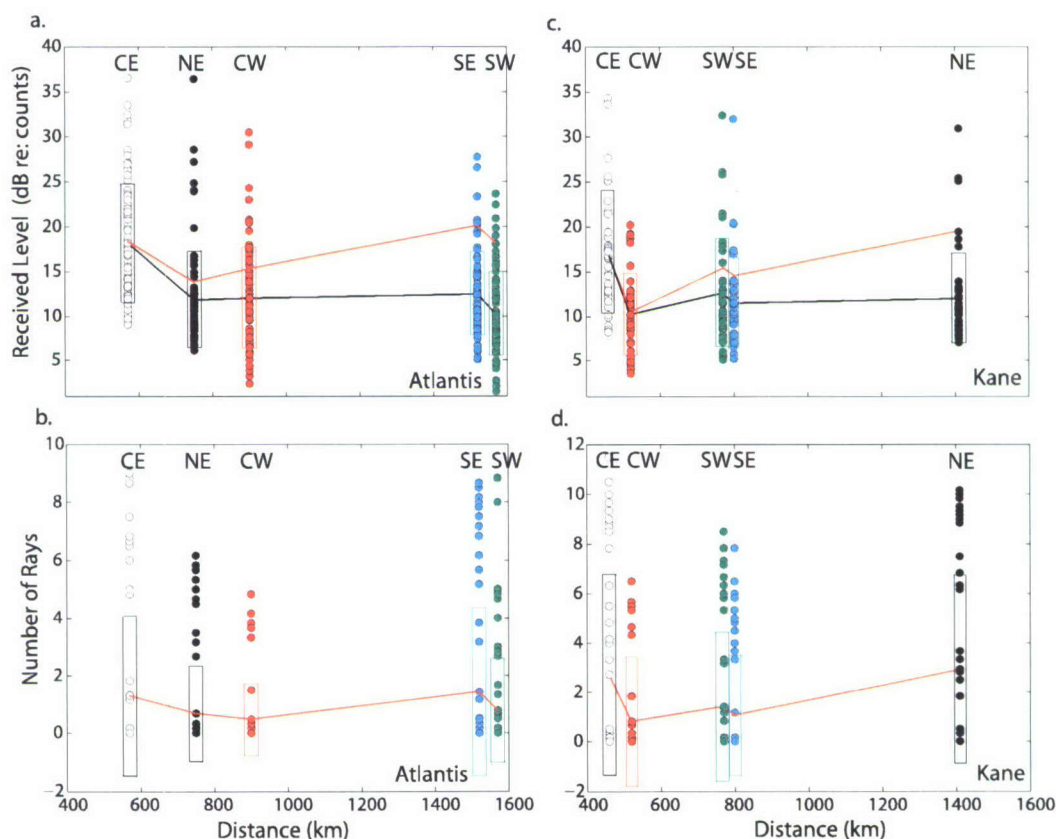
Figure 14. (a and c) Received Level versus range from the event to each hydrophone for the Atlantis and Kane study areas, respectively. These plots differ from the data used for Figure 8 because all of the data are used (we incorporate all of those hydrophones not used in the T-phase catalog to locate the T-phase events and all of the T-phase events with RMS Signal <1 dB re: counts). The mean Received Level (black line) is corrected for transmission loss to give the corrected mean Received Level (red line) in the same way as Figure 8. The vertical boxes represent one standard deviation from the mean. (b and d) The ray trace modeling results. The red line represents the mean number of rays for each hydrophone, for direct comparison with the red lines in Figures 14a and 14c, and the colored vertical bars are one standard deviation from the mean. The mean appears to be low for the model results, but this is due to the large number of events for which no rays made it to the hydrophone because of bathymetric blockage (i.e., there are multiple values of zero). In each of the study areas the ray trace model results and the observed Received Level reflect similar trends in the relative amount of energy that reaches the range of the hydrophones.

Instead some percentage of the energy may make it past topographic features, either by propagation scattering or wave front healing [*Claerbout*, 1985; *Pulli and Upton*, 2002]. Alternatively the theory of a critical depth is incorrect for T-phase propagation and some portion of the T-phase energy from an event below the critical depth is able to enter the SOFAR channel. In summary, the results of our model do not explain the Received Level of the T-phases based on the water depth of the events and highlight the complexity of the coupling process. However, the model does show that bathymetric blockage along the propagation path affects the amplitude of a T-phase. The model predicts two trends in relative energy levels between hydrophones as a function of distance from source to receiver for the two study areas and these trends are similar to the trends observed in the Received Levels.

6. Discussion

[49] A T-phase excitation and propagation model that explains all of the observed characteristics of T-phase arrivals (lens shape, risetime, multiple peaks, spectrogram behavior, etc.) does not exist.

In general, there are two regions to consider: a relatively short excitation region where the T-phase characteristics are established, and a propagation region where the T-phase energy is totally trapped in the ocean sound channel (there have been occasional observations of basin scale multipathing, with secondary scattering from continental margins [e.g., *Shurbet and Ewing*, 1957]). Some common hypotheses for excitation within the short region where the T-phase characteristics are established are summarized in Figure 3. Scattering from roughness and heterogeneities at and near the seafloor has been invoked to explain the excitation of abyssal (water depths greater than 3 km) T-phases (Figure 3b). Even this mechanism, however, is inadequate when the seafloor is well below the critical depth (Figure 3c).

[50] All T-phases by definition involve long range propagation in the ocean. There is growing evidence however that T-phase propagation involves the coupling of energy between the ocean sound channel and the shallow oceanic crust including the almost ubiquitous sediment layers [*Butler and Lomnitz*, 2002]. Recent observations have shown that the reciprocal process to excitation, getting energy out of the SOFAR channel into the crust, is commonplace even in deep water [*Butler and Lomnitz*, 2002; *Butler*, 2004]. In fact earthquake generated T-phases have been observed on borehole seismometers in the Western Pacific (WP-2) and Philippine Sea (WP-1) that are over 400 m below the seafloor in water depths exceeding 5.5 km [*Araki et al.*, 2004]. Hence scattering may also play a significant role in long-range T-phase propagation as well. The absence of water depth dependence in our T-phase data is consistent with the notion that T-phases are inadequately explained by models with perfect, laterally homogeneous waveguides, even when seafloor scattering is invoked in the excitation region.

[51] Our discussion of the water-depth dependence of T-phase excitation (section 2 and Figure 2) is based on a ray model. Long-range propagation in the ocean can be described by rays in three categories: refracted refracted paths, refracted surface-reflected paths and surface-reflected bottom-reflected paths [*Jensen et al.*, 1994]. For simple velocity depth profiles (e.g., Figures 2 and 11) the critical depth defines the waveguide for the refracted refracted paths. These totally trapped paths are the most efficient for transmitting energy because they are only subject to cylindrical spreading and the intrinsic attenuation of water.

The other paths suffer scattering losses at each bounce with either the sea surface or seafloor interface. Although these losses may be small for a single bounce, long range propagation involves many bounces so the losses can be significant. Multiple water bounces may play a role in the near-field T-phase excitation region [*Yang and Forsyth*, 2003], but refracted surface-reflected paths and surface-reflected bottom-reflected paths are not traditionally used to explain the long-range propagation.

[52] Alternatively, long-range ocean acoustic propagation can be described by modes. The low order modes correspond to the refracted refracted paths and the smallest grazing angles (high incidence angles). Observations of T-phases on vertical arrays show that the energy is concentrated in the lowest order modes (usually less than mode 7) with grazing angles less than $10°$ (incidence angles greater than $80°$) [*D'Spain et al.*, 2001]. For example, Figure 2 of *de Groot-Hedlin and Orcutt* [2001] shows the acoustic excitation as a function of seafloor depth for the first three modes at frequencies from 5 to 20 Hz. All of the modes decay substantially by 3 km water depth. This is the modal explanation of what we have described above using rays.

[53] Our knowledge of T-phase dynamics is deficient because we do not know the physical mechanisms responsible for getting abyssal T-phase energy from the earthquake epicenter into the SOFAR channel (in the excitation region) or for getting energy out of the SOFAR channel into the deep seafloor (in the propagation region). Some form of scattering at or near the seafloor has been shown to be necessary in the excitation region to convert the compressional and shear body waves from earthquakes into the high incidence angle paths necessary for propagation in the SOFAR channel [*de Groot-Hedlin and Orcutt*, 2001; *Park et al.*, 2001] but this process would not work when the seafloor is substantially below the critical depth. Also the ubiquitous observation of T-phases in the propagation region on seismometers at and below the seafloor even in water depths well below the critical depth, is not adequately explained by existing models. An improved understanding of the dynamics of T-phases is required. Until the coupling between the sound channel and the crust is adequately understood, quantitative consideration of more complex phenomena, such as reflection from continental margins, blockage by islands and seamounts, or the

inversion of T-phase characteristics for earthquake parameters, is premature.

7. Conclusions

[54] In this study we made two assumptions about the T-phase events located in the Atlantis and Kane study areas: (1) the T-phase event locations are accurate, and (2) the locations represent earthquake epicenters. We examined the detailed characteristics of 158 T-phase events and modeled their propagation to assess the dependence of T-phase amplitude on event water depth, source to receiver distance, the relationship to onset time and the effects of bathymetric blockage along the propagation path. From our analyses we make the following conclusions:

[55] 1. A greater number of T-phase events are located at shallow water depths (on the ICH massif and slopes at depths of 1–2 km) than deep water in both our study areas, when the number of events is normalized to the seafloor area. The events may be correctly located and our observations reflect clustering of real seismic events on the massifs due to local tectonic or volcanic processes or more efficient generation or propagation of shallow water T-phases. Alternatively, the events could be mislocated and the massifs may act as radiators for energy from earthquakes located in the adjacent valleys. It is impossible to say from our data which of these processes and mechanisms, if any, controls the spatial distribution of the T-phase events. Our two assumptions that T-phase event locations are accurate and the locations represent earthquake epicenters can only be addressed by comparing concurrent ocean bottom seismometer and hydrophone data. These types of surveys have been deployed recently and should provide answers in the near future.

[56] 2. Three events located in the Kane study area were recorded as both teleseisms and T-phases, the smallest of which was 4 m_b. The seismic body wave magnitude and mean amplitude (mean Received Level) recorded at the hydrophones for these three events are not correlated, but the small number of events makes it difficult to draw conclusions from this. However, seven events in the Atlantis study area with mean Received Level greater than the smallest of the three teleseismic events were not recorded as teleseisms. Therefore the relationship between seismic and acoustic magnitude may be location specific and more complex than previous studies have suggested.

[57] 3. The Received Level of a T-phase is not sensitive to water depth at the T-phase event location. T-phase data show large variations in the Received Level of an individual event at the five hydrophones but little variation in overall Received Level with changing event water depth. In contrast, our ray trace model predicts that the number of rays which reach a hydrophone from a T-phase event decreases with increasing water depth of the event location, and no rays reach hydrophones from events where the seafloor is located below the critical depth. Therefore omnidirectional scattering combined with ray trace theory cannot be used to explain T-phase excitation.

[58] 4. The ray trace model results combine two processes: the event location depth dependence from ray trace theory (which includes seasonal variations in the sound velocity profiles) and 1-D bathymetric blockage along the propagation path. On the basis of our model only 35% of the T-phase events included in the hydrophone catalog located in the Atlantis study region and 64% of the events in the Kane study region should have been recorded by the hydrophones. The assumption that a ray is terminated when it intersects the seafloor is likely too rigorous. Some portion of the T-phase energy is able to propagate past shallow features to the hydrophones, possibly by scattering or wave front healing, or the theory of a critical depth (based on a laterally homogeneous waveguide) is not appropriate for T-phase excitation and propagation.

[59] 5. The ray trace model did show that there is a correlation between the model mean number of rays and the mean Received Level of events versus distance from the source (earthquake epicenter) to the receiver (hydrophones). Having removed the effects of transmission loss from the signal, it appears that bathymetric blockage is an important process that causes variations in the magnitude of an event as recorded by different hydrophones in an array. The relative change in mean Received Level for increasing source to receiver distance is very different for the two study areas. The model is able to reproduce similar relative changes in the mean number of rays. Ray trace theory can therefore explain to some extent the process of bathymetric blockage but the data have large variances and more analysis with a larger number of events would be needed to confirm the accuracy of the model.

[60] 6. The onset time of the T-phase, defined as the time interval from when the T-phase emerges

above the ambient noise to the first peak in the T-phase, follows a pattern of short onset times for shallow water events and long onset times for deep water events. This is a remarkable correlation. At this time we do not have a physical explanation for this empirical observation. We suggest that the onset time is a function of several variables including: efficiency of energy conversion based on local topography, efficiency of propagation based on water depth of the event and hypocentral depth of the event. Length of the propagation path does not appear to correlate with onset time. The duration of the onset time and the frequency content of our T-phase events do not agree with earlier work which identify Abyssal (long onset time and high frequencies) and Slope (short onset time and low frequencies) type T-phases. This suggests that the T-phases generated at mid-ocean ridges cannot be classified using the same criteria and may define a new type of T-phase.

[61] Our observations of T-phase characteristics require an improved model for T-phase excitation and propagation that addresses: the process of introducing energy into the SOFAR channel from events located at water depths which exceed the critical depth, the influence of seafloor roughness on seismic to acoustic conversion and the affect of variations in the sound velocity profile between the event and the hydrophone, particularly around the sound channel axis minimum, on T-phase propagation.

Appendix A: Picking the Events

[62] The hydrophones in the NAHA record 1-byte resolution data at a sample rate of 112 samples per second (C. Fox, personal communication, 2001) with a 1–40 Hz band pass filter [Fox et al., 2001]. The frequency-pressure response function used corresponds with SW = 3 in Figure 2 of Fox et al. [2001].

[63] The first step in processing the T-phase data was to locate the seismic arrivals from the T-phase catalog in the raw hydrophone data. Summary plots of time series and spectrograms for arrivals at all six hydrophones for each event were compiled (examples shown in Figure 7). All 158 events recorded in the Atlantis and Kane study areas between 25 February 1999 and 9 March 2001 are shown in Tables 1 and 2, respectively. The spatial distribution of the T-phases includes all these events (Figure 5). For subsequent analysis of the T-phases those events with location errors greater

than 0.03° (∼3.4 km) in either latitude or longitude were removed from the data set to improve the data quality (∼15 events were removed from each data set).

[64] Ambient noise levels vary between hydrophones and high ambient noise levels reduce the detectable level of T-phases. In order to quantify the ambient noise, the RMS of the first 10 seconds of each 90 second window of the time series was computed with the assumption that this was "quiet time" before the arrival of the T-phase. We define this value as the RMS Ambient Noise. The RMS Signal of the T-phase was then calculated by subtracting the RMS Ambient Noise from the RMS Received Level in dB re: counts. Several of the RMS Signal calculations resulted in negative values. The majority of these negative values were traced back to air guns dominating the hydrophone recording as high amplitude, high frequency discrete signals (their removal is discussed below). Clipping of events that exceed the dynamic range of the hydrophones could also affect the calculated RMS Signal. Only one T-phase event in our analysis was clipped by the hydrophone. This was a teleseismic event (Event 32) located at the Kane study area on the CE hydrophone. Event 32 has an average magnitude of 4.0 m_b, however Fox et al. [2001] proposed the general relationship that >4.7 m_b would exceed the dynamic range of the hydrophones 8-bit systems. Newer generation PMEL instrument have a 16-bit system and others are 24-bit, leading to an increased dynamic range and reducing the occurrence of clipping for large events.

[65] To improve the quality of the data the following steps were carried out before plotting Received Level versus both event water depth and source to receiver distance:

[66] 1. The hydrophone catalog used 3 or more hydrophones to locate their events. On occasion we saw T-phase arrivals on hydrophones not used in the hydrophone catalog for locating the event. We only used arrivals that were identified in the catalog, except for the comparisons with ray trace modeling (because of the possibility that bathymetric blocking is responsible for the lack of a T-phase arrival on some hydrophones).

[67] 2. The negative RMS Signal values were dealt with in two ways. For those events with a small contribution from the air guns (one negative hydrophone signal per event) the individual negative hydrophone picks were removed. For an event with

a large contribution (greater than three negative values per event) the whole event was removed from the data set because the RMS Received Level values represent the noise and not the T-phase amplitude.

[68] 3. In order to work only with events of a significant magnitude, all events with an RMS Signal level of <1 dB re: counts were removed (except for comparison with ray trace modeling results because of possible bathymetric blocking as discussed in point (1)).

[69] After these steps, 72 events from Atlantis and 39 events from Kane were used to plot Received Level versus event location water depth and source to receiver distance. T-phase event amplitude versus distance was plotted using the Received Level rather than the RMS Signal because the Received Level defines the magnitude of the actual event as recorded by the hydrophone. The RMS Signal is a modified value and depends on the ambient noise levels at each hydrophone.

Appendix B: Transmission Loss Curves

[70] The range from source to receiver will affect the magnitude of the event due to transmission loss. One transmission loss curve was calculated for each study area on the basis of two contributions:

[71] 1. Cylindrical spreading - $10 \log_{10} r$ in dB where r is in kilometers [*Jensen et al.*, 1994].

[72] 2. Intrinsic attenuation - 0.00333r or 3.3 dB per 1000 km [*Fisher and Simmons*, 1977; *Clay and Medwin*, 1977].

[73] Each transmission loss curve was subtracted from the observed data to reduce the number of processes that affect the T-phase as a function of range in each region. Transmission loss was calculated as a relative value between hydrophones by assuming that the nearest hydrophone has zero transmission loss and the furthest hydrophone has the maximum.

Appendix C: Curve Fitting

[74] We quantify the onset time following the curve fitting method of *Yang and Forsyth* [2003]. Before computing the complex envelope, the time series is band pass filtered in an octave centered at 16 Hz. The complex envelope is then smoothed with a one second running average and the log of the smoothed envelope is taken.

[75] To define the onset time of the T-phase we fit a curve to the beginning of the log of the smoothed envelope. The amplitude of the envelope as a function of time is given by

$$A = \left[A_0^2 - A_1^2 \exp\left(\frac{-2\{t_0 - t\}}{t_b} \right) \right]^{\frac{1}{2}} t \leq t_0 \quad (C1)$$

where A_0 is the amplitude of the ambient noise, A_1 is the amplitude of the first peak in the T-phase, t_0 is the arrival time of the peak and t_b is the onset time. A_0, A_1 and t_0 are picked from the log of the smoothed envelope. The onset time, t_b is then calculated by fitting a curve with an exponential value which gives the minimum RMS fit.

[76] The average ambient noise levels recorded by the hydrophones are ~10.4 dB re: counts for Atlantis events and ~9.2 dB re: counts for Kane events. There is no significant difference between the ambient noise level of shallow events (<2 km) and deep events (>2 km) (difference is ~0.3 dB re: counts for Atlantis and 1.2 dB re: counts for Kane). Variability in ambient noise levels is therefore not a significant signal and does not affect our onset time results.

Appendix D: Ray Trace Model

[77]

$$\text{Snell's Law} \quad \frac{\sin i_1}{v_1} = \frac{\sin i_2}{v_2} \quad (D1)$$

where i is the incidence angle and v is the velocity for a two layer model.

[78] All those events with an RMS signal <1 dB re: counts were included in the data set for the modeling. A total of 79 events from Atlantis and 43 events from Kane were used to compare with the ray trace model results.

[79] Seasonal changes in the sound velocity profile were examined using data from the Generalized Digital Environmental Model (GDEM). Ten different velocity profiles between the Kane Study area and each of the six hydrophones were obtained for the months of December, March, June and September (i.e., 240 profiles in total). Five profiles, shown in Figure 11, were selected to encompass the full extent of this variation and were used in the modeling.

[80] Bathymetric profiles along the propagation path were obtained from Seabeam bathymetry

where available (grid spacing ∼150 m) and from *Smith and Sandwell* [1997] satellite altimetry data (grid spacing ∼3 km) otherwise. The bathymetric profiles were created by sampling the 2-D grids along 1-D tracks.

[81] For the model, ninety rays at equal $1°$ increments from horizontal to vertical are emitted from the event location. Two main assumptions are made. The first is that the seismic energy couples with the water column through the process of rough seafloor scattering, yielding a range in emergent angles. It is also assumed that when the rays intersect the seafloor or the sea surface, they are terminated and the number of rays which make it to the hydrophone are proportional to the amount of energy propagated (Figure 12). The model was run 5 times for each event with a different sound velocity profile each time. Those rays with low incidence angles (i.e., near vertical) are terminated at the first interaction with the sea surface. The remaining cone of rays that have a high enough incidence angle are able to refract downward, away from the sea surface and continue along their path to the hydrophone, unless they intersect the seafloor.

Acknowledgments

References

Araki, E., R. A. Stephen, M. Shinohara, T. Kanazawa, and K. Suyehiro (2004), T-phase observed at deep seafloor boreholes, paper presented at Seismo-acoustic Applications in Marine Geology and Geophysics Workshop, Appl. Phys. Lab., Univ. of Wash., Woods Hole Oceanogr. Inst., Woods Hole, Mass.

Behn, M. D., J. Lin, and M. T. Zuber (2002), Evidence for weak oceanic transform faults, *Geophys. Res. Lett.*, *29*(24), 2207, doi:10.1029/2002GL015612.

Blackman, D. K., J. R. Cann, B. Janssen, and D. K. Smith (1998), Origin of extensional core complexes: Evidence from the Mid-Atlantic Ridge at Atlantis Fracture Zone, *J. Geophys. Res.*, *103*, 21,315–21,333.

Blackman, D. K., et al. (2002), Geology of the Atlantis Massif (Mid-Atlantic Ridge, 30°N): Implications for the evolution of an ultramafic oceanic core complex, *Mar. Geophys. Res.*, *23*, 443–469.

Bohnenstiehl, D. R. (2001), Patterns of faulting and seismicity in the mid-ocean ridge environment, Ph.D. thesis, Append. B, Columbia Univ., New York.

Bohnenstiehl, D. R., and M. Tolstoy (2003), Comparison of teleseismically and hydroacoustically derived earthquake locations along the north-central Mid-Atlantic Ridge and equatorial East Pacific Rise, *Seismol. Res. Lett.*, *74*, 791–802.

Bohnenstiehl, D. R., M. Tolstoy, R. P. Dziak, C. G. Fox, and D. K. Smith (2002), Aftershock sequences in the mid-ocean ridge environment: An analysis using hydrophone data, *Tectonophysics*, *354*, 49–70.

Bohnenstiehl, D. R., M. Tolstoy, D. K. Smith, C. G. Fox, and R. P. Dziak (2003), Time-clustering behaviour of spreading-center seismicity between 15–35°N on the Mid-Atlantic Ridge: Observations from hydroacoustic monitoring, *Phys. Earth Planet. Inter.*, *138*, 147–161.

Bohnenstiehl, D. R., R. P. Dziak, M. Tolstoy, C. G. Fox, and M. Fowler (2004), Temporal and spatial history of the 1999–2000 Endeavour Segment seismic series, Juan de Fuca Ridge, *Geochem. Geophys. Geosyst.*, *5*, Q09003, doi:10.1029/2004GC000735.

Brown, J. R., and J. A. Karson (1989), Variations in the axial processes on the Mid-Atlantic Ridge: The median valley in the MAR area, *Mar. Geophys. Res.*, *10*, 109–138.

Butler, R. (2004), Observation of seismo-acoustic T-waves at and beneath the seafloor, paper presented at Seismo-acoustic Applications in Marine Geology and Geophysics Workshop, Appl. Phys. Lab., Univ. of Wash., Woods Hole Oceanogr. Inst., Woods Hole, Mass.

Butler, R., and C. Lomnitz (2002), Coupled seismoacoustic modes on the seafloor, *Geophys. Res. Lett.*, *29*(10), 1418, doi:10.1029/2002GL014722.

Canales, J. P., B. E. Tucholke, and J. A. Collins (2004), Seismic reflection imaging of an oceanic detachment fault: Atlantis Megamullion (Mid-Atlantic Ridge, 30°10′N), *Earth Planet. Sci. Lett.*, *222*, doi:10.1016/j.epsl.2004.02.023.

Cann, J. R., D. K. Blackman, D. K. Smith, E. McAllister, B. Janssen, S. Mello, E. Augerinos, A. R. Pascoe, and J. Escartin (1997), Corrugated slip-surface formed at ridge-transform intersections on the Mid-Atlantic Ridge, *Nature*, *385*, 329–332.

Chiu, C. (1994), Downslope modal energy conversion, *J. Acoust. Soc. Am.*, *5*, 1655–1657.

Claerbout, J. F. (1985), *Imaging the Earth's Interior*, pp. 224–226, Blackwell Sci., Malden, Mass.

Clay, C. S., and H. Medwin (1977), *Acoustic Oceanography*, 96 pp., Wiley-Interscience, Hoboken, N. J.

Colosi, J. (2004), Theory of long-range acoustic propagation, paper presented at Seismo-acoustic Applications in Marine Geology and Geophysics Workshop, Appl. Phys. Lab., Univ. of Wash., Woods Hole Oceanogr. Inst., Woods Hole, Mass.

Davis, T. M., K. A. Countryman, and M. J. Carron (1986), Tailored acoustic products utilizing the NAVOCEANO GDEM (a generalized digital environmental model), paper presented at 36th Naval Symposium on Underwater Acoustics, Nav. Ocean Syst. Cent., San Diego, Calif.

de Groot-Hedlin, C. D., and J. A. Orcutt (1999), Synthesis of earthquake-generated T-waves, *Geophys. Res. Lett.*, *26*, 1227–1230.

de Groot-Hedlin, C. D., and J. A. Orcutt (2001), Excitation of T-phases by seafloor scattering, *J. Acoust. Soc. Am.*, *109*, 1944–1954.

D'Spain, G. L., L. P. Berger, W. A. Kuperman, J. L. Stevens, and E. G. Baker (2001), Normal mode composition of earthquake T-phases, *Pure Appl. Geophys.*, *158*, 475–512.

Dziak, R. P. (2001), Empirical relationship of T-wave energy and fault parameters of northeast Pacific Ocean earthquakes, *Geophys. Res. Lett.*, 28, 2537–2540.

Dziak, R. P., and C. G. Fox (1999a), Long-term seismicity and ground deformation at Axial Volcano, Juan de Fuca Ridge, *Geophys. Res. Lett.*, 26, 3641–3644.

Dziak, R. P., and C. G. Fox (1999b), The January 1998 earthquake swarm at Axial Volcano, Juan de Fuca Ridge: Hydroacoustic evidence of seafloor volcanic activity, *Geophys. Res. Lett.*, 26, 3429–3432.

Dziak, R. P., C. G. Fox, and A. E. Schreiner (1995), The June–July 1993 seismo-acoustic event at CoAxial segment, Juan de Fuca Ridge: Evidence of lateral dike injection, *Geophys. Res. Lett.*, 22, 135–138.

Dziak, R. P., C. G. Fox, H. Matsumoto, and A. E. Schreiner (1997), The April 1992 Cape Mendocino earthquake sequence: Seismo-acoustic analysis utilising fixed hydrophone arrays, *Mar. Geophys. Res.*, 19, 137–162.

Dziak, R. P., D. K. Smith, D. R. Bohnenstiehl, C. G. Fox, D. Desbruyeres, H. Matsumoto, M. Tolstoy, and D. J. Fornari (2004), Evidence of a recent magma dike intrusion at the slow spreading Lucky Strike segment, Mid-Atlantic Ridge, *J. Geophys. Res.*, 109, B12102, doi:10.1029/2004JB003141.

Engeln, J. F., D. A. Wiens, and S. Stein (1986), Mechanisms and depths of Atlantic transform earthquakes, *J. Geophys. Res.*, 91, 548–577.

Escartin, J., and J. Lin (1995), Ridge offsets, normal faulting, and gravity anomalies of slow spreading ridges, *J. Geophys. Res.*, 100, 6163–6177.

Fisher, F. H., and V. P. Simmons (1977), Sound absorption in seawater, *J. Acoust. Soc. Am.*, 62, 558–564.

Fox, C. G., R. P. Dziak, H. Matsumoto, and A. E. Schreiner (1994), Potential for monitoring low-level seismicity on the Juan de Fuca Ridge using fixed hydrophone arrays, *Mar. Technol. Soc. J.*, 27, 22–30.

Fox, C. G., W. E. Radford, R. P. Dziak, and H. Matsumoto (1995), Acoustic detection of a seafloor spreading episode on the Juan de Fuca Ridge using military hydrophone arrays, *Geophys. Res. Lett.*, 22, 131–134.

Fox, C. G., H. Matsumoto, and T.-K. A. Lau (2001), Monitoring Pacific Ocean seismicity from an autonomous hydrophone array, *J. Geophys. Res.*, 103, 4183–4206.

Francis, T. J. G., I. T. Porter, and R. C. Lilwall (1978), Microearthquakes near the eastern end of St Paul's Fracture Zone, *Geophys. J. R. Astron. Soc.*, 53, 201–217.

Harben, P. E., E. Matsel, Z. Upton, and J. J. Pulli (2003), Hydroacoustic blockage calibration from discrimination, paper presented at 25th Seismic Research Review, U.S. Dep. of Energy and U.S. Dep. of Defense, Tucson, Ariz.

Johnson, R. H., J. Northrop, and R. Eppley (1963), Sources of Pacific T-phases, *J. Geophys. Res.*, 68, 4251–4260.

Johnson, R. H., R. A. Norris, and F. K. Duennebier (1968), Abysally generated T-phases, in *The Crust and Upper Mantle of the Pacific Area, Geophys. Monogr. Ser.*, vol. 12, edited by L. Knopoff, C. L. Drake, and P. J. Hart, pp. 70–78, AGU, Washington, D. C.

Karson, J. A. (1998), Internal structure of oceanic lithosphere: A perspective from tectonic windows, in *Faulting and Magmatism at Mid-Ocean Ridges, Geophys. Monogr. Ser.*, vol. 106, edited by W. R. Buck et al., pp. 177–218, AGU, Washington, D. C.

Keenan, R. E., and L. R. L. Merriam (1991), Artic abyssal T phases: Coupling seismic energy to the ocean sound channel via under-ice scattering, *J. Acoust. Soc. Am.*, 89, 1128–1133.

Kelley, D. S., et al. (2001), An off-axis hydrothermal vent field near the Mid Atlantic Ridge at 30°N, *Nature*, 412, 145–149.

Lalou, C., J.-L. Reyss, E. Brishet, M. Arnold, G. Thompson, Y. Fouquet, and P. A. Rona (1993), New age data for Mid-Atlantic Ridge hydrothermal sites: TAG and Snakepit chronology revisited, *J. Geophys. Res.*, 98, 9705–9713.

Mutter, J. C., and J. A. Karson (1992), Structural processes at slow-spreading ridges, *Science*, 257, 627–634.

Norris, R. A., and R. H. Johnson (1969), Submarine volcanic eruptions recently located in the Pacific by Sofar hydrophones, *J. Geophys. Res.*, 74, 650–664.

Pan, J., and A. M. Dziewonski (2005), Comparison of mid-oceanic earthquake epicentral differences of travel time, centroid locations, and those determined by autonomous underwater hydrophone arrays, *J. Geophys. Res.*, 110, B07302, doi:10.1029/2003JB002785.

Park, M., R. I. Odom, and D. J. Soukup (2001), Modal scattering: A key to understanding oceanic T-waves, *Geophys. Res. Lett.*, 28, 3401–3404.

Pulli, J. J., and Z. M. Upton (2002), Hydroacoustic observations of Indian earthquake provide new data on T-waves, *Eos Trans. AGU*, 83, p. 145.

Pulli, J. J., R. Bieri, and E. Dorfman (1999), Modeling hydroacoustic waveform envelopes: Implication for test ban treaty monitoring, paper presented at the 21st Seismic Research Symposium, U.S. Dep. of Energy and U.S. Dep. of Defense, Las Vegas, Nev.

Reid, I. (1976), The Rivera plate: A study in seismology and plate tectonics, Ph.D. thesis, p. 288, Univ. of Calif., San Diego.

Richardson, P. L., D. Walsh, L. Armi, M. Schroder, and J. F. Price (1988), Tracking three Meddies with SOFAR floats, *J. Phys. Oceanogr.*, 19, 371–383.

Richardson, P. L., M. S. McCartney, and C. Maillard (1991), A search for meddies in historical data, *Dyn. Atmos. Oceans*, 15, 241–265.

Roemmich, D., and C. Wunch (1985), Two transatlantic sections: Meridional circulation and heat flux in the subtropical North Atlantic Ocean, *Deep Sea Res., Part A*, 32, 619–664.

Rowlett, H. (1981), Seismicity at intersections of spreading centers and transform faults, *J. Geophys. Res.*, 86, 3815–3820.

Rowlett, H., and D. W. Forsyth (1984), Recent faulting and microearthquakes at the intersection of the Vema Fracture Zone and the Mid-Atlantic Ridge, *J. Geophys. Res.*, 89, 6079–6094.

Schreiner, A. E., C. G. Fox, and R. P. Dziak (1995), Spectra and magnitudes of T-waves from the 1993 earthquake swarm on the Juan de Fuca Ridge, *Geophys. Res. Lett.*, 22, 139–142.

Severinghaus, J. P., and K. C. Macdonald (1988), High inside corners at ridge-transform intersections, *Mar. Geophys. Res.*, 9, 353–367.

Shurbet, D. H., and M. Ewing (1957), T-phases at Bermuda and transformation of elastic waves, *Bull. Seismol. Soc. Am.*, 47, 251–262.

Slack, P. D., C. G. Fox, and R. P. Dziak (1999), P wave detection thresholds, Pn velocity estimates, and T wave location uncertainty from oceanic hydrophones, *J. Geophys. Res.*, 104, 13,061–13,072.

Smith, D. K., M. Tolstoy, C. G. Fox, D. R. Bohnenstiehl, H. Matsumoto, and M. J. Fowler (2002), Hydroacoustic monitoring of seismicity at the slow-spreading Mid-Atlantic Ridge, *Geophys. Res. Lett.*, 29(11), 1518, doi:10.1029/2001GL013912.

225

Smith, D. K., J. Escartin, M. Cannat, M. Tolstoy, C. G. Fox, D. R. Bohnenstiehl, and S. Bazin (2003), Spatial and temporal distribution of seismicity along the northern Mid-Atlantic Ridge (15°–35°N), *J. Geophys. Res.*, *108*(B3), 2167, doi:10.1029/2002JB001964.

Smith, W. H. F., and D. T. Sandwell (1997), Global sea floor topography from satellite altimetry and ship depth soundings, *Science*, *277*, 1956–1962.

Stephen, R. A., D. K. Smith, and C. M. Williams (2002), The dynamics of abyssal T-phases, *Eos Trans. AGU*, *83*(19), Spring Meet. Suppl., Abstract S51A-04.

Talandier, J., and E. A. Okal (1998), On the mechanism of conversion of seismic waves to and from T waves in the vicinity of island shores, *Bull. Seismol. Soc. Am.*, *88*, 621–632.

Teague, W. J., M. J. Carron, and P. J. Hogan (1990), A comparison between the Generalized Digital Environmental Model and Levitus climatologies, *J. Geophys. Res.*, *95*, 7167–7183.

Tilmann, F., E. Flueh, L. Planert, T. Reston, and W. Weinrebe (2004), Microearthquake seismicity of the Mid-Atlantic Ridge at 5°S: A view of tectonic extension, *J. Geophys. Res.*, *109*, B06102, doi:10.1029/2003JB002827.

Tolstoy, I., and M. Ewing (1950), The T phase of shallow-focus earthquakes, *Bull. Seismol. Soc. Am.*, *40*, 25–51.

Tucholke, B. E., and J. Lin (1994), A geological model of the structure of ridge segments in slow spreading ocean crust, *J. Geophys. Res.*, *99*, 11,937–11,958.

Tucholke, B. E., J. Lin, and M. C. Kleinrock (1996), Mullions, megamullions, and metamorphic core complexes on the Mid-Atlantic Ridge, *Eos Trans. AGU*, *77*(46), Fall Meet. Suppl., F724.

Tucholke, B. E., J. Lin, and M. C. Kleinrock (1998), Megamullions and mullion structure defining oceanic metamorphic core complexes on the Mid-Atlantic Ridge, *J. Geophys. Res.*, *103*, 9857–9866.

Walker, D. A., C. S. McCreery, and Y. Hiyoshi (1992), T-phase spectra, seismic moments, and tsunamigenesis, *Bull. Seismol. Soc. Am.*, *82*, 1275–1305.

Wolfe, C. J., G. M. Purdy, D. R. Toomey, and S. C. Solomon (1995), Microearthquake characteristics and crustal velocity structure at 29°N on the Mid-Atlantic Ridge: The architecture of a slow spreading segment, *J. Geophys. Res.*, *100*, 24,449–24,472.

Yang, Y., and D. W. Forsyth (2003), Improving epicentral and magnitude estimation of earthquakes from T phases by considering the excitation function, *Bull. Seismol. Soc. Am.*, *93*, 2106–2122.

APPENDIX 1

Magnetic data processing methods

The magnetic data in this Thesis were processed using several standard procedures before interpretation of the magnetic anomalies. These procedures include: correcting the data for the magnetic contribution of the vehicle to which the magnetometer was attached, continuing the data from an uneven surface onto a level plane, applying a reduction-to-the-pole transform that shifts the magnetic data into the vertical component, inverting the continued anomaly data for crustal magnetization and the adding annihilators to DC shift the magnetic data. Each of these procedures is discussed in detail below.

A1.1 Corrections for the submersible vehicle contribution

The magnetic field observed by a magnetometer installed on a submersible vehicle is affected by the motion and the magnetization of the vehicle. The effects are determined through either a full vector calibration correction for three component magnetic data [*Isezaki*, 1986; *Korenaga*, 1995] or a heading correction for the total field data.

A1.1.1 Full vector calibration correction

The observed magnetic field is a combination of the geomagnetic field in the vehicle's coordinates and the induced and permanent magnetic field produced by the vehicle body. The observed magnetic field H is described by

$$H = R \cdot F + A \cdot R \cdot F + M \tag{A1.1}$$

where F is the geomagnetic field vector, A is the induction magnetic field matrix, M is the permanent magnetic field vector, and R are rotational matrices due to the roll, pitch and heading (yaw) of the vehicle respectively. The matrix A' is defined as

$$A' = I + A \tag{A1.2}$$

where I is the unit matrix. Equation A1.1 can be written as

$$H = A' \cdot R \cdot F + M \tag{A1.3}$$

The 12 unknown parameters in A' and M, which are the magnetic effects of the vehicle body, can be estimated from observations where the geomagnetic field F is known. In practice International Geomagnetic Reference Field (IGRF) [*IAGA Division V Working Group, International Geomagnetic Reference Field*, 2000] values are substituted for the geomagnetic field when the 12 parameters are estimated. Data for the effects of the vehicle body are collected while the vehicle spins through a 360° turn on descent at the beginning of each dive. The measured field varies as a function of azimuth due to the magnetic field of the vehicle body. A set of parameters in the A' and M matrices are estimated from a least squares inversion. The geomagnetic field F is then calculated using estimated A' and M matrices

$$F = R^{-1} \cdot A'^{-1} \cdot (H - M) \tag{A1.4}$$

A1.1.2 Heading correction

The heading correction can be used to correct for the vehicle contribution when the vehicle pitch and roll data are not available, with the assumption that the vehicle rotates only in the horizontal plane (e.g., the ABE profiles in Chapter 4 of the Thesis). As with the full vector calibration, the IGRF field is calculated for the survey location and used as the reference field. Corrections are made for both the permanent and induced fields. The permanent field correction is calculated by varying the offsets and calibration factors such that the differences between the three components of the observed magnetic data and reference field are minimized. The induced field correction is calculated by fitting a 2θ cosine curve to the heading versus total observed field:

$$C_i = m.\cos(2hdg - D) \tag{A1.5}$$

where the induced field correction (C_i) is a function of the multiplication factor (m), heading (*hdg*) and declination (*D*).

A1.2 Fourier Series and transformations

Fourier analysis is a methodology that maps functions of space (or time) into functions of wavenumber (or frequency). A Fourier transformation of a magnetic anomaly over a layered body separates the anomaly into two multiplicative factors: a function that described the depth and thickness of the source layer and a function that describes the distribution of magnetization within the layer[*Blakely*, 1995]. The Fourier domain therefore provides insights into the source of a magnetic anomaly that are not observed in the space domain.

A Fourier series is an infinite sum of weighted sinusoids that can be used to approximate a periodic function:

$$f(x) = \sum_{n=-\infty}^{\infty} F_n e^{ik_n x} \tag{A1.6}$$

where $k = \dfrac{2\pi n}{\lambda}$ (wavenumber) and $i = \sqrt{-1}$.

The Fourier transform of this periodic function is

$$F(k) = \int_{-\infty}^{\infty} f(x) e^{-ikx} dx \tag{A1.7}$$

The Fourier transform $F(k)$ is a complex function of real and imaginary parts, that is

$$F(k) = \mathrm{Re}\{F(k)\} + i\,\mathrm{Im}\{F(k)\} \tag{A1.8}$$

$F(k)$ can also be written as

$$F(k) = |F(k)| e^{i\theta(k)} \tag{A1.9}$$

where

$$|F(k)| = \left[\operatorname{Re}\{F(k)\}^2 + (\operatorname{Im}\{F(k)\}^2 \right]^{\frac{1}{2}} \tag{A1.10}$$

$$\Theta(k) = \arctan \frac{\operatorname{Im} F(k)}{\operatorname{Re} F(k)} \tag{A1.11}$$

The functions $|F(k)|$ and $\Theta(k)$ are the amplitude parameter and phase parameter respectively. Using $F[k]$ as shorthand notation to denote the Fourier transform of a function, the Fourier transform of the total field anomaly $\Delta B(x)$ caused by a magnetic source layer with magnetization distribution M is:

$$F[\Delta B(x)] = 2\pi C e^{-i\theta} (e^{-ka} - e^{-kb}) F[M(x)] \tag{A1.12}$$

where
C : amplitude parameter
Θ: phase parameter
a : top of the layer
b : bottom of the layer
[*Schouten and McCamy*, 1972]

A1.2.1 Continuation of the data

Continuation transforms the magnetic field measured on one surface to the field that would be measured on another surface, either above (upward continuation) or below (downward continuation) the original surface. Upward continuation attenuates anomalies with respect to wavelength; the shorter the wavelength, the greater the attenuation. In this sense the process of continuation degrades the data, but tends to accentuate anomalies caused by deep sources at the expense of anomalies caused by shallow sources. Downward continuation has the opposite affect and accentuates short wavelength features such as noise and should therefore be used with caution [*Blakely*, 1995]. A continuation from one level plane to another is represented in the Fourier domain as

$$F[\Delta B_c] = F[\Delta B] F[\psi_c] \tag{A1.13}$$

where the continuation transform is

$$F[\psi_c] = e^{-z|k|}$$ (A1.14)

z is the distance to be continued between the observed anomaly (ΔB) and the computed anomaly at the new level (ΔB_c). A continuation is purely a real function and has no imaginary part. Thus no phase shift results from continuation of an anomaly. Magnetic data collected along an uneven trackline can be continued to a level plane using the approach of *Guspi* [1987], as in Chapter 2 and 4 of the Thesis [*Guspi*, 1987]

A1.2.2 Reduction-to-the-pole

Magnetic anomalies depend not only on the distribution of magnetization, but also on the direction of magnetization and direction in which the field was measured. Unless the directions of remanent magnetization (M) and geomagnetic field direction (F) are both vertical, the directional information from the phase parameters Θ_m and Θ_f will contribute a phase shift to the magnetic anomaly. The phase shift can distort the anomaly's shape or even change its sign, producing a 'skewed' magnetic anomaly. The reduction-to-the-pole filter transforms the observed total field into the vertical component of the field caused by the same source distribution magnetized in the vertical direction [*Blakely*, 1995].

$$F[\Delta B_r] = F[\Delta B] F[\psi_r]$$ (A1.15)

where the reduction-to-the-pole filter transform is

$$F[\psi_r] = \frac{1}{\Theta_m \Theta_f}$$ (A1.16)

ΔB_r is the anomaly that would be measured at the north magnetic pole, where the remanent magnetization and geomagnetic field would both be directed vertically down. Reduction-to-the-pole removes one level of complexity from the interpretive process by shifting the anomalies so they are symmetric over their causative body. The reduction-to-the-pole filter is a phase filter and passes all wave numbers components without

modifying their amplitudes. The amplitudes are then redistributed between the real and imaginary parts according to the phase shift [*Schouten and McCamy*, 1972]

A1.3 Inversion for crustal magnetization

The inverse method is used to determine source magnetization parameters from the observed data. The inverse Fourier transform of A1.7 is

$$f(x) = \frac{1}{2\pi} \int_{-\infty}^{\infty} F(k)e^{ikx} dk \tag{A1.17}$$

and the magnetization distribution of a magnetic source layer (A1.12) using the inverse model is

$$F[M(x)] = \frac{1}{2\pi C} e^{i\theta} (e^{-ka} - e^{-kb})^{-1} F[B(x)] \tag{A1.18}$$

However, interpretation of potential field data is limited by its non-uniqueness: there are an infinite number of bodies that can produce an anomaly with the same shape. In order to cope with the non-uniqueness, simplifying assumptions can be made about the source, such as uniform magnetization throughout the body or that the body extends infinitely in one direction for magnetic profile data [*Parker*, 1973]. The inversion corrects for skewness of the anomaly (reduction-to-the-pole) and topography at the survey location.

The *Parker and Huestis* [1974] approach, used in Chapters 2 and 4 of the Thesis, assumes a constant source layer thickness with the topography as the top surface of the layer. [*Parker and Huestis*, 1974]. The inversion is an iterative process to solve for magnetization, whereby an initial solution (e.g., $M(x)=0$) is assumed, and a new magnetization recalculated. The new magnetization is compared with the original, placed back into the equation and recalculated. The inversion converges towards a solution, with a bandpass filter typically used to suppress noise and ensure convergence.

232

A1.4 The Annihilators

The annihilator is a magnetization distribution that produces no magnetic field and represents the measure of non-uniqueness of the inversion solution since, theoretically, an infinite amount of annihilator can be added to a solution [*Blakely*, 1995]. Addition of annihilator is generally used to introduce a DC shift into the magnetization in order to balance the magnetization solution maximum and minimum vaules or to ensure all magnetizations are positive, as in Chapter 2 of the Thesis.

References

Blakely, R.J., *Potential Theory in Gravity and Magnetic Applications*, Cambridge University Press, Cambridge, UK, 1995.

Guspi, F. (1987),Frequency- domain reduction of potential field measurements to a horizontal plane, *Geoexploration, 24*, 87-98.

Isezaki, N. (1986),A new shipboard three-component magnetometer, *Geophysics, 51*, 1992-1998.

Korenaga, J. (1995),Comprehensive analysis of marine magnetic vector anomalies, *J. Geophys. Res., 100*, 365-378.

Parker, R.L. (1973),The rapid calculation of potential anomalies, *Geophys. J. R. Astr. Soc, 31* (4), 447-455.

Parker, R.L., and S.P. Huestis (1974),The inversion of magnetic anomalies in the presence of topography, *J. Geophys. Res., 79*, 1587-1594.

Schouten, H., and K. McCamy (1972),Filtering Marine Magnetic Anomalies, *J. Geophys. Res., 77*, 7089-7099.

APPENDIX 2

Rock magnetic data from East Pacific Rise basalts (9° 25'- 55'N)

Abstract

A systematic along axis trend in basalt magnetic properties is observed between 9° 30'N and 9° 50'N, with decreasing natural remanent magnetization (NRM) and susceptibility from south to north. We propose that a combination of both paleointensity and geochemical variations account for this observed gradient in magnetic properties, where younger, more primitive (iron-poor) basalts in the 9° 50'N region have mean NRM values ~ 45% less than the older, more evolved (iron-rich) basalts sampled in the 9° 30'N region.

A2.1 Introduction

The 9-10° N section of the East Pacific Rise (EPR) is a Ridge2000 Site of Special Scientific Interest (SSSI) as the type locality for a fast spreading mid-ocean ridge. The site has been the focus of a larger number of multidiscipline studies, yet only one detailed rock magnetic study between 9° 25-55'N has been published to date [*Bowles et al.*, 2006].

Previous global magnetic studies show that basalts have the highest natural remanent magnetization (NRM) of all the lithological layers in oceanic crust [*Atwater and Mudie*, 1973; *Bina et al.*, 1990; *Day et al.*, 1978; *Gee and Kent*, 1997; *Harrison*, 1987; *Sempere et al.*, 1988; *Talwani et al.*, 1971]. The source of NRM in unaltered basalts is thermoremanent magnetization (TRM), acquired as the iron-titanium (Fe-Ti) oxides cool through their Curie temperatures. The Fe-Ti oxide titanomagnetite with ulvopsinel content $x = 0.6$ (TM60, $Fe_{3-x}Ti_xO_4$) is the most common magnetic carrier in basalts [*Irving*, 1970; *Johnson and Hall*, 1978]. *Zhou et al.* [1997] identified three sets of titanomagnetites with varying grain size within pillow basalts and proposed that the most likely source of a basalt's TRM are single-domain sized, sub-micron titanomagnetite grains.

Basalts comprise the top ~ 0.5 km of oceanic crust and early models of the magnetic source layer assumed that the basalts were the source of marine magnetic anomalies [*Talwani et al.*, 1971]. Subsequent studies have shown that lower crust and upper mantle rocks can contribute to the magnetic anomalies off axis [*Arkani-Hamed*, 1988; *Kidd*, 1977; *Kikawa and Ozawa*, 1992; *Oufi et al.*, 2002; *Pariso and Johnson*, 1993a; *Pariso and Johnson*, 1993b; *Wilson and Hey*, 1981]. However, **along axis** the basalt layer does appear to be the most important lithological unit to contribute to the magnetic source layer; Chapter 2 of this thesis shows that along axis changes in the depth to the base of seismic layer 2A (assumed to be the basalt/dike transition) is the main magnetic signal reflected in the near-bottom magnetic anomaly.

A2.1.1 Geological setting

The EPR is a fast spreading mid-ocean ridge (full spreading rate 108 mm/yr [*Carbotte and Macdonald*, 1992]) (Fig. A2-1a). The ridge axis is a bathymetric high and recent eruptions occurred in 1991 and 2006 between 9° 46-56'N [*Cowen et al.*, 2007; *Haymon et al.*, 1993; *Tolstoy et al.*, 2006]. The sea-floor basalt samples for this study were collected aboard R/V Atlantis (AT11-7) in 2004. All samples were collected in situ by the submersible ALVIN in three regions along or near the ridge axis: 9° 50'N (Alvin dives 3963, 3965, 3973, 3974), 9° 44'N (Dives 3967, 3971) and 9° 30'N (Dives 3968, 3970, 3975) (Figure A2-1b).

This study reports the rock magnetic properties of basalts collected in these three regions. The data show systematic changes in rock magnetic properties along axis and are used to investigate the relationship between NRM, paleointensity of the geomagnetic field and geochemical properties of basalts.

A2.2 Methods

One inch diameter cores were taken from 27 basalt rocks. NRM was measured using a Molspin spinner magnetometer at the University of Massachusetts, Amherst.

Magnetic susceptibility (k) was measured on a Sapphire Instruments susceptibility bridge at room temperature, also at the University of Massachusetts, Amherst. Koenigsberger ratio (Q), the ratio of remanent (NRM) to induced magnetization (k) was calculated assuming an intensity of 35.84 A/m for the magnetic field at the survey location.

Geochemical analyses on the 27 samples were carried out by *A. Soule* using a JEOL JXA-8800L electron probe microanalyzer at 15 kV and 20 mA at the USGS microbeam facility in Denver [*Soule et al.*, 2005; *A. Soule*, personal comm.].

A2.3 Results

NRM ranges over an order of magnitude from 5-83 A/m (Table 1). The 9° 50'N basalts have the lowest mean NRM (15.7 A/m, Fig A2-2a) compared with the two regions to the south. They also have the lowest k values (mean 3.1(x10^3) SI) and plot in the lower left corner of the NRM versus k figure, along an approximately linear trend (Fig A2-2c).

The 9° 44'N basalts have the largest range in NRM (6-83 A/m) and highest mean NRM (32.8 A/m, Fig. A2-2a). However, the number of samples is small (6 samples from 4 rocks) and their variance is high (Fig. A2-2a). Mean NRM is reduced to ~ 23 A/m when sample 3971-5a with NRM of 83 A/m is removed from the dataset (Table 1). Their k values are intermediate compared with the 9° 50'N and 9° 30'N regions and they have an approximately linear trend in the NRM vs k plot, similar to the 9° 50'N basalts (Fig. A2-2c).

The 9° 30'N basalts have the highest mean NRM (28.6 A/m) and k values (12.8 (x10^3) SI). This is very apparent in the NRM vs k plot (Fig. A2-2c), which shows the 9° 30'N basalts do not follow the same linear trends as those at 9° 50'N and 9° 44'N. Instead, samples with similar NRMs have a large range of k values from ~ 7.5- 22.5 (x10^3) SI.

Koenigsberger ratios are high for all the samples (42 to 629), as expected for basalts. The 9° 50'N basalts have the lowest mean Q ratios (114), approximately half the mean Q ratio for the 9° 30'N (228) and 9° 44'N (252) basalts.

A2.3.1 NRM versus FeO

FeO content is generally highest in the 9° 30'N basalts (~ 10.25 wt%), intermediate in the 9° 44'N basalts (~ 10 wt %) and lowest in the 9° 50'N basalts (~ 9 wt%, Fig. A2-3a). A least squares fit to our data shows a linear relationship between the amount of weight percent FeO and NRM, but the R^2 value is low due to several outliers (Fig. A2-3a). *Gee and Kent* [1997] sampled EPR basalts between 14°-23° S and also proposed a linear relationship (NRM= 4.44FeO- 25.8) that is less steep than our data suggests i.e., the same increase in FeO wt % results in a smaller increase in NRM (green dashed line, Fig. A2-3a). *Batiza and Niu* [1992] sampled basalts between 9° 18'-54'N along the EPR. Their geochemical analyses show FeO content ranging from ~ 9.7-10.8 wt % (grey box, Fig. A2-3a).

A2.3.2 NRM versus Magnesium Number

Magnesium number (Mg #) is calculated from the ratio of the MgO and FeO weight percentages (MgO/(FeO+MgO)). Mg # is highest in the 9° 50'N basalts (~ 0.48), intermediate in the 9° 44'N basalts (~ 0.47) and lowest in the 9° 30'N basalts (~ 0.41, Fig. A2-3b). A least squares fit to the data has a low R^2 value, due to outliers, but generally shows an inverse correlation between NRM and Mg #. *Batiza and Niu* [1992] sampled basalts with Mg# between ~ 0.4-0.45 (grey box, Fig. A2-3b).

A2.3.3 FeO versus TiO_2

FeO and TiO_2 content in the basalts have a linear relationship ($R^2 > 0.9$, Fig A2-4) and therefore a constant ratio. The 9° 30'N basalts have both the highest FeO and TiO_2 content, compared to the 9° 50'N basalts, which have the lowest. A constant FeO:TiO_2

ratio is important because the magnetic properties of titanomagnetites vary significantly with Ti content and could be a source of NRM variation.

A2.4 Discussion

There are significant differences in magnetic properties and geochemistry between basalts collected in the 9° 30'N, 9° 44'N and 9° 50'N regions. Our basalt NRMs range from 5-83 A/m (mean NRM ~ 22 A/m) and compare well with other studies of axial EPR basalts including; 14°-23° S- NRM ranges from 0.5 to 81 A/m [*Gee and Kent*, 1997], 21° N- mean NRM of 15 ± 11 A/m [*Sempere et al.*, 1988] and the one published magnetic dataset in our study area, which shows basalts between 9° 31-36.5'N have a mean NRM 30 A/m (± 28) (NRM data are not available north of 9° 36.5 N)[*Bowles et al.*, 2006].

Our results suggest an along axis gradient in magnetic properties with higher NRM, k and Q values in the 9° 30'N region, which decrease northward towards 9° 50'N. The overall mean NRM decrease from south to north is ~ 13 A/m, or ~ 45 %. The source of these variations in magnetic properties may be due to differences in basalt geochemistry, paleointensity of the geomagnetic field when the basalts were deposited and/or low temperature alteration processes.

A2.4.1 Paleointensity variations

Paleointensity of the Earth's magnetic field at the time a rock cooled is reflected in the strength of its NRM. Global changes in the geomagnetic field have been dramatic over the last 10 ka [*Gee et al.*, 2000; *Guyodo and Valet*, 1999; *Yang et al.*, 2000]; the virtual axial dipole moment (VADM) has ranged from 7 to 11 ($x10^{22}$) Am^2 with a significant decline from ~ 11 to 8 ($x10^{22}$) Am^2 in the last 2 ka [*Yang et al.*, 2000]. Based on these paleointensity differences, *Bowles et al.* [2006] estimated crustal age of seafloor samples in our study area. In general, basalts between 9° 46'-45'N have lower paleointensities than basalts between 9° 30'-34'N and are interpreted to be younger,

because of the recent decline in the geomagnetic field. Indeed, *Bowles et al.* [2006] interpret the surface flows in this area to range in age from the 1991 eruption to ~ 150 y.b.p. (years before present). Paleointensities are generally higher in the 9° 30'N region (37-48 µT) and the lavas are interpreted to have erupted between 0.5- 4 k y.b.p. [*Bowles et al.*, 2006]. This interpretation agrees with images from the sidescan sonar which show increased sediment cover, faulting and fissures along the 9° 30'N section of the ridge [*Escartin et al.*, 2006; *Soule et al.*, 2005; *Wright et al.*, 1995]. Paleointensity results therefore indicate that basalt NRMs should be higher in the 9° 30'N region than the 9° 50'N, a result which agrees with the trend in our NRM data (there are no paleointensity measurements for samples in the 9° 44'N region).

We can estimate the maximum contribution paleointensity variations could make to the decrease in NRM from south to north by assuming that; 1) the 9° 30'N basalts were erupted ~ 2 ka ago, when the Virtual Axial Dipole Moment (VADM) peaked at ~ 11 (x10^{22}) Am^2, and 2) the 9° 50'N were erupted within the last ~ 150 years, when VADM decreased to ~ 8 (x10^{22} Am^2) [*Yang et al.*, 2000]. The strength of the geomagnetic field therefore decreased by ~ 25 % during this time and could account for a maximum NRM decrease of ~ 25 % or ~ 7 A/m from 9° 30'N to 9° 50'N.

A2.4.2. Low temperature alteration

NRM can also be reduced by lower temperature alteration processes, which oxidizes titanomagnetite into lower-magnetic moment titanomaghemite [*Dunlop and Ozdemir*, 1997 and references therein]. An older lava flow would therefore be expected to have a lower NRM. As discussed above, paleointensity data provide crustal age information but relies on global compilations of paleointensity measurements for comparison with the study area. Uranium-series (U-series) disequilibria data provide more accurate absolute ages. Three separate U-series studies were carried out at 9° 50'N [*Rubin et al.*, 1994; *Sims et al.*, 2003] and 9° 31'N[*Goldstein et al.*, 1994] on the EPR. The majority of 9° 50'N Th-Ra data show young ages, ranging from 0- 8 ka [*Sims et al.*,

2003]. The ^{210}Po-^{210}Pb chronometer used to date much younger samples (~ 3 yrs) shows that 9° 50'N basalts were erupted very recently (end 1990- beginning 1992) [*Rubin et al.*, 1994]. In comparison, 9° 31'N Th ages range from 0- 56 ka [*Goldstein et al.*, 1994]. Based on these ages, the 9° 50'N are younger, expected to have experienced less alteration and therefore have higher NRMs, which is the opposite of our observations. Consequently we rule out low temperature alteration as the source of lower NRMs in the 9° 50'N region and higher NRMs in the 9° 30'N region.

A2.4.3 Geochemical variations

Geochemical variations remain as a third possible source of the along axis variations in NRM. Basalts with high NRM have been associated with propagating limbs of overlapping spreading centers (OSC) in previous studies [*Bazin et al.*, 2001; *Carbotte and Macdonald*, 1992; *Sempere*, 1991; *Sempere et al.*, 1988]. For example, *Sempere et al.* [1988] measured higher basalt NRMs (50.3 ± 15.3 A/m) on the eastward, actively propagating limb of the 9° 03'N OSC compared with surrounding basalts (22.1 ± 16.0 A/m). In these cases, higher NRMs are assumed to be result of geochemical variations, where highly fractionated basalts are enriched in iron. The basalts in our study area do not appear to be as enriched as those at large OSC structures (only 7 samples have NRMs in the same range as the 9° 03'N eastern limb) however, our basalts may have experienced some level of fractionation in the magma chamber that increases their Fe-Ti oxide content along axis.

Batiza and Niu [1992] measured increasing MgO and decreasing TiO_2 and FeO content in along axis basalts between 9° 18'N and 9° 43'N (i.e. from south to north). *A. Soule* (personal comm.) observed that the same trends continue when sampling was extended to 9° 55'N (Fig. A2-3 and A2-4). Mg # indicates the maturity or level of reactions the melt had experienced; the higher the Mg # the less interaction between the melt and surrounding peridotites and the more primitive the magma. Higher Mg# in the 9° 50'N region basalts and lower Mg # in the 9° 30'N basalts indicate more primitive

magmas at 9° 50'N and evolved magmas at 9° 30'N (Fig. A2-3b). Evolved magmas likely experienced longer residence times in the magma chamber, resulting in increased fractionation.

Batiza and Niu [1992] proposed that along axis geochemical variations result from a laterally zoned magma chamber that acquires its zonation during emplacement or recharge. The chamber itself may be a long, narrow and laterally restricted melt lens. New melt batches (Mg-rich magma) injected in the 9° 50'N region might only migrate limited distances along axis and not reach the distal ends in the 9° 30'N region where older, fractionated magma could be preserved (Fe-rich magmas). A recent tomographic study by *Toomey et al.* [2007] between 10° and 8° 30'N offers an alternative explanation for geochemical variations. They show that mantle upwelling is not centered on the ridge axis throughout our study area. Instead, their imaged mantle low-velocity zone (assumed to be a melt body) follows two *en echelon* trends that are offset in a right lateral sense and rotated anticlockwise with respect to the axis of plate spreading. Upwelling is axis-centered in the 9° 50'N region (i.e., the magma chamber lies below the ridge axis), but shifts increasingly off-axis towards to east with distance southward. The maximum off-axis displacement of the low-velocity zone is located near 9° 37'N. In this region mantle melt is delivered off-axis and axial eruptions may source from magmas at the western edge of the chamber, closest to the ridge axis. These magmas are likely more fractionated than those from the center of the chamber, resulting in the along axis geochemical trend we observe.

Williams et al. [submitted] calculated NRM values based on FeO content and the *Gee and Kent* [1997] relationship (Fig. A2-3a). NRM ranged from ~ 22 A/m in the 9° 30'N region, to ~ 15 A/m in the 9° 50'N region, an overall decrease of ~ 7 A/m or ~ 25 %, which is similar to the estimated decrease in NRM due to paleointensity variations. However, our basalt NRM measurements appear to have a more steep relationship between NRM and FeO than the *Gee and Kent* [1997] relationship (Fig. A2-3a). This

may reflect a different NRM/FeO relationship for the basalts in our study area or, if the *Gee and Kent* [1997] NRM/FeO relationship is accurate, an additional, source of NRM variation, such as the paleointensity variations.

Measured NRM values decrease by ~ 45% (~13 A/m) along axis and we have shown that changing paleointensity could account for a maximum NRM decrease of ~ 25 % (7 A/m), while geochemical variations could also account for a decrease of ~ 25 % (7 A/m). Consequently, neither changing geochemistry nor paleointensity could account for the total NRM decrease alone, but a combination of the two sources of NRM variation can explain the along axis trend of decreasing NRM from south to north.

A2.5 Conclusions

Rock magnetic data from the EPR axis between 9° 55'-25'N show an along axis gradient in basalt magnetic properties. We make the following conclusions:

1. NRM, k and Q values are lowest in the 9° 50'N basalts and increase systematically to the south through the 9° 44'N region to 9° 30'N. Overall the NRM decrease is ~ 13 A/m, or 45 % along axis.

2. Basalts from the 9° 50'N region are younger than the 9° 30'N region, based on paleointensity variations, U-series disequilibria and morphological observations. The recent (< 2 ka) decrease in intensity of the geomagnetic field could account for a maximum decrease in NRM of ~ 25% from south to north (~ 7 A/m)

3. Low-temperature alteration is ruled out as a contributor to the along axis decrease in NRM because its affect would result in an opposite trend to the one we observe.

4. Along axis changes in FeO and TiO_2 content could be an additional source of NRM variation, accounting for a ~ 25 % decrease in NRM from south to north (assuming the relationship of *Gee and Kent* [1997]). This geochemical variation may result from increased fractionation of melts at the distal ends or edges of an along axis magma chambers. As neither the geochemical variations (~ 25 %) nor

243

the paleointensity variations (~ 25 %) could account for the total along axis NRM variation (~45 %), we propose that both sources of NRM variation contribute in the systematic along axis trend we observe.

Acknowledgements

References

Arkani-Hamed, J. (1988),Remanent magnetization of the oceanic upper mantle, *Geophys. Res. Letts.*, *15*, 48-51.

Atwater, T., and J.D. Mudie (1973),A detailed near-bottom geophysical study of the Gorda Rise, *J. Geophys. Res.*, *78*, 8865-8886.

Bazin, S., A.J. Harding, G.M. Kent, J.A. Orcutt, C.H. Tong, J.W. Pye, S.C. Singh, P.J. Barton, M.C. Sinha, R.S. White, R.W. Hobbs, and H.J.A. Van Avendonk (2001),Three-dimensional shallow crustal emplacement at the 9° 03'N overlapping spreading center on the East Pacific Rise: Correlations between magnetization and tomographic images, *J. Geophys. Res.*, *106*, 16010-16117.

Bina, M.M., Y.M. Hamano, K. Krammer, and A. Wooldridge (1990),Paleomagnetism of basalts from ODP hole 648B on the Mid-Atlantic Ridge, *Proc. Ocean Drill. Program Sci. Results*, *106/109*, 291-295.

Bowles, J., J.S. Gee, D.V. Kent, M.R. Perfit, S.A. Soule, and D.J. Fornari (2006),Paleointensity applications of timing and extent of eruptive activity, 9°-10° N East Pacific Rise, *Geochem. Geophys. Geosyst.*, *7*, Q06006,doi:10.1029/2005GC001141.

Cande, S.C., and D.V. Kent (1976),Constraints imposed by the shape of marine magnetic anomalies on the magnetic source, *J. Geophys.Res.*, *81*, 4157-4162.

Carbotte, S., and K.C. Macdonald (1992),East Pacific Rise 8°-10°30N': Evolution of Ridge Segments and Discontinuities From SeaMARC II and Three-Dimensional Magnetic Studies, *J. Geophys. Res.*, *97*, 6959-6982.

Cowen, J.P., D.J. Fornari, T. Shank, and e. al. (2007),Volcanic eruptions at East Pacific Rise near 9° 50'N, *EOS Trans.*, *in press*.

Day, R., S. Halgedahl, M. Steiner, K. Kobayashi, T. Furuta, T. Ishii, and A. Faller (1978),Magnetic properties of basalts from DSDP Leg 49, *Initial Rep. Deep Sea Drill. Proj.*, *49*, 781-791.

Escartin, J., S.A. Soule, D.J. Fornari, M.A. Tivey, H. Schouten, and M.R. Perfit (2006),Upper crustal construction along the East Pacific Rise crest (9°10'-50'N): The interplay between faults and lava flows, *Geochem. Geophys. Geosyst.*, in press.

Gee, J., and D.V. Kent (1997),Magnetization of axial lavas from the southern East Pacific Rise (14°-23°S): Geochemical controls on magnetic properties, *J. Geophys .Res.*, *102*, 24873-24886.

Gee, J.S., S.C. Cande, J.A. Hildebrand, K. Donnelly, and R.L. Parker (2000),Geomagnetic intensity variations over the past 780 kyr obtained from near-seafloor magnetic anomalies, *Nature, 408*, 827-832.

Goldstein, S.J., M.R. Perfit, R. Batiza, D.J. Fornari, and M.T. Murrell (1994),Off-axis volcanism at the East Pacific Rise detected by uranium-series dating of basalts, *Nature, 367*, 157-159.

Guyodo, Y., and J. Valet (1999),Global changed in intensity of the Earth's magnetic field during the past 800kyr, *Nature, 399*, 247-252.

Harrison, C.G.A. (1987), Marine magnetic anomalies- The origin of the stripes, *Annu. Rev. Earth. Planet. Sci, 15*, 505-543.

Haymon, R.M., D.J. Fornari, K.L. Von Damm, M.D. Lilley, M.R. Perfit, J.M. Edmond, W.C.I. Shanks, M.D. Lutz, J.M. Grebmeier, S. Carbotte, D. Wright, E. McLaughlin, M. Smith, N. Beedle, and E. Olson (1993),Volcanic eruption of the mid-ocean ridge along the East Pacific Rise crest at 9° 45'-53'N: Direct submersible observations of seafloor phenomenon associated with an eruption event in April, 1991, *Earth Planet. Sci. Letts., 119*, 85-101.

Irving, E. (1970),The Mid-Atlantic Ridge at 45 N, XIV, Oxidation and magnetic properties of basalts; review and discussion, *Can. J. Earth Sci., 7*, 1528-1538.

Johnson, H.P., and J.M. Hall (1978),A detailed rock magnetic and opaque mineralogy study of basalts from the Nazca Plate, *Geophys. J R. Astron. Soc., 52*, 45-64.

Kidd, R.G.W. (1977),A model for the process of formation of the upper oceanic crust, *Geophys. J R. Astron. Soc., 50*, 149-183.

Kikawa, E., and K. Ozawa (1992),Contribution of oceanic gabbros to sea-floor spreading magnetic anomalies, *Science, 258*, 796-799.

Oufi, O., M. Cannat, and H. Horen (2002),Magnetic properties of variably serpentinized abyssal peridotites, *Journal of Geophysical Research, 107*, 10.1029/2001JB000549.

Pariso, J.E., and H.P. Johnson (1993a),Do layer 3 rocks make a significant contribution to marine magnetic anomalies? In situ magnetization of gabbros from Ocean Drilling Program Hole 735B,, *J. Geophys. Res, 98*, 16033-16032.

Pariso, J.E., and H.P. Johnson (1993b),Do lower crustal rocks record reversals of the Earth's magnetic field? Magnetic petrology of oceanic gabbros from ocean drilling program Hole 735B., *J. Geophys. Res, 98*, 16013-16032.

Rubin, K.H., J.D. Macdougall, and M.R. Perfit (1994),[210]Po-^{210}Pb dating of recent volcanic eruptions on the sea floor, *Nature, 368*, 841-844.

Sempere, J.-C. (1991),High-magnetization zones near spreading center discontinuities, *Earth Planet. Sci. Letts., 107*, 389-405.

Sempere, J.-C., A. Meshkov, M. Thommeret, and K.C. Macdonald (1988),Magnetic properties of some young basalts from the East Pacific Rise, *Mar. Geophys. Res.*, *9*, 131-146.

Sims, K.W.W., J. Blichert-Toft, D.J. Fornari, M.R. Perfit, S.J. Goldstein, P. Johnson, D.J. DePaolo, S.R. Hart, M.T. Murrell, P.J. Michael, G.D. Layne, and L.A. Ball (2003),Aberrant youth: Chemical and isotopic constraints on the origin of off-axis lavas from the East Pacific Rise, 9°-10° N, *Geochemistry, Geophysics, Geosystems*, *4*, 8621, doi:10.1029/2002GC000443.

Soule, S.A., D.J. Fornari, M.R. Perfit, M.A. Tivey, W.I. Ridley, and H. Schouten (2005),Channelized lava flows at the East Pacific Rise crest 9°-10° N: The importance of off-axis lava transport in developing the architecture of young oceanic crust, *Geochemistry, Geophysics, Geosystems*, *6*, doi:10.1029/2005GC000912.

Talwani, M., C.C. Windisch, and M.G. Langseth (1971),Reykjanes ridge crest:a detailed geophysical study, *J. Geophys. Res.*, *76*, 473-517.

Tolstoy, M., J.P. Cowen, E.T. Baker, D.J. Fornari, K.H. Rubin, T.M. Shank, F. Waldhauser, D.R. Bohnenstiehl, D.W. Forsyth, R.C. Holmes, B. Love, M.R. Perfit, R.T. Weekly, S.A. Soule, and B. Glazer (2006),A sea-floor spreading event captured by seismometers, *Science*, *314*, 1920-1922.

Wilson, D.S., and R.N. Hey (1981),The Galapagos axial magnetic anomaly: evidence for the Emperor event within the Brunhes and for a two-layer magnetic source, *Geophys. Res. Letts.*, *8*, 1051-1054.

Wright, D.J., R.M. Haymon, and D.J. Fornari (1995),Crustal fissuring and its relationship to magmatic and hydrothermal processes on the East Pacific Rise crest (9°12' to 54'N), *J. Geophys. Res.*, *100*, 6097-6120.

Yang, S., H. Odah, and J. Shaw (2000),Variations in the geomagnetic dipole moment over the last 12000 years, *Geophys. J. Int.*, *140*, 158-162.

Table A2-1- Rock magnetic and bulk rock geochemistry results.

Sample No.	Lon °E	mins	Lat °N	mins	NRM (A/m)	K (SI x10³)	TiO2 % wt	FeO % wt	MgO % wt	Mg#
3963-6	-104	16.59	9	50.50	23.52	4.21	1.53	10.1	7.83	0.48
3963-6a	-104	16.59	9	50.50	9.12	2.39	1.53	10.1	7.83	0.48
3963-8	-104	16.73	9	50.45	15.83	2.79	1.58	10.2	8.00	0.48
3963-8a	-104	16.73	9	50.45	26.56	4.88	1.58	10.2	8.00	0.48
3963-10	-104	16.99	9	50.29	13.62	2.05	1.18	8.82	8.91	0.54
3963-10a	-104	16.99	9	50.29	11.39	2.02	1.18	8.82	8.91	0.54
3963-10b	-104	16.99	9	50.29	5.18	1.78	1.18	8.82	8.91	0.54
3965-1B-a	-104	16.54	9	49.69	9.53	2.11	1.23	9.01	8.72	0.53
3965-2a	-104	16.54	9	49.69	7.64	1.97	1.23	9.11	8.72	0.53
3965-5A-a	-104	16.46	9	49.46	10.19	1.92	1.37	9.84	8.17	0.49
3965-5A-b	-104	16.46	9	49.46	10.04	1.91	1.37	9.84	8.17	0.49
3965-6a-a	-104	16.32	9	49.16	55.53	12.00	1.5	9.97	7.77	0.48
3967-4B	-104	16.38	9	43.70	6.13	1.84	1.52	10.2	8.00	0.48
3967-4B-a	-104	16.38	9	43.70	9.12	2.32	1.52	10.2	8.00	0.48
3967-5A-a	-104	16.00	9	43.67	33.31	5.09	1.72	11	7.54	0.45
3968-1a	-104	14.60	9	28.77	58.73	12.60	1.71	10.66	7.52	0.45
3968-1b	-104	14.60	9	28.77	30.20	6.96	1.71	10.66	7.52	0.45
3968-2	-104	14.57	9	28.77	33.83	9.28	1.69	10.69	7.57	0.45
3968-7	-104	14.64	9	28.95	29.58	8.83	1.72	10.72	7.51	0.45
3968-8A-a	-104	14.82	9	28.92	37.15	13.20	1.68	10.75	7.47	0.45
3968-8A-b	-104	14.82	9	28.92	26.77	11.60	1.68	10.75	7.47	0.45
3970-6a	-104	13.78	9	30.61	8.11	21.60	1.45	10.07	7.76	0.48
3970-6b	-104	13.78	9	30.60	9.45	21.73	1.45	10.07	7.76	0.48
3970-9a	-104	13.63	9	30.05	26.20	7.12	1.49	10.2	7.64	0.47
3970-12	-104	13.65	9	29.61	14.76	11.12	1.69	10.66	7.49	0.45
3970-12a	-104	13.64	9	29.61	26.74	13.80	1.69	10.66	7.49	0.45
3971-5a	-104	15.32	9	43.49	82.98	9.90	1.49	9.9	7.65	0.48
3971-6a	-104	15.13	9	43.52	38.86	9.38	1.49	9.97	7.61	0.47
3971-6b	-104	15.13	9	43.52	26.65	6.18	1.49	9.97	7.61	0.47
3973-1-1a	-104	17.20	9	50.29	9.52	1.94	1.21	8.96	8.72	0.53
3973-1-2a	-104	17.20	9	50.29	6.28	1.66	1.21	8.96	8.72	0.53
3973-1-2b	-104	17.35	9	50.13	5.70	1.58	1.21	8.96	8.72	0.53
3973-2A-a	-104	17.35	9	50.13	7.21	2.01	1.23	8.92	8.69	0.53
3973-3a	-104	17.37	9	50.23	8.07	2.10	1.25	9.13	8.60	0.53
3974-3a	-104	18.46	9	50.20	56.18	7.86	1.41	9.73	8.05	0.49
3974-4a	-104	18.50	9	50.26	13.42	2.62	1.41	9.74	8.03	0.49
3974-6a	-104	18.42	9	50.35	14.58	3.29	1.59	10.04	7.68	0.47
3974-6b	-104	18.42	9	50.35	7.86	2.33	1.59	10.04	7.68	0.47
3974-9a	-104	18.23	9	50.29	15.87	2.86	1.41	9.55	8.45	0.51
3974-11	-104	17.94	9	50.39	15.22	2.96	1.32	9.51	8.70	0.52
3974-11a	-104	17.95	9	50.39	17.89	3.44	1.32	9.51	8.70	0.52
3975-1	-104	15.60	9	28.80	30.44	13.45	1.69	10.76	7.29	0.44
3975-1a	-104	15.61	9	28.79	40.21	15.60	1.69	10.76	7.29	0.44

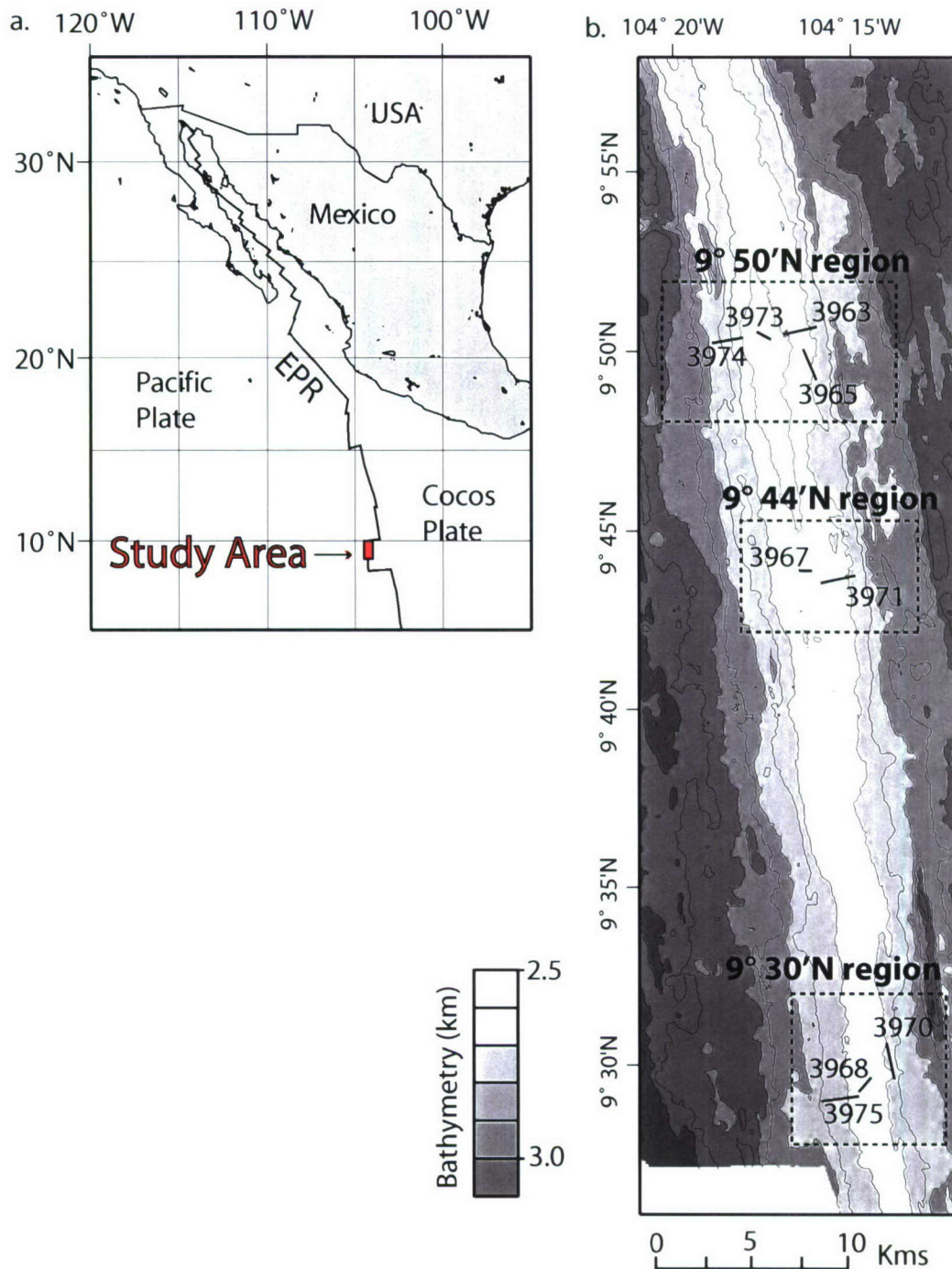NRM, natural remanent magnetization; k, susceptibility

Figure A2-1a. Regional location map of the eastern Pacific showing the East Pacific Rise (EPR) and plate boundary between the Cocos and Pacific plates. Our study area, outlined by the red box, is located between 9° 55'N and 9 °25'N on the EPR. **b.** Location map of the ALVIN dives completed in 2004. The dives can be separated into three regions; 9° 50'N region (Dives 3963, 3965, 3973, 3974), 9° 44'N region (Dives 3967, 3971) and 9° 30'N region (Dives 3968, 3970, 3975)
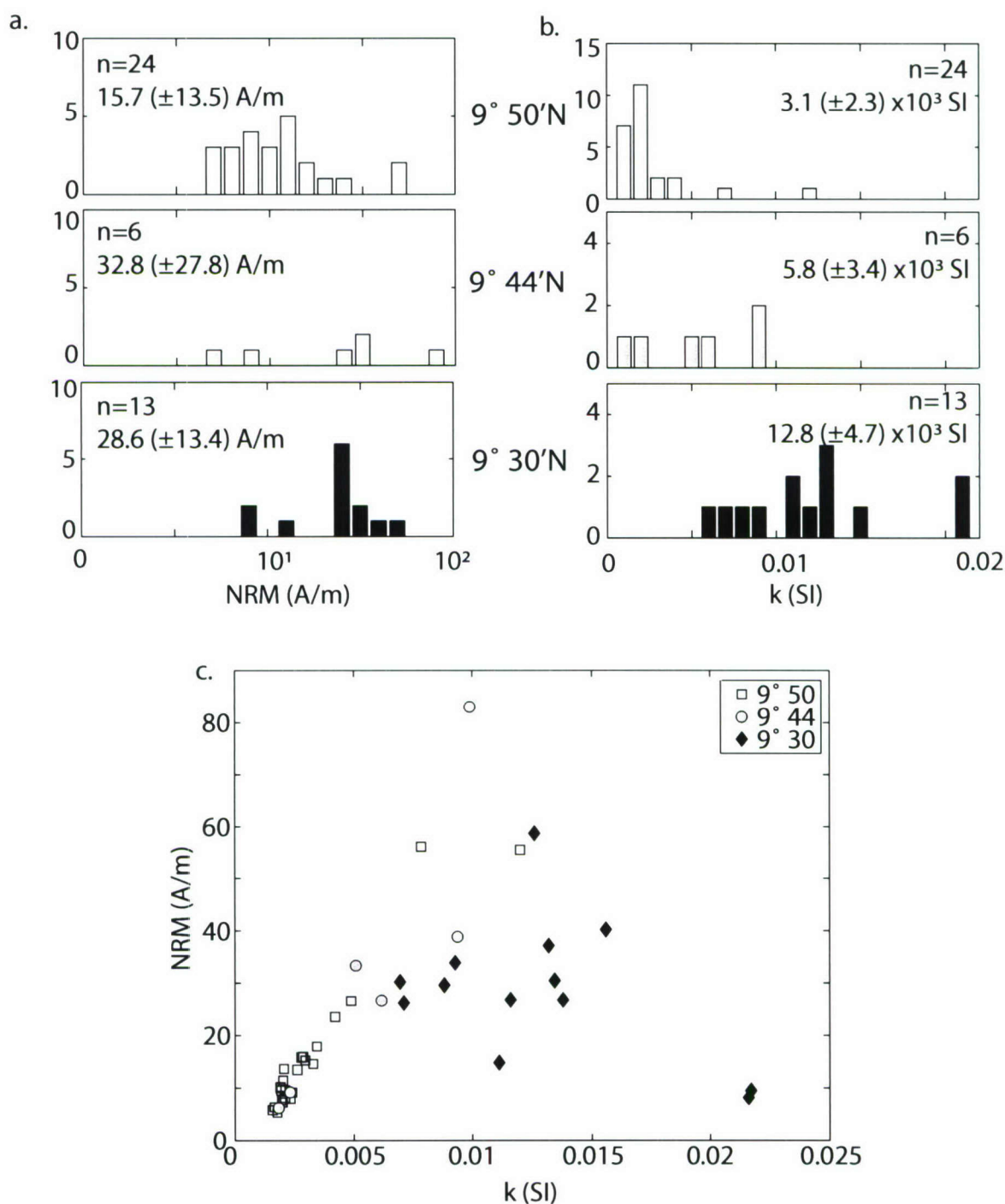
Figure A2-2a. Logarithmic histogram of natural remanent magnetization (NRM) for the 9° 50'N (white), 9° 44'N (grey) and 9° 30'N (black) regions respectively. Arithmetic mean is shown with one standard deviation in parenthesis, n is the numer of samples. **b**. Histogram of susceptibility (k) for the three regions. **c**. Plot of NRM versus k.
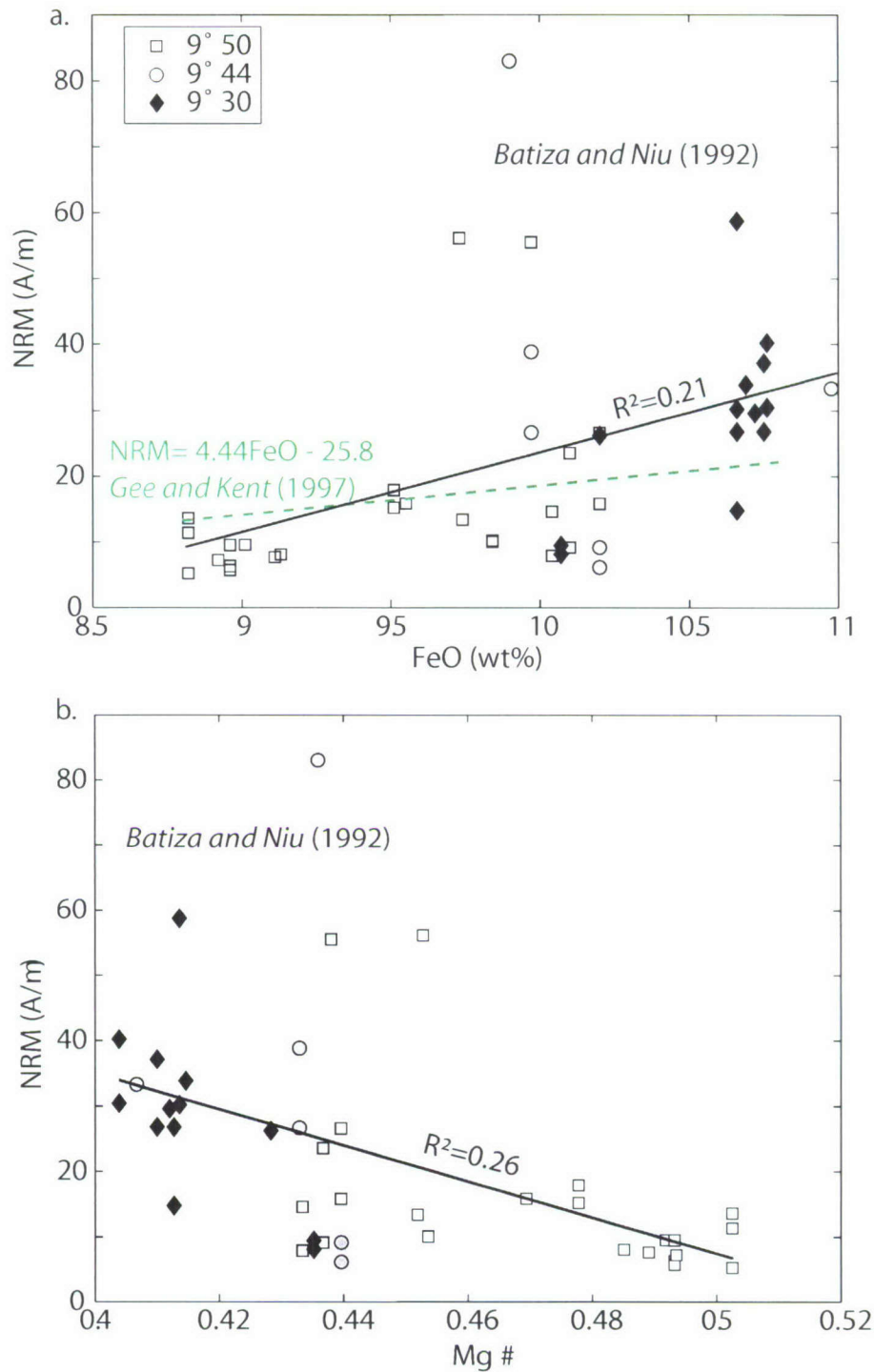
Figure A2-3.a. NRM versus iron oxide (FeO) content. Green dashed line shows relationship from *Gee and Kent* [1997], based on lavas collected between 14°-23°S on the East Pacific Rise (EPR). Grey box indicates range in FeO content from *Batiza and Niu* [1992], from samples collected between 9° 54-18'N on the EPR. **b**. NRM versus Mg# (MgO/(FeO+MgO)). Grey box represents results from *Batiza and Niu* [1992].
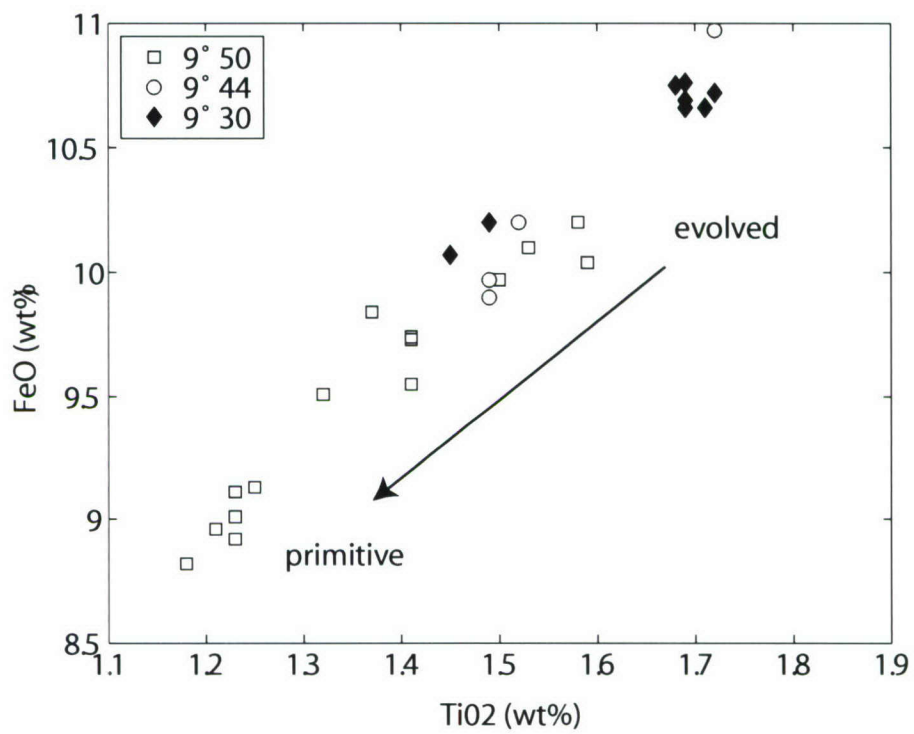
250

Figure A2-4. FeO versus TiO2 content for the three regions

GLOSSARY

ABE	Autonomous benthic explorer
AF	Alternating frequency
AMC	Axial magma chamber
AMS	Anisotropic magnetic susceptibility
AST	Axial summit trough
AUV	Autonomous underwater vehicle
BR	Basalt ridge
CA	Central anomaly
CAMH	Central anomaly magnetization high
CRM	Chemical remanent magnetization
EPR	East Pacific Rise
F	Planar degree of anisotropy
FLAC	Fast Lagrangian analysis of continua
FFT	Fast fourier transform
FORC	First-order reversal curve- class of partial hysteresis curves
FWHM	Full width at half maximum- FORC diagram parameter
GAD	Geocentric axial dipole- time averaged geomagnetic field
GMT	Generic mapping tool
GPS	Global positioning system
H_c	Coercivity- measure of magnetic stability. $(H_b-H_a)/2$ – coercivity distribution
H_{cr}	Coercivity of remanence- magnitude of the reverse field after saturation that results in zero net remanence
H_a	Specific reversal field for repeated FORC measurements
H_b	Specific applied field for repeated FORC measurements
H_u	$(H_a+H_b)/2$ – interaction field distribution
HWD	Hanging wall debris
IGRF	International geomagnetic reference field
k	Susceptibility
KMM	Kane Megamullion
L	Linear degree of anisotropy
MAR	Mid-Atlantic Ridge
MD	Multidomain
MDF	Median destructive field
Mr	Remanent magnetization- remaining magnetization after the inducing field is reduced to zero
Ms	Saturation remanent magnetization- samples largest magnetization
NRM	Natural remanent magnetization
NVZ	Neovolcanic zone
OCC	Ocean core complex
OSC	Overlapping spreading center
P	Average degree of anisotropy
PSD	Pseudo-single domain
Q ratio	Koenisberger ratio- ratio of remanent to induced magnetization

RMBA	Residual mantle Bouguer anomaly
ROV	Remotely operated vehicle
RTI	Ridge transform intersection
SD	Single domain
SF	Smoothing factor
SNOO	Small overlapping spreading center
SP	Superparamagnetic
SWIR	South West Indian Ridge
TRM	Thermoremanent magnetization
VADM	Virtual axial dipole moment- Earth's dipole moment with the dipole axis assumed to be the axis of rotation (geographic pole)

REPORT DOCUMENTATION PAGE	1. REPORT NO. **MIT/WHOI 2007-21**	2.	3. Recipient's Accession No.

4. Title and Subtitle

Oceanic Lithosphere Magnetization: Marine Magnetic Investigations of Crustal Accretion and Tectonic Processes in Mid-Ocean Ridge Environments

5. Report Date

September 2007

6.

7. Author(s) Clare M. Williams

8. Performing Organization Rept. No.

9. Performing Organization Name and Address

MIT/WHOI Joint Program in Oceanography/Applied Ocean Science & Engineering

10. Project/Task/Work Unit No.
MIT/WHOI 2007-21

11. Contract(C) or Grant(G) No.
(C) OCE-0221832
OCE-9819261
(G) OCE-0118445

12. Sponsoring Organization Name and Address

National Science Foundation
Geological Society of America
Academic Programs Office at Woods Hole Oceanographic Institution

13. Type of Report & Period Covered

Ph.D. Thesis

14.

15. Supplementary Notes

This thesis should be cited as: Clare M. Williams, 2007. Oceanic Lithosphere Magnetization: Marine Magnetic Investigations of Crustal Accretion and Tectonic Processes in Mid-Ocean Ridge Environments. Ph.D. Thesis. MIT/WHOI, 2007-21.

16. Abstract (Limit: 200 words)

The origin of symmetric alternating magnetic polarity stripes on the seafloor is investigated along East Pacific Rise (EPR) (9° 25'-9° 55'N) and Kane Megamullion (KMM) (23° 40'N) in the Atlantic. At the EPR, along-axis variations in the axial magnetic anomaly result from changing source layer thickness, consistent with observed changes in seismic Layer 2a. The extrusive basalts therefore constitute the magnetic source layer along the ridge axis and long term crustal accretion patterns are reflected in the axial anomaly appearance. At KMM the C2r.2r/C2An.1n (~2.581 Ma) polarity reversal boundary is recorded by lower crust (gabbro) and upper mantle (serpentinized peridotites) rocks exposed on the seafloor by detachment faulting. Both lithologies have stable remanent magnetization, capable of contributing to the magnetic source layer. The geometry of the polarity boundary in the northern KMM region, interpreted to be a gabbro pluton, dips away from the ridge axis and is consistent with a rotated conductively cooled isotherm. In the central region the boundary in the serpentinized peridotites dips towards the ridge axis and is thought to represent an alteration front. The linear appearance of the polarity boundary across the two regions suggests that both lithologies acquired their remanence at approximately the same time.

17. Document Analysis   a. Descriptors

mid-ocean ridge
magnetization
anomalies

b. Identifiers/Open-Ended Terms

c. COSATI Field/Group

18. Availability Statement

Approved for publication; distribution unlimited.

19. Security Class (This Report)
UNCLASSIFIED

20. Security Class (This Page)

21. No. of Pages
254

22. Price